

University of Windsor

Scholarship at UWindor

Electronic Theses and Dissertations

Theses, Dissertations, and Major Papers

2009

Methane Inverse Diffusion Flames with Co-flowing Air and Combustion Products

Michael Johnson
University of Windsor

Follow this and additional works at: <https://scholar.uwindsor.ca/etd>

Recommended Citation

Johnson, Michael, "Methane Inverse Diffusion Flames with Co-flowing Air and Combustion Products" (2009). *Electronic Theses and Dissertations*. 460.
<https://scholar.uwindsor.ca/etd/460>

This online database contains the full-text of PhD dissertations and Masters' theses of University of Windsor students from 1954 forward. These documents are made available for personal study and research purposes only, in accordance with the Canadian Copyright Act and the Creative Commons license—CC BY-NC-ND (Attribution, Non-Commercial, No Derivative Works). Under this license, works must always be attributed to the copyright holder (original author), cannot be used for any commercial purposes, and may not be altered. Any other use would require the permission of the copyright holder. Students may inquire about withdrawing their dissertation and/or thesis from this database. For additional inquiries, please contact the repository administrator via email (scholarship@uwindsor.ca) or by telephone at 519-253-3000ext. 3208.

Methane Inverse Diffusion Flames with Co-flowing Air and Combustion Products

by

Michael Bernard Johnson

A Dissertation

Submitted to the Faculty of Graduate Studies
through Mechanical Engineering
in Partial Fulfillment of the Requirements for
the Degree of Doctor of Philosophy at the
University of Windsor

Windsor, Ontario, Canada

2009

© 2009
Michael Bernard Johnson
All Rights Reserved

Methane Inverse Diffusion Flames with Co-flowing Air and Combustion Products

by

Michael Bernard Johnson

APPROVED BY:

Ö. Gülder, External Examiner
University of Toronto

J. Gauld
Department of Chemistry and Biochemistry

D. S.-K. Ting
Department of Mechanical, Automotive and Materials Engineering

G. W. Rankin
Department of Mechanical, Automotive and Materials Engineering

A. Sobiesiak, Adviser
Department of Mechanical, Automotive and Materials Engineering

R. J. Urbanic, Chair of Defense
Faculty of Graduate Studies and Research

May 29, 2009

Author's Declaration of Originality

I hereby certify that I am the sole author of this thesis and that no part of this thesis has been published or submitted for publication.

I certify that, to the best of my knowledge, my thesis does not infringe upon anyone's copyright nor violate any proprietary rights and that any ideas, techniques, quotations, or any other material from the work of other people included in my thesis, published or otherwise, are fully acknowledged in accordance with the standard referencing practices. Furthermore, to the extent that I have included copyrighted material that surpasses the bounds of fair dealing within the meaning of the Canada Copyright Act, I certify that I have obtained written permission from the copyright owner(s) to include such material(s) in my thesis and have included copies of such copyright clearances to my appendix.

I declare that this is a true copy of my thesis, including any final revisions, as approved by my thesis committee and the Graduate Studies office, and that this thesis has not been submitted for a higher degree to any other University or Institution.

Abstract

A geometry and reactant delivery method relevant to burners with low emission of nitrogen oxides is studied at the laboratory-scale. The design is an inverse diffusion flame of methane, with a central air jet discharging into a jet of fuel. Surrounding the fuel is an additional co-flow of either air or co-flowing combustion products from a premixed, burner-stabilized methane-air flame at lean, stoichiometric, or rich equivalence ratio. The co-flowing combustion products simulate the flow of combustion gases that would be present in a furnace employing a burner with low nitric oxide emissions. The location of the central air discharge is raised above the burner, to allow the fuel to mix with the co-flowing gas before reacting with the central air stream.

Characteristics of these flames are studied experimentally with excited-state CH^* chemiluminescence imaging, over the range of air velocities from zero to the transition to turbulent flow. Numerical simulations are validated through comparison with the experimental measurements of relative CH^* chemiluminescence emission. Simulation results are post-processed to account for chemiluminescent emission from the excited-state CH^* radical, and to model the non-ideality of the imaging system.

At low velocities of the central air jet, hysteresis behaviour of the inner flame is observed. A partially-premixed flame is formed on the centreline at a constant fraction of the outer diffusion flame height. When the central air velocity reaches a critical level, this flame propagates upstream and stabilizes closer to the burner face as an inverse diffusion flame. The spread in velocity between this transition, and the extinction of the inner flame as the central air velocity is decreased, is larger with co-flowing combustion products.

Simulation results are analyzed to explain the characteristics of the flames observed in the experimental images, and how these characteristics affect the heat release and pollutant emissions from the flames. As the central air velocity is increased, emission of nitric oxide is decreased, as more of the combustion takes place in a pre-mixed versus a diffusion flame, but this is offset by increased emissions of CO and

unburned fuel that are entrained into the central air jet and exit the simulation domain. Raising the discharge location of the central air stream tends to increase the emissions of nitric oxide, as the fuel is displaced outwards and more of it reacts in the diffusion flame.

Acknowledgements

Over 10 years ago, it was Prof. Andrzej Sobiesiak who sparked my interest in thermodynamics and combustion, and encouraged and inspired me to pursue research in this area. Working with him for my graduate research has been a pleasure. He gave me the freedom to pursue my own ideas, which was at times very difficult and frustrating, but ultimately lead to a deeper understanding which would not have been as rewarding otherwise. He was always enthusiastic for new results, always asking different questions, and helping me to look at things from a different perspective. I thank him for his help and support.

I thank Fengshan Liu of the National Research Council for his assistance with the numerical simulation code. This breadth of analysis would not have been possible without his assistance. Thanks to Dr. William Altenhof for lending us one of his computers, that was used for some of the initial calculations. The bulk of the numerical simulations were conducted on the WESTGRID and SHARCNET supercomputing facilities, and assistance from staff at both these facilities is much appreciated.

Andrew Jenner built the majority of the experimental facility and was always happy to take care of any problems I had, right away. His help was invaluable and is much appreciated. Our mountain biking discussions were a welcome break from the frustrations of graduate research.

Thanks to Dean Poublon, and Steve Budinsky and his staff at the Technical Support Centre for additional assistance with design and machining; to Patrick Seguin for his help with some of the electronics; to Bruce Durfy and Michael Charron for their help with lots of little issues that came up in the lab; and to Rose Gignac, Barb Denomey and Pattie LaFramboise for their administrative assistance.

This work was supported with NSERC Discovery, and Research Tools and Instrumentation grants. Funding from an Ontario Graduate Scholarship in Science and Technology, and from the University of Windsor Faculty of Graduate Studies is also gratefully acknowledged.

I appreciate the friendship of the other members of the research group—Chunyi

Xia, Prakash Gnanam, Dale Haggith, Hamid Toutouchian and Nima Gharib.

Thanks to my friend Jeffrey Bergthorson for always being available on the “technical support” line.

I thank my parents, Margaret and Keith, and my sister Sarah, for their unconditional love and support.

Contents

Author’s Declaration of Originality	iv
Abstract	v
Acknowledgements	vii
List of Tables	xi
List of Figures	xiii
List of Symbols	xxii
Chapter	
1 Introduction	1
1.1 Flameless oxidation	1
1.2 Inverse diffusion flames	3
1.3 Objective	4
1.4 Methodology	5
1.5 Outline	5
2 Experimental apparatus	7
2.1 Burner	7
2.2 Gas delivery	8
2.3 Chemiluminescence imaging system	11
3 Numerical modelling	13
4 Flame hysteresis behaviour at low central air velocities	17
5 Flame characteristics at higher central air velocities	29

6	Numerical simulation validation	36
6.1	CH* contours	36
6.2	Sensitivity analysis	47
7	Numerical simulation results	52
7.1	Flame characteristics	52
7.2	Heat release and emissions	62
8	Conclusions	78
Appendix		
A	Chemiluminescence imaging	80
A.1	Abel transform	80
A.2	Image averaging	84
A.3	Point-spread-function	88
B	Experimental chemiluminescence images	89
C	Experimental/numerical CH* contour comparisons	102
D	Numerical simulation analysis	127
D.1	Radial plots of species and temperature	127
E	Experiment and simulation matrix	135
	Bibliography	151
	Vita Auctoris	156

List of Tables

3.1	Co-flow velocities and temperatures used as inlet conditions in simulations.	14
3.2	Reactions used in calculation of CH^* concentration and emission (extracted from Walsh et al. 1998, and references therein).	15
7.1	Listing of in-flow conditions for three tube cases with $u_{\text{cf}} = 18.4$ cm/s.	74
E.1	Matrix of experimental conditions for air co-flow and flush central air tube.	136
E.2	Matrix of experimental conditions for air co-flow and central air tube raised 3 mm.	137
E.3	Matrix of experimental conditions for air co-flow and central air tube raised 6 mm.	138
E.4	Matrix of experimental conditions for $\Phi = 0.78$ co-flow and flush central air tube.	139
E.5	Matrix of experimental conditions for $\Phi = 0.78$ co-flow and central air tube raised 3 mm.	140
E.6	Matrix of experimental conditions for $\Phi = 0.78$ co-flow and central air tube raised 6 mm.	142
E.7	Matrix of experimental conditions for $\Phi = 1.0$ co-flow and flush central air tube.	143
E.8	Matrix of experimental conditions for $\Phi = 1.0$ co-flow and central air tube raised 3 mm.	144
E.9	Matrix of experimental conditions for $\Phi = 1.0$ co-flow and central air tube raised 6 mm.	145
E.10	Matrix of experimental conditions for $\Phi = 1.2$ co-flow and flush central air tube.	146
E.11	Matrix of experimental conditions for $\Phi = 1.2$ co-flow and central air tube raised 3 mm.	147

E.12 Matrix of experimental conditions for $\Phi = 1.2$ co-flow and central air
tube raised 6 mm. 149

List of Figures

2.1	Cross-section of experimental burner with example CH* flame image. The burner-stabilized flame is at equivalence ratio $\Phi = 0.78$	8
2.2	Top view of experimental burner, shown 1.5 times actual size. Perforated plate diameter 30 mm; central fuel tube 6.35 mm; central air tube 3.96 mm.	8
2.3	Section view of burner.	9
2.4	Gas delivery schematic.	10
3.1	Example simulation inlet velocity profile.	14
4.1	Flame chemiluminescence images illustrating the inner flame hysteresis, with co-flowing air and central air tube flush. From left to right are the normal diffusion flame, partially-premixed flame just before transition, stabilized inverse diffusion flame, and near-extinction inverse diffusion flame.	18
4.2	Flame chemiluminescence images with co-flowing combustion products at $\Phi = 0.78$ and central air tube flush. The burner-stabilized flame is visible at the bottom, and image intensity has been adjusted to improve visibility. From left to right are the normal diffusion flame, partially-premixed flame just before transition, stabilized inverse diffusion flame, and near-extinction inverse diffusion flame.	18
4.3	Velocities for transition from the partially-premixed flame (upper, thick line) and extinction of the inverse diffusion flame (lower, thin line).	19
4.4	(a) Flame heights of the partially-premixed flame (upper, thick line) and the near-extinction inverse diffusion flame (lower, thin line), plotted against the central fuel velocity. (b) Flame heights of the partially-premixed flame (upper, thick line) and the near-extinction inverse diffusion flame (lower, thin line), plotted against the central air velocity.	20

4.5	Experimental (thin line) and numerical (thick dashed line) contours of CH* emissions, scaled to the maximum value per image, showing the 10% contour. The three cases shown are the normal diffusion flame, partially-premixed flame, and stabilized inverse diffusion flame, and the experimental contours are calculated from the first three images in each set of Fig. 4.1. Co-flowing air and central fuel velocity (a) $u_{cf}=9.1$ cm/s, (b) $u_{cf}=17.3$ cm/s.	22
4.6	(a) Experimental (thin line) and numerical (thick dashed line) contours of CH* emissions, scaled as in Fig. 4.5. Experimental contours are calculated from the first three images in each set of Fig. 4.2. Co-flowing combustion products at $\Phi=0.78$, $u_{cf}=9.7$ cm/s.. (b) Simulated axial temperature (thick lines) and CH mass fraction (thin lines) on the centreline for the partially-premixed flame with co-flowing air (solid lines) at $u_{cf}=17.3$ cm/s, and co-flowing combustion products (dashed lines) at $u_{cf}=9.7$ cm/s.	23
4.7	(a) Centreline axial temperature from a series of simulations, starting with $u_{ca}=0$, and increasing u_{ca} , for $\Phi = 0.78$ co-flow and $u_{cf}=18.4$ cm/s. (b) Simulated contours of CH mass fraction for partially-premixed flame (grey dashed line) and inverse diffusion flame (black dashed line), scaled by the maximum for the partially-premixed flame, showing the 10% contour. Both simulations have the same in-flow conditions: $\Phi = 0.78$ co-flow, $u_{cf}=18.4$ cm/s, and $u_{ca}=64.0$ cm/s.	25
4.8	Sequence of CH mass fraction contours (10% of the maximum for the highest u_{ca} case) as u_{ca} is lowered towards extinction for (a) co-flowing air and (b) co-flowing combustion products at $\Phi = 0.78$, both at $u_{cf}=23.0$ cm/s.	26
4.9	Flame chemiluminescence images illustrating the inner flame hysteresis, with co-flowing air and central air tube raised 3 mm. From left to right are the normal diffusion flame, partially-premixed flame just before transition, stabilized inverse diffusion flame, and near-extinction inverse diffusion flame.	27

4.10	Flame chemiluminescence images with co-flowing combustion products at $\Phi = 0.78$ and central air tube raised 3 mm. The burner-stabilized flame is visible at the bottom, and image intensity has been adjusted to improve visibility. From left to right are the normal diffusion flame, partially-premixed flame just before transition, stabilized inverse diffusion flame, and near-extinction inverse diffusion flame.	27
4.11	(a) Central air velocity for transition from the partially-premixed flame with the central air tube raised by the amounts shown in the legend; (b) height of the partially-premixed flame (H_{premix}) above the burner, with the central air tube raised.	28
5.1	Sample sequence of flame images at $u_{\text{cf}} \sim 23.0$ cm/s, with central air tube flush, and co-flow given for each set of images.	31
5.2	Sample sequence of flame images at $u_{\text{cf}} \sim 23.0$ cm/s, with central air tube raised 3 mm, and co-flow given for each set of images.	32
5.3	Sample sequence of flame images at $u_{\text{cf}} \sim 23.0$ cm/s, with central air tube raised 6 mm, and co-flow given for each set of images.	33
6.1	Experimental (thin grey line: left side; thin black line: right side) and numerical (thick dashed line) CH^* contours with co-flowing air, $u_{\text{cf}} = 18.4$ cm/s, and u_{ca} given.	38
6.2	Experimental and numerical CH^* contours with co-flowing air, $u_{\text{cf}} = 23.0$ cm/s, and u_{ca} given. Legend as in Fig. 6.1.	39
6.3	Experimental and numerical CH^* contours with $\Phi = 0.78$ co-flow, $u_{\text{cf}} = 18.4$ cm/s, and u_{ca} given. Legend as in Fig. 6.1.	40
6.4	Experimental and numerical CH^* contours with $\Phi = 0.78$ co-flow, $u_{\text{cf}} = 23.0$ cm/s, and u_{ca} given. Legend as in Fig. 6.1.	41
6.5	Experimental and numerical CH^* contours with $\Phi = 1.0$ co-flow, $u_{\text{cf}} = 18.4$ cm/s, and u_{ca} given. Legend as in Fig. 6.1.	42
6.6	Experimental and numerical CH^* contours with $\Phi = 1.0$ co-flow, $u_{\text{cf}} = 23.0$ cm/s, and u_{ca} given. Legend as in Fig. 6.1.	43
6.7	Experimental and numerical CH^* contours with $\Phi = 1.2$ co-flow, $u_{\text{cf}} = 18.4$ cm/s, and u_{ca} given. Legend as in Fig. 6.1.	44
6.8	Experimental and numerical CH^* contours with $\Phi = 1.2$ co-flow, $u_{\text{cf}} = 23.0$ cm/s, and u_{ca} given. Legend as in Fig. 6.1.	45

6.9	Experimental and numerical CH* contours showing effects of in-flow temperature, with co-flowing air, central air tube flush, $u_{cf} = 23.0$ cm/s and (a) $u_{ca} = 124.9$ cm/s, (b) $u_{ca} = 603.0$ cm/s. Legend as in Fig. 6.1	48
6.10	Experimental and numerical CH* contours showing effects of in-flow temperature, with co-flowing air, central air tube raised 3 mm, $u_{cf} = 23.0$ cm/s and (a) $u_{ca} = 64.21$ cm/s, (b) $u_{ca} = 195.7$ cm/s (c) $u_{ca} = 595.9$ cm/s. Legend as in Fig. 6.1	49
6.11	Experimental and numerical CH* contours showing effects of in-flow temperature, with co-flowing air, central air tube raised 6 mm, $u_{cf} = 23.0$ cm/s and (a) $u_{ca} = 51.41$ cm/s, (b) $u_{ca} = 218.1$ cm/s. Legend as in Fig. 6.1	50
7.1	(a) Axial velocity and (b) temperature along streamline through the point of maximum destruction rate of CH ₄ , for co-flowing air and central air tube flush.	53
7.2	(a) Axial velocity and (b) temperature along streamline through the point of maximum destruction rate of CH ₄ , for co-flowing air and central air tube flush.	53
7.3	Radial profiles of species (solid: CH ₄ , dashed: O ₂ , dotted: CO ₂) and temperature (thick grey line) for co-flowing air, central air tube flush, $u_{cf} = 18.4$ cm/s, and $u_{ca} = 54.43$ cm/s. On the right is a contour of temperature (lightest shade of grey is 400 K, increasing by 200 K each contour line) and 10% of the maximum CH mass fraction in white.	54
7.4	Radial profiles of species and temperature, and contour plot of temperature and CH for co-flowing air, central air tube flush, $u_{cf} = 18.4$ cm/s, and $u_{ca} = 138.7$ cm/s (legend as in Fig. 7.3).	54
7.5	Radial profiles of species and temperature, and contour plot of temperature and CH for co-flowing air, central air tube flush, $u_{cf} = 18.4$ cm/s, and $u_{ca} = 506.9$ cm/s (legend as in Fig. 7.3).	55
7.6	Radial profiles of species and temperature, and contour plot of temperature and CH for co-flowing air, central air tube raised 6 mm, $u_{cf} = 18.4$ cm/s, and $u_{ca} = 78.97$ cm/s (legend as in Fig. 7.3).	56
7.7	Radial profiles of species and temperature, and contour plot of temperature and CH for co-flowing air, central air tube raised 6 mm, $u_{cf} = 18.4$ cm/s, and $u_{ca} = 239.6$ cm/s (legend as in Fig. 7.3).	56

7.8	Radial profiles of species and temperature, and contour plot of temperature and CH for co-flowing air, central air tube raised 6 mm, $u_{cf} = 18.4$ cm/s, and $u_{ca} = 754.2$ cm/s (legend as in Fig. 7.3).	57
7.9	Radial profiles of species and temperature, and contour plot of temperature and CH for $\Phi = 0.78$ co-flow, central air tube flush, $u_{cf} = 18.4$ cm/s, and $u_{ca} = 48.2$ cm/s (legend as in Fig. 7.3).	58
7.10	Radial profiles of species and temperature, and contour plot of temperature and CH for $\Phi = 0.78$ co-flow, central air tube flush, $u_{cf} = 18.4$ cm/s, and $u_{ca} = 108.2$ cm/s (legend as in Fig. 7.3).	58
7.11	Radial profiles of species and temperature, and contour plot of temperature and CH for $\Phi = 0.78$ co-flow, central air tube flush, $u_{cf} = 18.4$ cm/s, and $u_{ca} = 444.7$ cm/s (legend as in Fig. 7.3).	59
7.12	Radial profiles of species and temperature, and contour plot of temperature and CH for $\Phi = 0.78$ co-flow, central air tube raised 6 mm, $u_{cf} = 18.4$ cm/s, and $u_{ca} = 85.91$ cm/s (legend as in Fig. 7.3).	60
7.13	Radial profiles of species and temperature, and contour plot of temperature and CH for $\Phi = 0.78$ co-flow, central air tube raised 6 mm, $u_{cf} = 18.4$ cm/s, and $u_{ca} = 200.8$ cm/s (legend as in Fig. 7.3).	61
7.14	Radial profiles of species and temperature, and contour plot of temperature and CH for $\Phi = 0.78$ co-flow, central air tube raised 6 mm, $u_{cf} = 18.4$ cm/s, and $u_{ca} = 569.2$ cm/s (legend as in Fig. 7.3).	61
7.15	Total heat release, normalized by the chemical energy input from the fuel ($\dot{m}_{CH_4} \cdot LHV_{CH_4}$). Air tube: flush (solid line), raised 3 mm (dashed line), and raised 6 mm (dotted line).	63
7.16	Fraction of unburned fuel at the exit of the simulation domain. Air tube: flush (solid line), raised 3 mm (dashed line), and raised 6 mm (dotted line).	64
7.17	Change in mass flow-rate of CO, scaled by the inlet mass flow-rate of fuel. Air tube: flush (solid line), raised 3 mm (dashed line), and raised 6 mm (dotted line).	65
7.18	Emission index of NO. Air tube: flush (solid line), raised 3 mm (dashed line), and raised 6 mm (dotted line).	67
7.19	Radial integral of net production rate of NO for air co-flow at $u_{cf} = 18.4$ cm/s. The thick grey line is for $u_{ca} = 0$ and central air tube flush. The legend is above the small contours of 10% maximum CH mass fraction on the right, with u_{ca} given underneath each contour.	69

7.20	Radial integral of net production rate of NO for $\Phi = 0.78$ co-flow at $u_{cf} = 18.4$ cm/s. The thick grey line is for $u_{ca} = 0$ and central air tube flush. The legend is above the small contours of 10% maximum CH mass fraction on the right, with u_{ca} given underneath each contour.	70
7.21	Radial integral of net production rate of NO for $\Phi = 1.0$ co-flow at $u_{cf} = 18.4$ cm/s. The thick grey line is for $u_{ca} = 0$ and central air tube flush. The legend is above the small contours of 10% maximum CH mass fraction on the right, with u_{ca} given underneath each contour.	71
7.22	Radial integral of net production rate of NO for $\Phi = 1.2$ co-flow at $u_{cf} = 18.4$ cm/s. The thick grey line is for $u_{ca} = 0$ and central air tube flush. The legend is above the small contours of 10% maximum CH mass fraction on the right, with u_{ca} given underneath each contour.	72
7.23	Contours of NO production—10% of maximum (black line); 10% of minimum (grey line)—and contours of local equivalence ratio equal to one (dotted line) for the flames listed in Table 7.1, at $u_{cf} = 18.4$ cm/s, and co-flow given.	75
7.24	Radially-integrated net production rates of NO for flames listed in Table 7.1 at $u_{cf} = 18.4$ cm/s, and co-flow given.	76
A.1	Example flame image, with centreline in white.	81
A.2	Abel inversion of data from Fig. A.1. Data from the right-hand side in black, and from the left-hand side in grey.	81
A.3	Sequence of images with increasing $f/\#$	83
A.4	Percent error in CH* layer thickness (relative to value at $f/32$) as a function of $f/\#$ for flames shown in Fig. A.3.	83
A.5	Image of resolution target taken at nominal focus position. Streaks from Group 0, Element 1 used for calculating magnification are seen at the lower-left corner, and the square (Group 0, Element 2) used for estimating the point-spread function (Section A.3) of the imaging system can be seen on the right-hand side.	84
A.6	Scaled and inverted pixel intensity through Group 0, Element 1 line pairs, and start (S) and end (E) of streaks.	85
A.7	Magnification changes. Dashed lines are at $\pm 1\%$ of the magnification at the nominal position.	85
A.8	CH* emission data from one pixel row and one image (dashed line), and fit (solid line) from Eqn. A.2.	86

A.9	Histogram of (a) peak CH* location and (b) CH* layer width from curve fits to single images.	87
A.10	CH* emission data from one pixel row and the average of 256 images (dashed line), and fit calculated from average fit parameters (solid line) and Eqn. A.2.	87
A.11	Normalized intensity profile through square of target image (Fig. A.5). Experimental data (circles) and fit (line) using Eqn. A.3.	88
B.1	Air co-flow, central air tube flush.	90
B.2	Air co-flow, central air tube raised 3mm.	91
B.3	Air co-flow, central air tube raised 6mm.	92
B.4	$\Phi = 0.78$ co-flow, central air tube flush.	93
B.5	$\Phi = 0.78$ co-flow, central air tube raised 3 mm.	94
B.6	$\Phi = 0.78$ co-flow, central air tube raised 6 mm.	95
B.7	$\Phi = 1.0$ co-flow, central air tube flush.	96
B.8	$\Phi = 1.0$ co-flow, central air tube raised 3 mm.	97
B.9	$\Phi = 1.0$ co-flow, central air tube raised 6 mm.	98
B.10	$\Phi = 1.2$ co-flow, central air tube flush.	99
B.11	$\Phi = 1.2$ co-flow, central air tube raised 3 mm.	100
B.12	$\Phi = 1.2$ co-flow, central air tube raised 6 mm.	101
C.1	Air co-flow, $u_{cf}=18.4$ cm/s, air tube flush.	103
C.2	Air co-flow, $u_{cf}=18.4$ cm/s, air tube raised 3 mm.	104
C.3	Air co-flow, $u_{cf}=18.4$ cm/s, air tube raised 6 mm.	105
C.4	$\Phi = 0.78$ co-flow, $u_{cf}=18.4$ cm/s, air tube flush.	106
C.5	$\Phi = 0.78$ co-flow, $u_{cf}=18.4$ cm/s, air tube raised 3mm.	107
C.6	$\Phi = 0.78$ co-flow, $u_{cf}=18.4$ cm/s, air tube raised 6mm.	108
C.7	$\Phi = 1.0$ co-flow, $u_{cf}=18.4$ cm/s, air tube flush.	109
C.8	$\Phi = 1.0$ co-flow, $u_{cf}=18.4$ cm/s, air tube raised 3mm.	110
C.9	$\Phi = 1.0$ co-flow, $u_{cf}=18.4$ cm/s, air tube raised 6mm.	111
C.10	$\Phi = 1.2$ co-flow, $u_{cf}=18.4$ cm/s, air tube flush.	112
C.11	$\Phi = 1.2$ co-flow, $u_{cf}=18.4$ cm/s, air tube raised 3 mm.	113
C.12	$\Phi = 1.2$ co-flow, $u_{cf}=18.4$ cm/s, air tube raised 6 mm.	114
C.13	Air co-flow, $u_{cf}=23.0$ cm/s, air tube flush.	115
C.14	Air co-flow, $u_{cf}=23.0$ cm/s, air tube raised 3 mm.	116
C.15	Air co-flow, $u_{cf}=23.0$ cm/s, air tube raised 6 mm.	117
C.16	$\Phi = 0.78$ co-flow, $u_{cf}=23.0$ cm/s, air tube flush.	118

C.17	$\Phi = 0.78$ co-flow, $u_{cf}=23.0$ cm/s, air tube raised 3mm.	119
C.18	$\Phi = 0.78$ co-flow, $u_{cf}=23.0$ cm/s, air tube raised 6mm.	120
C.19	$\Phi = 1.0$ co-flow, $u_{cf}=23.0$ cm/s, air tube flush.	121
C.20	$\Phi = 1.0$ co-flow, $u_{cf}=23.0$ cm/s, air tube raised 3mm.	122
C.21	$\Phi = 1.0$ co-flow, $u_{cf}=23.0$ cm/s, air tube raised 6mm.	123
C.22	$\Phi = 1.2$ co-flow, $u_{cf}=23.0$ cm/s, air tube flush.	124
C.23	$\Phi = 1.2$ co-flow, $u_{cf}=23.0$ cm/s, air tube raised 3 mm.	125
C.24	$\Phi = 1.2$ co-flow, $u_{cf}=23.0$ cm/s, air tube raised 6 mm.	126
D.1	Radial profiles of species (solid: CH ₄ , dashed: O ₂ , dotted: CO ₂) and temperature (thick grey line) for $\Phi = 1.0$ co-flow, central air tube flush, $u_{cf} = 18.4$ cm/s, and $u_{ca} = 54.61$ cm/s. On the right is a contour of temperature (lightest shade of grey is 400 K, increasing by 200 K each contour line) and 10% of the maximum CH mass fraction in white.	128
D.2	Radial profiles of species and temperature, and contour plot of temperature and CH for $\Phi = 1.0$ co-flow, central air tube flush, $u_{cf} = 18.4$ cm/s, and $u_{ca} = 145.7$ cm/s (legend as in Fig. D.1).	128
D.3	Radial profiles of species and temperature, and contour plot of temperature and CH for $\Phi = 1.0$ co-flow, central air tube flush, $u_{cf} = 18.4$ cm/s, and $u_{ca} = 611.9$ cm/s (legend as in Fig. D.1).	129
D.4	Radial profiles of species and temperature, and contour plot of temperature and CH for $\Phi = 1.0$ co-flow, central air tube raised 6 mm, $u_{cf} = 18.4$ cm/s, and $u_{ca} = 105.8$ cm/s (legend as in Fig. D.1).	129
D.5	Radial profiles of species and temperature, and contour plot of temperature and CH for $\Phi = 1.0$ co-flow, central air tube raised 6 mm, $u_{cf} = 18.4$ cm/s, and $u_{ca} = 272.3$ cm/s (legend as in Fig. D.1).	130
D.6	Radial profiles of species and temperature, and contour plot of temperature and CH for $\Phi = 1.0$ co-flow, central air tube raised 6 mm, $u_{cf} = 18.4$ cm/s, and $u_{ca} = 446.5$ cm/s (legend as in Fig. D.1).	130
D.7	Radial profiles of species and temperature, and contour plot of temperature and CH for $\Phi = 1.2$ co-flow, central air tube flush, $u_{cf} = 18.4$ cm/s, and $u_{ca} = 57.27$ cm/s (legend as in Fig. D.1).	131
D.8	Radial profiles of species and temperature, and contour plot of temperature and CH for $\Phi = 1.2$ co-flow, central air tube flush, $u_{cf} = 18.4$ cm/s, and $u_{ca} = 127.9$ cm/s (legend as in Fig. D.1).	131

D.9	Radial profiles of species and temperature, and contour plot of temperature and CH for $\Phi = 1.2$ co-flow, central air tube flush, $u_{cf} = 18.4$ cm/s, and $u_{ca} = 434.0$ cm/s (legend as in Fig. D.1).	132
D.10	Radial profiles of species and temperature, and contour plot of temperature and CH for $\Phi = 1.2$ co-flow, central air tube raised 6 mm, $u_{cf} = 18.4$ cm/s, and $u_{ca} = 109.2$ cm/s (legend as in Fig. D.1).	133
D.11	Radial profiles of species and temperature, and contour plot of temperature and CH for $\Phi = 1.2$ co-flow, central air tube raised 6 mm, $u_{cf} = 18.4$ cm/s, and $u_{ca} = 193.7$ cm/s (legend as in Fig. D.1).	134
D.12	Radial profiles of species and temperature, and contour plot of temperature and CH for $\Phi = 1.2$ co-flow, central air tube raised 6 mm, $u_{cf} = 18.4$ cm/s, and $u_{ca} = 383.1$ cm/s (legend as in Fig. D.1).	134

List of Symbols

Φ	equivalence ratio
$\dot{\omega}_i$	net production rate of species i [kmol/cm ³ /s]
$[i]$	molar concentration of species i [kmol/cm ³]
C	circle of confusion
$f/\#$	lens f -number, ratio of focal length to aperture diameter
FWHM	full width at half maximum
ICCD	Intensified Charge Coupled Device
IDF	inverse diffusion flame
LHV	lower heating value of methane fuel (50.07 MJ/kg)
\dot{m}_i	mass flow-rate of species i [kg/s]
PPF	partially-premixed flame
Re	Reynolds number
u_{cf}	central fuel plug-flow velocity based on measured volumetric flow-rate at room temperature
u_{ca}	central air plug-flow velocity based on measured volumetric flow-rate at room temperature
V_{em}	volume in the flow corresponding to one pixel

Chapter 1

Introduction

1.1 Flameless oxidation

In order to increase the thermal efficiency of reheating furnaces, regenerative burners have been employed. These burners use a heat exchanger to extract thermal energy from exhaust gases and preheat incoming air. However, increased air temperatures lead to higher emissions of nitrogen oxides (NO_x) through the thermal mechanism (Miller and Bowman 1989). Flameless oxidation is a mode of combustion that can be employed with or without air preheat, while maintaining low NO_x emissions.

In flameless oxidation, fuel and oxidizer are injected directly into the furnace cavity. Through design and placement of the fuel and air nozzles, each jet entrains combustion products from within the furnace that have been cooled by heat transfer to the load. This spreads the reaction zone over a large area compared to premixed flames, and lowers the peak temperatures in the reaction zone, decreasing the NO_x emissions from the thermal mechanism. In practice, there is no definite flame visible within the furnace, hence the name. This extended reaction zone also provides more uniform heat transfer to the load, minimizing the appearance of hot-spots.

Wünning and Wünning (1997) were one of the first to pioneer the concept and produced a map of the stability regions for flameless oxidation. They characterized the regions of combustion stability in terms of the furnace temperature and the exhaust gas recirculation rate,

$$K_V = \frac{\dot{M}_E}{\dot{M}_F + \dot{M}_A} \quad (1.1)$$

where \dot{M} is the flow-rate of (E) recirculated exhaust gas, (F) fuel, and (A) air into the reaction zone. They found that stable combustion is possible at all furnace temperatures for $K_V \leq 0.5$ (somewhat higher K_V is possible at higher furnace temperatures).

For $K_V \geq 3$ another stable mode of combustion is possible, with furnace temperatures greater than 800 °C, which is approximately the auto-ignition temperature of the fuel. This region is called flameless oxidation. Variations on the concept also call it moderate and intense low-oxygen dilution (MILD) combustion, and high-temperature air combustion (HTAC). It is not possible to operate a furnace solely in flameless oxidation mode, and a premixed burner typically needs to be fired to bring the furnace to a sufficiently high temperature before switching to flameless mode.

Much work has been done on fairly large-scale furnace experiments operating in flameless oxidation mode. One common setup is the use of the regenerative burner coupled to various nozzle designs. Flow enters alternately from each side of the furnace and the enthalpy of the exhaust gases is transferred to a regenerative heat exchanger which is then used to preheat the incoming air. A pilot flame is used to heat up the furnace before switching to flameless oxidation mode, and in some cases is fired at all times, to ensure continuous combustion. In flameless oxidation mode, the fuel jet is separated from the air jet, allowing for the fuel and air jets to entrain furnace combustion products before entering the reaction zone.

Yang and Blasiak (2005) used a variation on the switching regenerative furnace. In their burner, a central fuel jet is surrounded by 6 pairs of jets. Within each pair, one jet is an air inlet and the other is an exhaust gas outlet. Each jet is connected to a regenerator and the air inlet and exhaust gas outlet is switched every 10 seconds. As the fuel jet remains in the same position and the air jets are only slightly shifted each time, a nearly-constant flame position is produced.

Other studies have used steady-flow regenerative burners that are simpler to measure and interpret, as the flow is not being alternated. Plessing et al. (1998) studied the FLOX burner of Wüning and Wüning (1997), which consists of a central fuel jet surrounded by six air jets, again surrounded by an annulus of reverse-flowing combustion products. They measured temperature with Rayleigh thermometry and OH radical concentration with laser-induced predissociative fluorescence. They compared the flameless oxidation combustion zone to a turbulent bunsen flame and noted the relatively uniform temperature and OH concentration fields in flameless oxidation. Özdemir and Peters (2001) studied a similar type of burner and measured velocities with LDV, residence times with Mie scattering, and temperature and OH concentration with the same techniques as Plessing et al. (1998). They note that the high inert content of the fuel and air jets leads to slower chemistry, with time scales on the order of the flow time scales. The temperature rise is thus much lower than in typical combustion, suppressing the thermal NO_x formation.

Sobiesiak et al. (1998) studied the Canadian Gas Research Institute (CGRI) burner. The burner has 7 pairs of fuel and air jets arranged in a circle around a central pilot flame. Several burners were tested with air jets angled at 10° to the burner axis, and fuel jet angles ranging from 30 – 65° . These burners were tested under various furnace configurations, loads, temperatures and air preheat levels. They related the flow and mixing to the “strong-jet/weak-jet” model of Grandmaison et al. (1998). In the initial zone of this model, fuel and air jets each entrain combustion products from the furnace, and the weak fuel jet is itself entrained by the strong air jet, up to the point where they begin to mix. In the main combustion zone, fuel and air, and entrained combustion products react, and downstream the combustion products are further diluted with furnace gases. They found very low NO_x emissions and postulated that this might be due to fuel-rich oxidation and NO_x reburning in the fuel jets as they entrain combustion products from within the furnace.

Fleck (1998) and Fleck et al. (2000) made more detailed measurements on a single burner with 10° air and 15° fuel jet angles. They measured velocity, temperature and concentrations of O_2 , CO_2 , CO , NO_x , and CH_4 . From the CH_4 measurements they estimate that the fuel jet was diluted with 7-8 parts furnace gas to one part fuel at the point where it meets the air jet. NO_x emissions were also very low, around 6 ppm.

In another variation, Weber et al. (1999, 2000, 2001, 2005) used a pre-combustor with lean combustion of natural gas with air to which oxygen was added to maintain the oxygen concentration at 21%. This simulates the air preheating present in the regenerative furnaces. To this system they coupled several different nozzle configurations and tested different fuels—natural gas, light and heavy fuel oils, and coal. They measured velocity, temperature, radiation, and concentrations of O_2 , CO , CO_2 , CH_4 , H_2 , and soot. The burners in their studies consisted of a plate with a central air jet surrounded by 2 or 4 fuel jets/atomizers. They note the uniform temperature and chemistry fields within the furnace, similar to a well-stirred reactor, as well as the significant entrainment of combustion products into both the fuel and air jets. In their 1999 study they note a need for more fundamental study on a fuel jet injected into hot combustion products, similar to Sobiesiak et al. (1998), who postulated fuel-rich oxidation in the fuel jets.

1.2 Inverse diffusion flames

From these studies, an essential aspect of the flameless oxidation regime is the mixing of fuel with combustion products before reacting with air. In several of these studies,

the burner consisted of a central air jet surrounded by fuel jets. This is similar to the inverse diffusion flame (IDF), where a central air jet discharges into a co-flowing fuel jet, the inverse of a “normal” diffusion flame (NDF), with fuel discharging into co-flowing air.

Wu and Essenhigh (1984) mapped the structure of inverse diffusion flames of methane. They identified six different flame types in a map of air and fuel jet velocities. They used gas chromatography to measure species concentrations, and found a pool of CO and H₂ at the top of the flames. Wentzell (1998) extended the study to turbulent methane-air inverse diffusion flames with co-flowing air and inert gases, and Sobiesiak and Wentzell (2005) characterized the stability limits of these flames. They note the presence of partial premixing which evolves into a well-mixed reaction zone on the flame centerline. As the level of premixing increases, the range of fuel jet velocities producing stable flames is increased.

At the laboratory-scale, flames generated by reaction with combustion products have been studied in several different configurations. Partridge et al. (1999) studied inverse diffusion flames of air burning with combustion products from a fuel-rich premixed ethane-air flat flame and measured temperature with thermocouples, and NO concentration with laser-saturated fluorescence. They note that most of the additional NO was generated at the tip of the flame. Cabra et al. (2005) studied a fuel jet in a vitiated co-flow created from an array of lean hydrogen-air flames. Dally et al. (2002) studied methane-hydrogen flames stabilized in a hot co-flow of variable oxygen concentrations, [O₂], of 3, 6 and 9%, called jet in hot co-flow (JHC). Using Raman-Rayleigh-laser-induced fluorescence they measured point-wise temperature and species concentrations, and found that at [O₂] = 3%, a different chemical pathway is present for NO formation.

1.3 Objective

While these studies looked at either fuel flowing in an oxidizer co-flow, or air in a fuel co-flow, the current work focuses on an initially non-premixed configuration of fuel and air issuing into an additional co-flow of either air or co-flowing combustion products from a burner-stabilized flame. The products of the burner-stabilized flame act as the furnace gases that the fuel and air jets would entrain in the flameless oxidation burners. A central air jet discharges inside an annular fuel jet, which is surrounded by the co-flowing air or combustion products. This creates a “double” flame structure—an outer diffusion flame between the fuel and the co-flow, and an

inner flame between the central air and fuel flows.

This three-feed mixing configuration is analogous to that encountered in the flameless oxidation burners. The central air jet is raised above the burner face, providing additional time for the fuel to mix with the co-flowing combustion products before reacting with the air. It is postulated that raising the central air jet will reduce the NO_x emissions, as occurs in flameless oxidation.

The configuration studied here has also been called a tri-axial burner by Ko et al. (2005). They analyzed the flames both theoretically, using a modified Burke-Schumann (Burke and Schumann 1928) analysis including the effects of axial diffusion and unequal stream velocities (Chung and Law 1984), and experimentally. They note the history-dependent flame configuration of the inner diffusion flame as the inner air flow rate is changed. Kamal (2008) studied a similar burner configuration of an air tube inside a fuel tube with an outer co-flow of air, and were able to decrease NO_x emissions with high turbulence and entrainment between air and fuel.

1.4 Methodology

Flames are imaged with excited-state CH^* radical chemiluminescence (Schefer 1997), and these results are compared to numerical simulation data from a two-dimensional laminar flame calculation with detailed chemical kinetics. The numerical simulation methodology is validated through comparison with experiments conducted over a wide range of co-flow stoichiometries, and central air and fuel inlet velocities. Detailed information about the flames is extracted from the simulation data. Characteristic features of the flames are discussed, and the effects of these on the total heat release and pollutant emissions is analyzed.

1.5 Outline

The experimental burner, gas delivery and chemiluminescence imaging systems are described in Chapter 2, and the numerical simulation methodology is presented in Chapter 3. Chapter 4 discusses the behaviour of the flames at low central air velocities, where there is a hysteresis behaviour associated with the inner flame. Chapter 5 discusses the flame behaviour at higher central air velocities from the experimental images. Chapter 6 shows a comparison between the experimental and numerical results to validate the numerical simulation methodology, including a discussion of the sensitivity of the flames to the inlet temperatures. Chapter 7 presents the de-

tailed analysis of the numerical simulation results, discussing the characteristics of the flames, the overall heat release and emissions, and how these are affected by raising the central air tube above the burner face. Conclusions are presented in Chapter 8.

Chapter 2

Experimental apparatus

2.1 Burner

Figure 2.1 shows a cross-section along the centreline of the burner used in this work, and an example flame image. Flame images presented have been inverted so that dark regions correspond to higher levels of CH^* chemiluminescence emission. A 30 mm diameter brass plate with an array of 1114 0.5 mm diameter holes provides co-flowing air, or co-flowing combustion products from a flat, premixed, burner-stabilized flame. The flame visible in Fig. 2.1 is a burner-stabilized flame at equivalence ratio $\Phi = 0.78$. Within the centre of the perforated plate, a 6.35 mm outer diameter tube supplies methane fuel and, within this tube, a 3.96 mm outer diameter tube supplies air. Both tubes have a wall thickness of 0.254 mm. An outer, normal diffusion flame is formed between the central fuel flow and the co-flowing gas, and an inner, inverse diffusion flame is formed between the central air and fuel flows. The inner flame is called an inverse diffusion flame as the delivery of reactants, air into fuel, is the inverse of the “normal” reactant delivery of fuel into co-flowing air. Figure 2.2 shows a top-view photograph of the burner face.

Three cases were studied, with the air tube positioned flush with the burner face, and raised above the burner face by 3 mm and 6 mm. For flames in this work with co-flowing air, the co-flow velocity was 16.27 cm/s. For flames with co-flowing combustion products, these were generated from a premixed methane-air flame at equivalence ratios $\Phi = 0.78, 1.0$ and 1.2. Surrounding the perforated plate is a curtain of inert nitrogen gas to stabilize and shield the flames from ambient air. The flow-rate of the nitrogen was set just high enough to damp out any visible flame oscillations, as much as possible. Flames were studied at central fuel velocities over the range $u_{\text{cf}}=8.5\text{--}27.6$ cm/s, and central air velocities over the range $u_{\text{ca}}=0\text{--}1000$ cm/s, with

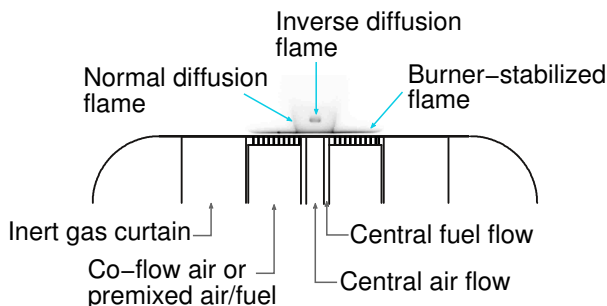


Figure 2.1: Cross-section of experimental burner with example CH^* flame image. The burner-stabilized flame is at equivalence ratio $\Phi = 0.78$.

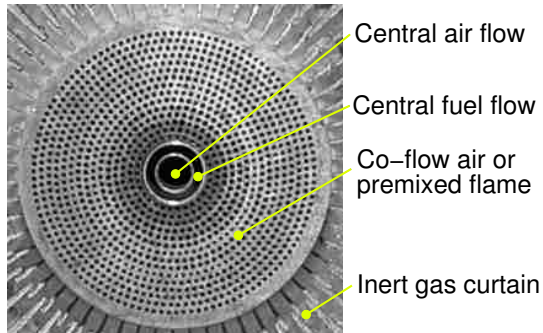


Figure 2.2: Top view of experimental burner, shown 1.5 times actual size. Perforated plate diameter 30 mm; central fuel tube 6.35 mm; central air tube 3.96 mm.

the complete list of experimental conditions listed in Appendix E.

Figure 2.3 shows a section view of the gas flow to the burner head. The central fuel and air flows are delivered through stainless steel tubes and separated at the bottom of the burner with a Swagelok union connector. Below the surface of the burner, a sintered metal sleeve in the fuel annulus helps align the tubes concentrically. The co-flow stream flows through two inlets at the bottom of the outer annulus. Glass beads distribute the flow around the annulus, and the teflon nozzle at the top accelerates the flow towards the perforated plate. The gas for the inert curtain is delivered into an annular channel surrounding the burner, and distributed through glass beads.

2.2 Gas delivery

Figure 2.4 shows a schematic of the gas delivery system for the burner. All gases are supplied from compressed gas bottles. Flow-rates are controlled with metering valves (Swagelok B-SS4 for co-flow fuel and central fuel, B-SS2-D for central air, and B-4MG for co-flow air), and measured with electronic mass flow-meters (Alicat Scientific M-2SLPM-D/5M for co-flow fuel and central fuel, M-2SLPM-D/5M or M-10SLPM-D/5M for central air, and M-20SLPM-D/5M for co-flow air). The gas for the inert gas curtain is supplied from a bottle of compressed nitrogen gas and metered through a rotameter (Omega FL-1448-G). Over the course of each flame experiment, the flow-rates fluctuated by no more than 1% of the reading. Central fuel and air velocities quoted in this work (u_{cf} and u_{ca}) are the plug-flow velocities based on the measured flow-rate at room temperature and pressure, upstream of the burner.

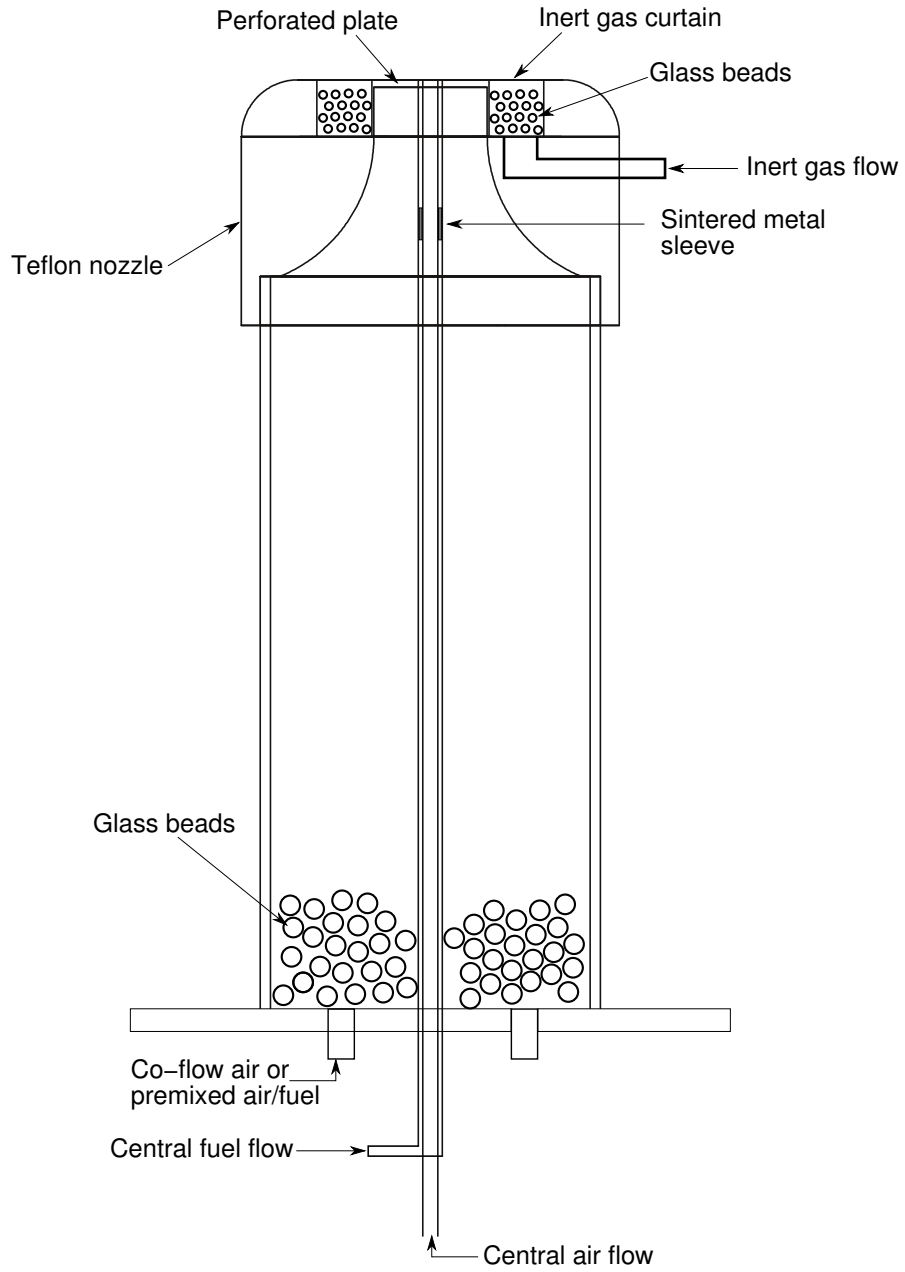


Figure 2.3: Section view of burner.

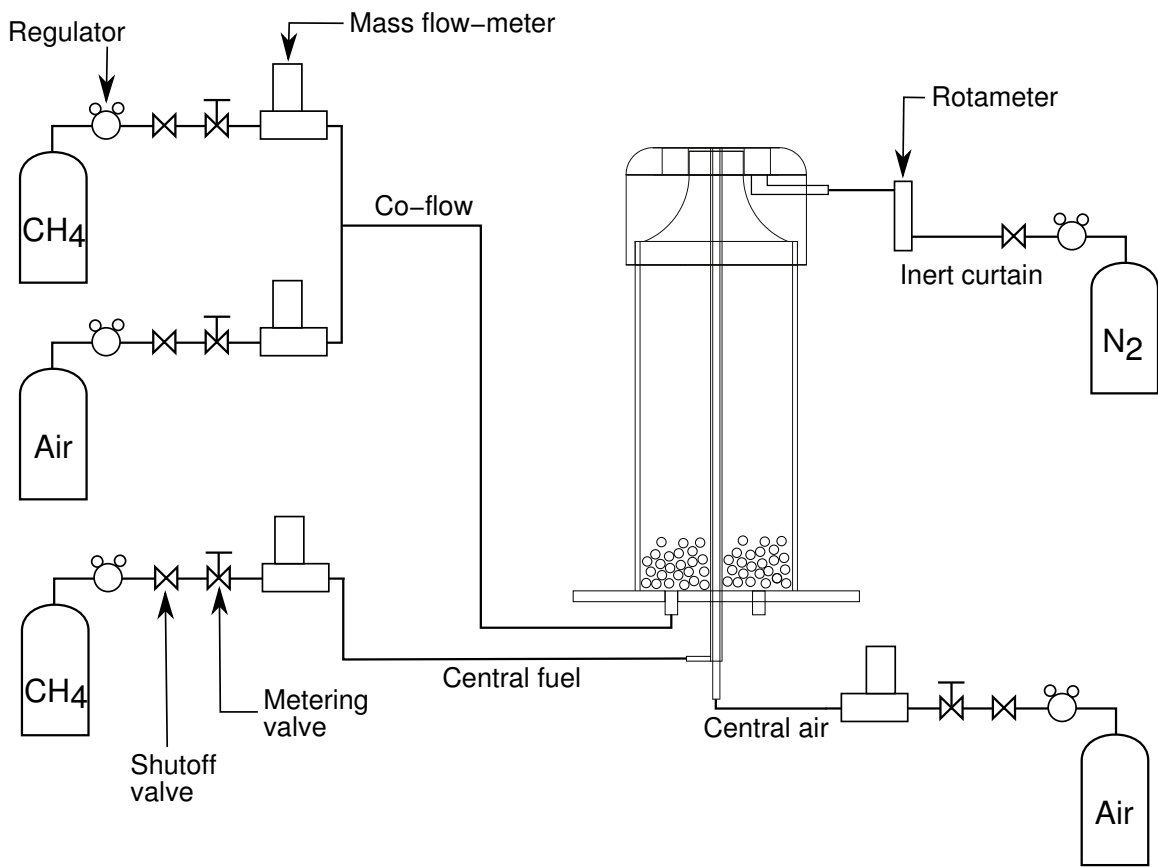


Figure 2.4: Gas delivery schematic.

2.3 Chemiluminescence imaging system

In this work, flame structure is measured by imaging chemiluminescence from the excited-state CH radical (denoted CH^{*}). The CH radical was chosen as it exists “near the flame-front, and reveals where the combustion chemistry is taking place” (Crosley 1989). It is also important in the “prompt” NO formation mechanism, responsible for NO formation at lower temperatures, typical of advanced low-NO_x burners (Renfro et al. 2001).

Point-wise measurements of CH^{*} and OH^{*} chemiluminescence have been used to investigate the local flame-front structure in a premixed laminar Bunsen flame (Kojima et al. 2005), and in a turbulent premixed flame (Ikeda et al. 2000). Marley and Roberts (2005) used high-speed imaging of CH^{*} chemiluminescence to determine flame speeds of premixed spherical flames. Schefer (1997) imaged moderately turbulent CH₄-air jet flames at Reynolds numbers 7000 and 12100, also noting that the CH chemiluminescence signal originates in the flame zone. Walsh et al. (1998) studied laminar diffusion flames with ground-state CH planar laser induced fluorescence, and excited-state CH^{*} and OH^{*} chemiluminescence, finding good agreement between their experiments and computations using the GRI 2.11 mechanism with additional reactions for the excited-state species. De Leo et al. (2007) measured CH^{*} and OH^{*} chemiluminescence in opposed flow diffusion flames of methane and oxygen-enriched air and found good agreement with numerical predictions using the GRI 3.0 mechanism (Smith et al.), also with additional reactions for the excited-state species. CH^{*} chemiluminescence imaging has also been used for active control of high-pressure Bunsen flames (Docquier et al. 2000), and low-NO_x industrial burners (Delabroy et al. 1998).

The CH^{*} radical chemiluminescence signal from the flames is imaged through a 10 nm bandpass (full width at half-maximum) optical filter centred at 430 nm (Andover Corp. 430FS10-50) with a 90 mm macro lens (Tamron) onto an intensified CCD camera (Cooke Corp. DiCAM-Pro). Exposure time was adjusted to maximize the collected signal while ensuring that no pixels in the image became saturated. For flames with co-flowing combustion products, chemiluminescence emission from the flat flame was blocked, so as to maximize the signal from the rest of the flame. The lens operates at f/32, and magnification 1:4, at a distance of 45 cm from the burner axis to the front of the lens. At this magnification and image distance, one pixel corresponds to 47 μm in the flow. Each image used for analysis is the average of 256 individual images, from which a reference “dark” image, taken at the same exposure

with no flame, has been subtracted, thus reducing image noise. Relative CH^* concentrations are calculated from the images with a three-point Abel transform based on the formulas of Dasch (1992), after correcting for typographical errors in Eq. 7 (Ayrancı et al. 2007). Details on the chemiluminescence imaging system and the image processing methodology can be found in Appendix A.

Chapter 3

Numerical modelling

Numerical modelling is conducted with the National Research Council (NRC) 2-D Laminar Flame Code. A detailed description of the code is given by Guo et al. (2002). The governing equations for axisymmetric flow in cylindrical coordinates, including soot formation, are solved on a non-uniform grid with points closely spaced near the flame, and farther apart downstream and away from the centreline. Simulations are carried out at two different central fuel velocities, $u_{cf}=18.4$ and 23.0 cm/s, with grid sizes of 230 and 300 grid points in the axial direction, respectively, and 75 in the radial direction, corresponding to physical sizes of 3.39 and 5.47 cm in the axial direction, and 1.52 cm in the radial direction. Along the centreline and outer boundary, a no-through-flow and zero-gradient boundary condition is applied, and a zero-gradient condition is applied at the top out-flow boundary. The GRI-MECH 3.0 (Smith et al.) chemical kinetics mechanism is used throughout, with standard thermodynamic and transport properties.

The mass flow-rates of the co-flow, central fuel and central air streams are matched to those of the experiments, and top-hat velocity profiles are used for the three streams, as shown in Fig.3.1. For this case, the central air velocities were $u_{ca} = 49.8$ cm/s, and $u_{cf} = 23.0$ cm/s. As explained in Chapter 2, u_{ca} and u_{cf} are the plug-flow velocities at ambient temperature. The inlet velocities in the simulation are increased from these by two factors — one to account for the increased temperature and reduced density, and the other to account for the edges of the top-hat profile, in order to maintain the same mass flux as the experiments. The inlet temperature for the central fuel and air flows is set to 400 K. For cases with co-flowing air, the inlet temperature for the co-flow is also set to 400 K. For cases with co-flowing combustion products, the composition, velocity and temperature of the co-flow stream are calculated from a premixed, burner-stabilized flame calculation using the CANTERA

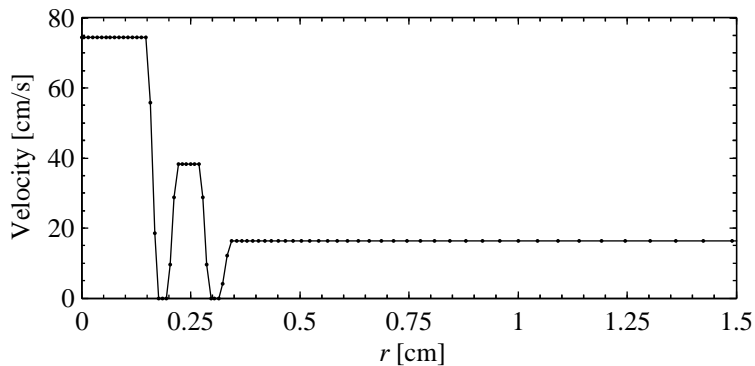


Figure 3.1: Example simulation inlet velocity profile.

Table 3.1: Co-flow velocities and temperatures used as inlet conditions in simulations.

Co-flow	Velocity [cm/s]	Temperature [K]
air	16.27	400.0
$\Phi = 0.78$	104.70	1855.8
$\Phi = 1.0$	206.78	2135.4
$\Phi = 1.2$	119.28	1957.5

simulation package (Goodwin 2003), with the same mass-flux and burner area as in the experiments. The velocities and temperatures used for the co-flow inlet are shown in Table 3.1. Chapter 6 compares the numerical simulation results to the experimental results, and includes a discussion of the sensitivity of the numerical results to the in-flow temperatures.

The calculation domain is initialized with a high-temperature region near the centreline, in order to “ignite” the flame. The flow is then marched forward in time until convergence is reached. The convergence criterion used here is that the root mean square difference in the quantity of interest between successive iterations, over the entire solution domain, scaled by the maximum of that quantity, should be less than 10^{-5} . In the first calculation, reactions involving nitrogen dissociation and NO_x production are removed, and the system is solved until convergence is reached in the temperature and CH mole fraction. The calculation is then restarted, including the previously removed reactions, until convergence is reached in the NO mole fraction as well.

For cases with a raised central air tube, properties of the cells occupied by the air tube are modified as follows. Axial and radial velocities are set to zero, viscosity is set to a large value, here 10^5 g/cm·s, and diffusion velocities for all species are set to zero. Simulations with a raised central air tube are initialized from a converged

Table 3.2: Reactions used in calculation of CH* concentration and emission (extracted from Walsh et al. 1998, and references therein).

#	Reaction	A	B	E _a
1	C ₂ H + O ₂ \longleftrightarrow CH* + CO ₂	1.08 · 10 ¹³	0.00	0
2	C ₂ H + O \longleftrightarrow CH* + CO	2.17 · 10 ¹⁰	0.00	0
3	CH* \longrightarrow CH	1.85 · 10 ⁶	0.00	0
4	CH* + N ₂ \longleftrightarrow CH + N ₂	3.03 · 10 ²	3.40	-381
5	CH* + O ₂ \longleftrightarrow CH + O ₂	2.48 · 10 ⁶	2.14	-1720
6	CH* + H ₂ O \longleftrightarrow CH + H ₂ O	5.30 · 10 ¹³	0.00	0
7	CH* + H ₂ \longleftrightarrow CH + H ₂	1.47 · 10 ¹⁴	0.00	1361
8	CH* + CO ₂ \longleftrightarrow CH + CO ₂	2.40 · 10 ⁻¹	4.30	-1694
9	CH* + CO \longleftrightarrow CH + CO	2.44 · 10 ¹²	0.50	0
10	CH* + CH ₄ \longleftrightarrow CH + CH ₄	1.73 · 10 ¹³	0.00	167

solution with a flush tube, and then solved until convergence is reached, as described above.

In order to compare to the experimental measurements of chemiluminescent emission from CH*, the concentration of CH* is calculated in a post-processing step, using the reactions in Table 3.2 (Walsh et al. 1998). As explained by Nori and Seitzman (2009), the highly reactive radical CH* has a very small net formation rate, and a very high destruction rate through quenching by collisions with other molecules, and so the quasi-steady-state approximation can be applied. The production rate of CH* is

$$\frac{d[\text{CH}^*]^+}{dt} = k_1 [\text{C}_2\text{H}] [\text{O}_2] + k_2 [\text{C}_2\text{H}] [\text{O}] \quad (3.1)$$

and the destruction rate is

$$\frac{d[\text{CH}^*]^-}{dt} = k_3 [\text{CH}^*] + \sum_{j=4}^{10} k_j [\text{CH}^*] [\text{M}_j] \quad (3.2)$$

where k_i is the rate of reaction i from Table 3.2 and $[\text{M}_j]$ is the molar concentration of the quenching species in reactions 4–10 (N₂, O₂...). Invoking the steady-state approximation, the production and destruction rates are set equal to each other, and the concentration of CH* is then given by

$$[\text{CH}^*] = \frac{k_1 [\text{C}_2\text{H}] [\text{O}_2] + k_2 [\text{C}_2\text{H}] [\text{O}]}{k_3 + \sum_{j=4}^{10} k_j [\text{M}_j]} \quad (3.3)$$

Among the destruction reactions, reaction 3 is the one from which a photon of

light is emitted. To compare to the experimental data, the rate of photon emission is then calculated at each grid point in the simulation, using Eqn. (4) from Walsh et al. (1998):

$$S_{\text{em}} = k_3 [\text{CH}^*] V_{\text{em}} \frac{\Omega \varepsilon \eta}{4\pi} \tau \quad (3.4)$$

where V_{em} is the volume in the flow corresponding to one pixel, $\Omega \varepsilon \eta$ are constants of the optical system—taking into account the solid angle of light collection, and the sensitivity of the imaging system—and τ is the exposure time. Within one image, the pixel volume, integration time, and optical system constants are unchanged, so the ratio of the collected signal at one pixel to the maximum signal over the entire image is

$$\frac{S_{\text{em}}}{S_{\text{em,max}}} = \frac{k_3 [\text{CH}^*]}{(k_3 [\text{CH}^*])_{\text{max}}}. \quad (3.5)$$

Finally, the numerical simulation data of relative CH^* emission is convolved with the point-spread function of the imaging system (Sec. A.3), and this is compared to the experimental data.

Chapter 4

Flame hysteresis behaviour at low central air velocities

At low central air velocities, there is a hysteresis behaviour associated with the inverse diffusion flame as the central air velocity is changed. Two sequences of flame chemiluminescence images taken at the four flame-states of interest for this hysteresis phenomenon are shown in Fig. 4.1 for co-flowing air at two different central fuel velocities. In the first image in each sequence, the central air velocity is zero, and there is only fuel flowing through the annulus and reacting with the co-flowing air. As the central air velocity is increased from zero, a partially-premixed flame becomes visible on the centerline. The second image was taken at the point just before this partially-premixed flame propagates upstream and stabilizes closer to the air tube as an inverse diffusion flame. The third image shows the inverse diffusion flame, taken at the same air velocity as the second image. Decreasing the air velocity, the inverse diffusion flame will move towards the air tube, getting weaker and weaker, until it extinguishes. The fourth image was taken just before this extinction point.

A similar sequence is shown in Fig. 4.2 with co-flowing combustion products from a premixed, burner-stabilized methane-air flame at equivalence ratio $\Phi = 0.78$. The burner-stabilized flame is visible at the bottom of the image. The sequence of images in Fig. 4.2 shows the same four flame-states as Fig. 4.1: normal diffusion flame with no central air, partially-premixed flame just before transition, stabilized inverse diffusion flame, and near-extinction inverse diffusion flame, visible just above the tip of the central air tube. With co-flowing combustion products, the overall flame height is higher than with co-flowing air at a similar fuel velocity, as would be expected from the correlation of Roper (1977) due to the reduced oxygen mole fraction in the co-flow, which is estimated at 4% for this equivalence ratio of premixed flame, and the

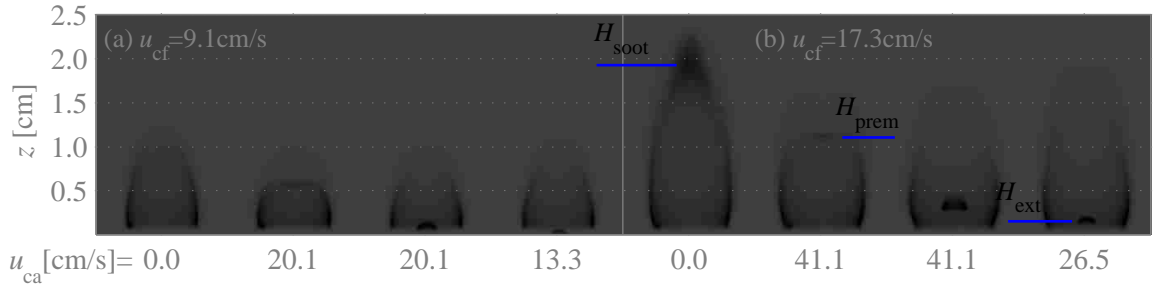


Figure 4.1: Flame chemiluminescence images illustrating the inner flame hysteresis, with co-flowing air and central air tube flush. From left to right are the normal diffusion flame, partially-premixed flame just before transition, stabilized inverse diffusion flame, and near-extinction inverse diffusion flame.

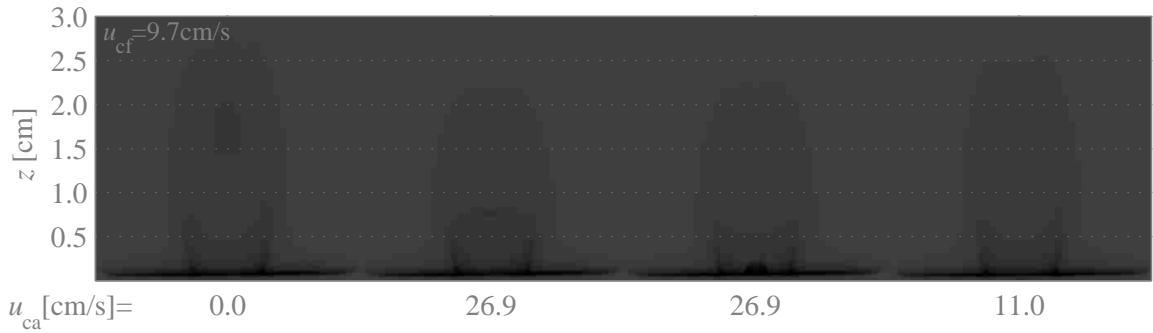


Figure 4.2: Flame chemiluminescence images with co-flowing combustion products at $\Phi = 0.78$ and central air tube flush. The burner-stabilized flame is visible at the bottom, and image intensity has been adjusted to improve visibility. From left to right are the normal diffusion flame, partially-premixed flame just before transition, stabilized inverse diffusion flame, and near-extinction inverse diffusion flame.

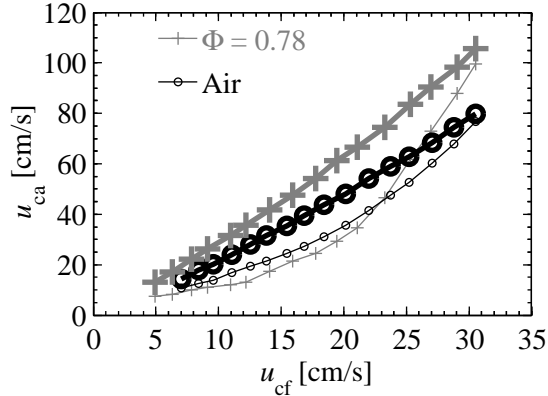


Figure 4.3: Velocities for transition from the partially-premixed flame (upper, thick line) and extinction of the inverse diffusion flame (lower, thin line).

outer diffusion flame is much weaker and more diffuse.

As shown in Fig. 4.1, flame heights are measured from the images. For flames with no central air, and central fuel velocities high enough for soot to be visible along the centreline, the soot height, H_{soot} , is the location of the peak image intensity along the centreline. The height of the partially-premixed flame just before transition, H_{prem} , is measured by taking the location of the peak CH^* intensity in a 20 pixels-wide swath near the centreline. The height of the near-extinction inverse diffusion flame, H_{ext} , is the location of maximum image intensity within the central flame region, away from the outer diffusion flame.

From the experiments, the two central air velocities of interest—at the transition from partially-premixed to inverse diffusion flame, and at the extinction of the inverse diffusion flame—are plotted in Fig. 4.3 for flames with co-flowing air and co-flowing combustion products. For a given central fuel velocity, as the central air velocity is increased from zero, the partially-premixed flame becomes more and more prominent, until the transition to the inverse diffusion flame at the upper curve. As the central air velocity is decreased from the upper curve, the flame height is reduced, and the flame gets weaker until it is extinguished at the lower curve. Figure 4.3 shows the hysteresis character of the flames—at a given central fuel velocity, for central air velocities between the upper and lower curves, there are two possible flame states, depending on the history of the flame. This is similar to the hysteresis behaviour between lift-off and drop-back of non-premixed jet flames (Law 2006, p.363). The difference between the stabilization and extinction velocities is larger with co-flowing combustion products than with co-flowing air.

Flame heights measured from the images are shown in Fig. 4.4(a), plotted versus

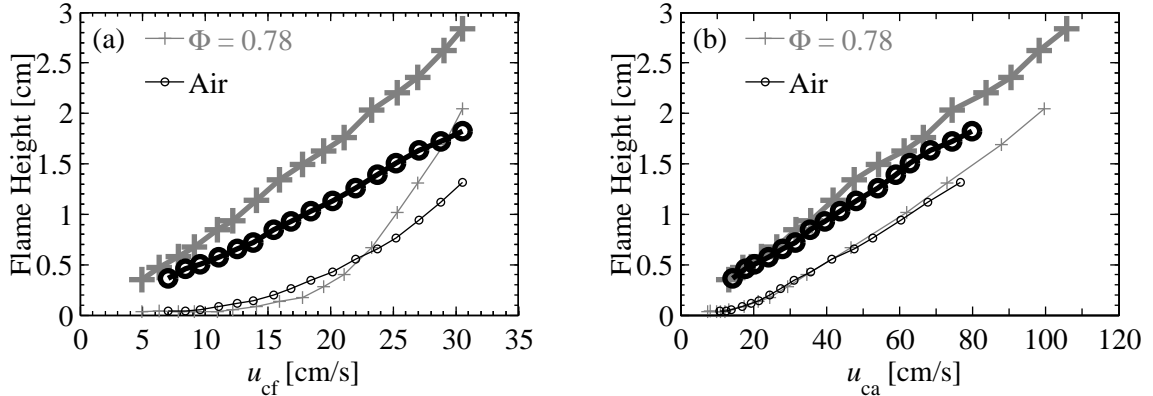


Figure 4.4: (a) Flame heights of the partially-premixed flame (upper, thick line) and the near-extinction inverse diffusion flame (lower, thin line), plotted against the central fuel velocity. (b) Flame heights of the partially-premixed flame (upper, thick line) and the near-extinction inverse diffusion flame (lower, thin line), plotted against the central air velocity.

central fuel velocity, and Fig. 4.4(b) versus central air velocity. The upper, thick line is the height of the partially-premixed flame just before transition, and the lower, thin line is the height of the inverse diffusion flame just before extinction.

The repeatability error in flame heights and velocities are low due to the averaging of 256 images (Appendix A) for the flame height, and the small fluctuations in mass flow-rate during the recording of each image, on the order of 1% (Chapter 2). However, there is a bias error associated with the measurements of this hysteresis phenomenon. In order to capture the partially-premixed flame before transition, the central air velocity is gradually increased until a point as close as possible to the transition point is reached, and the images and velocities are recorded there. Thus, the true velocity for transition from the partially-premixed flame will be under-predicted. To capture the inverse diffusion flame before extinction, the central air velocity is gradually decreased until a point just before extinction. Thus, the velocity and flame height at extinction will be over-predicted.

Both the central air velocity for transition from the partially-premixed to inverse diffusion flame, and the height of the partially-premixed flame before transition are generally linear with fuel velocity in both cases, and are consistently higher for flames with co-flowing combustion products. Close examination of the experimental images reveals that the outer diffusion flame is connected to the partially-premixed flame at the tip. This suggests that the partially-premixed flame is sustained by the outer diffusion flame, and in fact, over the range of fuel velocities with visible soot, taking the soot height, H_{soot} , as a measure of the outer diffusion flame height, the height

of the partially-premixed flame before transition is a constant fraction of the outer diffusion flame height: $H_{\text{prem}}/H_{\text{soot}} \sim 0.53$ for co-flowing air, and $H_{\text{prem}}/H_{\text{soot}} \sim 0.37$ for co-flowing combustion products at $\Phi = 0.78$. As the outer diffusion flame height is linear with fuel velocity, from the correlation of Roper (1977), then the partially-premixed flame height should also be linear with fuel velocity. As the central fuel velocity is increased, the height of the partially-premixed flame increases, so the central air velocity required to reach that location and create a flammable mixture will also be increased.

At low central fuel velocities, there is not a significant difference in the extinction velocities between co-flowing air and combustion products. This is the region in Fig. 4.4(b) at low central air velocities where the extinction height is nearly constant, near zero, as the flames at extinction are very close to the burner. In these cases, the inverse diffusion flame is stabilized by the presence of the outer flame, but only in so far as it is getting heated by heat transfer both through the gas from the base of the outer diffusion flame, and through the burner, with co-flowing combustion products, as the entire burner gets hot due to the proximity of the burner-stabilized flame.

At higher fuel velocities, there is a larger difference in the extinction velocities between co-flowing air and co-flowing combustion products. At these higher fuel velocities, the inverse diffusion flame extinguishes at a location above the burner face, and so is more affected by the co-flowing combustion products. In Fig. 4.4(b), this is the region for higher central air velocities where the slope of the extinction height curve increases and matches the slope of the partially-premixed flame height, showing the effect of the co-flow.

Flames shown in Figs. 4.1 and 4.2 were analyzed with numerical simulations. Contour plots of measured and simulated CH^* radical chemiluminescence are shown in Fig. 4.5 for co-flowing air and in Fig. 4.6(a) for co-flowing combustion products. The three cases shown are the normal diffusion flame ($u_{\text{ca}}=0$), partially-premixed flame, and stabilized inverse diffusion flame. The small rectangles along the bottom of each figure represent the locations of the central air and fuel tubes. The numerical simulations with partially-premixed flames are started from a converged solution of the normal diffusion flame with no central air flow, adding central air at the in-flow boundary, and re-calculating until convergence is reached. This is analogous to the way the experiments are conducted, starting from a normal diffusion flame with no central air flow and increasing the air velocity slowly until the partially-premixed flame becomes visible.

With co-flowing air, the numerical simulations predict taller CH^* contours for the

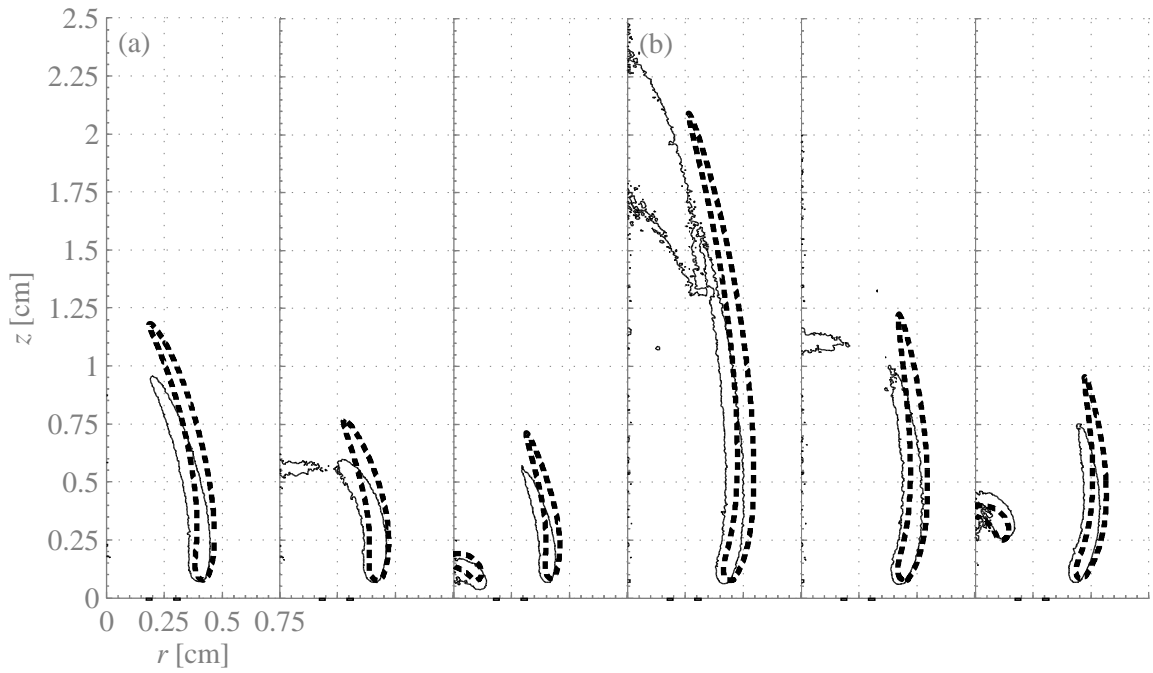


Figure 4.5: Experimental (thin line) and numerical (thick dashed line) contours of CH^* emissions, scaled to the maximum value per image, showing the 10% contour. The three cases shown are the normal diffusion flame, partially-premixed flame, and stabilized inverse diffusion flame, and the experimental contours are calculated from the first three images in each set of Fig. 4.1. Co-flowing air and central fuel velocity (a) $u_{cf} = 9.1$ cm/s, (b) $u_{cf} = 17.3$ cm/s.

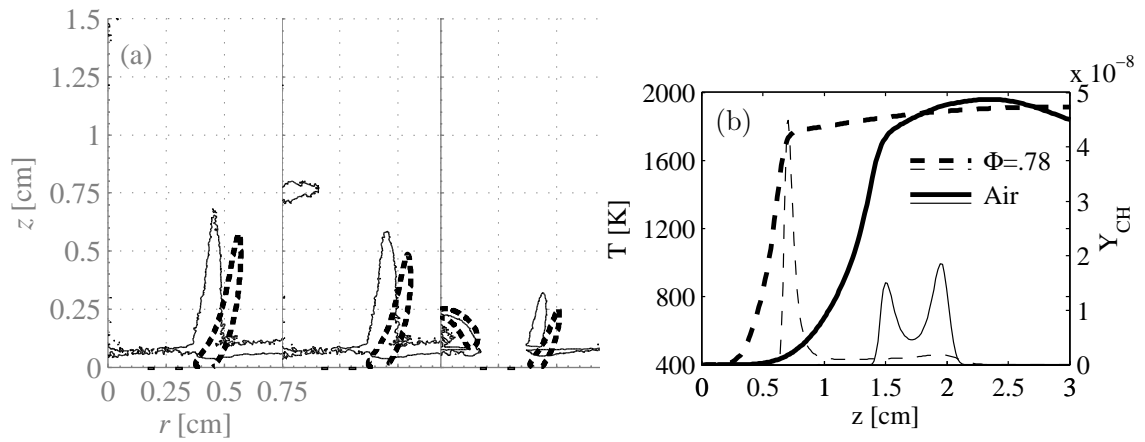


Figure 4.6: (a) Experimental (thin line) and numerical (thick dashed line) contours of CH^* emissions, scaled as in Fig. 4.5. Experimental contours are calculated from the first three images in each set of Fig. 4.2. Co-flowing combustion products at $\Phi=0.78$, $u_{\text{cf}}=9.7$ cm/s.. (b) Simulated axial temperature (thick lines) and CH mass fraction (thin lines) on the centreline for the partially-premixed flame with co-flowing air (solid lines) at $u_{\text{cf}}=17.3$ cm/s, and co-flowing combustion products (dashed lines) at $u_{\text{cf}}=9.7$ cm/s.

outer normal diffusion flame, most likely due to preheating of the reactants, as flame height is very sensitive to the temperature of the incoming reactants (McEnally et al. 1997). With co-flowing combustion products, the CH^* emission from the burner stabilized flames is visible in the experimental data, lifted off the burner face by the flame standoff distance of approximately 0.8 mm (Fig. 4.6(a)). The base of the outer diffusion flame is attached to the burner-stabilized flame. In the numerical simulations, the in-flow is already combustion products at elevated temperature, so there is no standoff and the outer diffusion flame stabilizes at the face of the burner. However, the radial location and overall height of the outer flame still match well. With both co-flows, the overall shape, width and axial location of the inner, inverse diffusion flames are well predicted by the numerical simulations.

Numerical simulation does not predict the presence of the strong partially-premixed flame near the centerline in the CH^* contour at these central air velocities. However, there is a partially-premixed flame along the centreline, even though the CH^* concentration is not high enough to show up in the contour plot. Figure 4.6(b) shows the axial distribution of temperature and CH mass fraction on the centreline of the partially-premixed flame simulations for co-flowing air at $u_{\text{cf}}=17.3$ cm/s, and co-flowing combustion products at $u_{\text{cf}}=9.7$ cm/s. The premixed character of the flame along the centreline is evident from the rapid temperature rise. For co-flowing air, the first peak of CH on the centreline is from the partially-premixed flame, and the second is from the tip of the outer diffusion flame as it wraps around to the centreline. This corroborates the observation from the experimental images that the partially-premixed flame is sustained by the outer diffusion flame. For co-flowing air, the predicted height of the partially-premixed flame is $H_{\text{premix}} \simeq 1.5$ cm, which is higher than the observed flame in the experiments at $H_{\text{premix}} \simeq 1.1$ cm. This is consistent with the simulations predicting taller outer diffusion flames, as the partially-premixed flame height scales linearly with the outer diffusion flame height, as mentioned above. For co-flowing products, the predicted height is $H_{\text{premix}} \simeq 0.7$ cm, closer to the experimentally measured flame height of $H_{\text{premix}} \simeq 0.75$ cm.

A sequence of simulations was conducted with co-flowing combustion products at $u_{\text{cf}}=18.4$ cm/s, increasing the central air velocity from zero until the partially-premixed flame formed on the centreline. Figure 4.7(a) shows the axial temperature profiles for increasing central air velocities. In this case, when the central air velocity was increased from 64.0 to 73.6 cm/s, the partially-premixed flame propagated upstream and stabilized as an inverse diffusion flame. Figure 4.7 shows the 10% contours of CH mass fraction, scaled to the maximum for the partially-premixed flame,

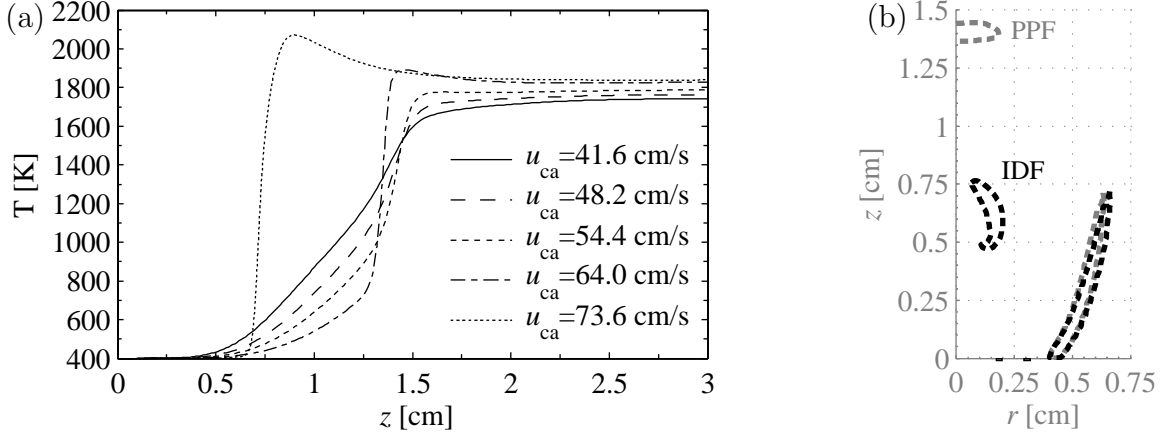


Figure 4.7: (a) Centreline axial temperature from a series of simulations, starting with $u_{ca}=0$, and increasing u_{ca} , for $\Phi = 0.78$ co-flow and $u_{cf}=18.4$ cm/s. (b) Simulated contours of CH mass fraction for partially-premixed flame (grey dashed line) and inverse diffusion flame (black dashed line), scaled by the maximum for the partially-premixed flame, showing the 10% contour. Both simulations have the same in-flow conditions: $\Phi = 0.78$ co-flow, $u_{cf}=18.4$ cm/s, and $u_{ca}=64.0$ cm/s.

for two simulations with the same in-flow conditions: co-flowing products at $\Phi = 0.78$, $u_{cf}=18.4$ cm/s, $u_{ca}=64.0$ cm/s. The partially-premixed flame case was started from a normal diffusion flame with $u_{ca}=0$, as described above, and the inverse diffusion flame case was initialized with a high-temperature region in the centre of the simulation domain, in order to ignite the inner flame, as described in Chapter 3. This illustrates the two flame states that are possible for central air velocities in the region of hysteresis between stabilization and extinction.

The mechanism for formation of the partially-premixed flame is that the fluid velocity should be balanced by the flame propagation velocity for the local mixture composition and temperature. As the central air velocity is increased, the mixture on the centreline upstream of the partially-premixed flame location is becoming more lean, towards stoichiometry. In the simulations at $u_{ca}=64.0$ cm/s, the local equivalence ratio reaches a peak of 1.09 upstream of the partially-premixed flame. Beyond this value, a critical point is reached where the propagation velocity overtakes the fluid velocity and the flame propagates upstream to stabilize as an inverse diffusion flame.

As for the inner inverse diffusion flame, the mechanism for its stabilization is the triple, or tribrachial flame, where the base of the flame is premixed and stabilizes at a location where its propagation velocity is equal to the fluid velocity. In the analysis of non-premixed jet flames (Lee and Chung 1997), it is predicted, and has been confirmed

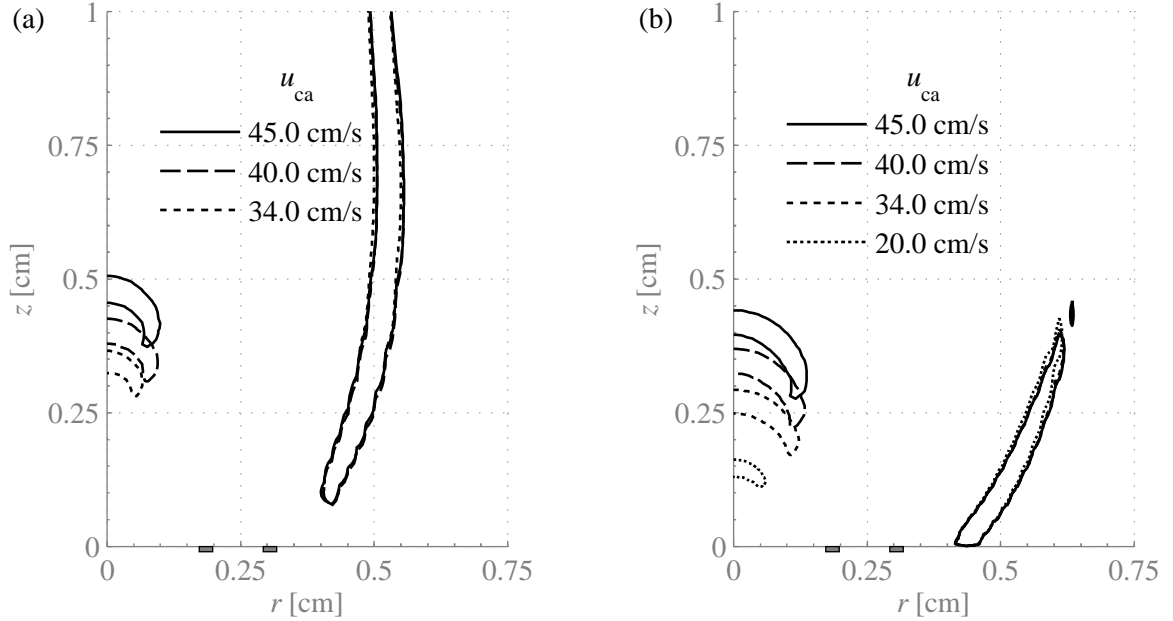


Figure 4.8: Sequence of CH mass fraction contours (10% of the maximum for the highest u_{ca} case) as u_{ca} is lowered towards extinction for (a) co-flowing air and (b) co-flowing combustion products at $\Phi = 0.78$, both at $u_{cf}=23.0$ cm/s.

experimentally, that lifted diffusion flames of methane are unstable. In their analysis of the structure of inverse flames of methane in air, Wu and Essenhig (1984) did not see any lifted flames, and their flames blow off directly from the attached state. Thus, the lifted methane inverse diffusion flame requires the presence of the outer diffusion flame to be stabilized.

A sequence of simulations was conducted with co-flowing air and co-flowing combustion products at $\Phi = 0.78$, both at $u_{cf}=23.0$ cm/s, in order to investigate the behaviour of the flames near extinction. Starting with a converged solution of a stabilized inverse diffusion flame, the central air velocity was gradually reduced in increments of 1 cm/s, until the inner flame extinguished. Figure 4.8 shows the CH mass fraction contours for a selection of simulations from this sequence. For co-flowing air, when the central air velocity was reduced from 34.0 to 33.0 cm/s, the flame extinguished. For co-flowing products, the flame extinguished when the central air velocity was reduced from 20.0 to 19.0 cm/s. As the central air velocity is reduced, the inverse diffusion flame moves closer to the burner, and eventually begins to shrink in radial extent as the extinction velocity is approached.

At this central fuel velocity in the experiments, the heights and central air velocities for the near-extinction flame are nearly equal for co-flowing air and co-flowing combustion products. In the simulations, flames extinguish lower, and at lower central

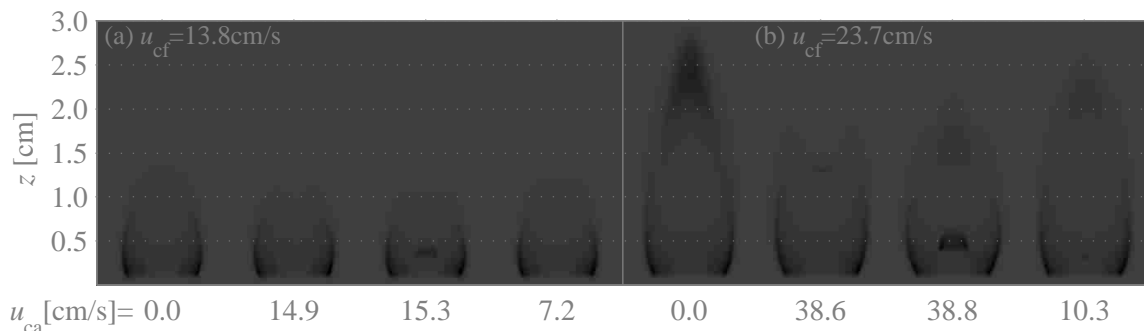


Figure 4.9: Flame chemiluminescence images illustrating the inner flame hysteresis, with co-flowing air and central air tube raised 3 mm. From left to right are the normal diffusion flame, partially-premixed flame just before transition, stabilized inverse diffusion flame, and near-extinction inverse diffusion flame.

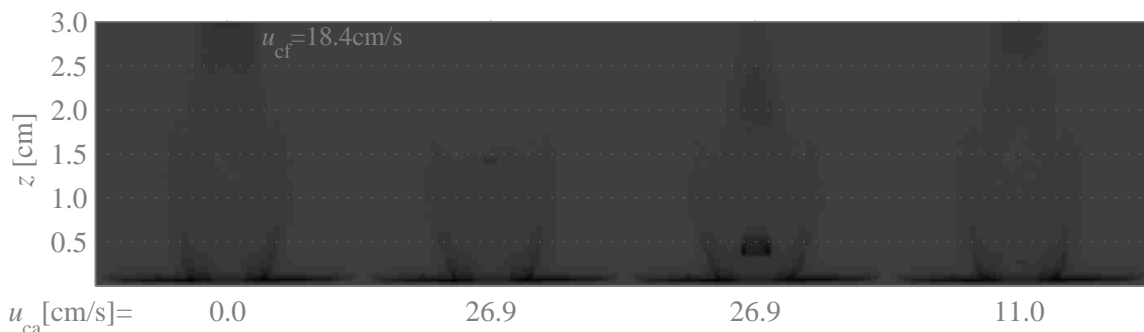


Figure 4.10: Flame chemiluminescence images with co-flowing combustion products at $\Phi = 0.78$ and central air tube raised 3 mm. The burner-stabilized flame is visible at the bottom, and image intensity has been adjusted to improve visibility. From left to right are the normal diffusion flame, partially-premixed flame just before transition, stabilized inverse diffusion flame, and near-extinction inverse diffusion flame.

air velocities for co-flowing combustion products versus co-flowing air.

Figure 4.9 shows two sequences of flame chemiluminescence images for co-flowing air, with the central air tube raised above the burner face by 3 mm. Figure 4.10 shows the same sequence for co-flowing combustion products at $\Phi = 0.78$, with the central air tube raised above the burner by 3 mm.

Figure 4.11(a) shows the velocity for transition from the partially-premixed to the inverse diffusion flame as the central air tube is raised above the burner. As the tube is raised, the central air velocity needed to stabilize the partially-premixed flame is reduced. However, as shown in Fig. 4.11(b), the height of the partially-premixed flame just before transition to the inverse diffusion flame is fairly insensitive to the height of the central air tube above the burner. The height of the partially-premixed flame is insensitive to the tube being raised, because, as discussed above, the partially-

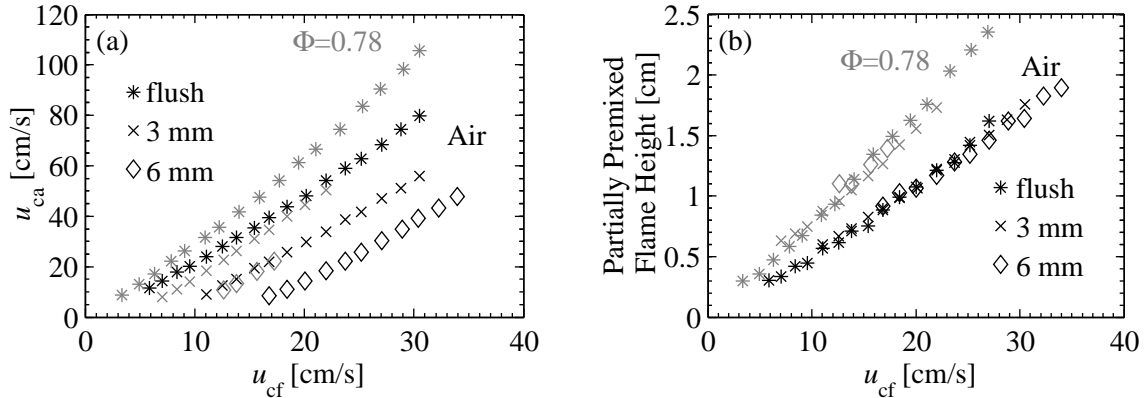


Figure 4.11: (a) Central air velocity for transition from the partially-premixed flame with the central air tube raised by the amounts shown in the legend; (b) height of the partially-premixed flame (H_{prem}) above the burner, with the central air tube raised.

premixed flame is sustained by the outer flame, and its height is scaled by that of the outer flame. The central air velocity required for the partially-premixed flame is decreased because, as the air is being injected closer to the flame, the air velocity need not be as high in order to bring the mixture closer to stoichiometry and form the partially-premixed flame.

In summary, for low central air velocities, there is a hysteresis behaviour associated with the flames in this work. As the central air velocity is increased from zero, a partially-premixed flame forms on the centreline, whose height scales with the outer diffusion flame height, and is insensitive to the height of the central air tube above the burner. When the central air velocity reaches a critical value, the partially-premixed flame propagates upstream to stabilize as an inverse diffusion flame. Simulation results suggest that the critical condition for this transition is when the local equivalence ratio upstream of the flame approaches one. The inverse diffusion flame would be unstable without the presence of the outer diffusion flame, and as the central air velocity is decreased, it moves closer to the burner, shrinks in size and eventually extinguishes.

Chapter 5

Flame characteristics at higher central air velocities

This chapter discusses the experiments conducted on flames with higher central air velocities, outside of the hysteresis region discussed in the previous chapter.

The entire set of experimental images that were acquired during this work is shown in Appendix B. Figures 5.1, 5.2, and 5.3 show sample sequences of flame chemiluminescence images at $u_{cf} \sim 23.0$ cm/s with the four different co-flows (air, and combustion products at $\Phi = 0.78, 1.0$ and 1.2). Across each sequence of images, the central air velocity is increasing, with the value given underneath each image. Down each page, images are shown at similar central air velocities for the four different co-flows.

The intensity of all images has been inverted, so that dark regions correspond to high levels of CH^* chemiluminescence emission. Also, exposure times were adjusted to maximize the signal-to-noise ratio for each individual image, without saturating any pixels. This is why the background intensity varies across the images, particularly in Fig. 5.1(c), where there is significant emission of CH^* chemiluminescence from the burner-stabilized flame. For this particular sequence, at low and high central air velocities, the exposure times were long, resulting in high image intensity in the background. In the middle range of central air velocities, the CH^* chemiluminescence emission from the lifted flame was higher, so the exposure times were shorter, resulting in lower background intensity. Thus, comparisons among different flame images should be made on flame shape, location, and relative chemiluminescence intensity within each image, but not on absolute image intensity across different images. In all cases, the darkest points in each image represent the highest emission of CH^* chemiluminescence within that flame, along the line-of-sight.

For those cases with co-flowing combustion products, the burner-stabilized flame is not visible in these images. Emission from the burner-stabilized flame was blocked from reaching the camera, since collecting sufficient signal for the rest of the flame would have resulted in saturated pixels for the burner-stabilized flame, especially with stoichiometric and rich combustion product co-flows. This is most evident at the bottom of Fig. 5.3(c), where the light was blocked up to $z \sim 0.25$ cm, resulting in a white region in these inverted images.

Asymmetries are evident in some of the flames, particularly with co-flowing combustion products and a raised central air tube. As mentioned in Chapter 2, there is a sintered metal sleeve in the fuel annulus, designed to maintain the air and fuel tubes concentric, but there are still asymmetries that were unavoidable. For example, in Fig. 5.1(c), for $u_{ca} = 606.5$ and 955.2 cm/s, the flame is tilted down and to the right, along an axis perpendicular to the imaging direction. In Fig. 5.2(c), for central air velocities above $u_{ca} = 101.4$ cm/s, the flame gets distorted more along an axis parallel to the imaging direction, resulting in an oval shape. Similar behaviour is evident at the higher central air velocities in Fig. 5.3. In all cases, though, asymmetries are not evident at lower central air velocities.

Starting in Fig. 5.1(a) with co-flowing air and flush central air tube, there is the outer, normal diffusion flame between the central fuel and co-flowing air, and the inner, inverse diffusion flame between the central air and fuel. At low central air velocities, the inverse diffusion flame is lifted off the burner and separate from the outer diffusion flame ($u_{ca} = 49.45$ cm/s). As the central air velocity is increased, the inner flame moves higher, the tip of the flame opens, and it connects with the outer diffusion flame in a ring-shaped flame. The ring-shaped flame looks flat in many of these images since they are line-of-sight, but in cases with asymmetries, it is clear that the flame is ring-shaped. The ring-flame reaches a maximum height around $u_{ca} \sim 200$ cm/s. As the central air velocity is raised further, from 200–1000 cm/s, the height of the ring flame gradually decreases, and the outer diffusion flame gets pulled closer to the centreline by the entrainment of the central air jet. At $u_{ca} \simeq 1000$ cm/s, the Reynolds number for the central air flow reaches $Re_{ca} \simeq 2000$, which is the beginning of the transition to turbulence for pipe flow. Above this velocity, the flame oscillates between two flame states, and only reaches steady-state when the central air velocity reaches $u_{ca} = 1500$ cm/s. At this velocity, the Reynolds number for the central air flow is $Re_{ca} \simeq 3500$, which is nearly outside of the transition to turbulence for pipe flow. With turbulent flow in the central air tube, the contraction of the outer flame is quite pronounced, and the flame height is lowered considerably.

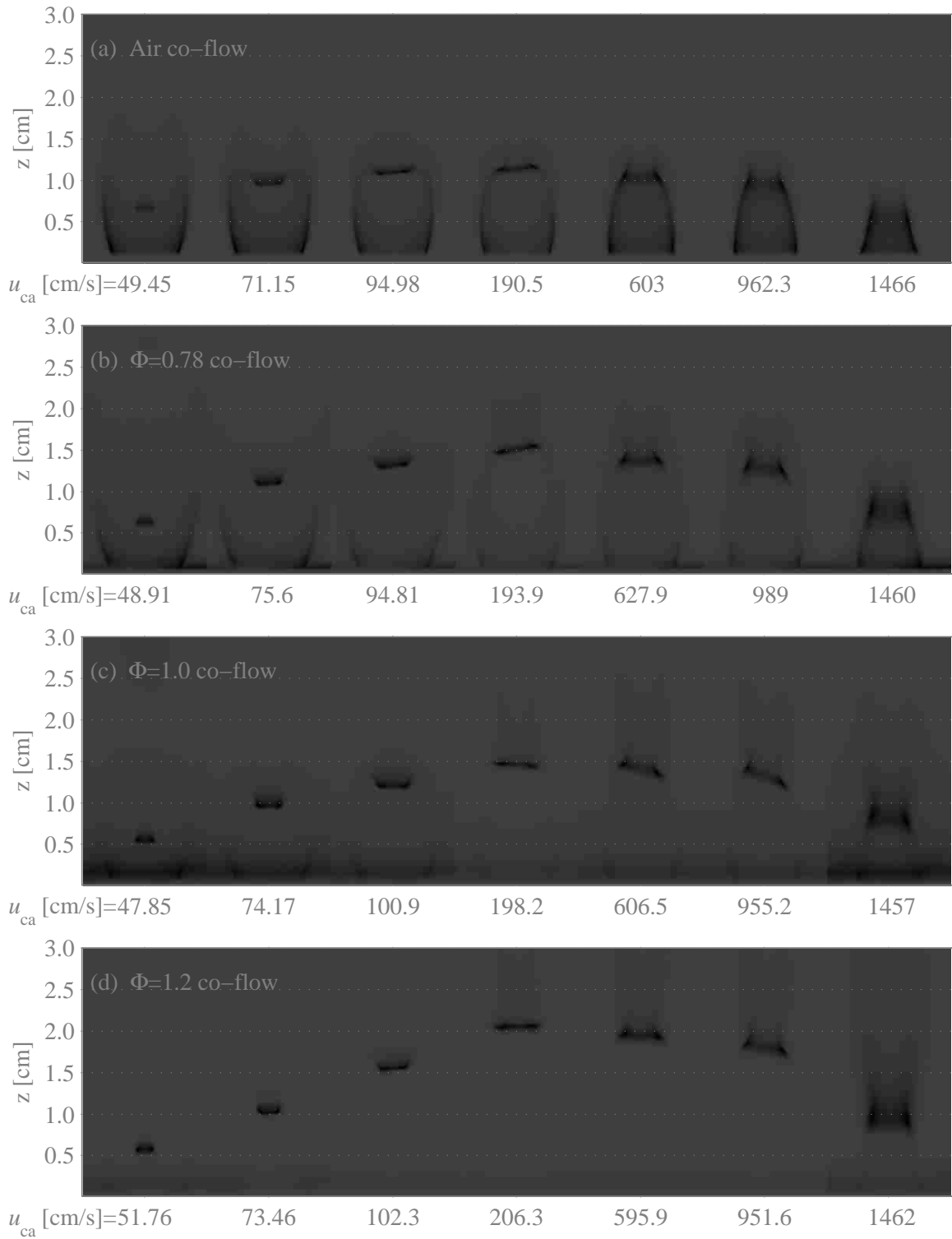


Figure 5.1: Sample sequence of flame images at $u_{cf} \sim 23.0$ cm/s, with central air tube flush, and co-flow given for each set of images.

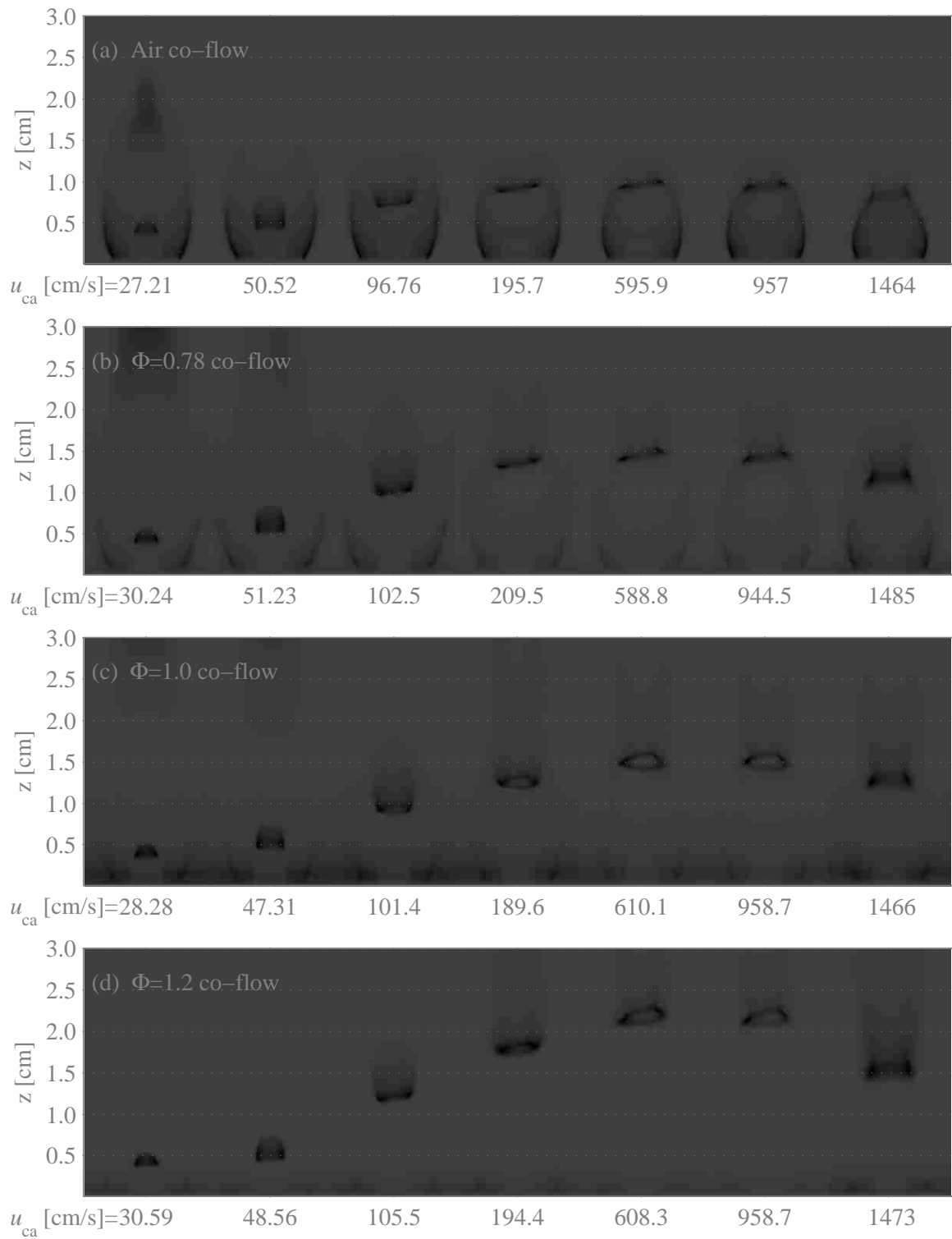


Figure 5.2: Sample sequence of flame images at $u_{cf} \sim 23.0$ cm/s, with central air tube raised 3 mm, and co-flow given for each set of images.

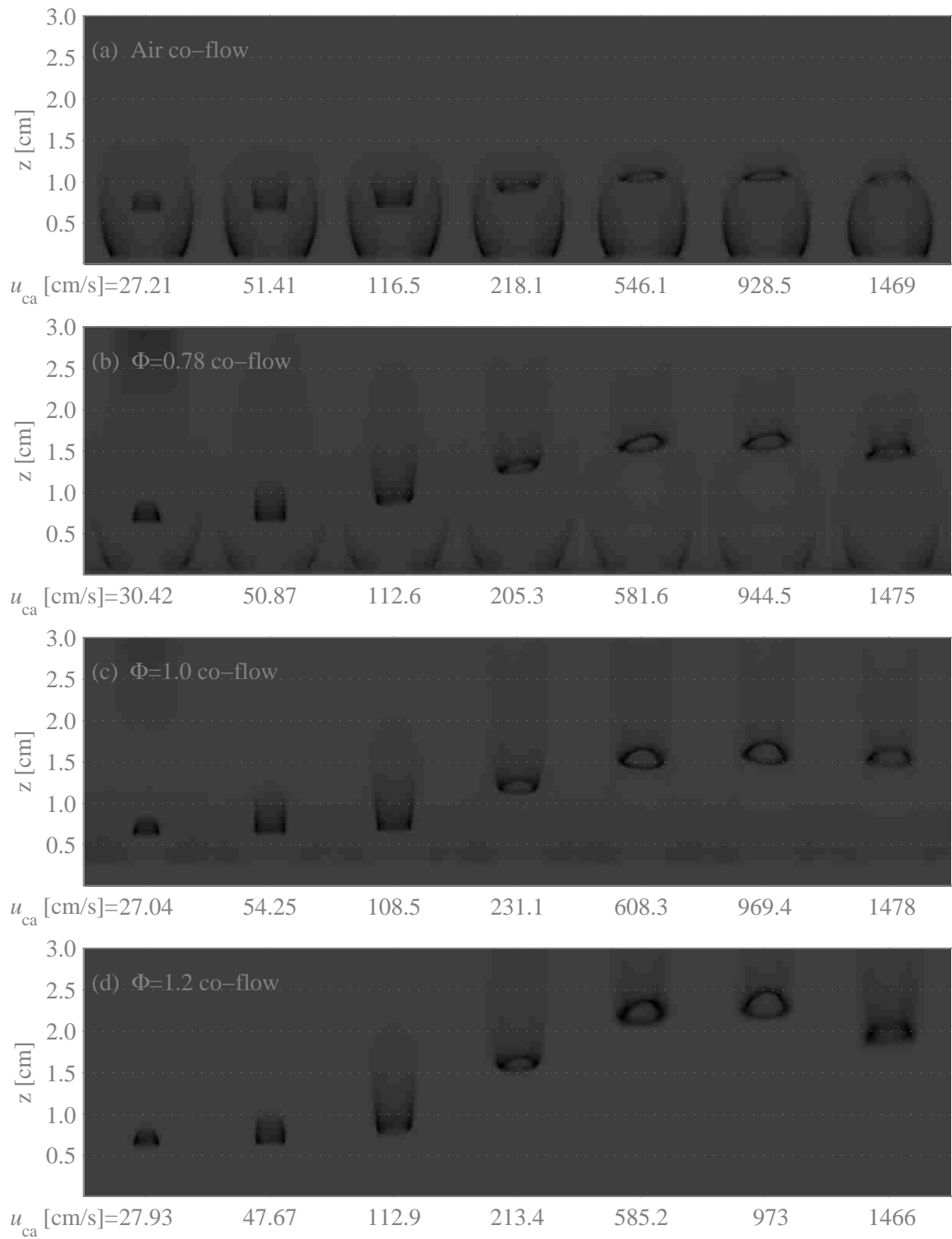


Figure 5.3: Sample sequence of flame images at $u_{cf} \sim 23.0$ cm/s, with central air tube raised 6 mm, and co-flow given for each set of images.

For co-flowing combustion products at $\Phi = 0.78$ (Fig. 5.1(b)), the outer diffusion flame is weaker than with the air co-flow, as the oxygen content in the co-flowing gas is reduced. The behaviour of the inner flame is similar, though. At low central air velocities, the inverse diffusion flame is lifted off the burner and separate from the outer diffusion flame. As the central air velocity is increased, the tip of the flame opens up, and the inner flame joins the outer flame in the ring-shaped flame. The height of the ring-flame reaches a maximum around $u_{ca} \sim 200$ cm/s, and decreases gradually as the central air velocity is further increased. Similar behaviour is also seen in the transition to turbulence at $u_{ca} = 1460$ cm/s, as the outer diffusion flame is drawn in towards the centreline, and the height of the ring-flame is reduced.

For co-flowing combustion products at $\Phi = 1.0$ (Fig. 5.1(c)), the outer diffusion flame is again weaker, and is barely visible near the burner face. At $\Phi = 1.2$ (Fig. 5.1(d)), the outer diffusion flame is not visible, as there is no longer any oxygen in the co-flow to react with the central fuel. For these two co-flows, the behaviour of the inner flame is similar to that described above.

With the three combustion product co-flows, starting at $u_{ca} \sim 200$ cm/s, there is a diffusion-type flame downstream of the ring flame. This flame is particularly evident for the $\Phi = 1.2$ co-flow, as there is more unburned fuel in the co-flow available to react with the central air jet in a diffusion-type flame.

Flames with the central air tube raised 3 mm are shown in Fig. 5.2. For co-flowing air, at the lowest central air velocity shown, the inner flame has a closed tip and is attached to the central air tube. As the central air velocity is increased, the tip of the flame opens up, the base lifts off the central air tube, and the flame joins the outer flame in the ring-flame structure. The height of the ring-flame gradually increases for all central air velocities up to $u_{ca} \sim 1000$ cm/s, where there is the transition to turbulent pipe flow. For the turbulent flame, the height of the ring flame is slightly decreased, but not as much as with the central air tube flush. The base of the outer flame is not entrained towards the centreline, leading to the bulbous shape of the outer flame.

With co-flowing combustion products, the behaviour is similar. At low central air velocities, the inner flame is attached to the central air tube with a closed tip. As the central air velocity is increased, the tip opens up and the flame lifts off the tube. The diffusion flame downstream of the ring flame is more prominent with the raised tube, starting around $u_{ca} \sim 100$ cm/s, and gets longer as the central air velocity is increased. A similar bulbous shape for the turbulent outer flame is evident with the $\Phi = 0.78$ co-flow.

Flames with the central air tube raised 6 mm are shown in Fig. 5.3. At the lowest central air velocity shown, the inner flame has a closed tip and is attached to the central air tube. For co-flowing air, at $u_{ca} = 51.41$ cm/s, the tip of the inner flame has opened up and joined with the outer flame, although the base of the inner flame is still attached to the central air tube. At $u_{ca} = 116.5$ cm/s, the base of the inner flame is still attached to the central air tube, and the chemiluminescence emission from the diffusion flame that joins with the outer flame is more intense, relative to the base of the outer flame. At $u_{ca} = 218.1$ cm/s, the flame has lifted off the central air tube, and for higher central air velocities, the height of the ring-flame does not change significantly, even for the turbulent flow case at $u_{ca} = 1469$ cm/s.

With co-flowing combustion products the behaviour is similar. At the lowest central air velocity shown, the inner flame has a closed tip and is attached to the central air tube. As the central air velocity is increased, the diffusion flame downstream of the ring-flame lengthens, and the flame lifts off from the central air tube. The change in flame height going to the turbulent flame is not as large as with the central air tube flush.

Chapter 6

Numerical simulation validation

Flames with central fuel velocities of $u_{cf} = 18.4$ and $u_{cf} \simeq 23.0$ cm/s were analyzed with numerical simulations, as described in Section 3. In this chapter, the numerical results are compared to the experimental CH* chemiluminescence measurements in order to validate the simulation methodology. Simulation results are post-processed to calculate the CH* radical concentration and CH* chemiluminescence emission rate, then convolved with a matrix corresponding to the point-spread function of the imaging system, which models the experimental measurements.

A series of simulations was conducted to study the effects of the in-flow boundary conditions on the flame shape. A number of flames were chosen, and the inlet temperature was modified, to find the sensitivity of the flame shape and location to the in-flow conditions. The in-flow temperature for the three separate streams was increased to 500 K, separately, and the velocity for that stream was adjusted to maintain a constant mass flux.

6.1 CH* contours

Figures 6.1–6.8 show a selection of comparisons between experimental and numerical CH* contours. The complete set of contour plots of experimentally measured and numerically calculated CH* chemiluminescence emission is included in Appendix C. A summary of the comparisons is presented here.

Simulation data is plotted with the thick dashed line, and the thin lines are the experimental data from the Abel transform of the images. As discussed in Appendix A, flame images are split into the left- and right-hand side, and both are calculated through the Abel transform. Generally, the two sides are in good agreement, but there are differences when the flames are asymmetric. In Figs. 6.1–6.8, the thin black

line is data from the right-hand side, and the thin grey line is data from the left-hand side.

For co-flowing air with central fuel velocity $u_{cf} = 18.4$ cm/s and the central air tube flush (Fig. 6.1(a)), the outer flame is well predicted up to $u_{ca} = 89.11$ cm/s. For the inner flame, at low central air velocities, simulations predict a lower flame height. At $u_{ca} = 89.11$ cm/s, the simulations predict a higher location for the inner flame, although the shape of the flame is in good agreement. Above this velocity, as the inner flame joins with the outer flame, the simulated flame is drawn in towards the centreline much more than in the experiments. This phenomenon is particularly visible at $u_{ca} = 506.9$ cm/s. With the central air tube raised 3 mm (Fig. 6.1(b)), the outer flame is displaced further outwards in the simulations, although the location of the base of the outer flame is in good agreement with the experiments. The location and height of the inner flame agree well up to $u_{ca} = 50.87$ cm/s. For higher central air velocities, the simulations predict higher inner flames, but the shapes of the flames are in good agreement. At the highest central air velocities, the base and tip of the flame are in good agreement, but the middle portion of the flame is entrained more towards the centreline in the simulations, as was seen with the central air tube flush. With the central air tube raised 6 mm (Fig. 6.1(c)), the trends are similar to those at 3 mm. The outer flame is displaced further outwards in the simulations, although the location of the base of the outer flame is in good agreement. At low central air velocities, up to $u_{ca} = 171.1$ cm/s, the inner flame location and shape are well predicted. Above that, the simulations predict a higher location for the inner flame, such as at $u_{ca} = 384.2$ cm/s. At the highest central air velocity, here $u_{ca} = 1109$ cm/s, the agreement is excellent for all parts of the flame.

For co-flowing air at central fuel velocity $u_{cf} = 23.0$ cm/s (Fig. 6.2), the agreement is similar to that at $u_{cf} = 18.4$ cm/s. With the central air tube flush, the simulations predict a lower flame location for central air velocities up to $u_{ca} = 80.75$ cm/s. Above this, the simulations predict a higher flame, and at high central air velocities, as the inner flame joins with the outer flame, the simulated flame is drawn in towards the centreline much more than in the experiments. With the central air tube raised 3 mm, at low central air velocities, there is good agreement in the location and shape of the inner flame. At the middle range of central air velocities, the simulations predict a higher location for the inner flame. At high central air velocities, the base and tip of the flame are in good agreement, but the middle portion of the flame is entrained more into the centreline in the simulations. With the central air tube raised 6 mm, at low central air velocities, when the flame is still attached to the tip of the central air

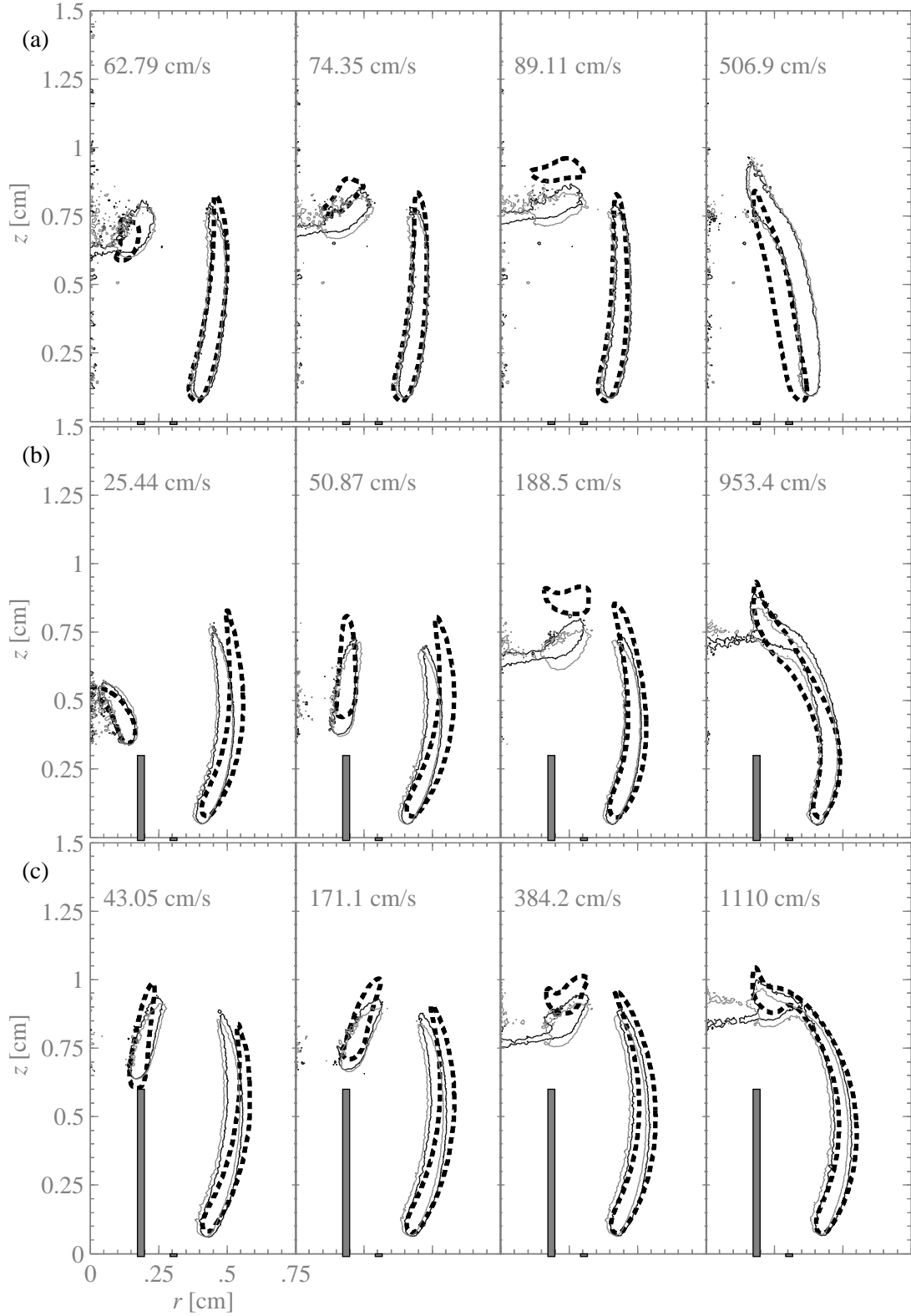


Figure 6.1: Experimental (thin grey line: left side; thin black line: right side) and numerical (thick dashed line) CH* contours with co-flowing air, $u_{cf} = 18.4$ cm/s, and u_{ca} given.

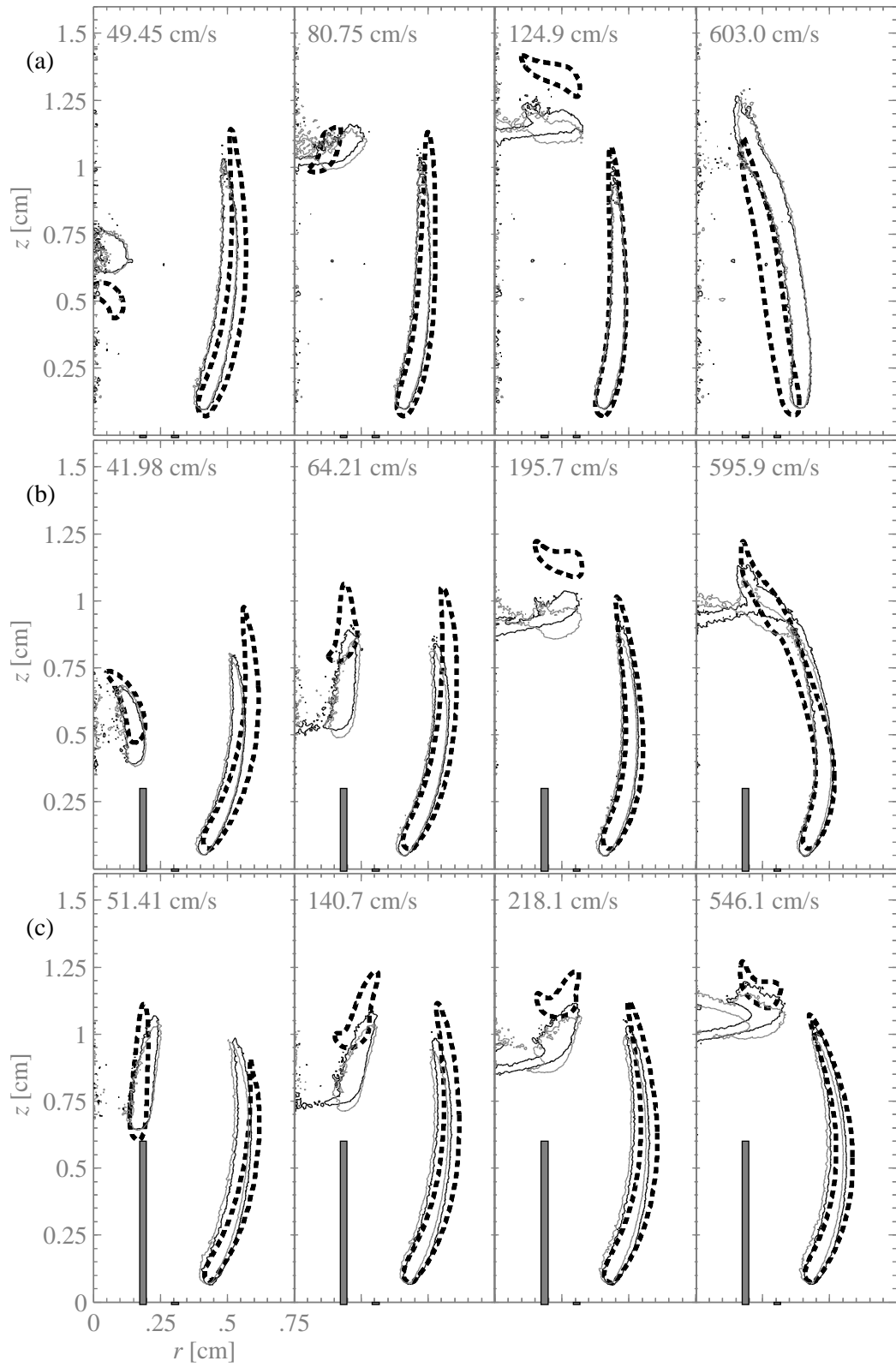


Figure 6.2: Experimental and numerical CH^* contours with co-flowing air, $u_{cf} = 23.0 \text{ cm/s}$, and u_{ca} given. Legend as in Fig. 6.1.

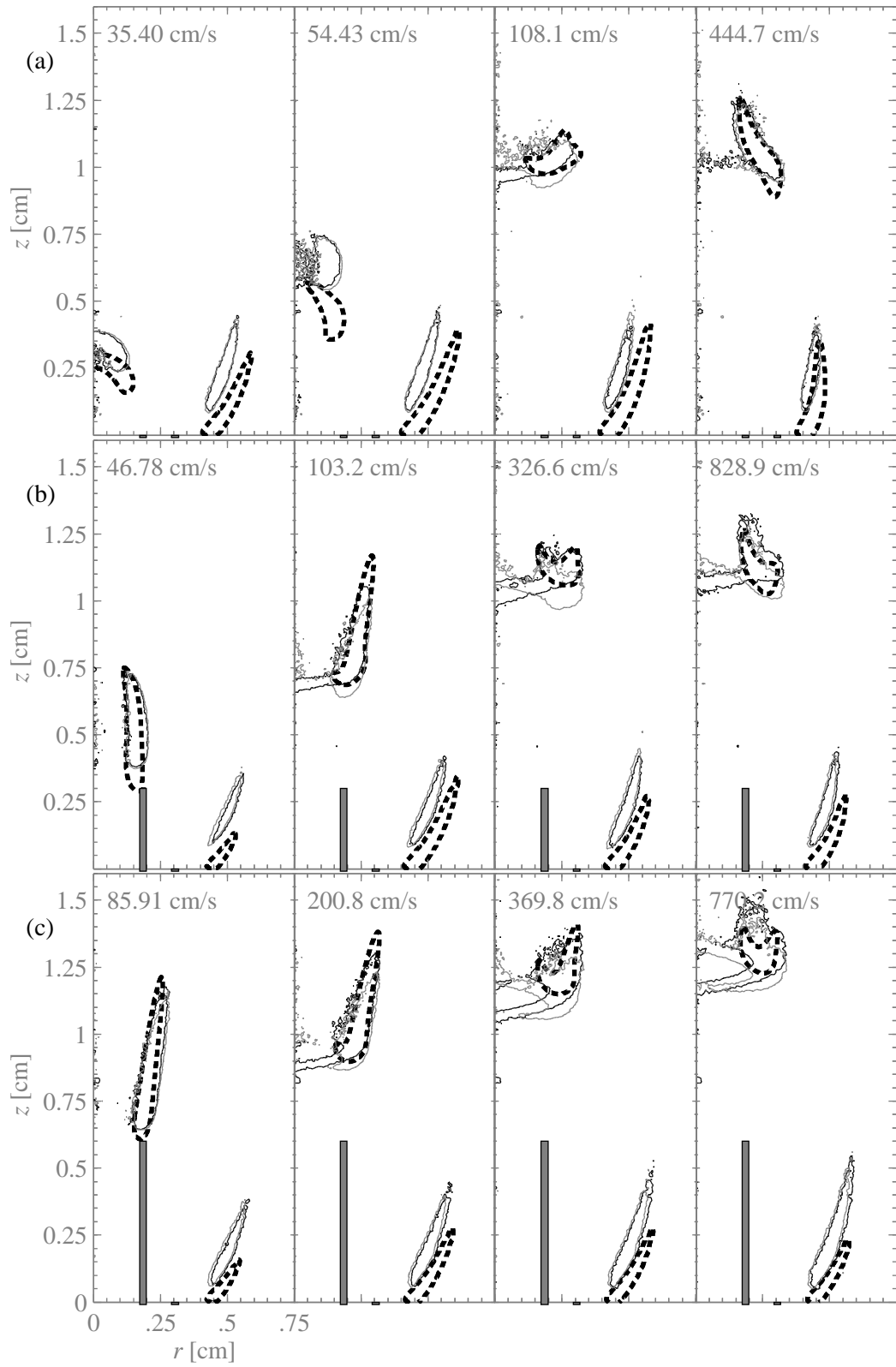


Figure 6.3: Experimental and numerical CH^* contours with $\Phi = 0.78$ co-flow, $u_{\text{cf}} = 18.4 \text{ cm/s}$, and u_{ca} given. Legend as in Fig. 6.1.

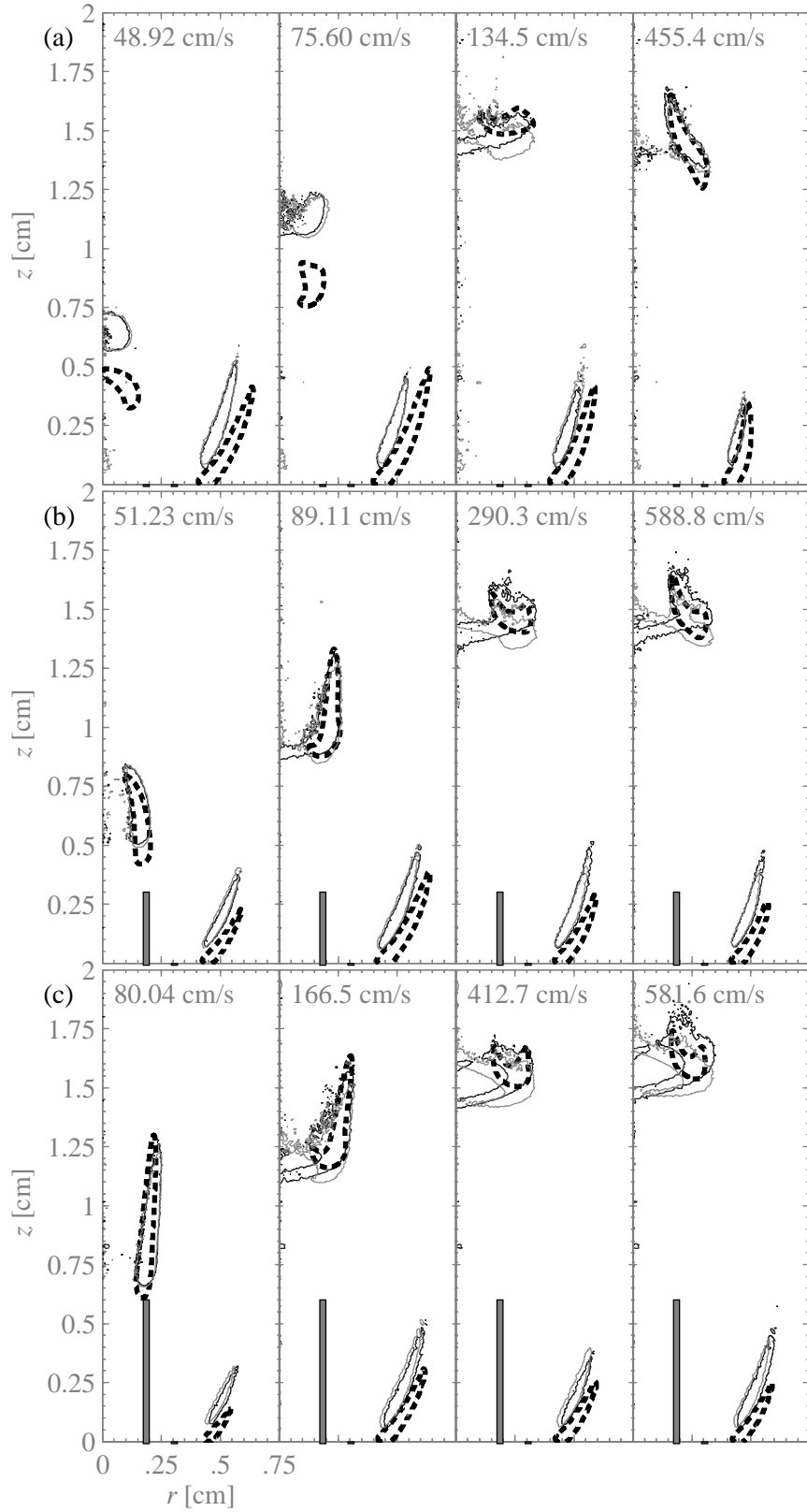


Figure 6.4: Experimental and numerical CH^* contours with $\Phi = 0.78$ co-flow, $u_{cf} = 23.0$ cm/s, and u_{ca} given. Legend as in Fig. 6.1.

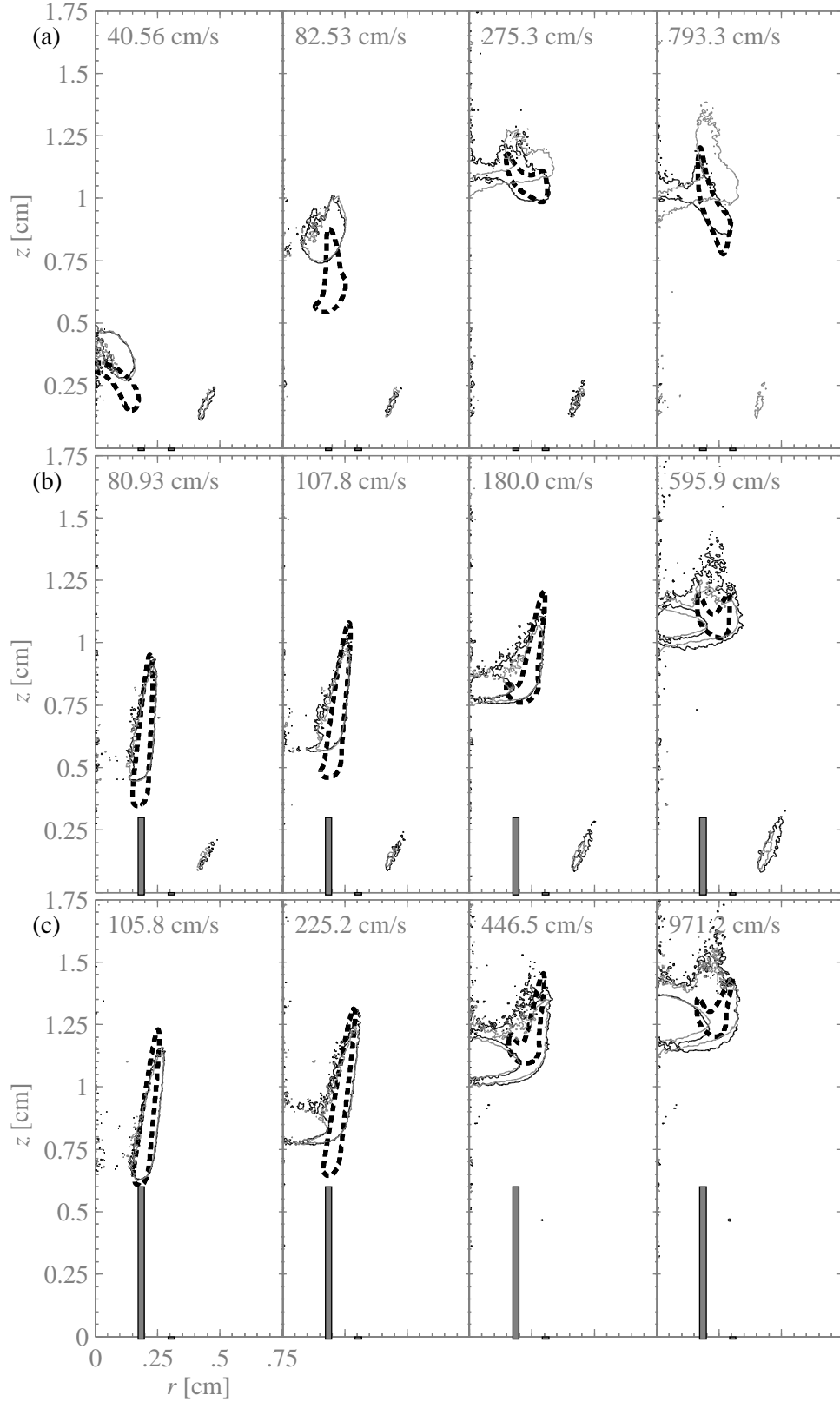


Figure 6.5: Experimental and numerical CH^* contours with $\Phi = 1.0$ co-flow, $u_{\text{cf}} = 18.4 \text{ cm/s}$, and u_{ca} given. Legend as in Fig. 6.1.

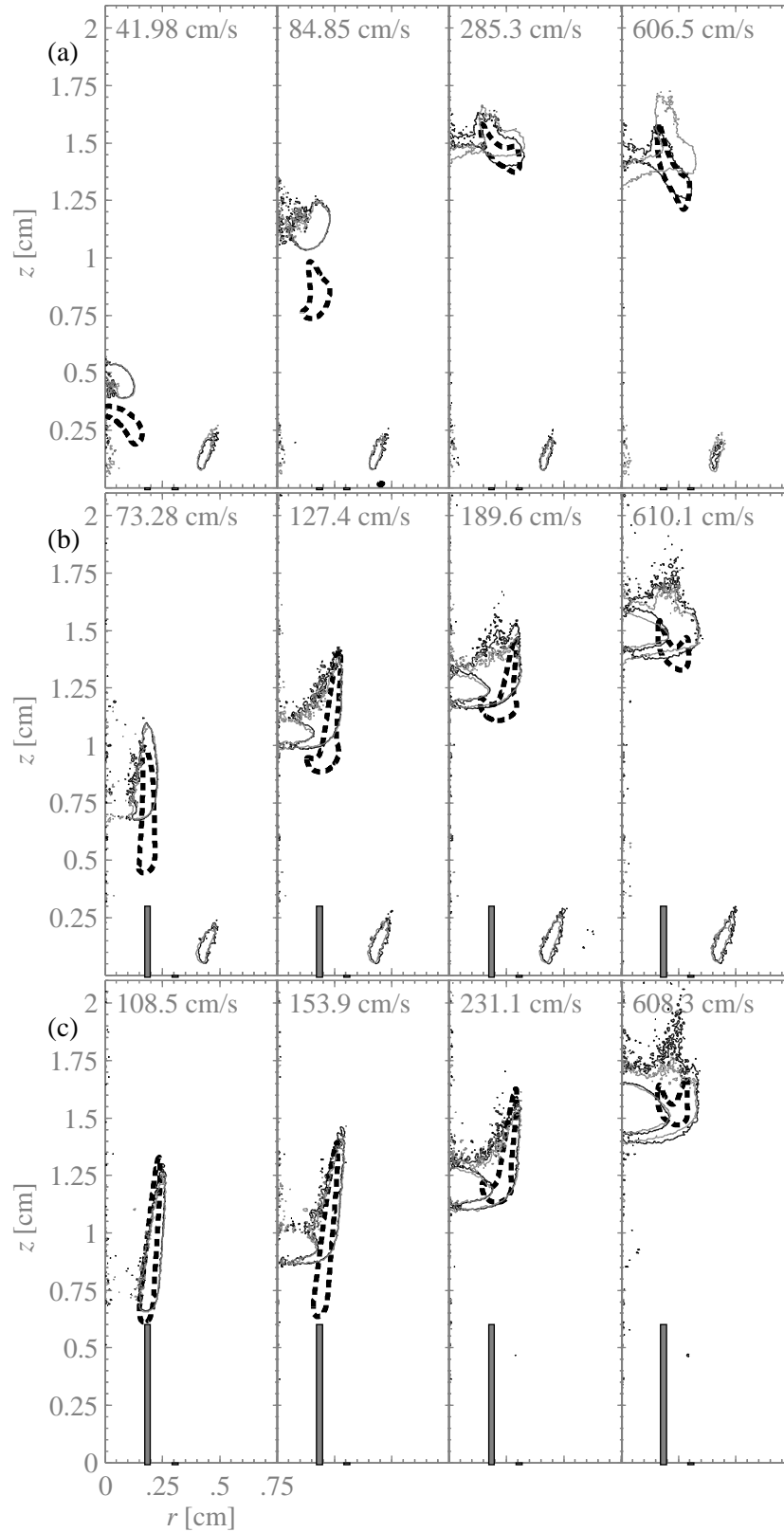


Figure 6.6: Experimental and numerical CH^* contours with $\Phi = 1.0$ co-flow, $u_{\text{cf}} = 23.0 \text{ cm/s}$, and u_{ca} given. Legend as in Fig. 6.1.

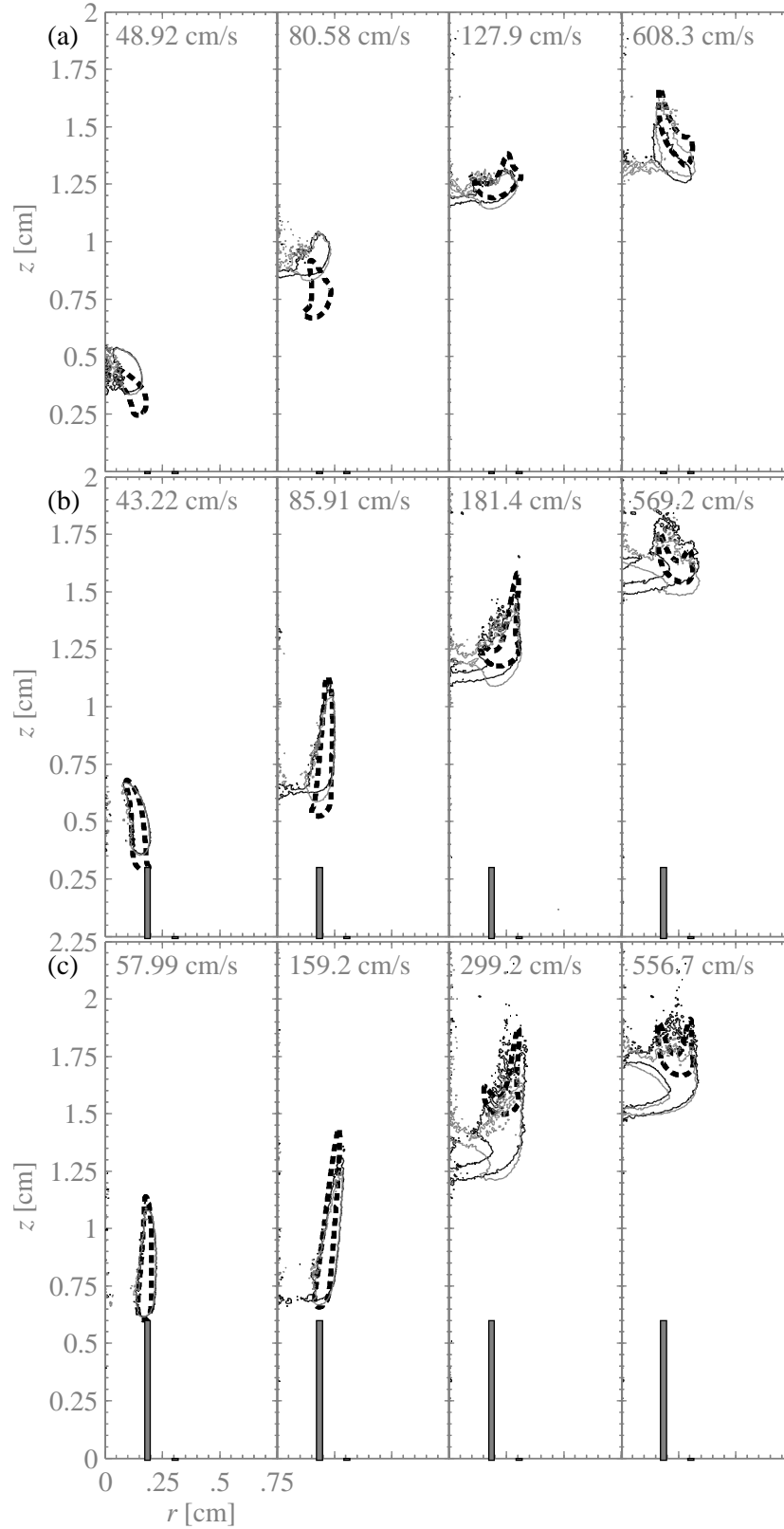


Figure 6.7: Experimental and numerical CH^* contours with $\Phi = 1.2$ co-flow, $u_{\text{cf}} = 18.4$ cm/s, and u_{ca} given. Legend as in Fig. 6.1.

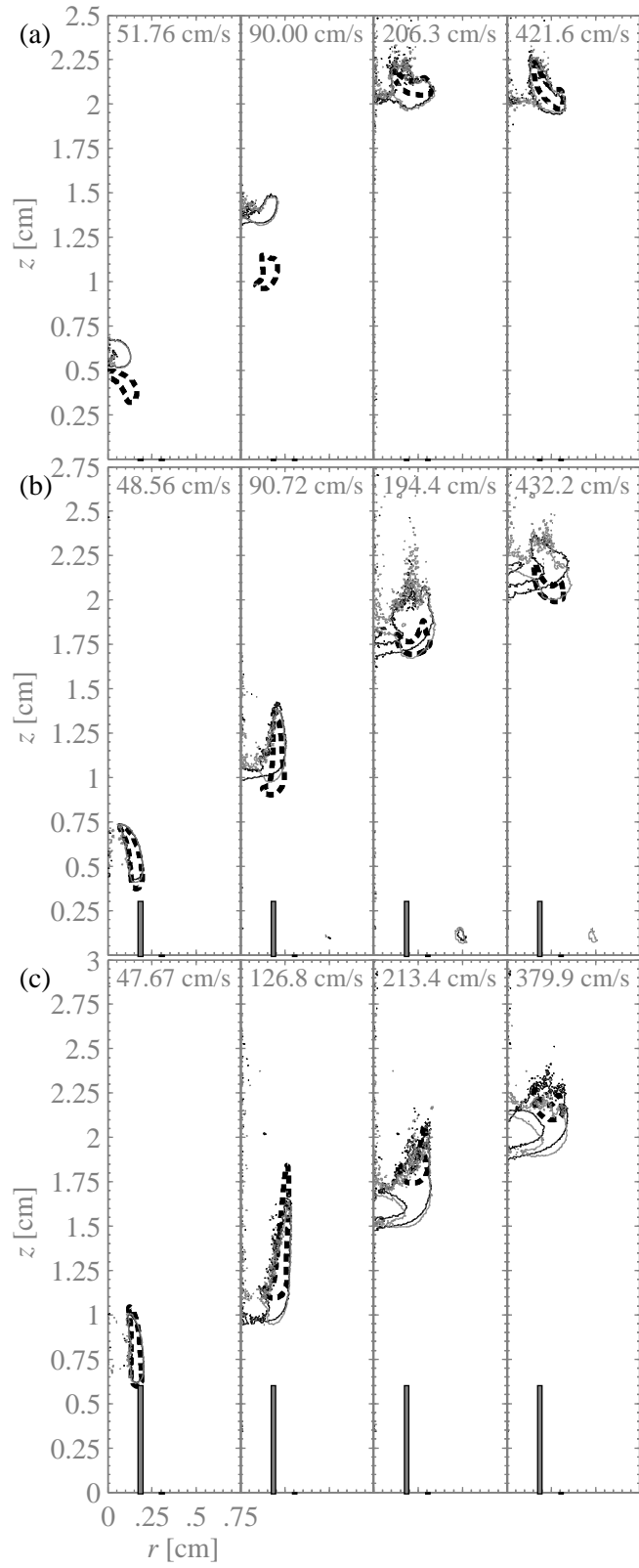


Figure 6.8: Experimental and numerical CH^* contours with $\Phi = 1.2$ co-flow, $u_{\text{cf}} = 23.0 \text{ cm/s}$, and u_{ca} given. Legend as in Fig. 6.1.

tube, the agreement is good. At the middle range of central air velocity, simulations predict a higher location for the inner flame. At high central air velocities, the outer flame is in good agreement, asymmetries are more prominent in the experiments, and the simulations again predict a higher location for the inner flame.

For co-flowing combustion products at $\Phi = 0.78$ (Fig. 6.3), the locations of the burner-stabilized flame in the simulations and experiments are different because in the experiments the flame is stabilized on top of the perforated plate, with a standoff distance. This was discussed in Chapter 4 (Fig. 4.2, pg. 18), but in these experiments, emission from the burner stabilized flame was blocked from reaching the camera, so the burner stabilized flame is not visible in Fig. 6.3. In the simulations, the combustion products are flowing directly from the inlet, with no standoff distance, so the outer flame stabilizes at the burner face.

For the $\Phi = 0.78$ co-flow at central fuel velocity $u_{cf} = 18.4$ cm/s, with the central air tube flush (Fig. 6.3(a)), at low central air velocities the simulations predict a lower flame height than the experiments, although the flame shape is in good agreement. At $u_{ca} = 108.2$ cm/s, and above, the location and shape of the inner flame are in good agreement between experiments and simulations. With the central air tube raised 3 mm (Fig. 6.3(b)), the simulations predict a lower base of the inner flame at low central air velocities, but flame shape and location are well predicted over the entire range of central air velocities. With the central air tube raised 6 mm (Fig. 6.3(c)), at low central air velocities, the location and vertical extent of the inner flame are well predicted. At higher central air velocities, asymmetries in the experimental flames become more and more pronounced, starting with the arc-shaped flame region at $u_{ca} = 200.8$ cm/s. This is the result of taking the Abel transform of an asymmetric flame image, where the ring-shaped flame is tilted along the imaging axis, as discussed in Chapter 5. Despite these asymmetries, the location of the inner flame is in good agreement. At central fuel velocity $u_{cf} = 23.0$ cm/s (Fig. 6.4), the trends are very similar to those at $u_{cf} = 18.4$ cm/s.

For the $\Phi = 1.0$ co-flow at central fuel velocity $u_{cf} = 18.4$ cm/s, with the central air tube flush (Fig. 6.5(a)), at low central air velocities, below $u_{ca} = 275.4$ cm/s, the simulations predict a lower flame height than the experiments. Above $u_{ca} = 275.4$ cm/s, the flame shape and location are in good agreement, although tilting of the flame perpendicular to the imaging axis is visible, particularly at $u_{ca} = 793.3$ cm/s. With the central air tube raised 3 mm (Fig. 6.5(b)), at low central air velocities, the location of the tip of the inner flame is in good agreement, although the simulations predict a lower location for the base of the inner flame. For central air velocities of

$u_{ca} = 180.0$ cm/s and above, asymmetries are evident. Despite these asymmetries, the location of the inner flame is in good agreement. With the central air tube raised 6 mm (Fig. 6.5(c)), the agreement is similar to that at 3 mm. At low central air velocities, the location of the tip of the inner flame is in good agreement, although the simulations predict a lower location for the base of the inner flame. Despite the asymmetries visible at $u_{ca} = 225.2$ cm/s and above, the location of the inner flame is in good agreement. At central fuel velocity $u_{cf} = 23.0$ cm/s (Fig. 6.6), the trends are similar to those at $u_{cf} = 18.4$ cm/s.

For the $\Phi = 1.2$ co-flow at central fuel velocity $u_{cf} = 18.4$ cm/s, with the central air tube flush (Fig. 6.7(a)), the simulations predict a lower location for the inner flame at low central air velocities, up to $u_{ca} = 127.9$ cm/s. At $u_{ca} = 127.9$ cm/s, the inner flame agrees well, but above this velocity the simulations predict a higher location for the inner flame. Over the entire range of central air velocities, though, the shape of the inner flame is well predicted. With the central air tube raised 3 mm (Fig. 6.7(b)), the location of the tip of the inner flame is in good agreement, although the simulations predict a lower location for the base of the inner flame. At higher central air velocities, asymmetries are more pronounced, but the location of the inner flame is in good agreement. With the central air tube raised 6 mm (Fig. 6.7(c)), at low central air velocities, the location of the base and tip of the inner flame are in good agreement. At higher central air velocities, asymmetries are more pronounced, but the location of the inner flame is in good agreement.

At central fuel velocity $u_{cf} = 23.0$ cm/s (Fig. 6.8), the trends are similar to those at $u_{cf} = 18.4$ cm/s. With the central air tube flush, at low central air velocities, simulations predict a lower inner flame, but at and above $u_{ca} = 206.3$ cm/s, there is good agreement. With the central air tube raised 3 mm and 6 mm, there is good agreement in the tip of the inner flame, and despite asymmetries in the experimental images at high central air velocities, the location of the inner flame is in good agreement.

6.2 Sensitivity analysis

Sensitivity calculations were carried out for a selection of flames with co-flowing air and central fuel velocity $u_{cf} = 23.0$ cm/s. Calculations were run changing individually the inlet temperature of the co-flow, central fuel and central air streams from 400 K to 500 K. The velocities for the streams were increased in order to maintain a constant mass flow-rate.

Figures 6.9–6.11 show the contours of 10% of the maximum CH^* chemilumines-

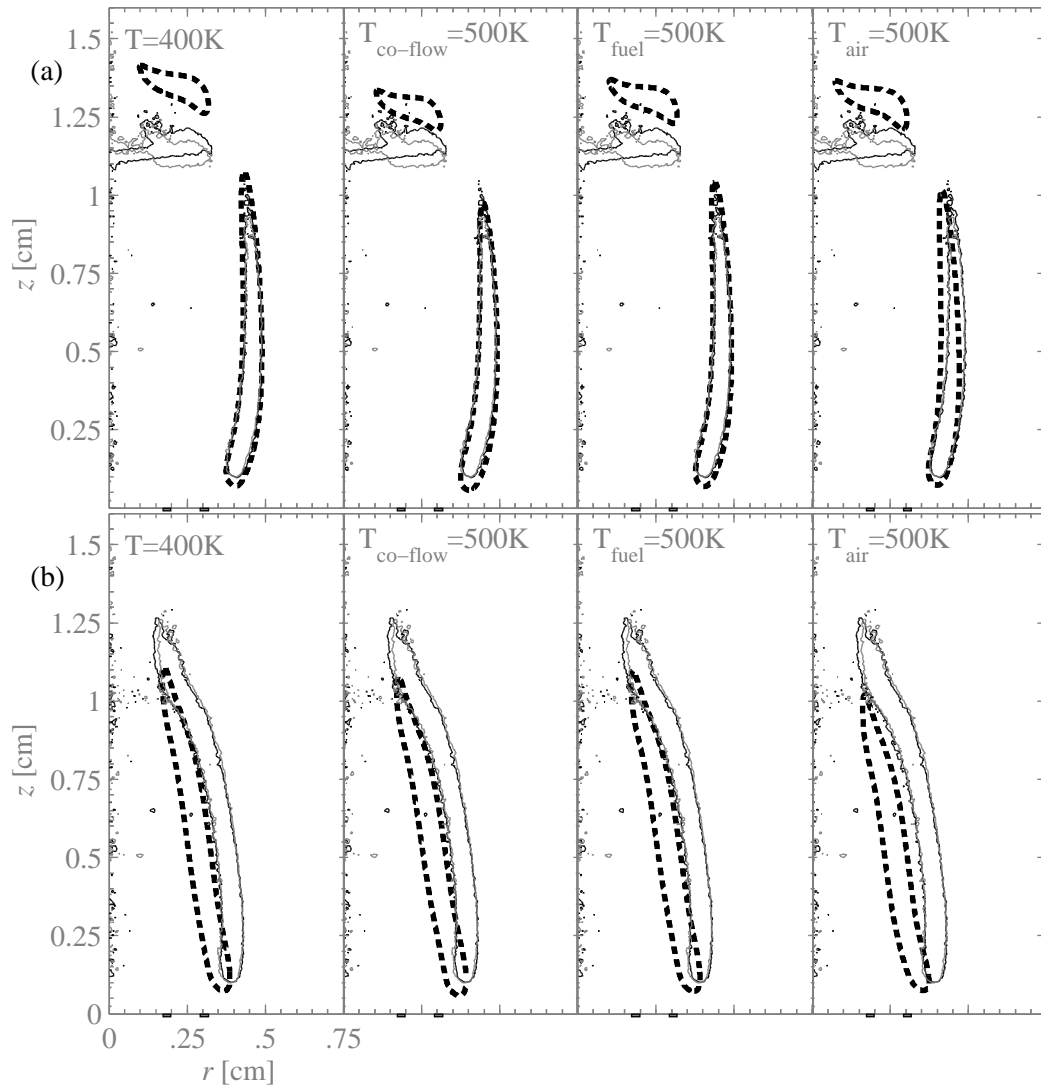


Figure 6.9: Experimental and numerical CH^* contours showing effects of in-flow temperature, with co-flowing air, central air tube flush, $u_{cf} = 23.0 \text{ cm/s}$ and (a) $u_{ca} = 124.9 \text{ cm/s}$, (b) $u_{ca} = 603.0 \text{ cm/s}$. Legend as in Fig. 6.1

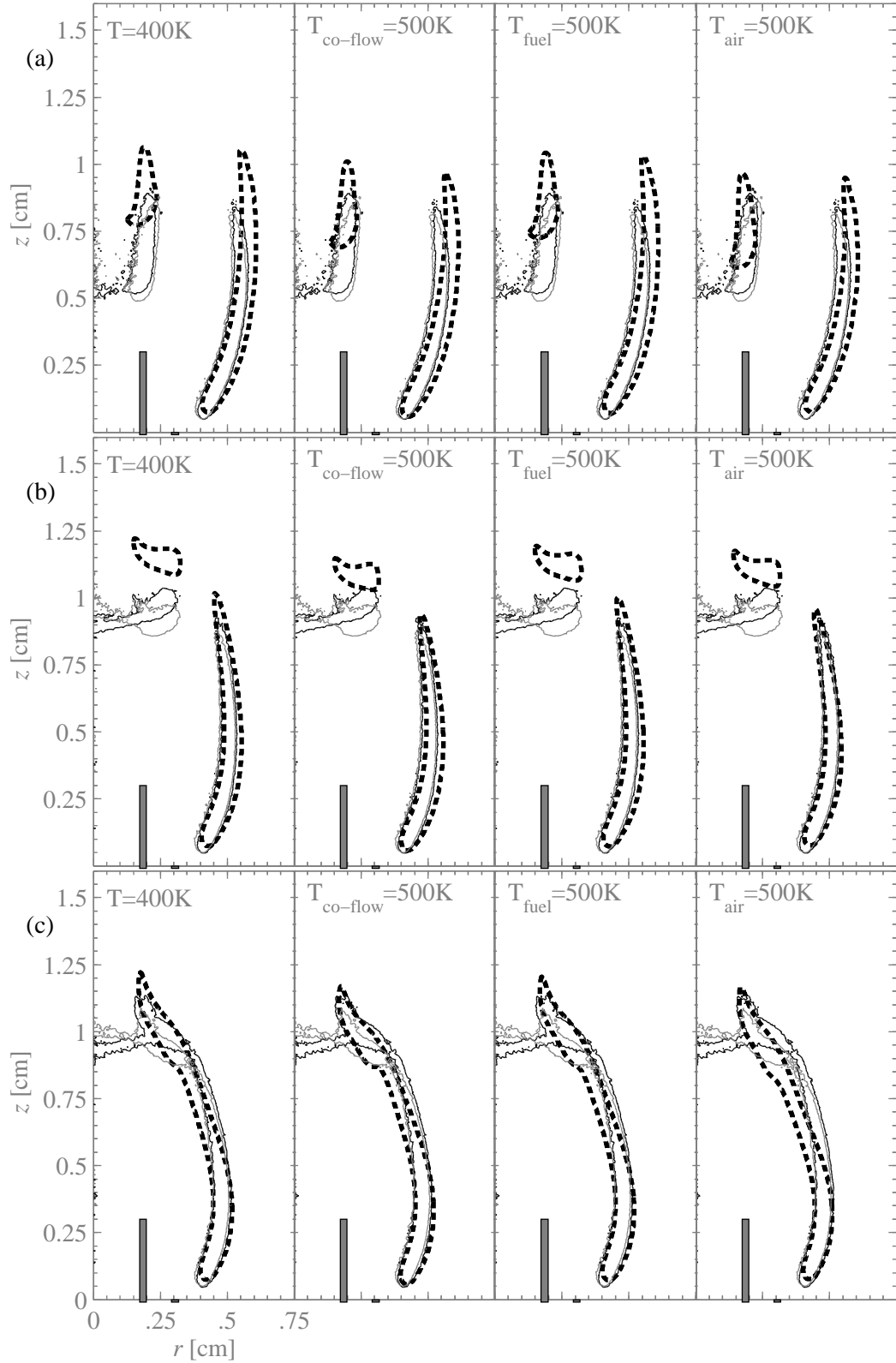


Figure 6.10: Experimental and numerical CH^* contours showing effects of in-flow temperature, with co-flowing air, central air tube raised 3 mm, $u_{\text{cf}} = 23.0$ cm/s and (a) $u_{\text{ca}} = 64.21$ cm/s, (b) $u_{\text{ca}} = 195.7$ cm/s (c) $u_{\text{ca}} = 595.9$ cm/s. Legend as in Fig. 6.1

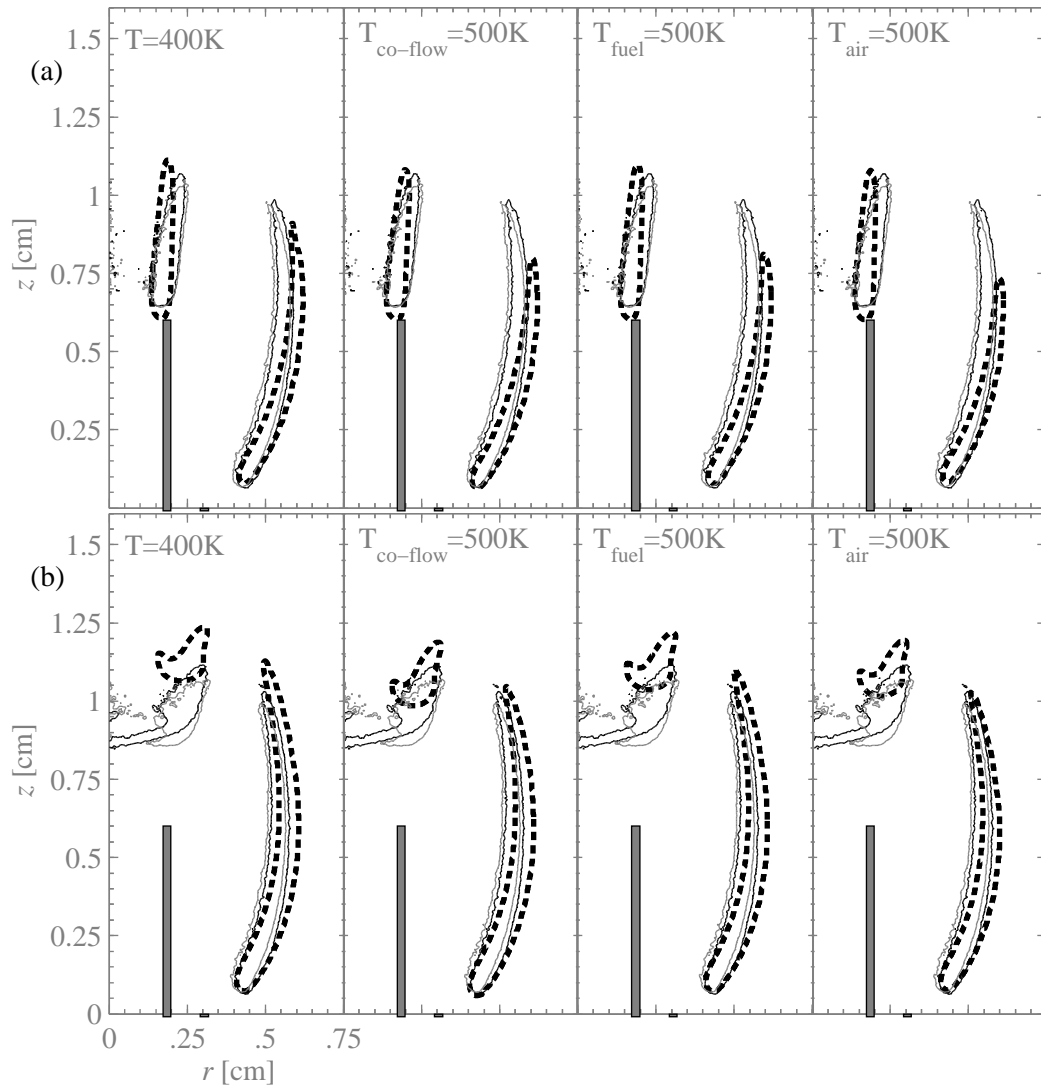


Figure 6.11: Experimental and numerical CH* contours showing effects of in-flow temperature, with co-flowing air, central air tube raised 6 mm, $u_{\text{cf}} = 23.0$ cm/s and (a) $u_{\text{ca}} = 51.41$ cm/s, (b) $u_{\text{ca}} = 218.1$ cm/s. Legend as in Fig. 6.1

cence emission. With the central air tube flush, in Fig. 6.9(a), increasing the temperature does move the inner flame down, into better agreement with experiments. In Fig. 6.9(b), increasing the inlet temperature causes the flame to move further inward towards the centreline, with poorer agreement with experiments.

With the central air tube raised 3 mm, in Figs. 6.10(a) and (b), increasing the inlet temperature moves the inner flame lower, giving better agreement with experiments. The smallest effect is from increasing the fuel temperature, with the co-flow and central air stream temperatures having a greater effect. In Fig. 6.10(c), increasing the inlet temperature has very little effect on the base or tip of the flame, but does cause the middle portion of the flame to be drawn closer to the centreline.

With the central air tube raised 6 mm, in Fig. 6.11(a), changing the inlet temperature has very little effect on the diffusion flame attached to the lip of the central air tube. With the air temperature increased, the outer flame seems to get shorter, but this is most likely due to an increase in the maximum CH^* concentration in the inner flame, causing the 10% contour of the outer flame to shorten. In Fig. 6.11(b), increasing the temperature does move the inner flame down, into better agreement with experiments.

In summary, for lifted inner flames, increasing the inlet temperature of the central air or co-flow streams by 100 K does have a small effect on the flame location, moving it towards better agreement with the experiments. At the high central air velocities, though, the small changes in the flame from an increase in inlet temperature cause the agreement with experiments to worsen.

Chapter 7

Numerical simulation results

This chapter presents the numerical simulation results. After comparing the numerical and experimental results, and validating the numerical method, the numerical results are analyzed in order to address the question of whether NO_x emissions can be reduced through this type of burner.

The first section describes the relevant characteristics of the flames through contour plots and radial distributions of species and temperature at different heights, illustrating important elements of the flames that contribute to the emissions. The second section describes the trends in heat release and emission of CO and NO for the different co-flows as the central air velocity is increased. These trends are explained with detailed analysis of some flames in particular, illustrating the changes as the central air velocity is increased, and as the central air tube is raised.

7.1 Flame characteristics

As mentioned in Chapter 4, the lifted inverse diffusion flame is stabilized with a premixed base. This is evident from data taken along the streamline through the point of the maximum destruction rate of CH_4 in the inner flame. Figures 7.1 and 7.2 show axial velocity and temperature along this streamline for flames with co-flowing air and $u_{cf} = 18.4 \text{ cm/s}$. At low central air velocities, the premixed nature of the flame is evident as the velocity and temperature rise steeply through the flame. At higher central air velocities, the inner flame joins with the outer diffusion flame, but retains the premixed character along the streamline, again evident from the rapid rise in temperature along the streamline. At higher central air velocities the same character is evident in the velocity plot, although the sudden rise in velocity is not as evident since the scale of the velocity plot is so much greater. At higher central

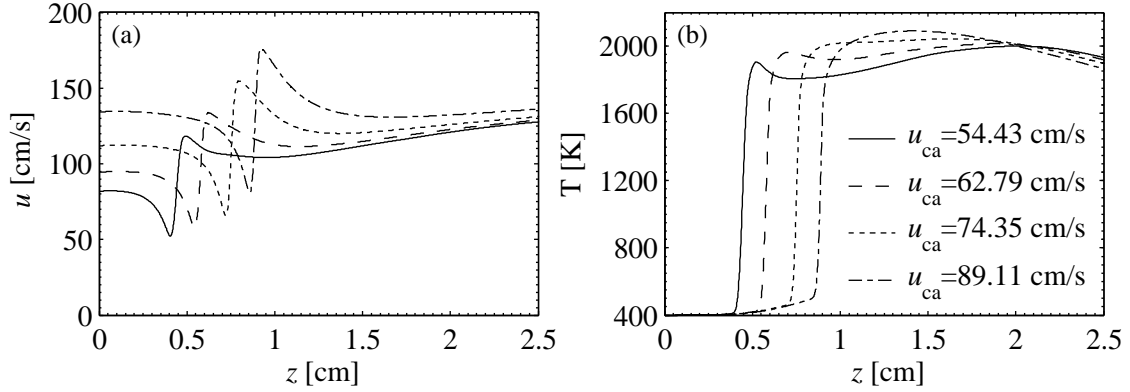


Figure 7.1: (a) Axial velocity and (b) temperature along streamline through the point of maximum destruction rate of CH_4 , for co-flowing air and central air tube flush.

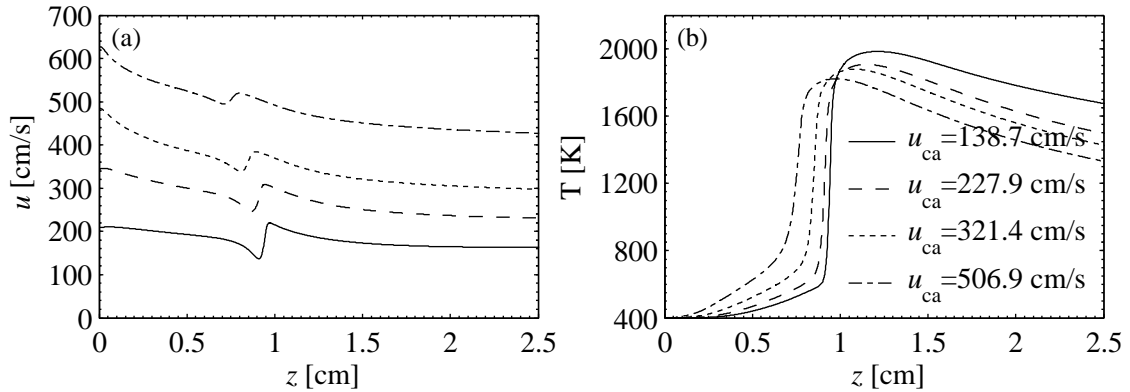


Figure 7.2: (a) Axial velocity and (b) temperature along streamline through the point of maximum destruction rate of CH_4 , for co-flowing air and central air tube flush.

air velocities, the temperature increase along the streamline before the flame location is greater, due to increased entrainment of products from the outer diffusion flame as the central air velocity is increased. This increased temperature is necessary for the propagation velocity of the flame to match fluid velocities on the order of several metres per second. The premixed nature of the base of the inner flame is also seen with the combustion product co-flows, and with the raised central air tube.

Figures 7.3–7.5 show the radial distribution of temperature, CH_4 , O_2 , and CO_2 at two different heights—upstream and downstream of the inner flame—and contour plots of temperature and CH mass fraction, with co-flowing air and central air tube flush.

For $u_{ca} = 54.43 \text{ cm/s}$, upstream of the inner flame at $z = 0.4 \text{ cm}$, there is the outer diffusion flame at $r \sim 0.45 \text{ cm}$. In this flame, central fuel, as well as some central air that has mixed with the central fuel, are reacting with the co-flowing

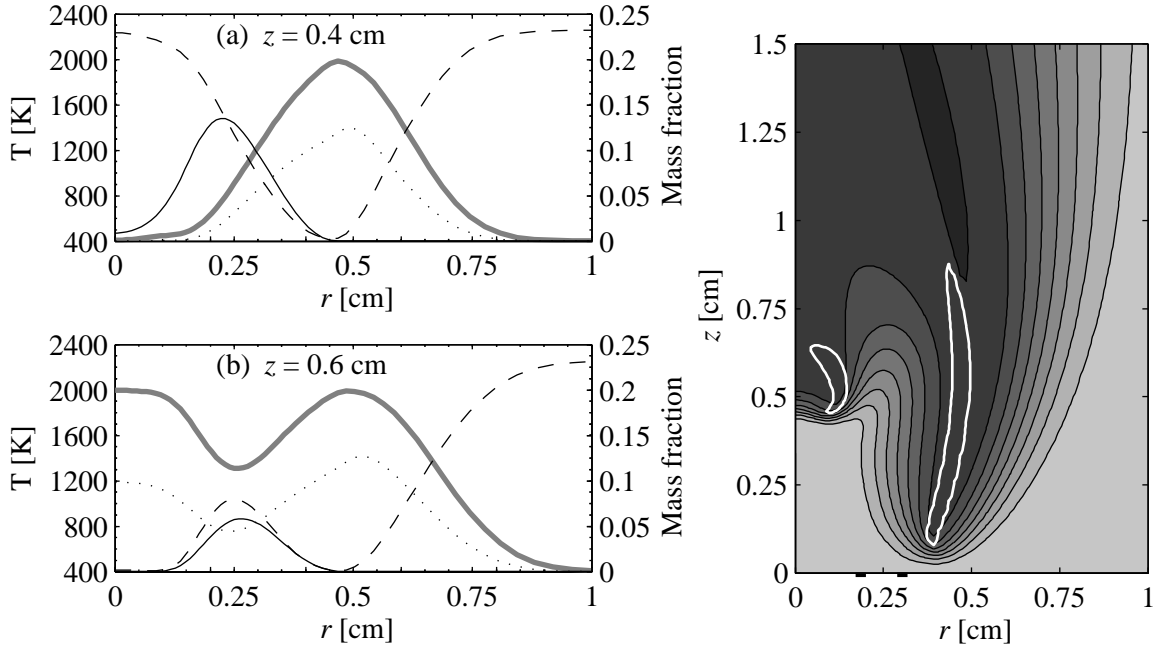


Figure 7.3: Radial profiles of species (solid: CH₄, dashed: O₂, dotted: CO₂) and temperature (thick grey line) for co-flowing air, central air tube flush, $u_{cf} = 18.4$ cm/s, and $u_{ca} = 54.43$ cm/s. On the right is a contour of temperature (lightest shade of grey is 400 K, increasing by 200 K each contour line) and 10% of the maximum CH mass fraction in white.

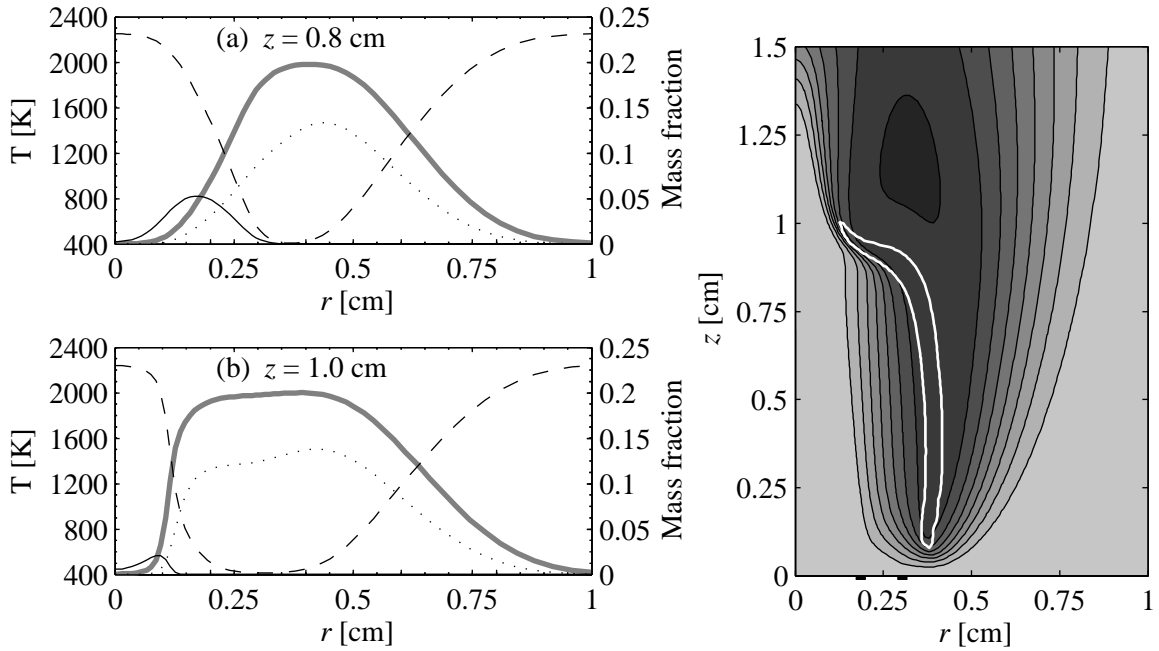


Figure 7.4: Radial profiles of species and temperature, and contour plot of temperature and CH for co-flowing air, central air tube flush, $u_{cf} = 18.4$ cm/s, and $u_{ca} = 138.7$ cm/s (legend as in Fig. 7.3).

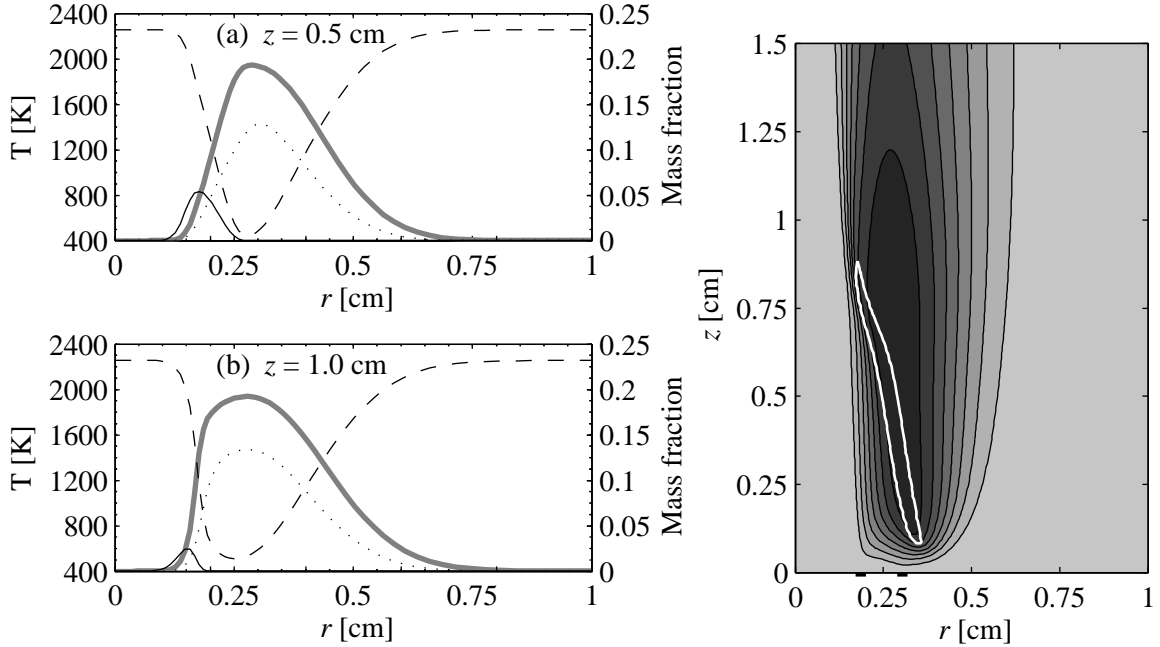


Figure 7.5: Radial profiles of species and temperature, and contour plot of temperature and CH for co-flowing air, central air tube flush, $u_{cf} = 18.4$ cm/s, and $u_{ca} = 506.9$ cm/s (legend as in Fig. 7.3).

air, and there is a corresponding peak in temperature and CO_2 at that location. Downstream of the inner flame, at $z = 0.6$ cm, the air and fuel near the centreline have been completely consumed, with a corresponding increase in the temperature and CO_2 near the centreline. The fuel and air that remain around $r \sim 0.25$ cm continue to react with the co-flowing air in the outer diffusion flame.

For $u_{ca} = 138.7$ cm/s (Fig. 7.4), the inner flame has started to join with the outer flame. At $z = 0.8$ cm, central fuel and air have mixed and are reacting with co-flowing air in the outer diffusion flame, now located closer to the centreline at $r \sim 0.4$ cm, due to the entrainment of the higher velocity central air jet. Above the location of the inner flame, at $z = 1.0$ cm, the fuel and oxygen have been reacted through the inner flame, but some of the unburned fuel has been entrained into the central air jet, and is visible near the centreline.

For $u_{ca} = 506.9$ cm/s (Fig. 7.5), the entrainment into the central air jet is even stronger. At $z = 0.5$ cm, the outer diffusion flame is located at $r \sim 0.25$ cm, with a peak in temperature and CO_2 at that location. Through the tip of the flame, between $z = 0.5$ – 1.0 cm, fuel is consumed, with some unburned fuel around $z = 0.15$ cm that is entrained into the central air jet.

Figures 7.6–7.8 show the contours and radial distributions for co-flowing air with

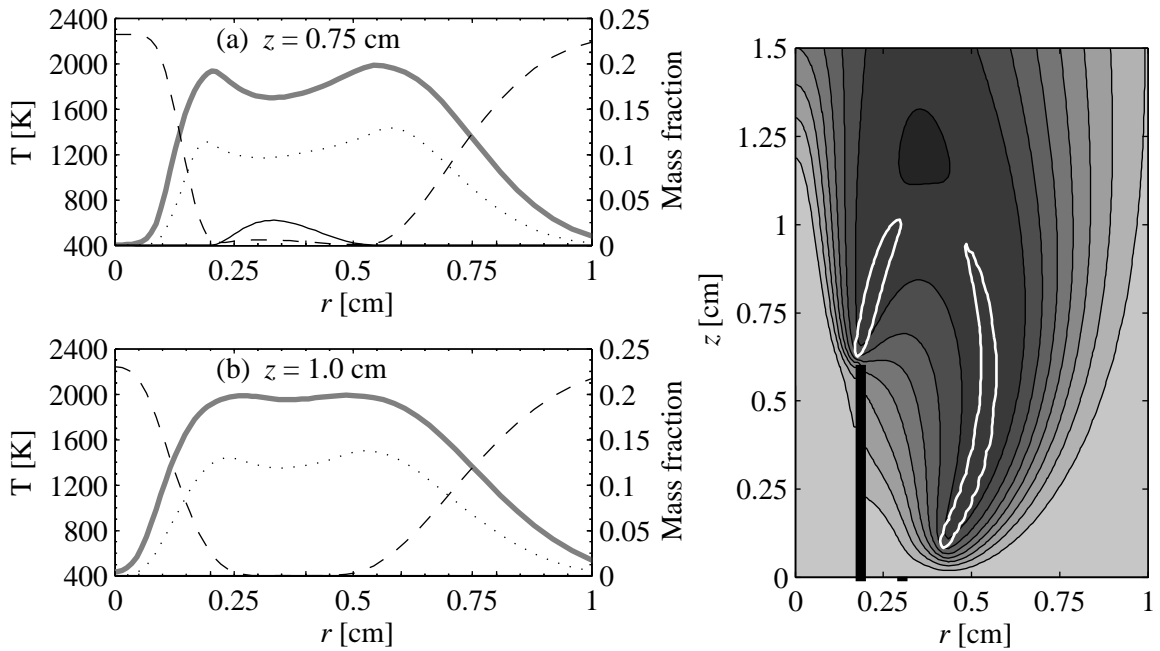


Figure 7.6: Radial profiles of species and temperature, and contour plot of temperature and CH for co-flowing air, central air tube raised 6 mm, $u_{cf} = 18.4$ cm/s, and $u_{ca} = 78.97$ cm/s (legend as in Fig. 7.3).

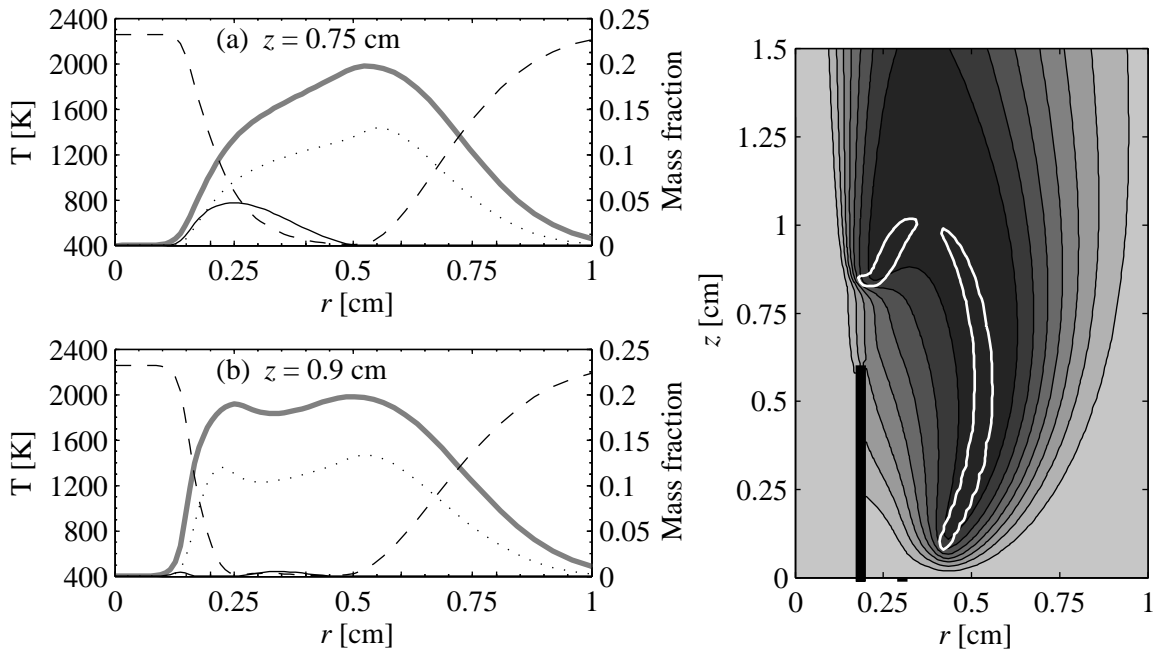


Figure 7.7: Radial profiles of species and temperature, and contour plot of temperature and CH for co-flowing air, central air tube raised 6 mm, $u_{cf} = 18.4$ cm/s, and $u_{ca} = 239.6$ cm/s (legend as in Fig. 7.3).

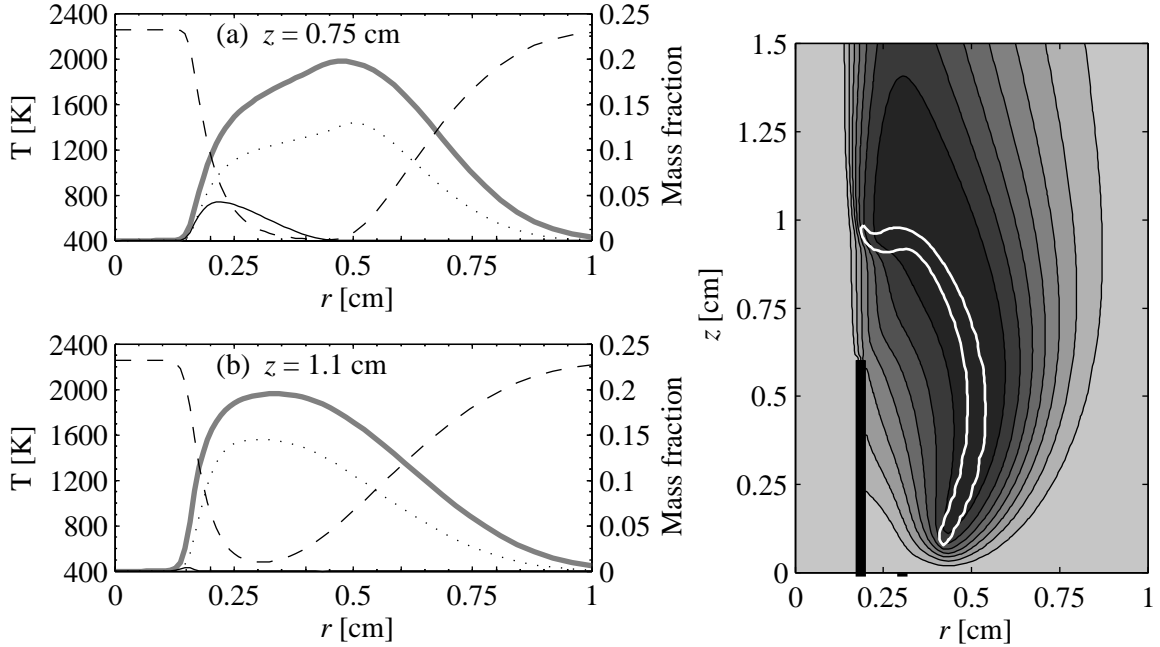


Figure 7.8: Radial profiles of species and temperature, and contour plot of temperature and CH for co-flowing air, central air tube raised 6 mm, $u_{cf} = 18.4$ cm/s, and $u_{ca} = 754.2$ cm/s (legend as in Fig. 7.3).

the central air tube raised 6 mm. For $u_{ca} = 78.97$ cm/s (Fig. 7.6), the inner flame is attached to the lip of the central air tube as a diffusion flame. At $z = 0.75$ cm, fuel from the central fuel tube is reacting in two diffusion flames—the outer diffusion flame at $r \sim 0.55$ cm, and the inner diffusion flame attached to the central air tube at $r \sim 0.2$ cm, with corresponding peaks in temperature and CO_2 at those two radial locations. At $z = 1.0$ cm, all the central fuel has been consumed through those two flames.

For $u_{ca} = 239.6$ cm/s (Fig. 7.7), the inner flame has lifted off the central air tube and, as described earlier, the base of that flame is premixed, with a diffusion flame attached to it. At $z = 0.75$ cm, central fuel is reacting in the outer diffusion flame at $r \sim 0.5$ cm. Fuel near $r \sim 0.25$ cm is consumed through the premixed lifted flame, and downstream of the lifted flame at $z = 0.9$ cm, the small amount of remaining fuel is reacting in the two diffusion flames at $r \sim 0.3$ and 0.45 cm, with an additional small pocket of unburned fuel around $r \sim 0.15$ cm.

For $u_{ca} = 754.2$ cm/s (Fig. 7.8), the entrainment into the central air jet is stronger, so the diffusion flame that was attached to the premixed flame is no longer present, and most of the fuel has been consumed downstream of the premixed flame with a small pocket of unburned fuel at $r \sim 0.15$ cm.

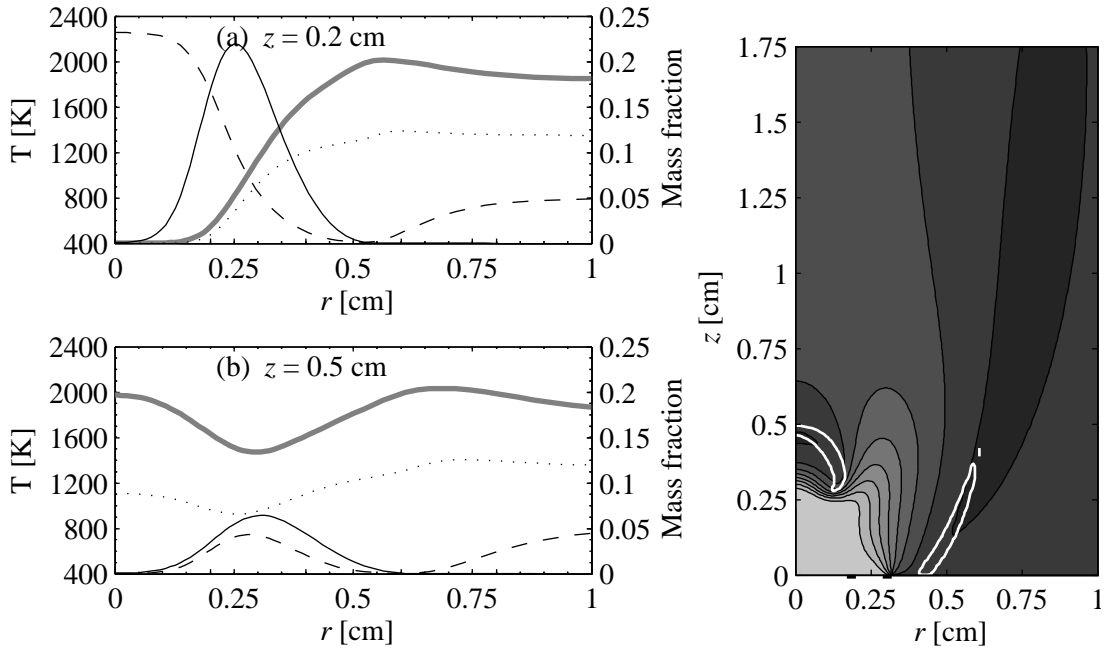


Figure 7.9: Radial profiles of species and temperature, and contour plot of temperature and CH for $\Phi = 0.78$ co-flow, central air tube flush, $u_{cf} = 18.4$ cm/s, and $u_{ca} = 48.2$ cm/s (legend as in Fig. 7.3).

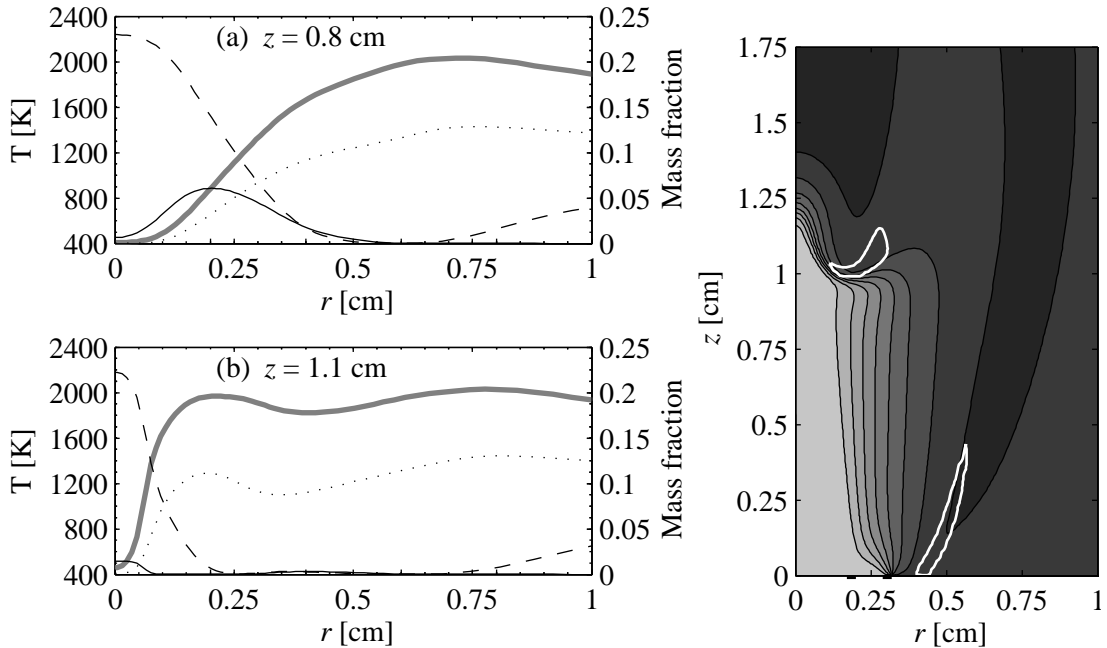


Figure 7.10: Radial profiles of species and temperature, and contour plot of temperature and CH for $\Phi = 0.78$ co-flow, central air tube flush, $u_{cf} = 18.4$ cm/s, and $u_{ca} = 108.2$ cm/s (legend as in Fig. 7.3).

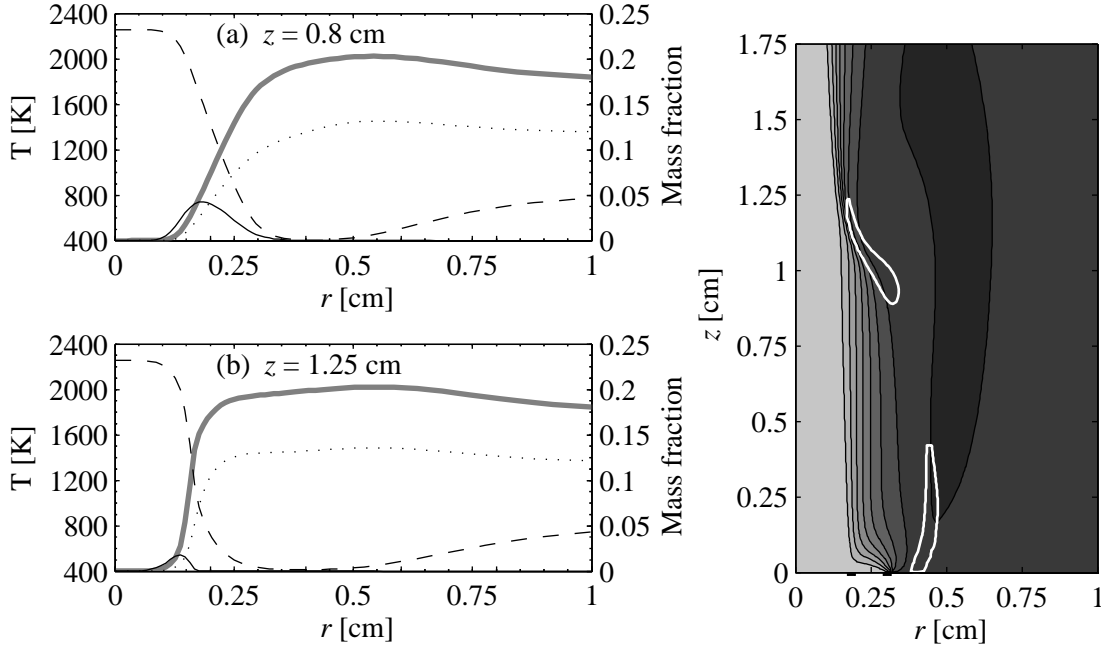


Figure 7.11: Radial profiles of species and temperature, and contour plot of temperature and CH for $\Phi = 0.78$ co-flow, central air tube flush, $u_{cf} = 18.4$ cm/s, and $u_{ca} = 444.7$ cm/s (legend as in Fig. 7.3).

Figures 7.9–7.11 show the contours and radial distributions for $\Phi = 0.78$ co-flow and central air tube flush. The general flame characteristics are similar to those observed with co-flowing air.

For $u_{ca} = 48.20$ cm/s (Fig. 7.9), the outer diffusion flame is located further away from the centreline, due to the reduced oxygen concentration in the co-flow. Upstream of the inner flame at $z = 0.2$ cm, central fuel and air are reacting in the outer diffusion flame at $r \sim 0.55$ cm. The peaks in temperature and CO_2 at the outer flame, are not as defined as with the air co-flow, since the co-flowing combustion products already contain CO_2 at elevated temperature. At $z = 0.5$ cm, fuel and air near the centreline have been consumed through the inner flame, with a corresponding increase in temperature and CO_2 . The remaining fuel and air continue to react in the outer diffusion flame, now pushed further outwards at $r \sim 0.6$ cm, due to expansion from the inner flame.

For $u_{ca} = 108.2$ cm/s (Fig. 7.10), the lifted inner flame has separated from the centreline. Central fuel and air around $r \sim .25$ cm are consumed through the inner flame, but there is some unburned fuel entrained into the central air jet at the centreline.

For $u_{ca} = 444.7$ cm/s (Fig. 7.11), upstream of the inner flame at $z = 0.8$ cm,

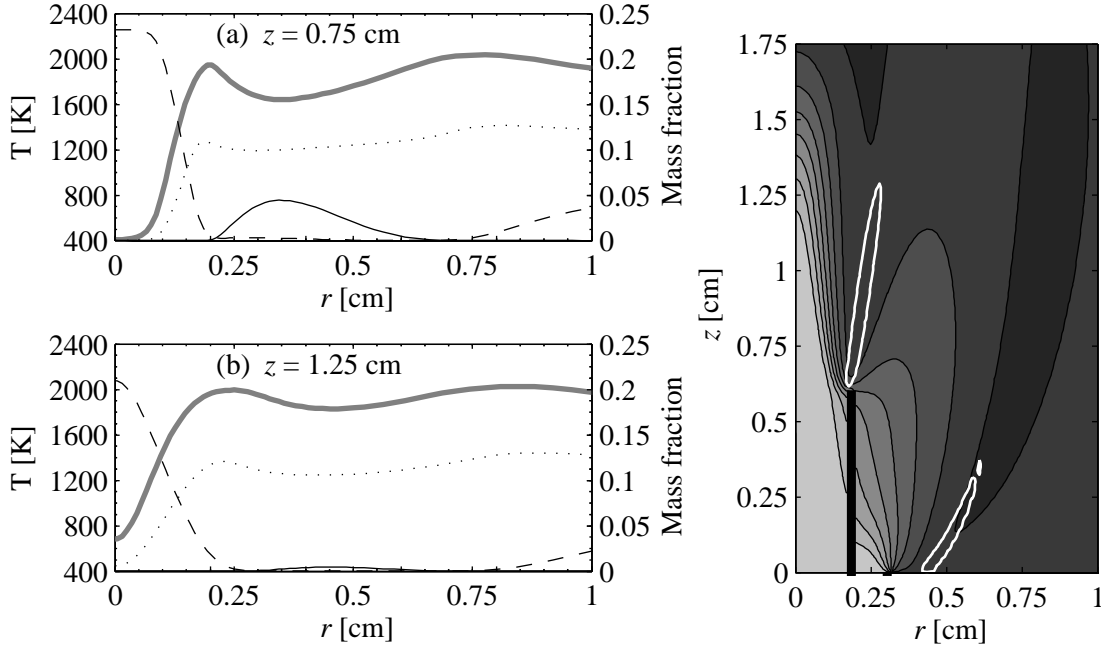


Figure 7.12: Radial profiles of species and temperature, and contour plot of temperature and CH for $\Phi = 0.78$ co-flow, central air tube raised 6 mm, $u_{cf} = 18.4$ cm/s, and $u_{ca} = 85.91$ cm/s (legend as in Fig. 7.3).

the outer diffusion flame has been pulled in towards the centreline and is now at $r \sim 0.4$ cm. Through the inner flame, a large portion of the fuel and air around $r \sim 0.15$ cm is consumed, but there is a small pocket of fuel that is un-reacted and entrained into the central air jet.

Figures 7.12–7.14 show the contours and radial distributions for the $\Phi = 0.78$ co-flow and central air tube raised 6 mm.

For $u_{ca} = 85.91$ cm/s (Fig. 7.12), the inner flame is attached to the lip of the central air tube. At $z = 0.75$ cm, central fuel is reacting in two diffusion flames—the inner flame attached to the central air tube, and the outer diffusion flame which has been pushed further out into the co-flow due to the presence of the raised central air tube, and is now around $r \sim 0.75$ cm. There are corresponding peaks of CO_2 and temperature at those two locations. Most of the central fuel has been consumed by $z = 1.25$ cm, with the remainder continuing to react in the inner and outer diffusion flames.

For $u_{ca} = 200.8$ cm/s (Fig. 7.13), the inner flame has lifted off the central air tube. Through the inner flame, a large portion of the central fuel and air are consumed at $r \sim 0.25$ cm. Downstream, at $z = 1.0$ cm, the remaining fuel is reacting in the diffusion flame attached to the premixed flame at $r \sim 0.25$ cm, and in the outer diffusion flame

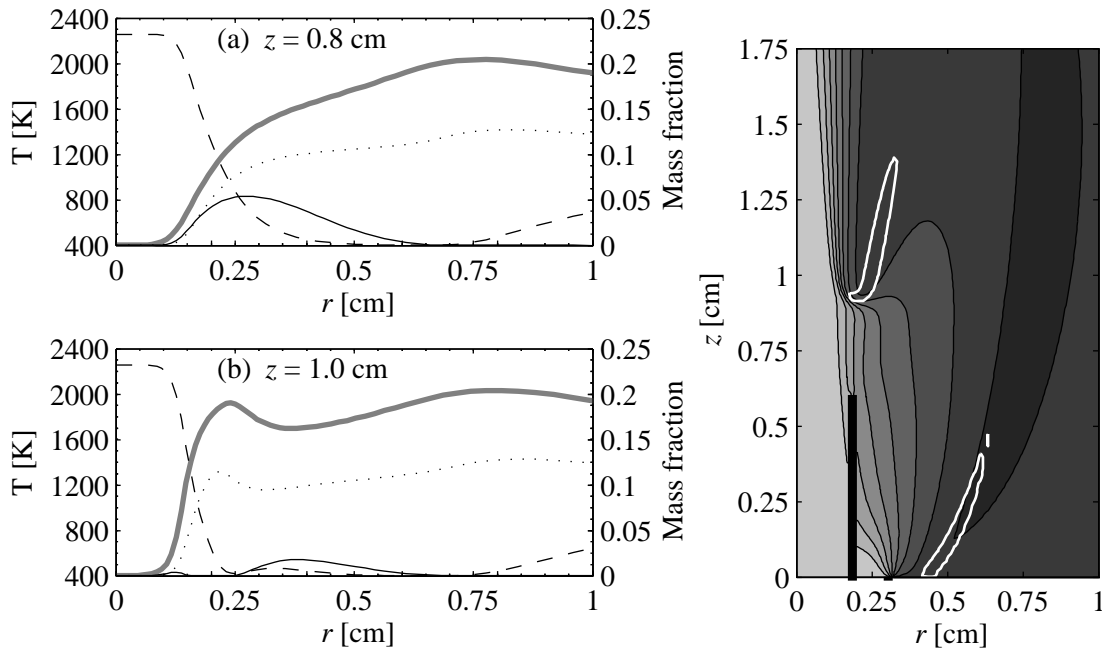


Figure 7.13: Radial profiles of species and temperature, and contour plot of temperature and CH for $\Phi = 0.78$ co-flow, central air tube raised 6 mm, $u_{cf} = 18.4$ cm/s, and $u_{ca} = 200.8$ cm/s (legend as in Fig. 7.3).

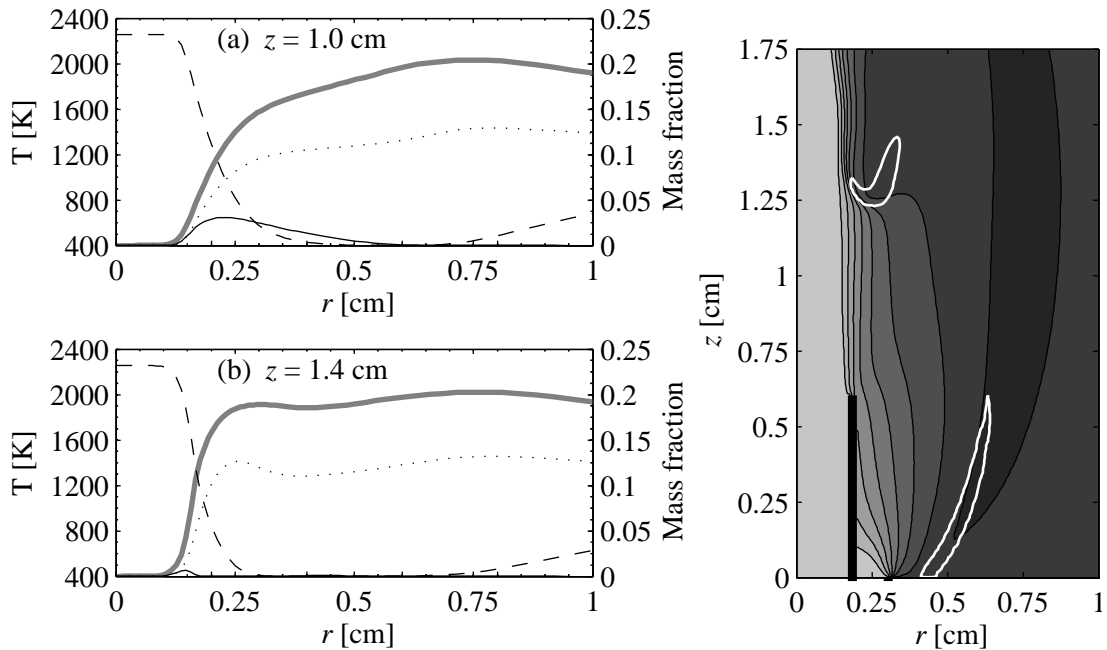


Figure 7.14: Radial profiles of species and temperature, and contour plot of temperature and CH for $\Phi = 0.78$ co-flow, central air tube raised 6 mm, $u_{cf} = 18.4$ cm/s, and $u_{ca} = 569.2$ cm/s (legend as in Fig. 7.3).

at $r \sim 0.75$ cm, with a small pocket of unburned fuel remaining around $r \sim .15$ cm.

For $u_{ca} = 569.2$ cm/s (Fig. 7.14), the diffusion flame attached to the lifted flame is no longer present. Through the lifted flame, the central fuel and air at $r \sim 0.25$ cm are consumed, with a small pocket of fuel entrained into the central air jet at $r \sim 0.15$ cm.

The behaviour of the flames with the $\Phi = 1.0$, and $\Phi = 1.2$ co-flows is similar to that with co-flowing air. Plots of radial species and temperature for those flames are included in Appendix D. The outer diffusion flame is weaker with the $\Phi = 1.0$ co-flow, and disappears completely with the $\Phi = 1.2$ co-flow as there is no longer any oxygen in the co-flow, but the flames retain the same general characteristics.

In summary, the general characteristics of these flames are as follows. For the central air tube flush, at low central air velocities, there is a lifted inner flame near the centreline. Some of the central fuel and air are consumed in this flame, and the rest react in the outer diffusion flame. With the $\Phi = 1.0$ co-flow, this outer flame is very weak and so the remaining reaction of fuel in that region is very slow. With the $\Phi = 1.2$ co-flow, this outer flame is no longer present, as the co-flow is devoid of oxygen. As the central air velocity is increased, the inner flame moves away from the centreline and joins with the outer diffusion flame, if one is present. The entrainment of fuel and co-flowing gas into the central air jet increases. This entrained mixture is consumed through the lifted flame, but some fuel remains entrained into the central air jet, and at high central air velocities, can exit the domain unburned.

With the central air tube raised, the inner flame is attached to the lip of the central air tube at low central air velocities. In this configuration, central fuel reacts with central air in the inner diffusion flame attached to the central air tube, and also in the outer diffusion flame, if one is present. Increasing the central air velocity, the inner flame will lift off the central air tube with a premixed base, and an attached diffusion flame. As the central air velocity is increased further, the length of the attached diffusion flame decreases as more of the central fuel is entrained into the central air jet to react in the premixed lifted flame.

7.2 Heat release and emissions

Figure 7.15 plots the total heat release within the simulation domain, normalized by the chemical energy input from the fuel stream, $\dot{m}_{CH_4} \cdot LHV_{CH_4}$. Figure 7.16 plots the percent unburned CH_4 exiting the simulation domain, and Fig. 7.17 plots the change in mass flow rate of CO (mass flow rate at the end of the simulation domain minus the mass flow rate at the beginning of the domain, to remove the contribution of CO

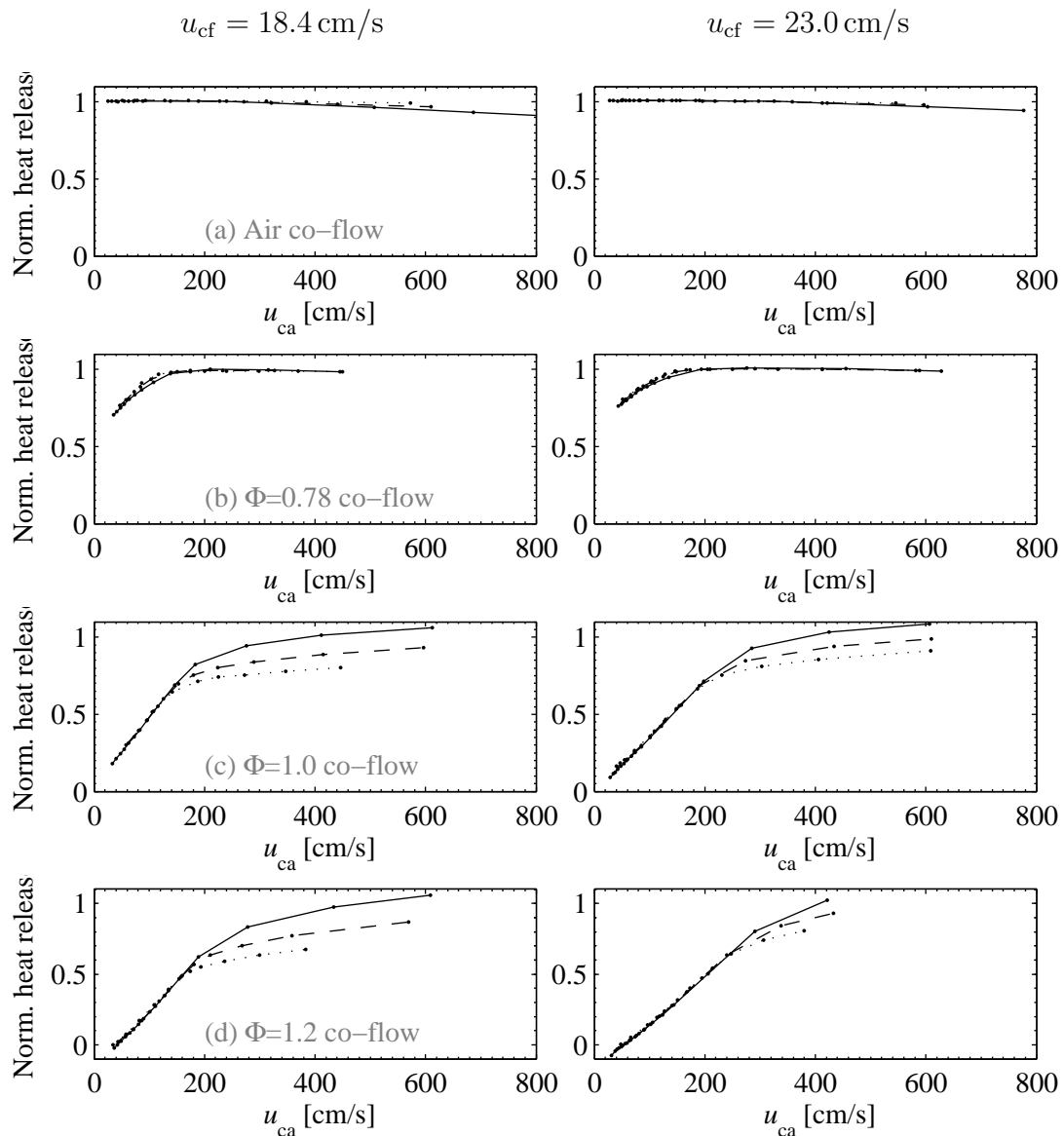


Figure 7.15: Total heat release, normalized by the chemical energy input from the fuel ($\dot{m}_{\text{CH}_4} \cdot \text{LHV}_{\text{CH}_4}$). Air tube: flush (solid line), raised 3 mm (dashed line), and raised 6 mm (dotted line).

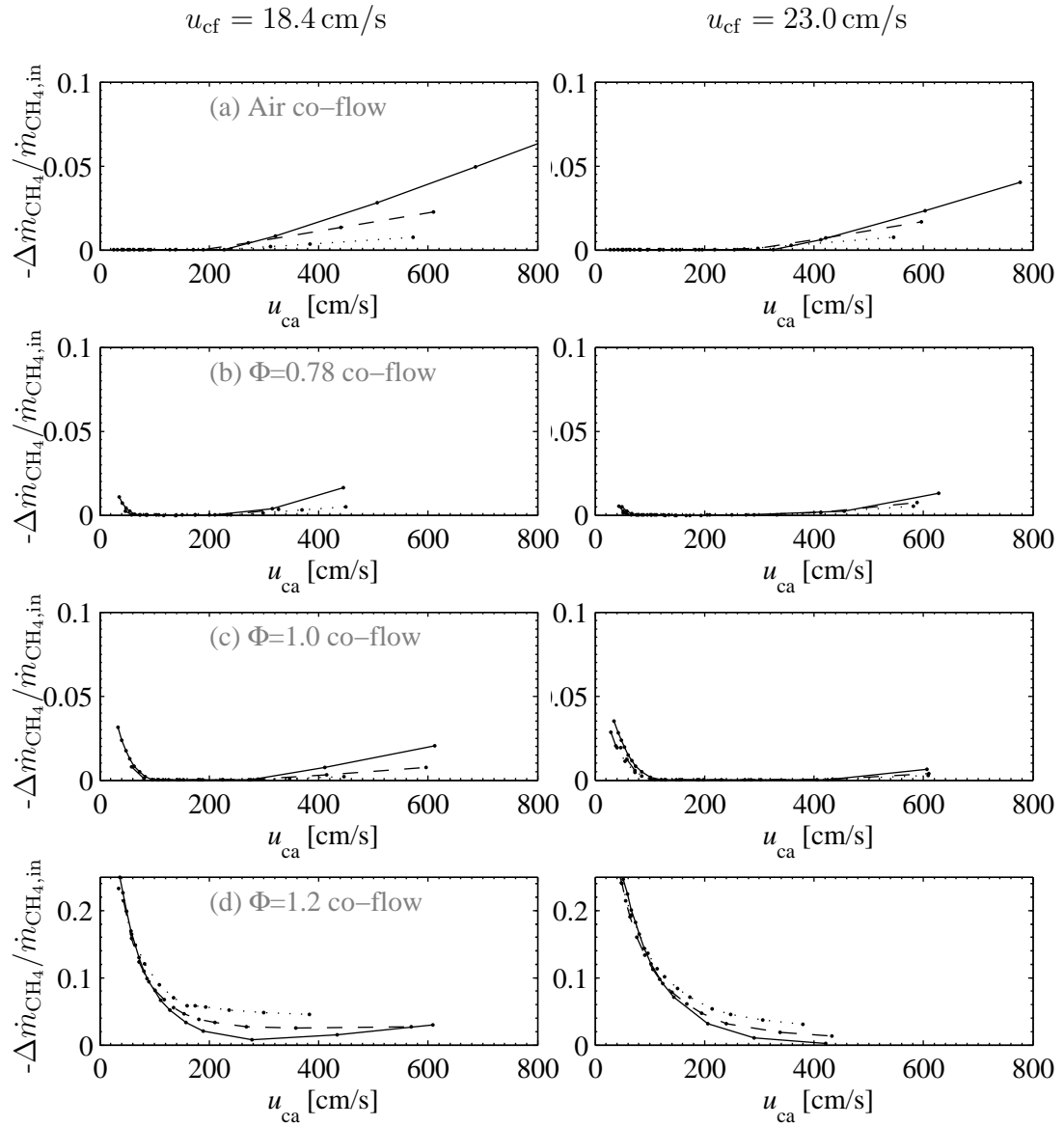


Figure 7.16: Fraction of unburned fuel at the exit of the simulation domain. Air tube: flush (solid line), raised 3 mm (dashed line), and raised 6 mm (dotted line).

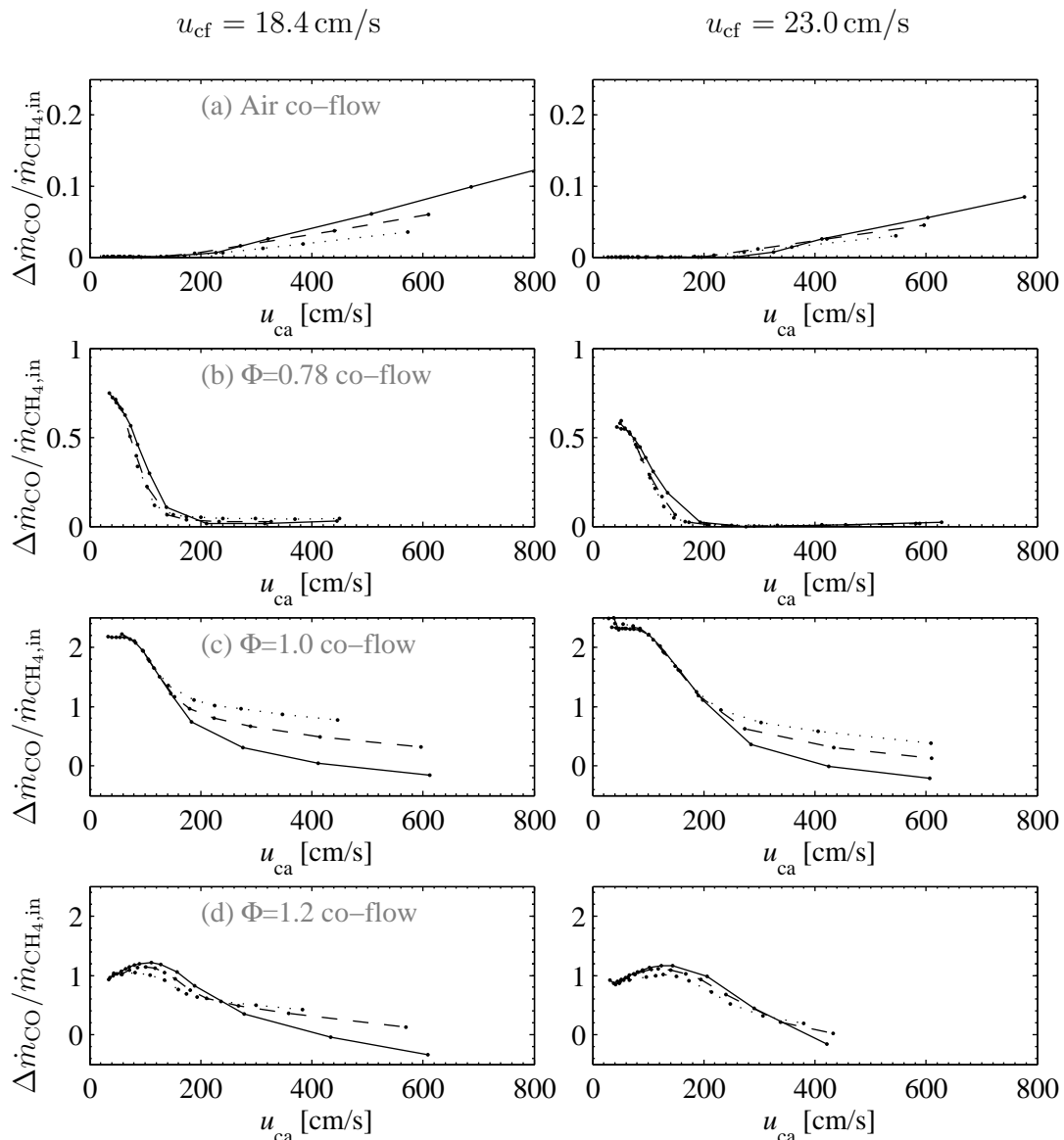


Figure 7.17: Change in mass flow-rate of CO, scaled by the inlet mass flow-rate of fuel. Air tube: flush (solid line), raised 3 mm (dashed line), and raised 6 mm (dotted line).

that enters with the combustion product co-flows), scaled by the inlet mass flow rate of fuel.

For co-flowing air, there is a slight decrease in the total heat release as the central air velocity is increased, along with a slight increase in unburned fuel and CO. This is due to the high velocity air jet. Fuel that gets entrained into the central air jet does not react and gets carried out of the simulation domain. Also, the reaction zone at the edge of the jet gets more diluted with cold air, leaving less chance for CO to oxidize before exiting the simulation domain. As the central air tube is raised there is less unburned fuel and CO, because of the reduced entrainment into the central air jet, due to the presence of the raised central air tube.

For the $\Phi = 0.78$ co-flow, at low central air velocities there is low total heat release and high emissions of CO. This is due to the reduced oxygen content in the co-flow, which is insufficient to oxidize the fuel and CO within the simulation domain. Around $u_{ca} \sim 200$ cm/s, the normalized heat release reaches one and emissions of CO are very low, as there is enough oxygen in the system to oxidize the CO and generate heat release. Over the middle range of central air velocities, there is very little unburned fuel, but at high central air velocities, above $u_{ca} \sim 400$ cm/s, unburned fuel starts increasing, as the entrainment into the central air jet increases.

For the $\Phi = 1.0$ and $\Phi = 1.2$ co-flows, at low central air velocities the heat release is very low. At the lowest central air velocities with the $\Phi = 1.2$ co-flow, the heat release is slightly negative, indicating the presence of some endothermic reactions between the fuel and the co-flow. At high central air velocities with the central air tube flush, though, the heat release is greater than one, as some of the co-flow reacts with the central air jet. Raising the central air tube has very little effect on the heat release and CO emissions for $u_{ca} \lesssim 200$ cm/s, and above this, raising the central air tube decreases the heat release and increases the emission of CO. This is because as the central air tube is raised, more of the fuel is displaced outwards into the co-flow, and there is less chance for entrainment into the central air jet.

For the $\Phi = 1.0$ co-flow, the behaviour of the unburned fuel is similar to the $\Phi = 0.78$ co-flow. In the middle range of central air velocities there is very little unburned fuel, with a slight increase at high central air velocities due to increased entrainment into the central air jet. For the $\Phi = 1.2$ co-flow, the unburned fuel is much higher at low central air velocities, reaches a minimum in the middle range, and increases slightly at higher central air velocities.

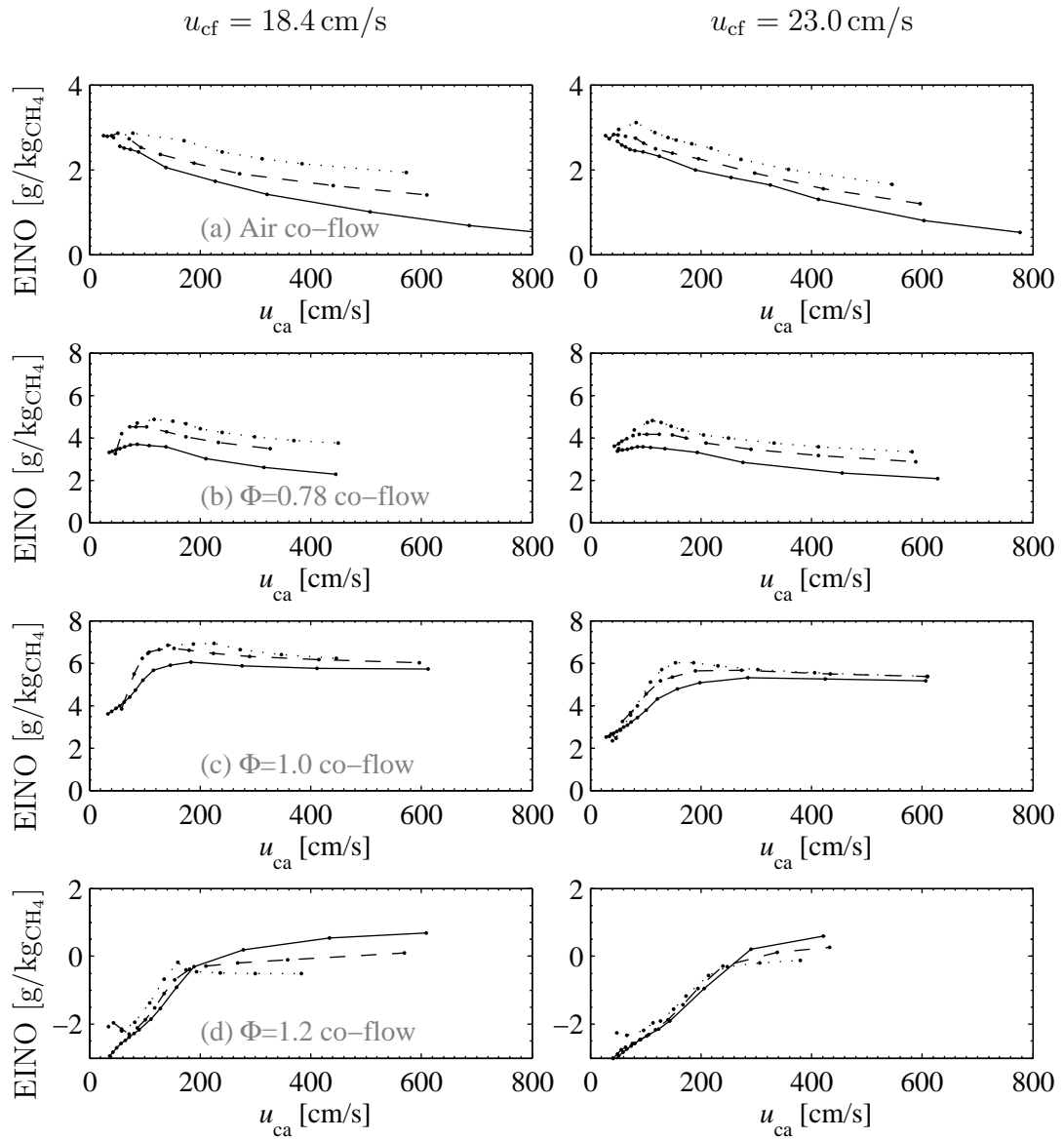


Figure 7.18: Emission index of NO. Air tube: flush (solid line), raised 3 mm (dashed line), and raised 6 mm (dotted line).

Figure 7.18 shows the emission index of NO,

$$\text{EINO} [\text{g}/\text{kg}_{\text{CH}_4}] = \frac{1000 \cdot \text{MW}_{\text{NO}} \int_z \int_r \dot{\omega}_{\text{NO}} 2\pi r dr dz}{-\text{MW}_{\text{CH}_4} \int_z \int_r \dot{\omega}_{\text{CH}_4} 2\pi r dr dz} \quad (7.1)$$

which is the ratio of the total mass of NO produced within the simulation domain to the total mass of CH₄ consumed.

For co-flowing air and combustion products at $\Phi = 0.78$, NO emissions are reduced as the central air velocity is increased, and increased as the central air tube is raised. For the $\Phi = 1.0$ co-flow, NO emissions gradually decrease with increasing central air velocities above $u_{\text{ca}} \sim 200$ cm/s, with a slight increase as the central air tube is raised. For the $\Phi = 1.2$ co-flow, EINO is negative at low central air velocities, indicating a reduction of the NO present in the co-flowing stream through reburn reactions with the fuel. Above $u_{\text{ca}} \sim 200$ cm/s, NO destruction in this region is overtaken by NO production in the inner reaction zone. Emissions of NO are higher with the central air tube flush, as more of the fuel is entrained and reacted with the central air jet.

To explain the trends in emissions of NO as the central air velocity is increased, Figs. 7.19–7.22 plot the mass flow-rate, and the radially-integrated net production rate of NO versus the axial distance above the burner. The normal diffusion flame ($u_{\text{ca}} = 0$) is included for reference.

For the air co-flow (Fig. 7.19), NO is produced in the normal diffusion flame up to the tip of the flame around $z \sim 2.6$ cm. With the central air tube flush, at $u_{\text{ca}} = 54.4$ cm/s, due to the dilatation from the inner flame, the production of NO near the burner face is increased slightly, as the outer diffusion flame is pushed outwards into the co-flow. Some of the central air reacts in the inner lifted flame, causing a small peak in NO production at $z \sim 0.5$ cm. The rest of the central air mixes with fuel and reacts in the outer diffusion flame, reducing the length of the flame to approximately 1.9 cm, and decreasing the production of NO. At $u_{\text{ca}} = 138.7$ cm/s, production of NO is concentrated in the premixed flame at $z \sim 0.9$ cm. At $u_{\text{ca}} = 686.6$ cm/s, entrainment from the central air jet is very strong. The initial production of NO near the burner is reduced as the outer flame is drawn closer to the centreline. There is a small peak in NO production at $z \sim 0.6$ cm, and a slight reduction of NO above the flame as the fuel that was entrained into the central air jet slowly reacts.

With the central air tube raised 6 mm, the production of NO near the burner face is increased relative to the normal diffusion flame, as the central air tube pushes the outer flame into the co-flow. At $u_{\text{ca}} = 239.67$ cm/s, there is a peak in NO formation from the premixed flame at $z \sim 0.9$ cm, and another peak in the radial integral

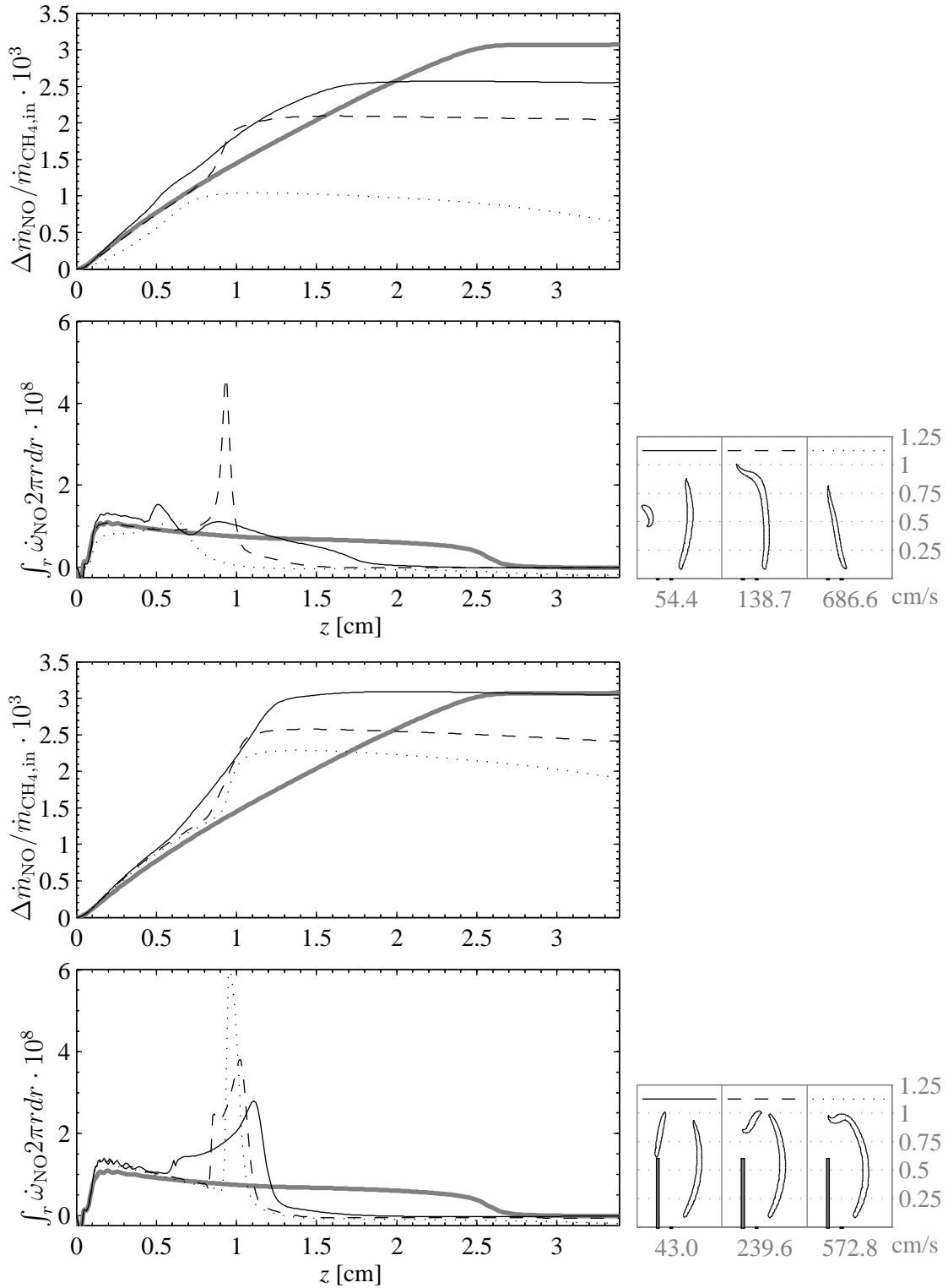


Figure 7.19: Radial integral of net production rate of NO for air co-flow at $u_{cf} = 18.4$ cm/s. The thick grey line is for $u_{ca} = 0$ and central air tube flush. The legend is above the small contours of 10% maximum CH mass fraction on the right, with u_{ca} given underneath each contour.

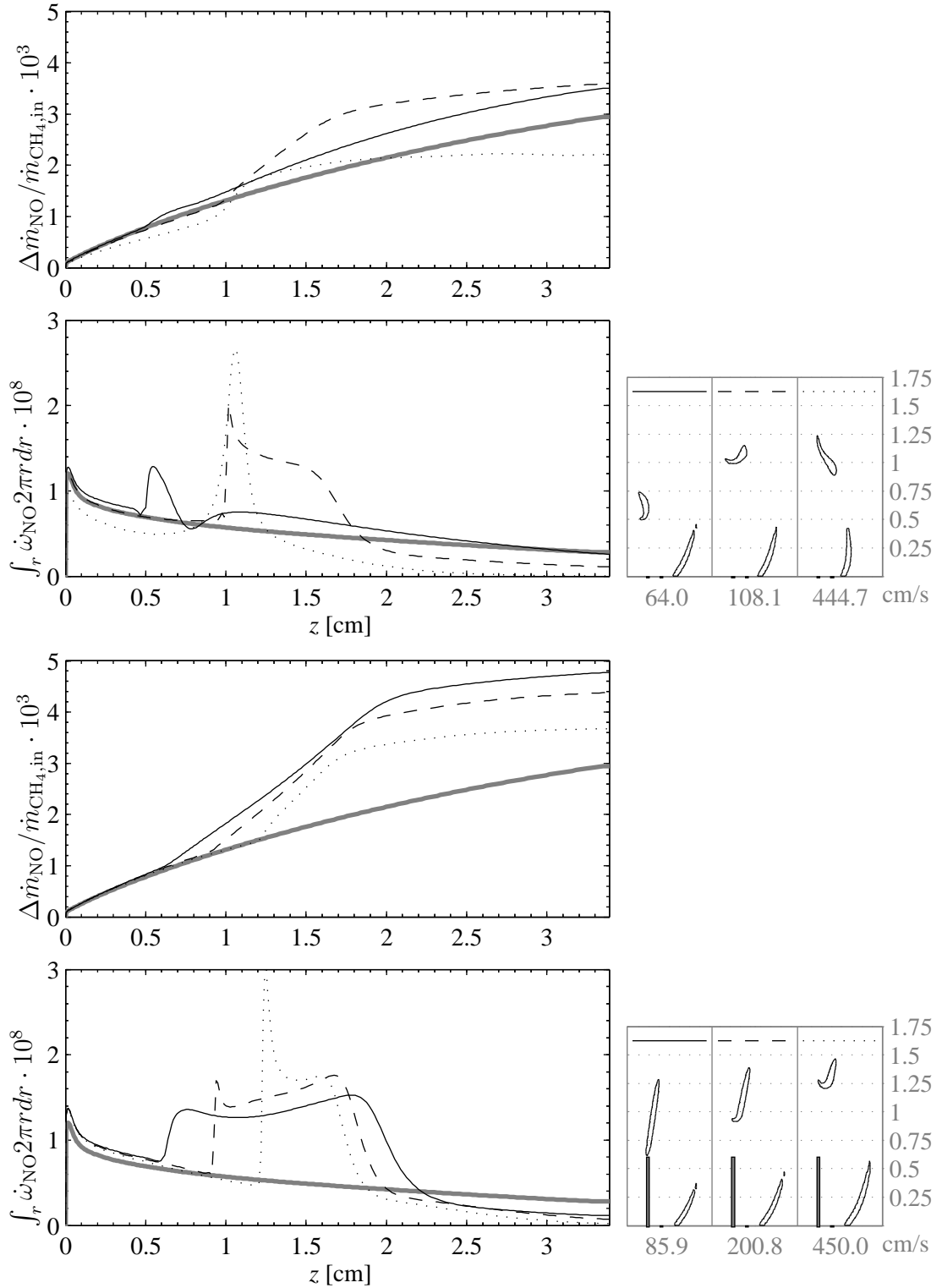


Figure 7.20: Radial integral of net production rate of NO for $\Phi = 0.78$ co-flow at $u_{cf} = 18.4$ cm/s. The thick grey line is for $u_{ca} = 0$ and central air tube flush. The legend is above the small contours of 10% maximum CH mass fraction on the right, with u_{ca} given underneath each contour.

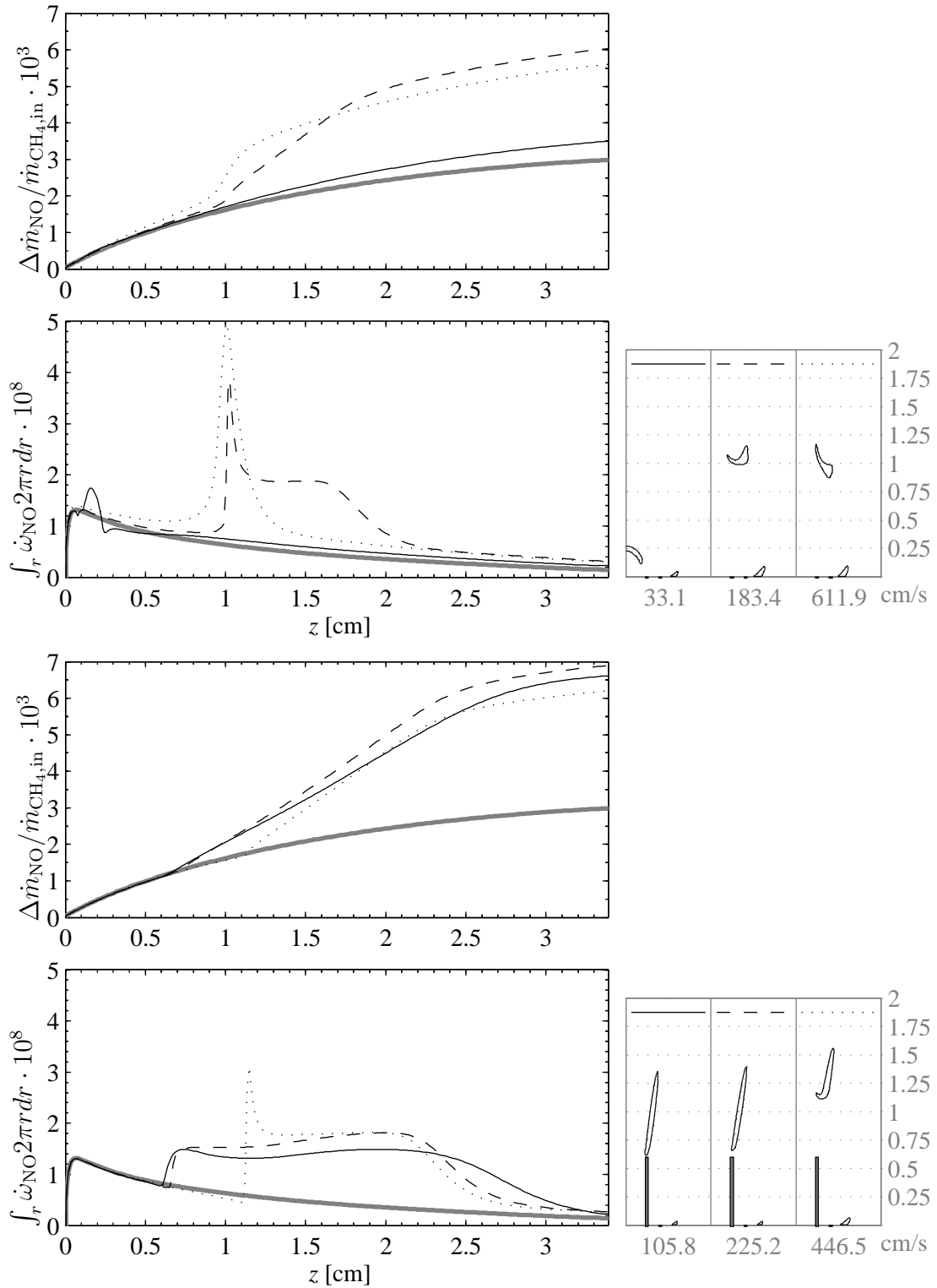


Figure 7.21: Radial integral of net production rate of NO for $\Phi = 1.0$ co-flow at $u_{cf} = 18.4$ cm/s. The thick grey line is for $u_{ca} = 0$ and central air tube flush. The legend is above the small contours of 10% maximum CH mass fraction on the right, with u_{ca} given underneath each contour.

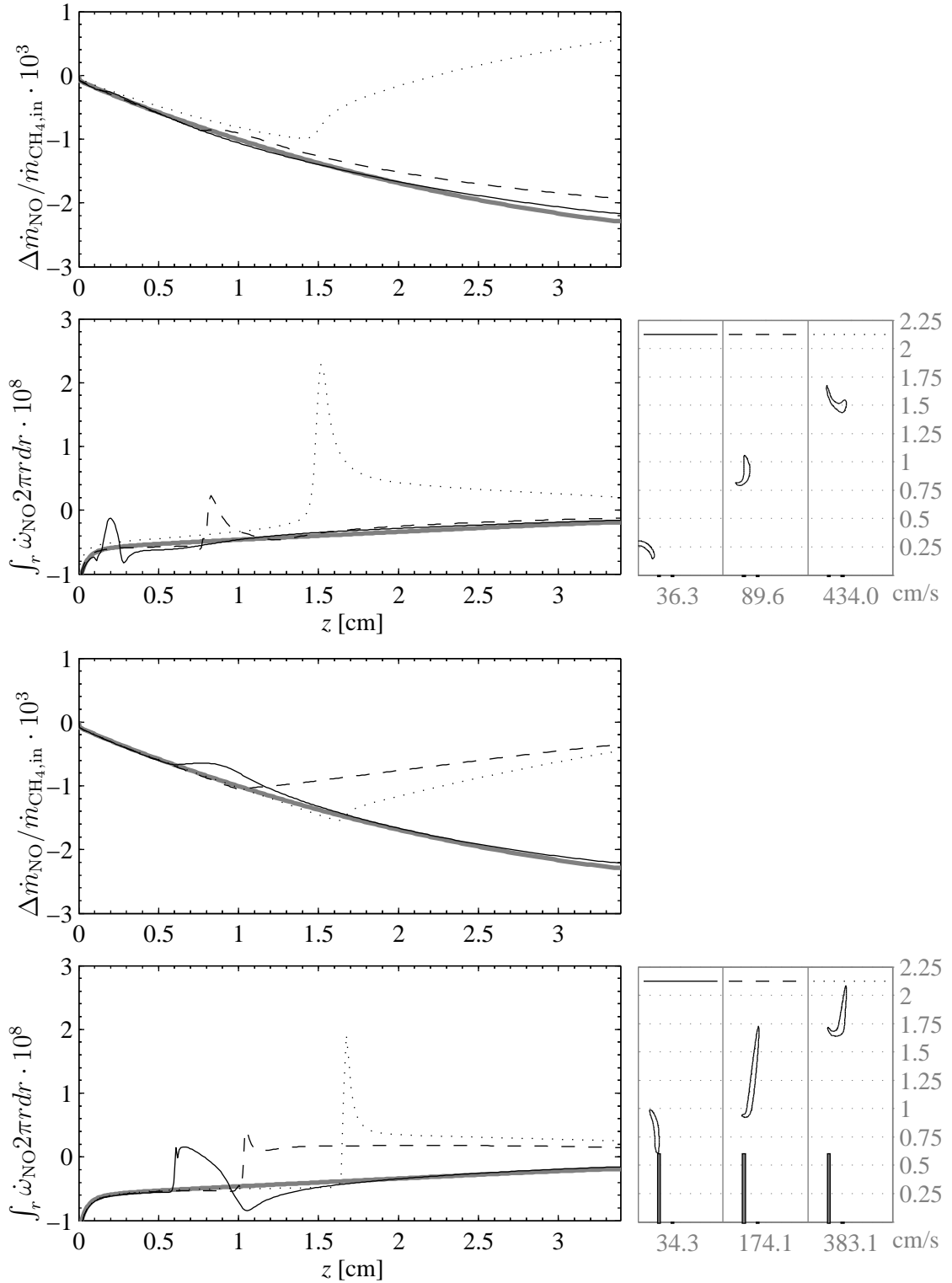


Figure 7.22: Radial integral of net production rate of NO for $\Phi = 1.2$ co-flow at $u_{cf} = 18.4$ cm/s. The thick grey line is for $u_{ca} = 0$ and central air tube flush. The legend is above the small contours of 10% maximum CH mass fraction on the right, with u_{ca} given underneath each contour.

downstream of this, as the attached inner diffusion flame wraps around and joins with the outer diffusion flame. At $u_{ca} = 572.8$ cm/s, NO production is concentrated in the premixed flame at $z \sim 1.0$ cm, with a slight reduction due to reaction of the entrained fuel in the central air jet.

For the $\Phi = 0.78$ co-flow (Fig. 7.20), NO is produced up to the end of the simulation domain. With the central air tube flush, at $u_{ca} = 64.0$ cm/s, there is a peak in NO production from the lifted inner flame at $z \sim 0.5$ cm. At $u_{ca} = 108.1$ cm/s, there is a peak in NO production from the premixed flame at $z \sim 1.0$ cm, and a plateau of NO production from the attached diffusion flame. At $u_{ca} = 444.7$ cm/s, NO production near the burner is reduced as the outer flame is drawn towards the centreline, and NO production is concentrated in the premixed flame at $z = 1.0$ cm, with no attached diffusion flame.

With the central air tube raised 6 mm, NO production in the near-burner region is increased compared to the normal diffusion flame. At $u_{ca} = 85.9$ cm/s, the inner flame is attached to the lip of the central air tube, with a plateau of NO production between $z \sim 0.6$ – 2.1 cm. As the central air velocity is increased, NO production is concentrated in the premixed flame, and the axial extent of the attached diffusion flame decreases, with a corresponding decrease in total NO production.

The behaviour of the NO production for the $\Phi = 1.0$ co-flow is similar to that for the $\Phi = 0.78$ co-flow. With the central air tube flush, at low central air velocity, there is a small peak of NO production at the lifted inner flame. At $u_{ca} = 183.4$ cm/s, there is a peak in NO production at the lifted premixed flame ($z \sim 1.0$ cm), and a plateau from the attached diffusion flame. At $u_{ca} = 611.9$ cm/s, NO production is concentrated in the premixed flame at $z \sim 1.0$ cm. With the central air tube raised 6 mm, the inner diffusion flame is attached to the lip of the central air tube, with a plateau of NO production. As the central air velocity is increased, the axial extent of the diffusion flame decreases, and NO production is concentrated in the lifted premixed flame.

For the $\Phi = 1.2$ co-flow at $u_{ca} = 0$, NO production is negative throughout the domain, meaning that NO from the co-flowing gas is being consumed in reactions between the co-flow and the injected fuel. As the central air velocity is increased, there are peaks in NO production from the lifted inner flame. With the central air tube raised 6 mm, there are the characteristic peaks at the location of the lifted premixed flame, and the attached diffusion flame downstream.

For each of the co-flows studied, there is a central air velocity where the flames for the three different central air tube conditions have nearly the same height at

Table 7.1: Listing of in-flow conditions for three tube cases with $u_{cf} = 18.4$ cm/s.

Co-flow	Central air tube	u_{ca} [cm/s]
Air	flush	227.9
	3 mm	271.8
	6 mm	239.6
$\Phi = 0.78$	flush	314.8
	3 mm	326.6
	6 mm	298.7
$\Phi = 1.0$	flush	410.9
	3 mm	414.4
	6 mm	347.2
$\Phi = 1.2$	flush	278.2
	3 mm	358.8
	6 mm	299.2

nearly the same central air and fuel velocities. These flames are listed in Table 7.1. Examination of these flames will show how raising the central air tube affects the NO production.

Figure 7.23 shows contours of 10% of the maximum and minimum of NO production, and stoichiometric local equivalence ratio for these flames. In general, the stoichiometric line neatly divides the NO production on the lean side, towards the co-flow or central air stream, from the NO destruction on the rich side, towards the central fuel stream. The exception is the tail of NO destruction above the lifted premixed flame, near the centreline. This is due to the slow reaction of fuel that has been entrained into the central air jet, and not reacted in the lifted premixed flame.

As the central air tube is raised, the fuel is displaced outwards into the co-flow, due to the presence of the raised central air tube. There is less chance for fuel to be entrained into the central air jet, so more of the fuel reacts in the outer diffusion flame, and the axial extent of the diffusion flame attached to the lifted premixed flame is increased.

Figure 7.24 shows the radially integrated net production rate of NO for the flames listed in Table 7.1. For the air co-flow with the central air tube flush, there is a small peak in NO production at the location of the lifted premixed flame ($z \sim 0.9$ cm). With the central air tube raised 3 mm, there is a larger peak at $z \sim 0.9$ cm, from a combination of the lifted premixed flame and the attached diffusion flame which wraps around and is oriented horizontally at that location. With the central air tube raised 6 mm, there is a small peak from the lifted premixed flame, and a larger peak at $z \sim 1.0$ cm, where the two diffusion flames join together.

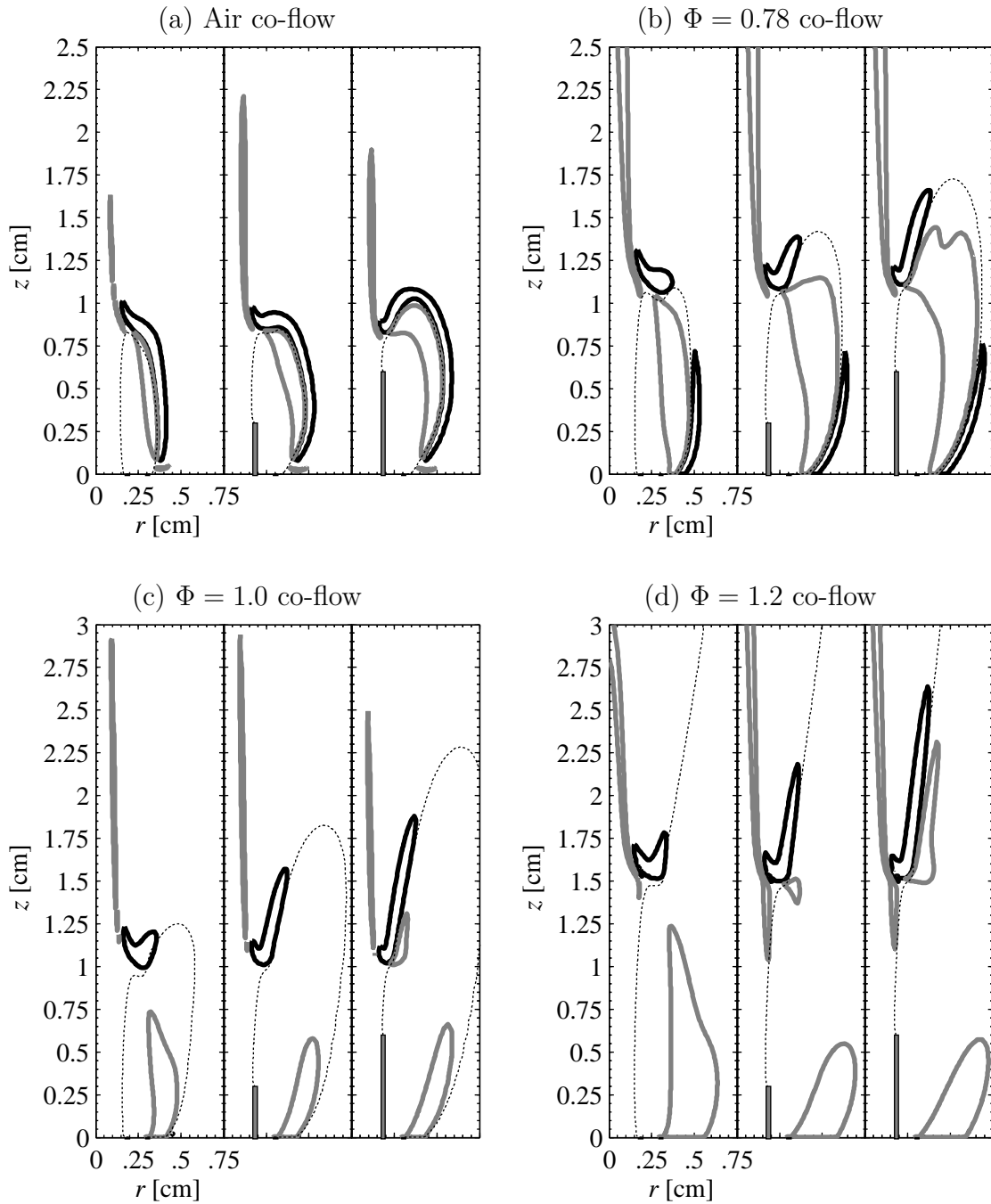


Figure 7.23: Contours of NO production—10% of maximum (black line); 10% of minimum (grey line)—and contours of local equivalence ratio equal to one (dotted line) for the flames listed in Table 7.1, at $u_{cf} = 18.4$ cm/s, and co-flow given.

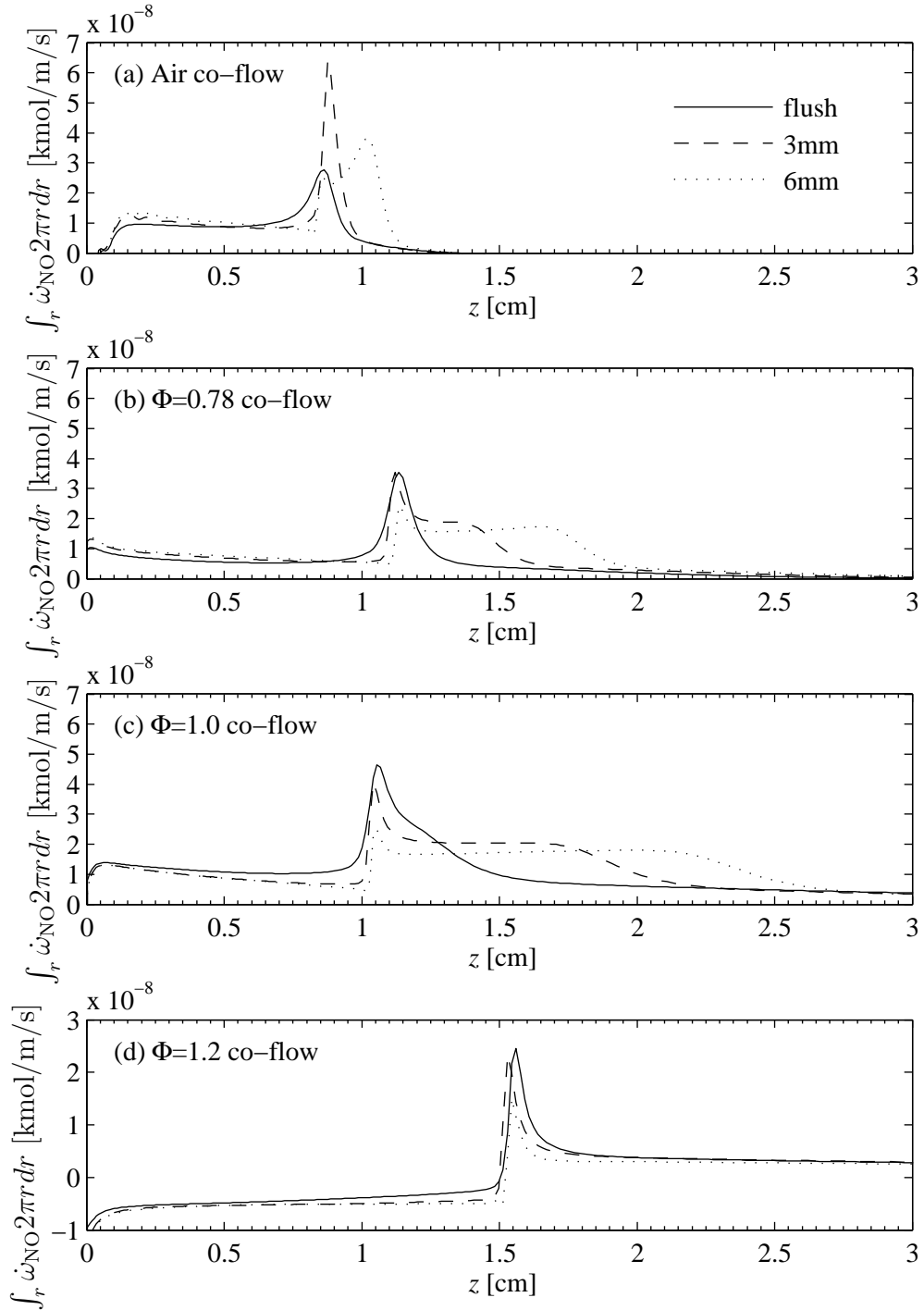


Figure 7.24: Radially-integrated net production rates of NO for flames listed in Table 7.1 at $u_{cf} = 18.4$ cm/s, and co-flow given.

For the $\Phi = 0.78$ and $\Phi = 1.0$ co-flows, there are peaks in NO production from the lifted premixed flame at $z \sim 1.15$ and 1.05 cm, respectively. As the central air tube is raised, those peaks from the premixed flame become smaller, and the plateaus in NO production from the attached diffusion flames grow longer, increasing the total production of NO.

For the $\Phi = 1.2$ co-flow, production of NO is negative up to the location of the premixed flame. There is a peak in NO production from the lifted premixed flame at $z \sim 1.55$ cm, which gets smaller as the central air tube is raised, but without the corresponding increase in NO from the attached diffusion flame seen for the $\Phi = 0.78$ and $\Phi = 1.0$ co-flows.

Chapter 8

Conclusions

A flame geometry and reactant delivery configuration of interest to flameless oxidation and low-NO_x combustion has been investigated, experimentally and numerically. The geometry is an inverse diffusion flame burner with a co-flow of either air or co-flowing combustion products at $\Phi = 0.78, 1.0$ or 1.2 . The tube delivering the central air stream is raised above the burner by up to 6 mm, providing time for the fuel and co-flowing gas to mix and react before reacting with the central air.

At low central air velocities, there is a hysteresis behaviour associated with the inner flame between the central air and fuel streams. As the central air velocity is increased from zero, the central air mixes with fuel and forms a partially-premixed flame on the centreline. The height of the partially premixed flame is scaled by the soot height of the corresponding normal diffusion flame, and this ratio is 0.53 for co-flowing air, and 0.37 for co-flowing combustion products at $\Phi = 0.78$. The height of the partially-premixed flame is insensitive to the height of the central air tube, as it is scaled by the outer diffusion flame. When the central air velocity reaches a critical level, the partially-premixed flame propagates upstream and stabilizes closer to the burner face as an inverse diffusion flame. Numerical simulation results suggest that this critical point is reached when the local equivalence ratio upstream of the flame approaches one.

As the central air velocity is decreased, the inverse diffusion flame gets weaker and moves closer to the burner face until it extinguishes. The region of hysteresis between transition to, and extinction of the inner inverse diffusion flame is extended with co-flowing combustion products at $\Phi = 0.78$, compared to co-flowing air. This effect is most evident when the flame stabilizes above the burner face, giving the heat and combustion products from the outer flame time to diffuse inwards.

For higher central air velocities, the inverse diffusion flame lifts higher off the

burner face and joins with outer flame in a premixed ring-shaped flame. Numerical simulation data for these flames are post-processed to calculate the chemiluminescent emission from the excited-state CH^* radical, and convolved with a matrix corresponding to the point-spread function of the imaging system, modeling the experimental diagnostic. The simulation data are in good agreement with experimental measurements of CH^* chemiluminescence emission for these flames.

The data from the numerical simulations is analyzed for the behaviour of heat release and pollutant emissions. For co-flowing air, as the central air velocity is increased, there is a slight decrease in the total heat release and a slight increase in CO and unburned fuel emissions, as the central air jet entrains fuel and dilutes the reaction zone, preventing oxidation of CO before the end of the simulation domain. As the central air tube is raised, entrainment into the central air jet is delayed, and these emissions are reduced.

For co-flowing products at $\Phi = 0.78$, the co-flowing stream has lower oxygen content and so has less heat release and higher CO emissions at low central air velocities, but CO is reduced and normalized heat release approaches one as the central air velocity is increased. For the $\Phi = 1.0$ and $\Phi = 1.2$ co-flows, the heat release at low central air velocities is even lower, but increases with increasing central air velocity, and at the highest central air velocities, some of the co-flow gas is also oxidized.

In general, emissions of NO are decreased as the central air velocity is increased, except for the $\Phi = 1.2$ co-flow where NO from the co-flow is being reduced through reactions with the injected fuel. Contrary to the proposed hypothesis, the mixing of fuel with the co-flowing gas before reacting with the central air does not reduce the emissions of NO. As the central air tube is raised above the burner, fuel is pushed outwards into the outer diffusion flame, and less fuel is entrained into the central air jet to react in the lifted premixed flame. Thus, more fuel is burned in a diffusion flame and emissions of NO are increased.

Appendix A

Chemiluminescence imaging

As explained in Chapter 2, flame chemiluminescence from the CH^* radical is imaged with an ICCD camera. This appendix provides a detailed description of the image processing methodology.

A.1 Abel transform

An example image is shown in Fig. A.1. The white line at the centre of the image is the axis of symmetry. The image is split into the left- and right-hand sides. Each side is processed through a three-point Abel transform based on the formulas of Dasch (1992), after correcting for typographical errors in Eq. 7 (Ayrancı et al. 2007), producing a two-dimensional distribution of the emitted signal, in detector counts. This is scaled by the maximum within the flame, and 10% contours are plotted, as shown in Fig. A.2. The centreline is adjusted until the distributions from each side line up as well as possible. Distributions shown throughout this thesis in comparison to the numerical simulation data are taken from the right-hand side. The zero reference point in the axial direction is measured from a reference image of the burner with no flame, and an illuminated background.

Singla et al. (2005) explained the conditions that must be satisfied for inversion of imaging data into 2-D slices to be valid:

This type of numerical tomography is suitable if (1) the flame is axisymmetric, (2) self-absorption of the light radiated by the flame is not too large, (3) light ray deflection by refraction index gradients remains limited, and (4) distance between the camera and the flame is large, compared to the radial size of the combustion chamber

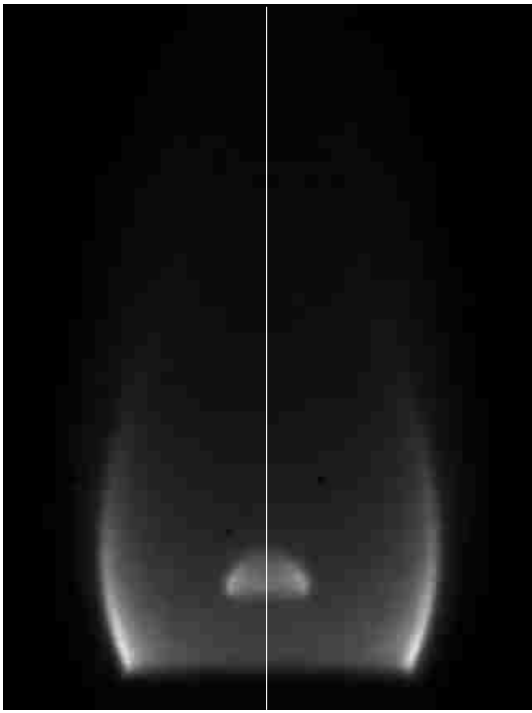


Figure A.1: Example flame image, with centreline in white.

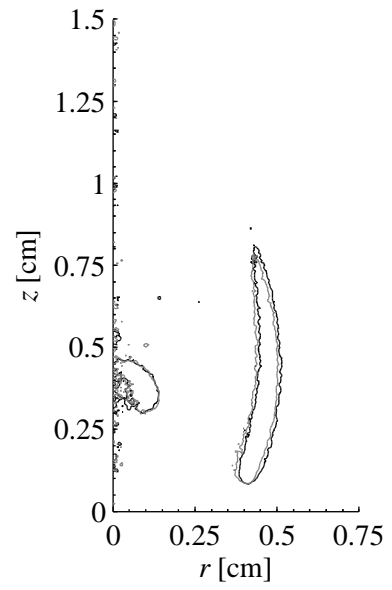


Figure A.2: Abel inversion of data from Fig. A.1. Data from the right-hand side in black, and from the left-hand side in grey.

Furthermore, “flame luminosity [must be] contained within the focal depth of the camera system” (Yoo et al. 2002), and magnification changes over the flame depth should be limited to 1% (Walsh et al. 1998).

In this work, the flames are axisymmetric, although there are some asymmetries at high central air velocities, especially when the central air tube is raised above the burner. It was very difficult to maintain perfect axisymmetry for these cases. Self-absorption of the light radiated from the CH^* radicals is assumed to be negligible, because its spatial distribution is narrow, and its mole fraction is low (Singla et al. 2005). Light-ray deflection by index-of-refraction gradients (shadowgraph effect) is minimized by focusing the camera on the mid-plane of the burner (Snelling et al. 1999). The nominal position of the camera is such that the front end of the lens is located 45 cm away from the axis of the burner. This distance is large compared to the typical flame diameter of approximately 1 cm.

Ray (1988) gives the following formula for the depth of field, T , for macro photography

$$T = \frac{2Cf/\# (1 + m)}{m^2} \quad (\text{A.1})$$

where C is the so-called “circle of confusion” and m is the magnification. For the optical setup used in this work, the circle of confusion is $C = 1.22$ pixels (see Section A.3), corresponding to $8.2 \cdot 10^{-4}$ cm at the sensor plane, and the magnification is 1:4 ($m = .25$). Using $f/32$ results in a depth-of-field of $T = 1.04$ cm, comparable to the typical flame diameters in this work.

To confirm this choice, a typical flame was imaged at a series of $f/\#$ settings, $f/4$, $f/8$, $f/16$, and $f/32$. Figure A.3 shows the images of the flame at each $f/\#$, where each image shown is the average of 256 individual images (see Section A.2). As the $f/\#$ is reduced, the CH^* layer appears more blurred and spread out. Each of these images was processed through the Abel inversion to yield 2-D data of the relative CH^* emission levels. The width (FWHM) of the CH^* layer was calculated near the base of the flame, and the percent error relative to the width at $f/32$ is shown in Fig. A.4. Thus, images are recorded at $f/32$ in order to get the thinnest CH^* profile.

To confirm that the magnification changes are limited over the flame depth, the standard USAF 1951 resolution target (Edmund Optics Part# NT38-257) was imaged, translating the camera relative to the target, up to 1.5 cm on each side, while keeping the focus fixed. Figure A.5 shows an example image of the resolution target, taken at the nominal focus position. To calculate the magnification of the optical system, a pixel intensity profile was taken through the Group 0 Element 1 line pairs

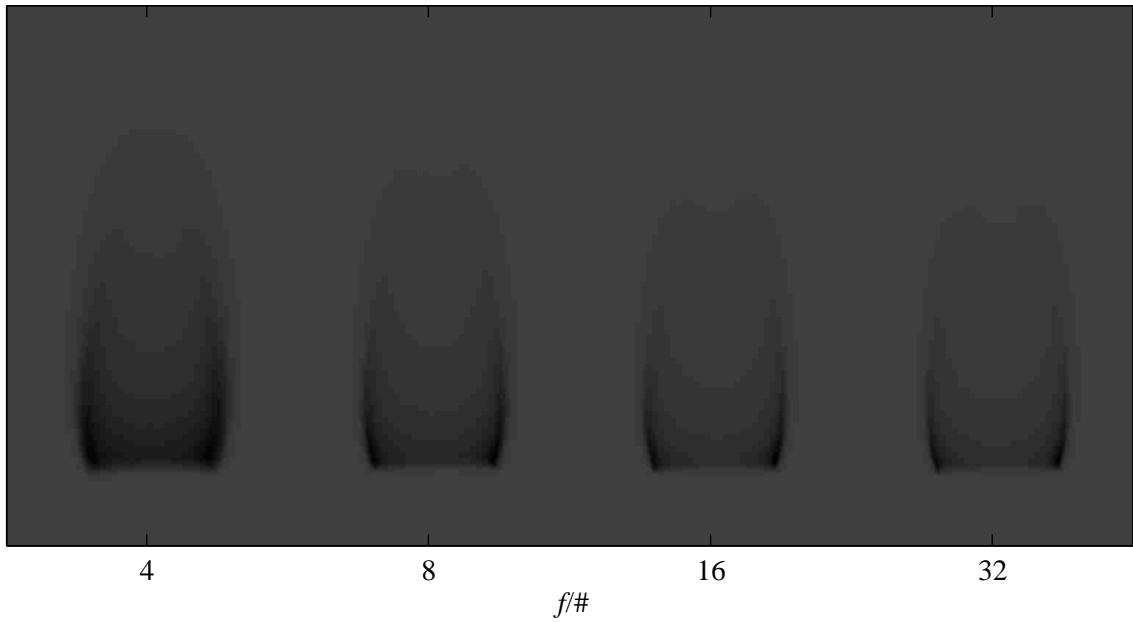


Figure A.3: Sequence of images with increasing $f/\#$.

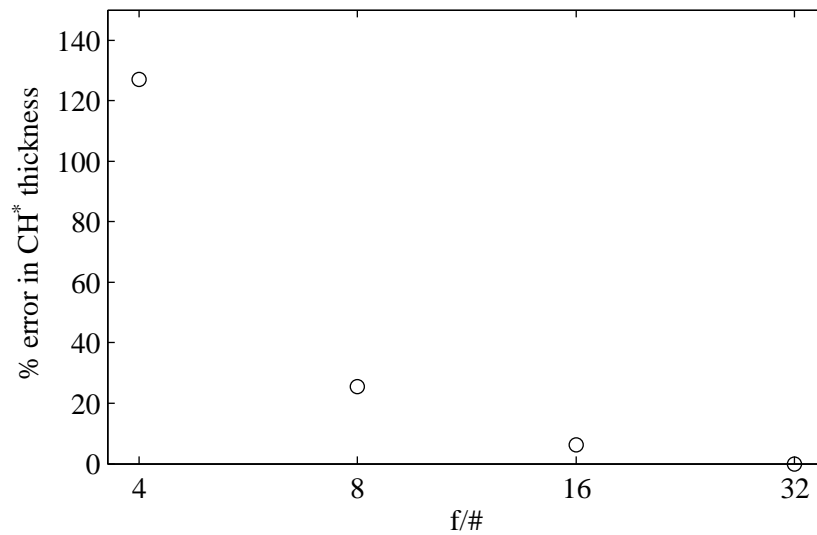


Figure A.4: Percent error in CH^* layer thickness (relative to value at $f/32$) as a function of $f/\#$ for flames shown in Fig. A.3.

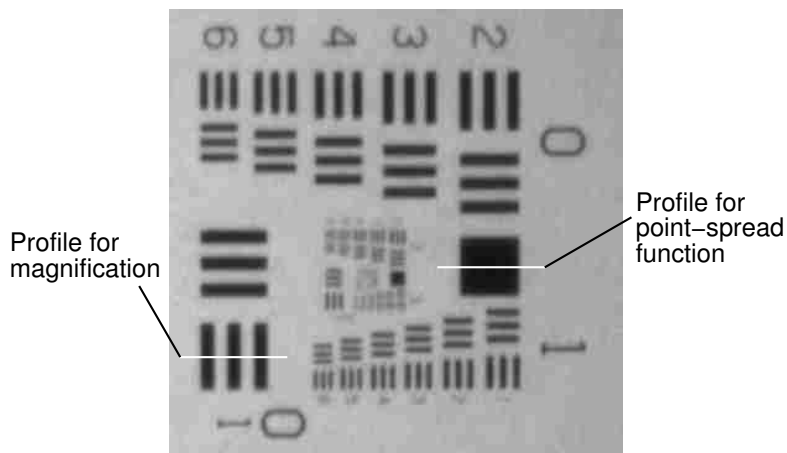


Figure A.5: Image of resolution target taken at nominal focus position. Streaks from Group 0, Element 1 used for calculating magnification are seen at the lower-left corner, and the square (Group 0, Element 2) used for estimating the point-spread function (Section A.3) of the imaging system can be seen on the right-hand side.

(1 line pair per millimetre), averaging the central 20 pixel-rows. This data was inverted and scaled to yield the profile shown in Fig. A.6. Similar to the methodology of Bergthorson (2005) in calculating particle-streak velocimetry (PSV) data, these “streaks” were thresholded to a level of 0.4 times the peak intensity and the distance from the start-to-start (points S_1 , S_2 and S_3) and end-to-end (points E_1 , E_2 and E_3) of the streaks was taken as the number of pixels corresponding to 1 mm. This yields four estimates for the magnification, two from the start-to-start and two from the end-to-end of the streaks. The magnification is taken as the average of these four estimates.

Figure A.7 shows the calculated optical system magnification (pixels/cm) over a range of ± 1.5 cm from the nominal focus position. The dashed lines represent a difference of 1% relative to the nominal position. Over the range of typical flame radii (~ 0.5 cm), the magnification changes are within 1% of the nominal value.

A.2 Image averaging

When using intensified cameras for imaging, noise in the signal is also amplified. To improve the signal-to-noise ratio, the final image used for analysis is the average of multiple individual images, as long as the phenomenon is steady, which it is in this work. In order to determine how many images to average, a large number of images (4096) were taken of the example flame shown at the right-hand side of Fig.A.3. The

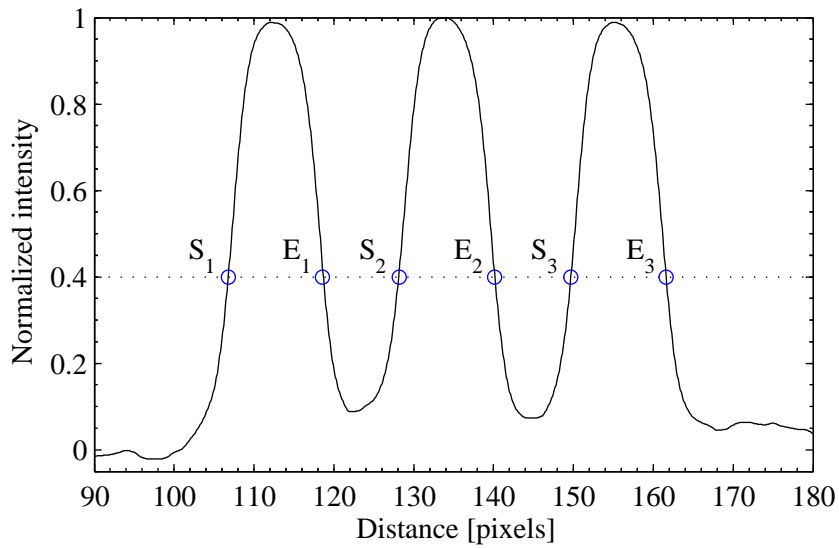


Figure A.6: Scaled and inverted pixel intensity through Group 0, Element 1 line pairs, and start (S) and end (E) of streaks.

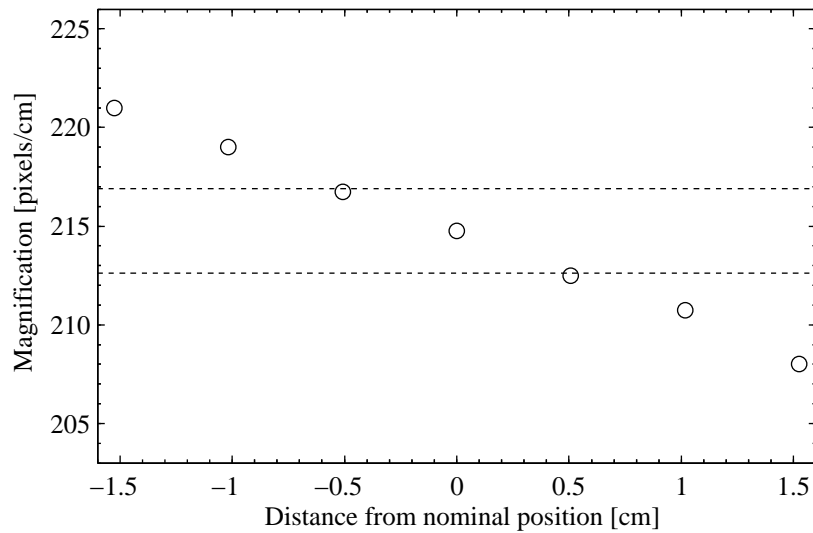


Figure A.7: Magnification changes. Dashed lines are at $\pm 1\%$ of the magnification at the nominal position.

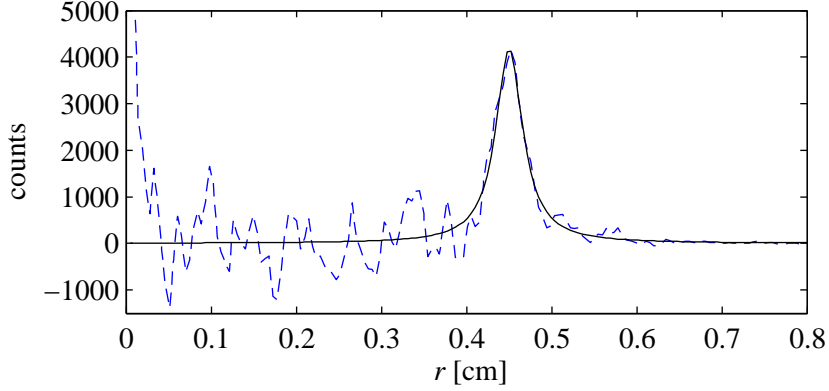


Figure A.8: CH* emission data from one pixel row and one image (dashed line), and fit (solid line) from Eqn. A.2.

data from each image was processed through the Abel inversion (Sec. A.1).

For each of the 4096 images, a two-sided Lorentzian function (Bergthorson 2005) of the form

$$S_{\text{CH}^*} = \begin{cases} \frac{S_{\text{CH}^*,\text{max}} w_1^2}{(x - x_{\text{CH}^*})^2 + w_1^2}, & x < x_{\text{CH}^*} \\ \frac{S_{\text{CH}^*,\text{max}} w_2^2}{(x - x_{\text{CH}^*})^2 + w_2^2}, & x > x_{\text{CH}^*} \end{cases} \quad (\text{A.2})$$

was fit to a pixel row near the base of the flame. Here, the location of the peak CH* is x_{CH^*} , and the width is $(w_1 + w_2)/2$. Figure A.8 shows the raw data and the fit using Eqn. A.2. As is typical for data processed through the Abel inversion, there is a large amount of scatter in the inner region, from $r = 0 - 0.4$ cm.

Figure A.9 shows the histograms for the fit parameters from Eqn. A.2 (peak location and width). The uncertainties in the fit parameters when fitting to data from a single image are $6.5 \cdot 10^{-3}$ cm (corresponding to 1.4 pixels at the ICCD sensor plane) in the peak CH* location, and $3.5 \cdot 10^{-3}$ cm (0.75 pixels) for the CH* layer thickness. Calculating the mean fit parameters from the average of 256 images reduces the uncertainty in the mean values by a factor of 16, to $4.1 \cdot 10^{-4}$ cm (0.087 pixels) for the peak CH* location, and $2.2 \cdot 10^{-4}$ cm for the CH* layer thickness, which is 1.1% of the mean layer thickness of $2.0 \cdot 10^{-2}$ cm.

With these results, data for processing is taken as the average of 256 individual images. Figure A.10 shows CH* emission data from one pixel row processed from the average of 256 individual images, and a curve fit using the average fit parameters and Eqn. A.2.

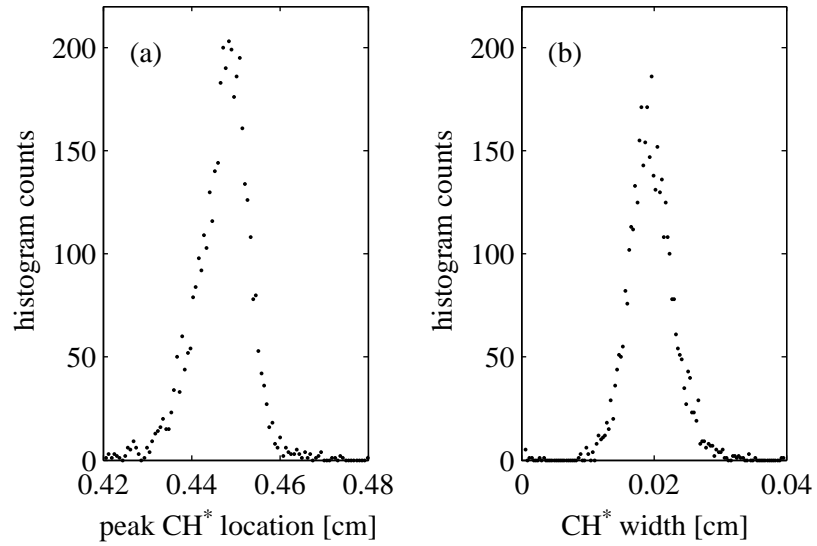


Figure A.9: Histogram of (a) peak CH* location and (b) CH* layer width from curve fits to single images.

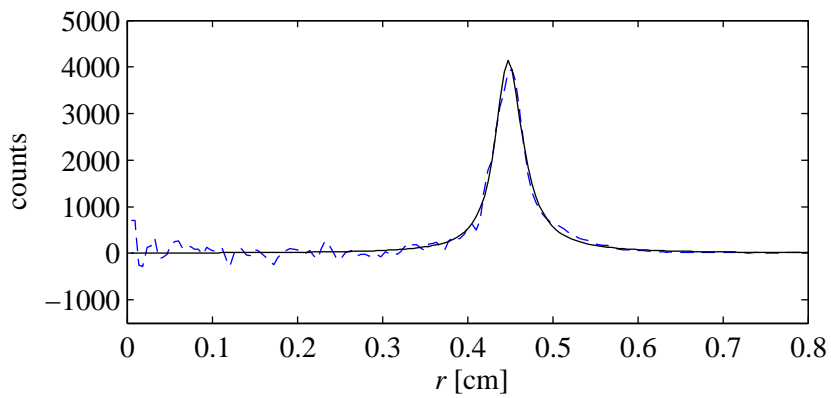


Figure A.10: CH* emission data from one pixel row and the average of 256 images (dashed line), and fit calculated from average fit parameters (solid line) and Eqn. A.2.

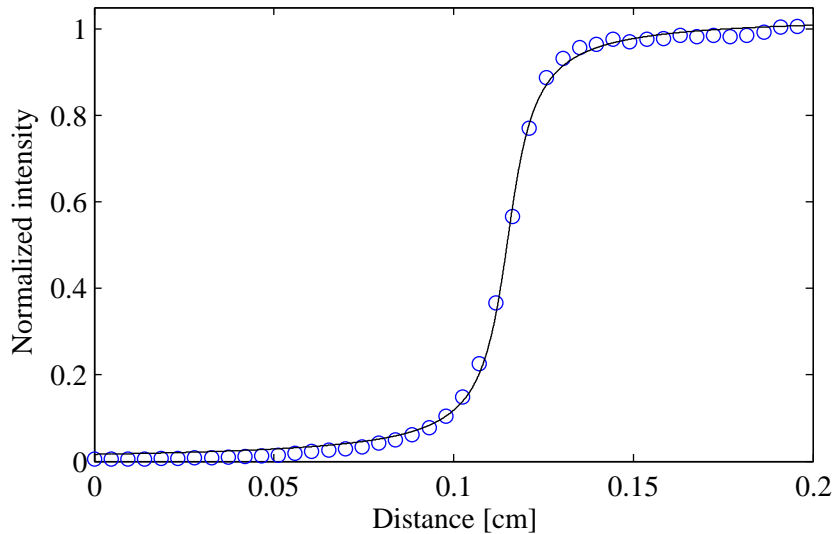


Figure A.11: Normalized intensity profile through square of target image (Fig. A.5). Experimental data (circles) and fit (line) using Eqn. A.3.

A.3 Point-spread-function

Through imaging, the ideal CH^* distribution is blurred by the point-spread function of the imaging system. This is a common problem in astronomical imaging, where an image of a point-source, such as a distant star, ends up as a disk on the detector. Imaging the resolution target provides a means to estimate this blurring.

The square shown in Fig. A.5 was imaged and the profile of inverted and normalized intensity through the central 20 pixel rows is shown in Fig. A.11. This shows how the ideal step-change in intensity on the target image gets blurred on the CCD sensor.

A Cauchy distribution function, of the form

$$D(x) = S \left[\frac{\pi}{2} + \tan^{-1} \left(\frac{x - m}{w} \right) \right] \quad (\text{A.3})$$

was fit to the experimental normalized intensity, yielding a width of $w = 5.67 \cdot 10^{-3}$ cm (corresponding to 1.22 pixels). Thus, the line-spread function for the imaging system is given by a Lorentzian function with a half-width of 1.22 pixels. The point-spread function (PSF) of the imaging system is the Abel inversion of the line-spread function (Jones 1958). In processing the simulation data to compare to the experiments, the simulation data is convolved with a matrix corresponding to the PSF, and this is compared to the experimental image data.

Appendix B

Experimental chemiluminescence images

Included in this appendix are the complete set of chemiluminescence images acquired in this work.

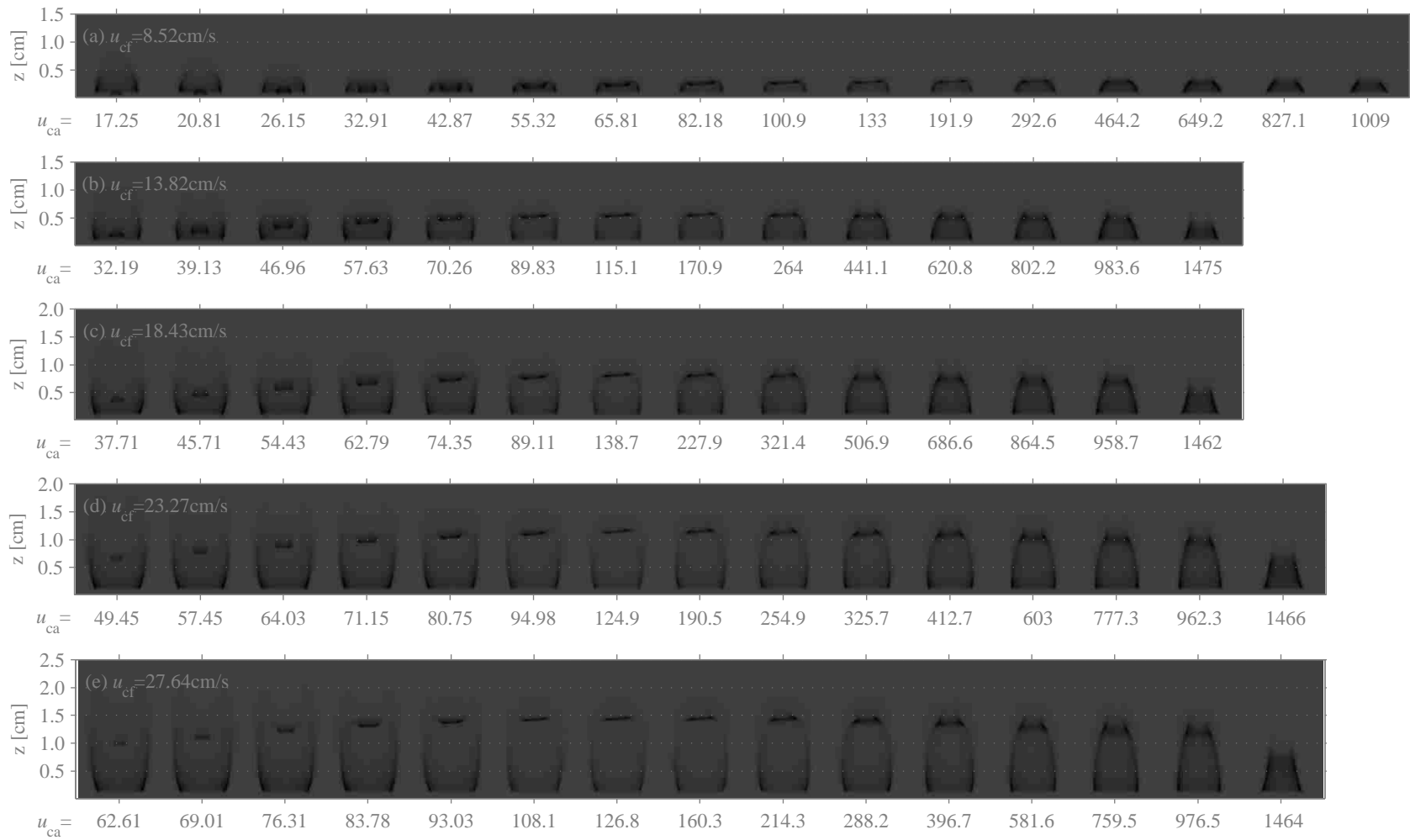


Figure B.1: Air co-flow, central air tube flush.

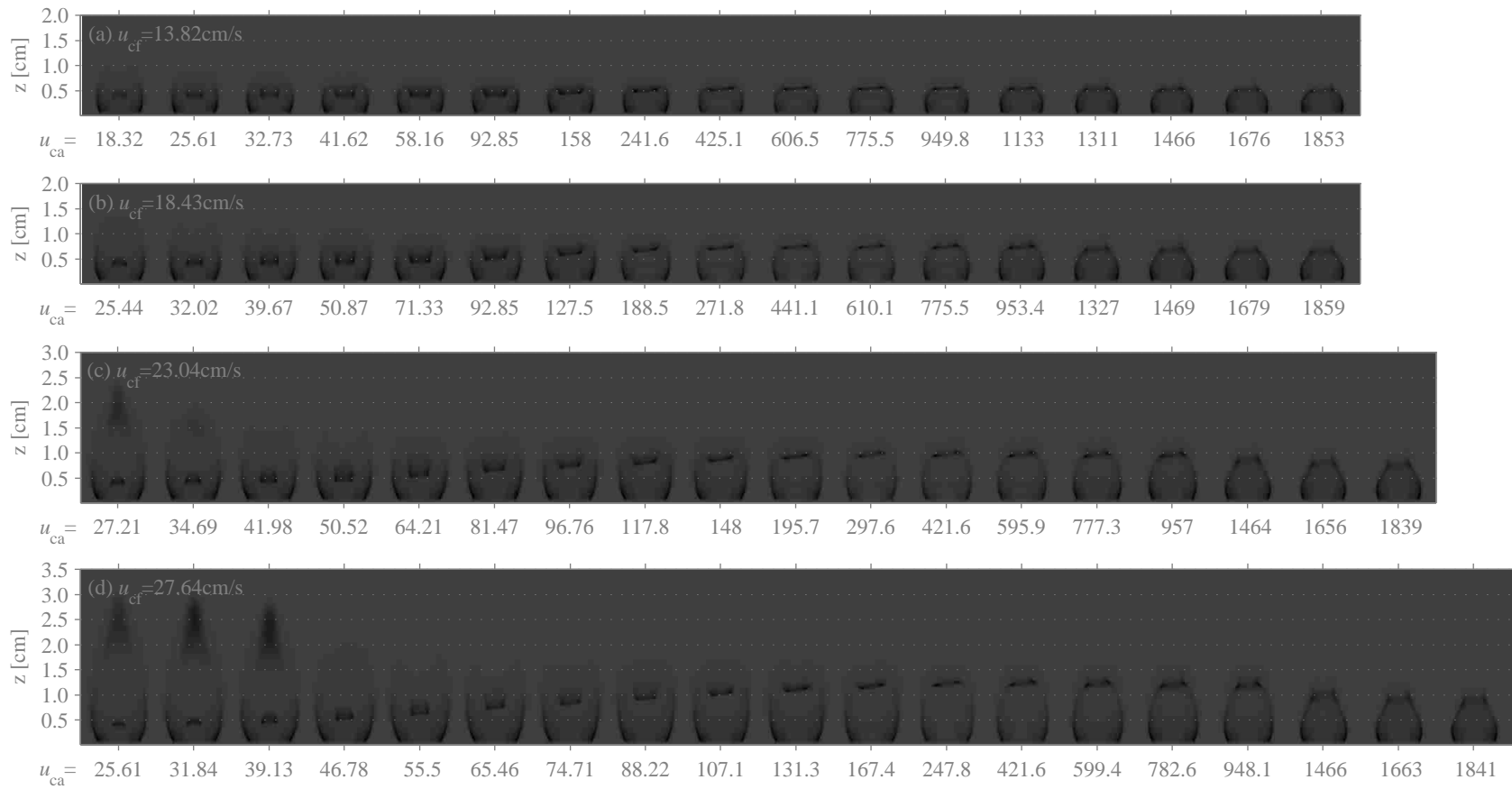


Figure B.2: Air co-flow, central air tube raised 3mm.

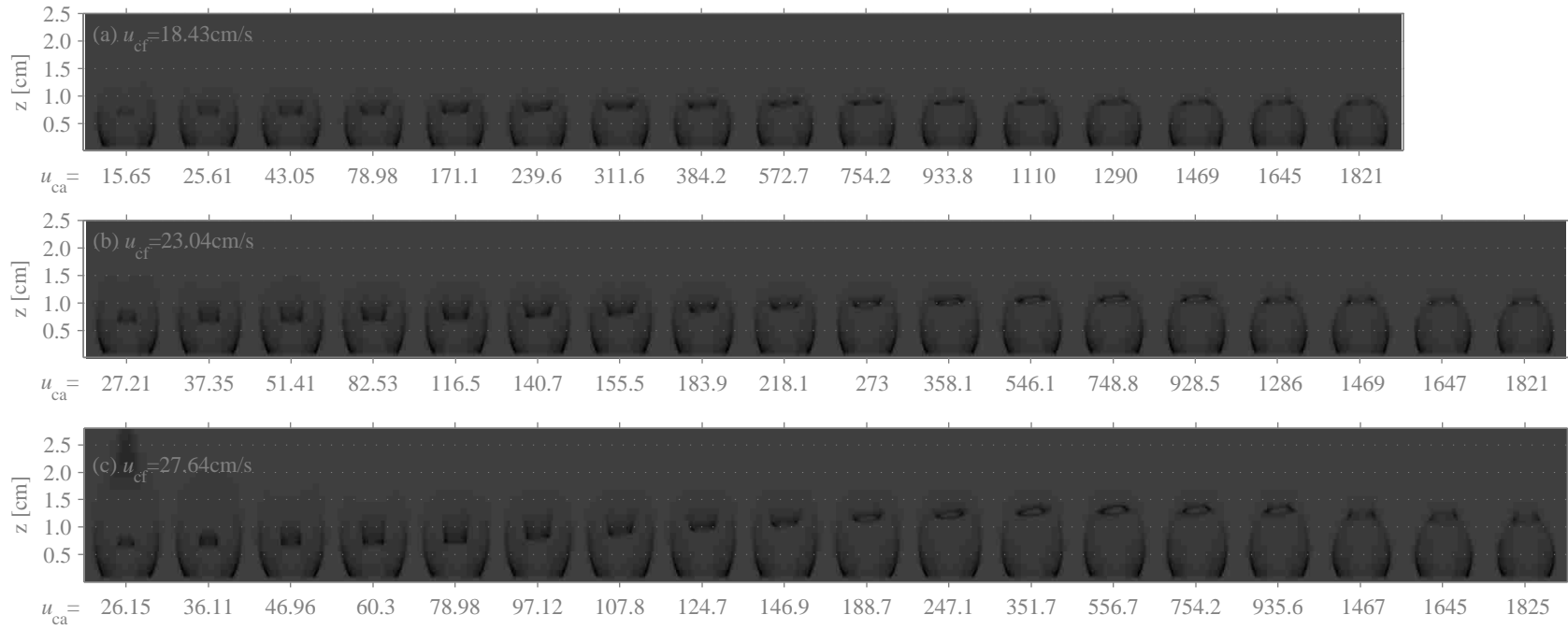


Figure B.3: Air co-flow, central air tube raised 6mm.

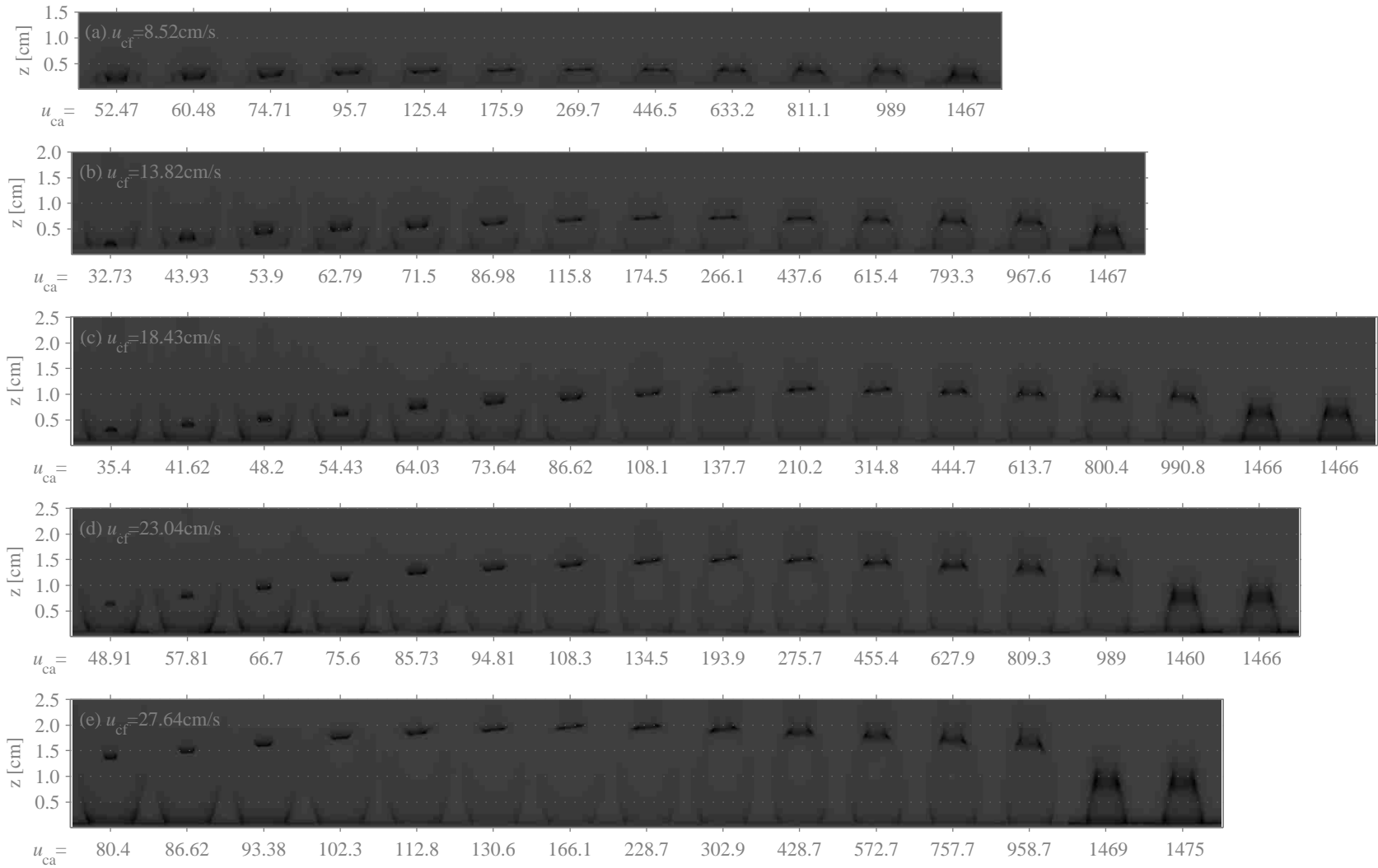


Figure B.4: $\Phi = 0.78$ co-flow, central air tube flush.

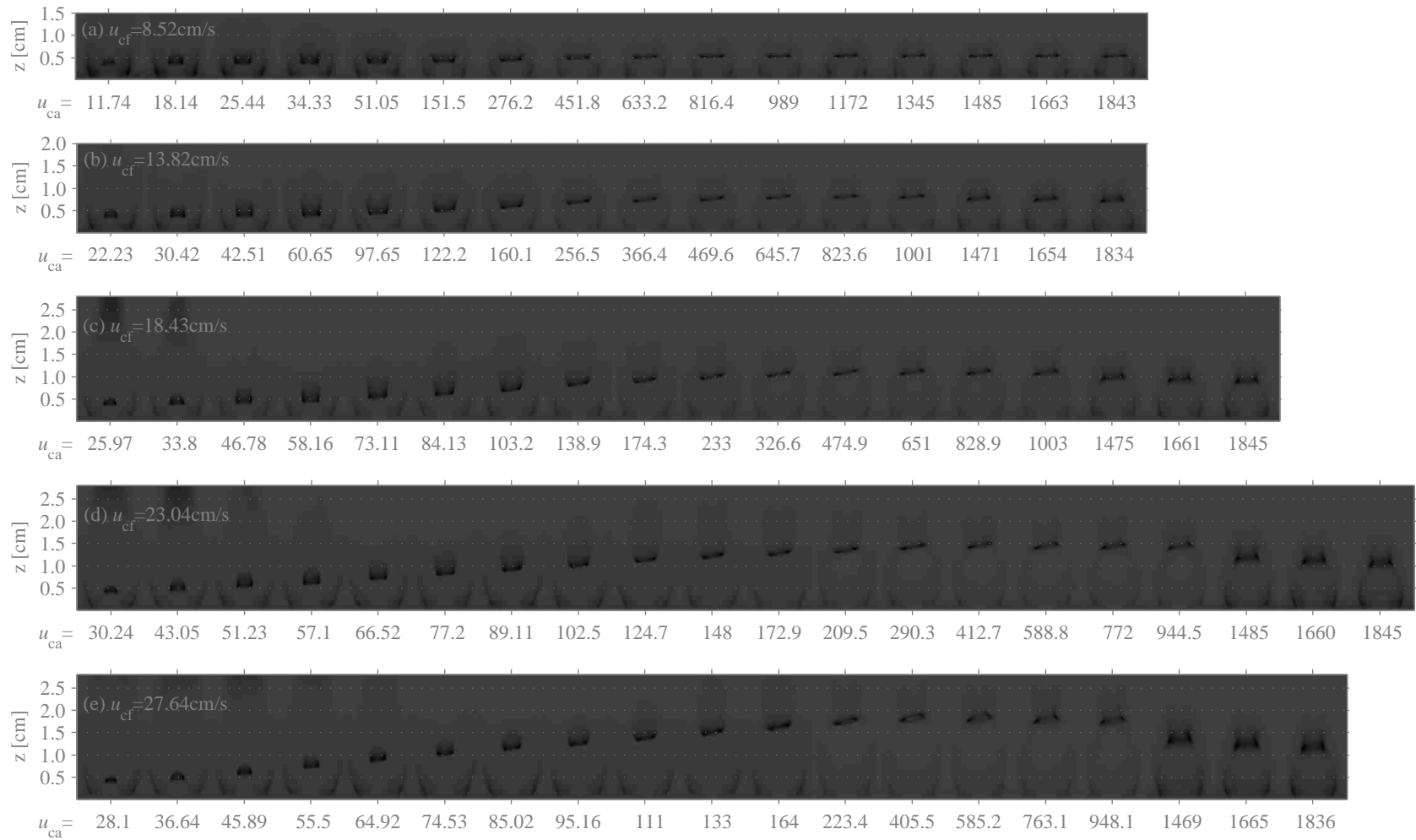


Figure B.5: $\Phi = 0.78$ co-flow, central air tube raised 3 mm.

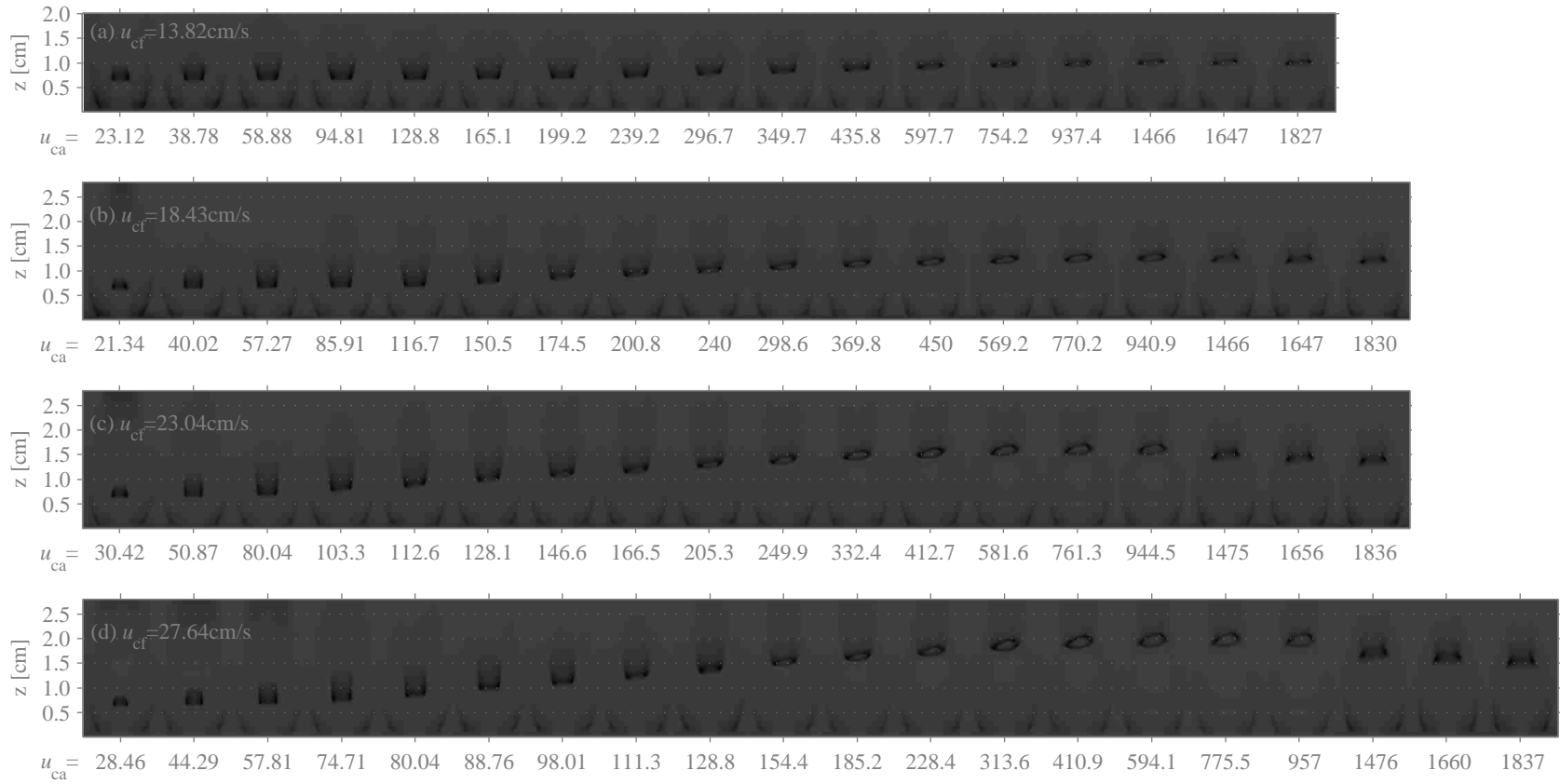


Figure B.6: $\Phi = 0.78$ co-flow, central air tube raised 6 mm.

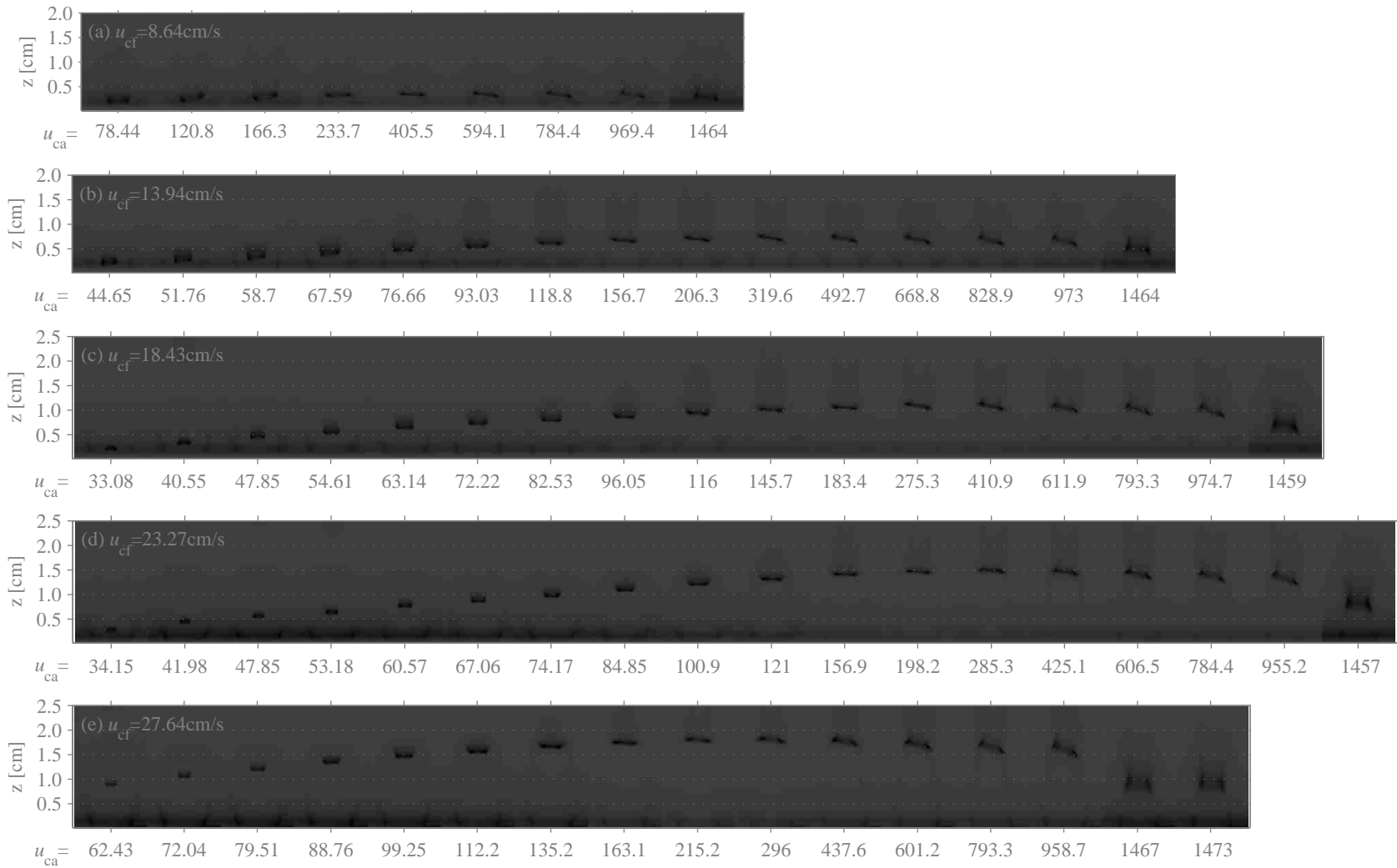


Figure B.7: $\Phi = 1.0$ co-flow, central air tube flush.

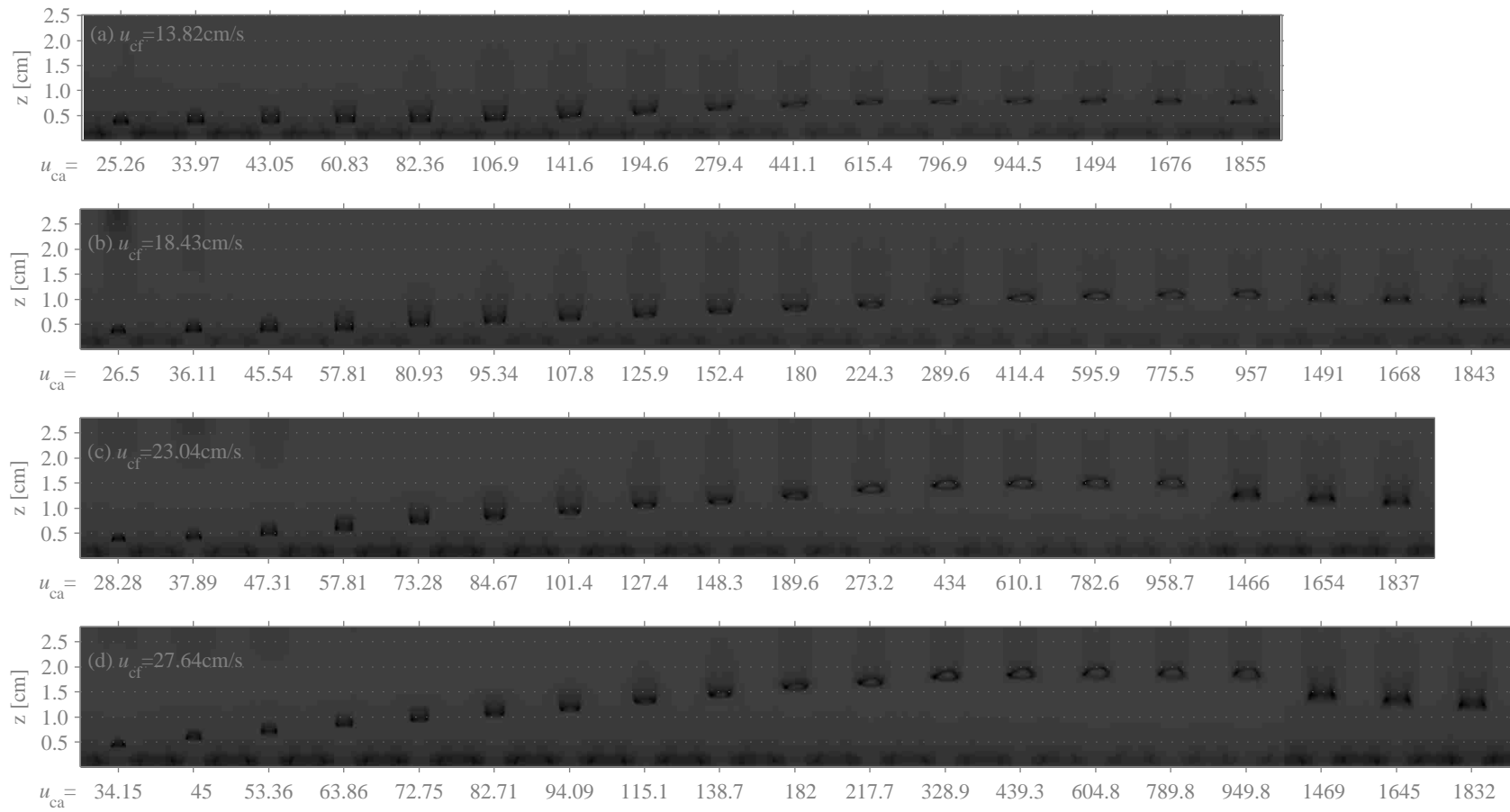


Figure B.8: $\Phi = 1.0$ co-flow, central air tube raised 3 mm.

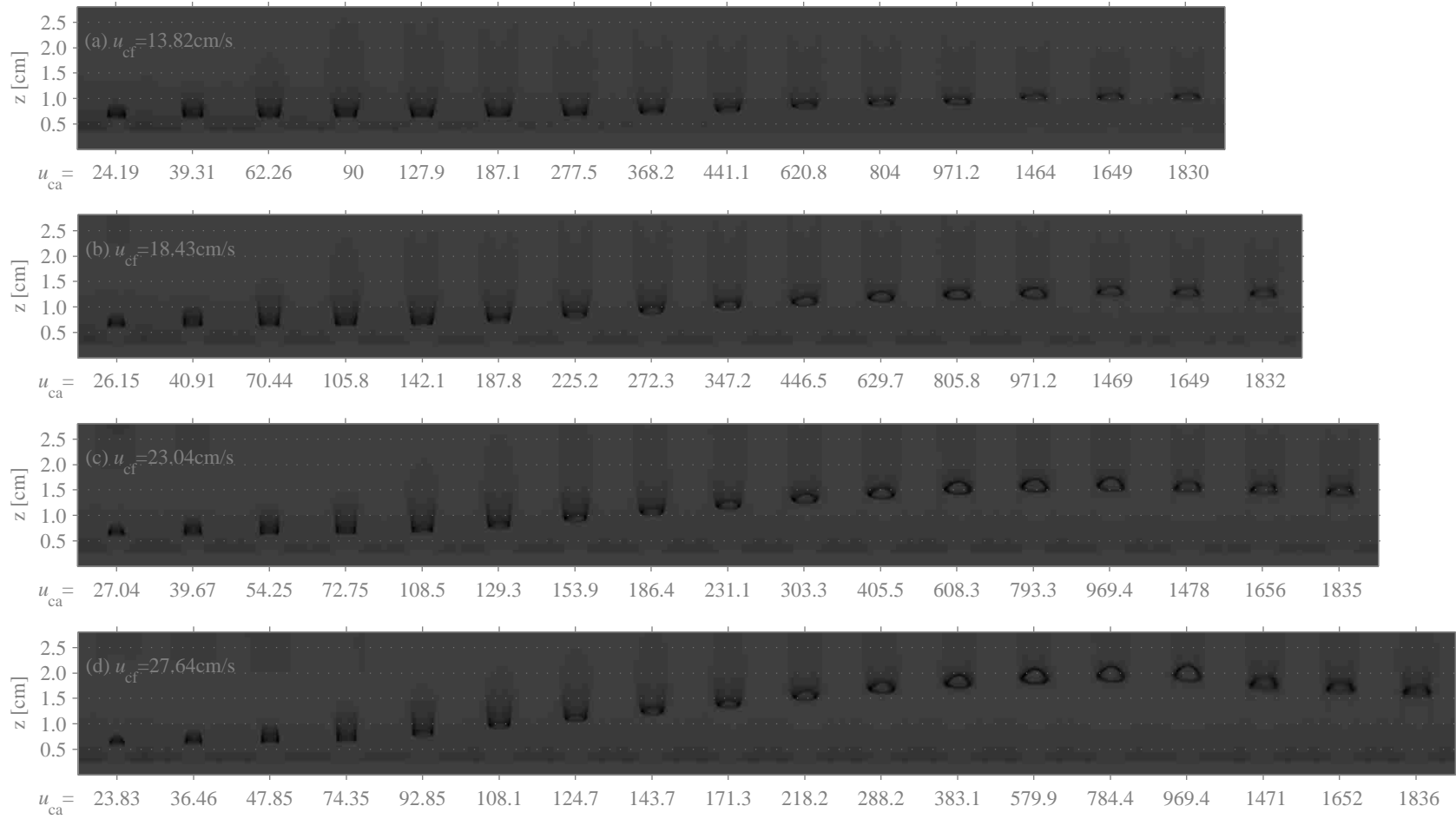


Figure B.9: $\Phi = 1.0$ co-flow, central air tube raised 6 mm.

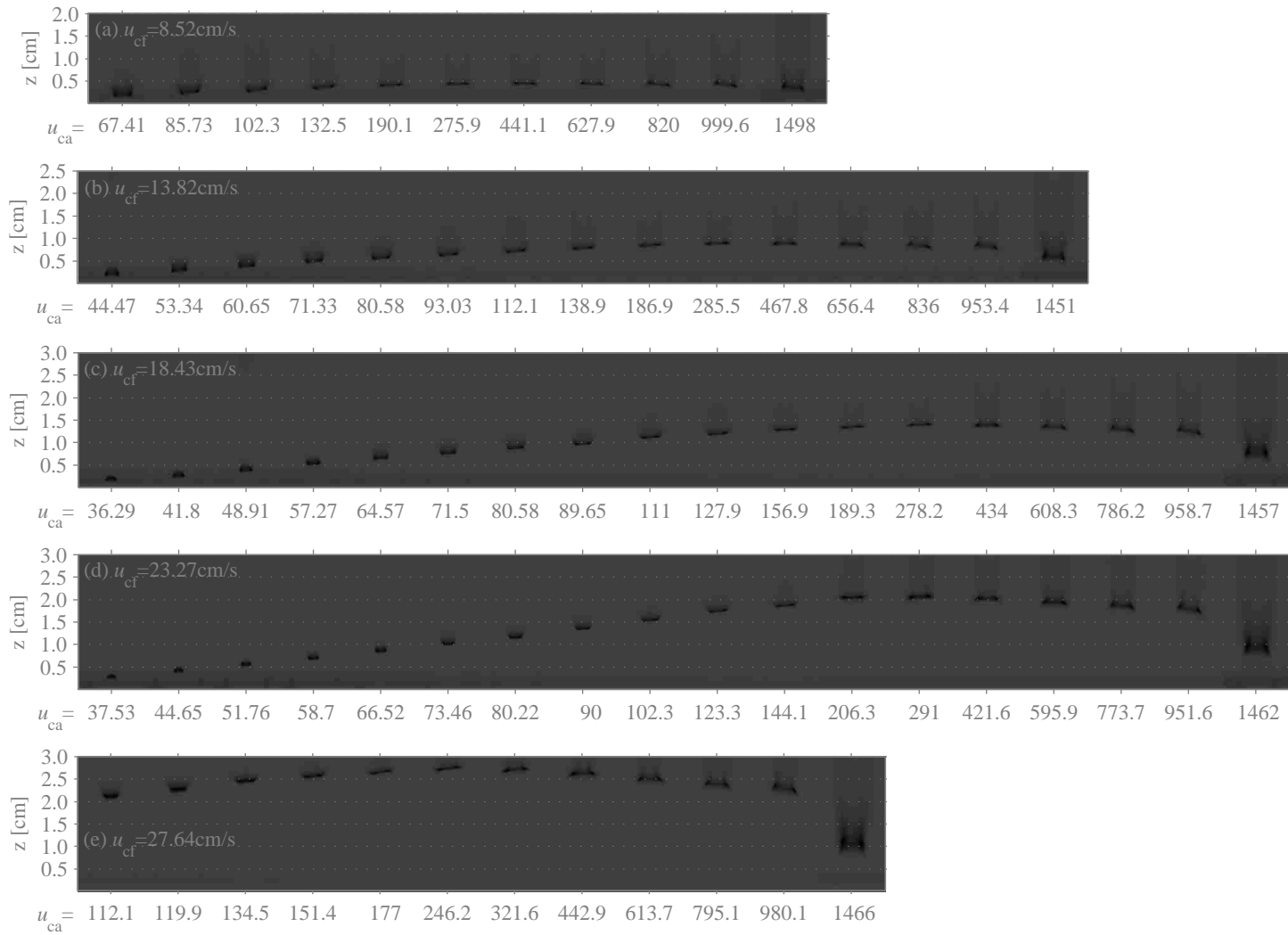


Figure B.10: $\Phi = 1.2$ co-flow, central air tube flush.

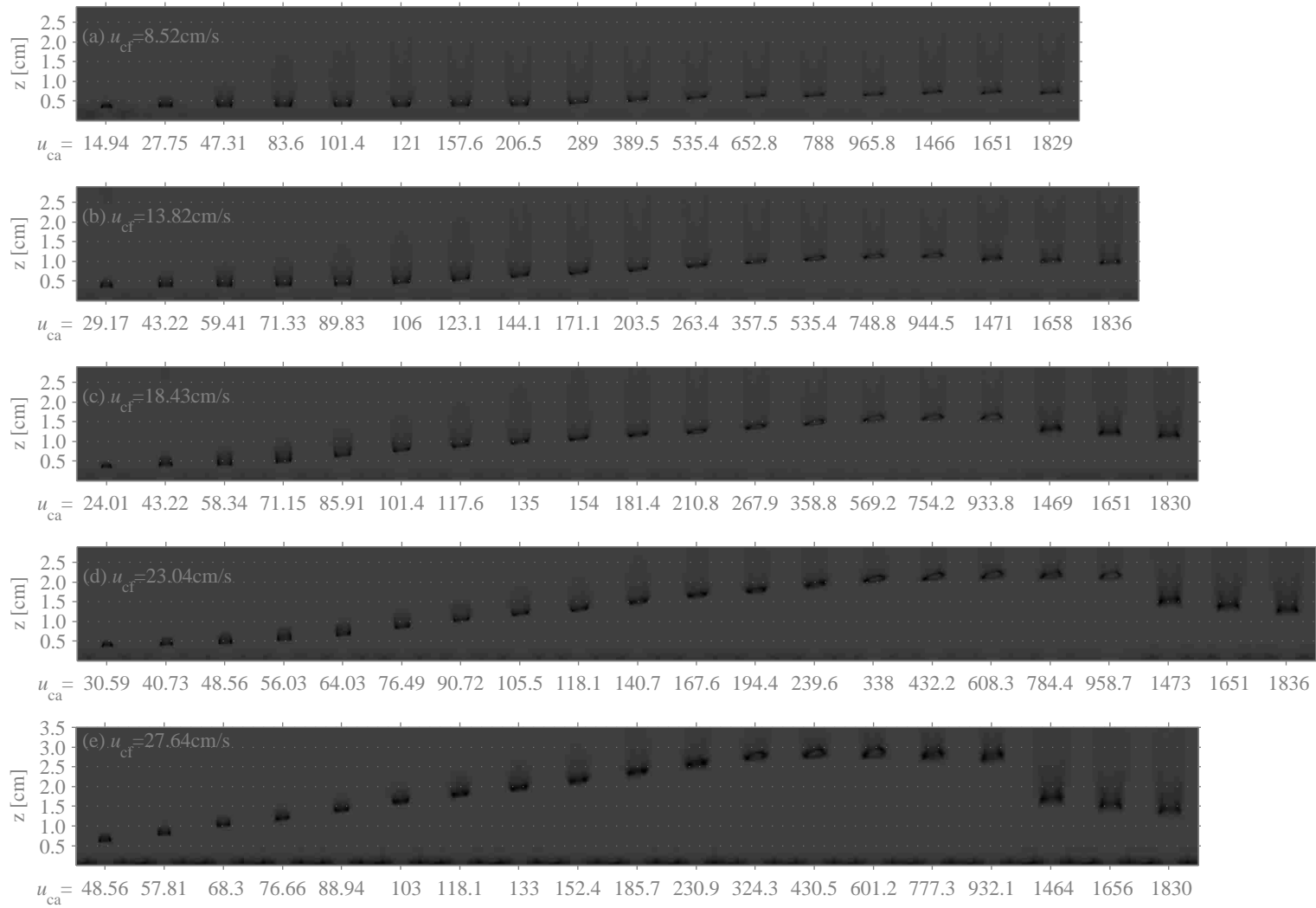


Figure B.11: $\Phi = 1.2$ co-flow, central air tube raised 3 mm.

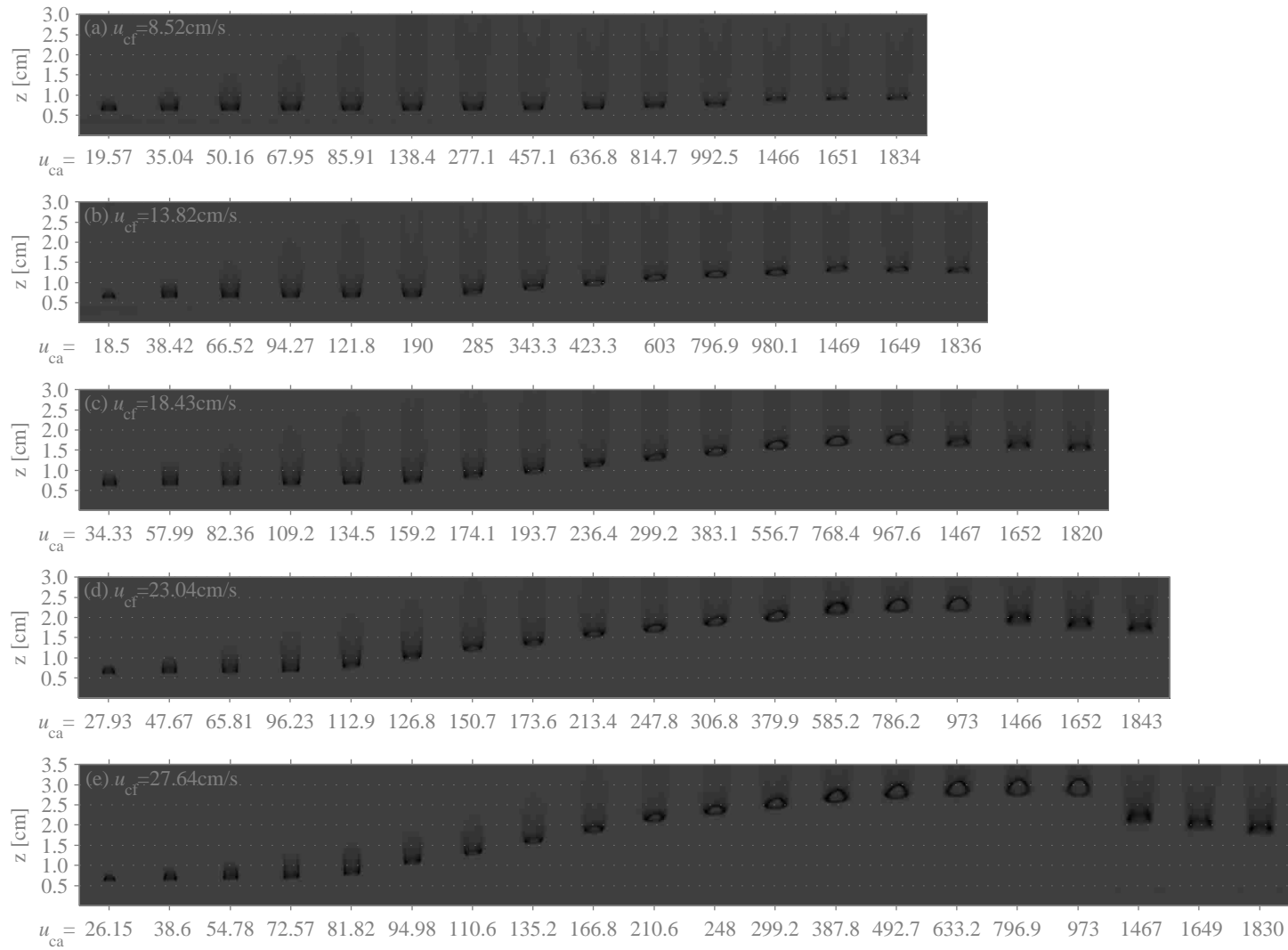


Figure B.12: $\Phi = 1.2$ co-flow, central air tube raised 6 mm.

Appendix C

Experimental/numerical CH* contour comparisons

Included here are all the contour plots comparing experimental and numerical CH* emissions in this work, with the central air velocity given in each case. Experimental contours are plotted with the thin lines. The thin black line is data from the Abel transform of the left-hand side of the images, and the thin grey line is data from the right-hand side of the images. Simulations are post-processed to model the CH* chemiluminescence emission, and the point-spread function of the imaging system, and plotted with the thick dashed line.

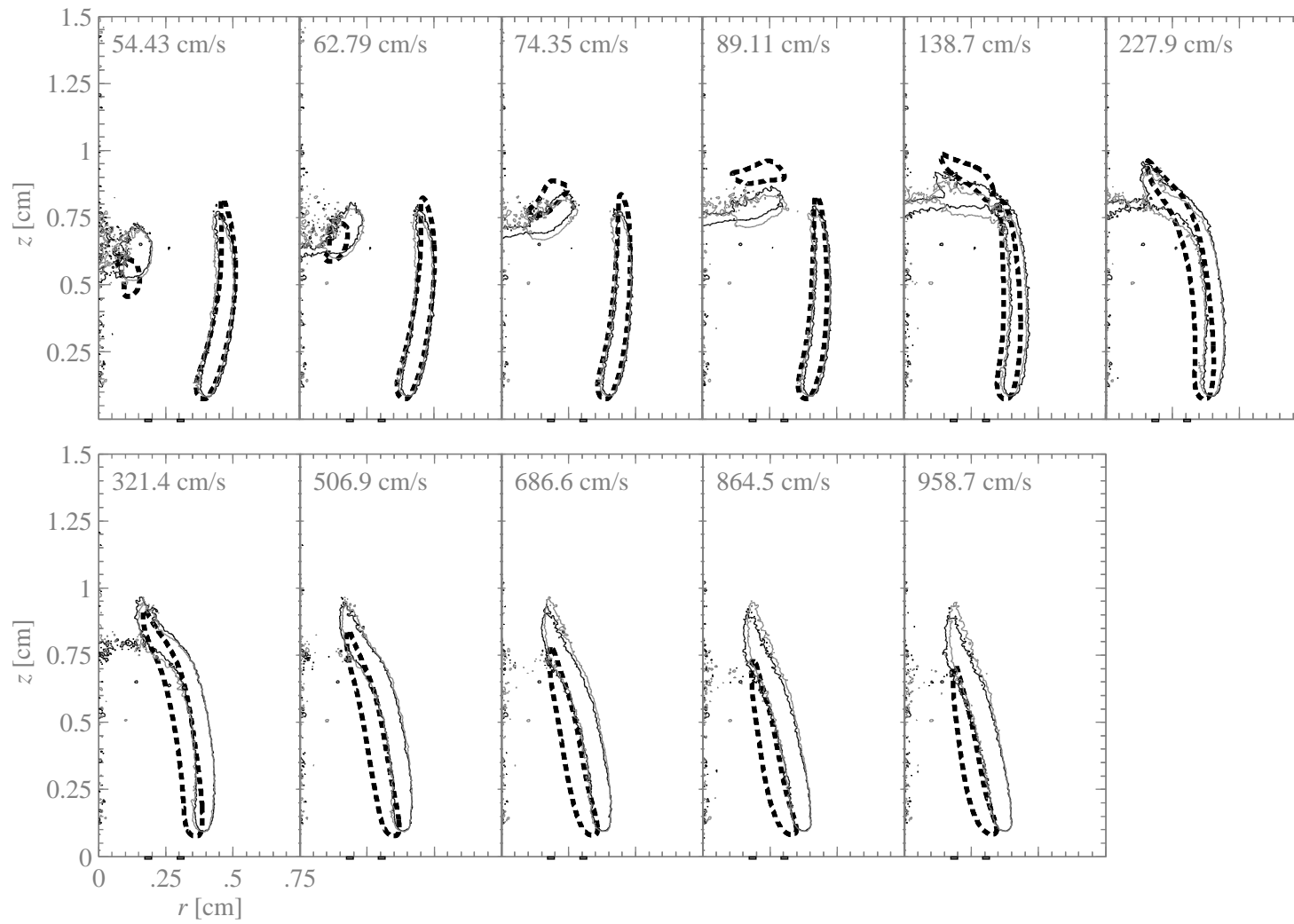


Figure C.1: Air co-flow, $u_{cf}=18.4$ cm/s, air tube flush.

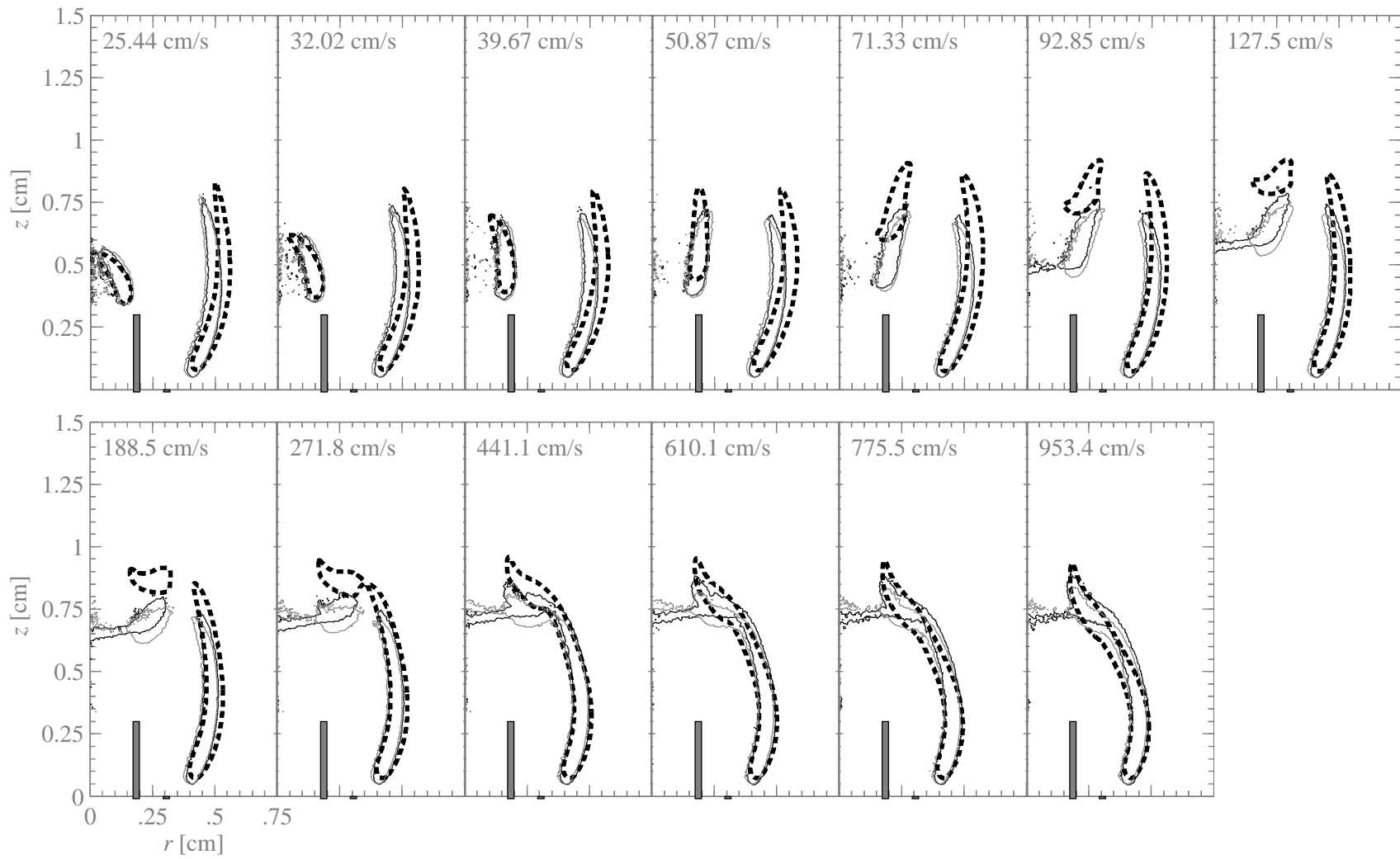


Figure C.2: Air co-flow, $u_{cf}=18.4$ cm/s, air tube raised 3 mm.

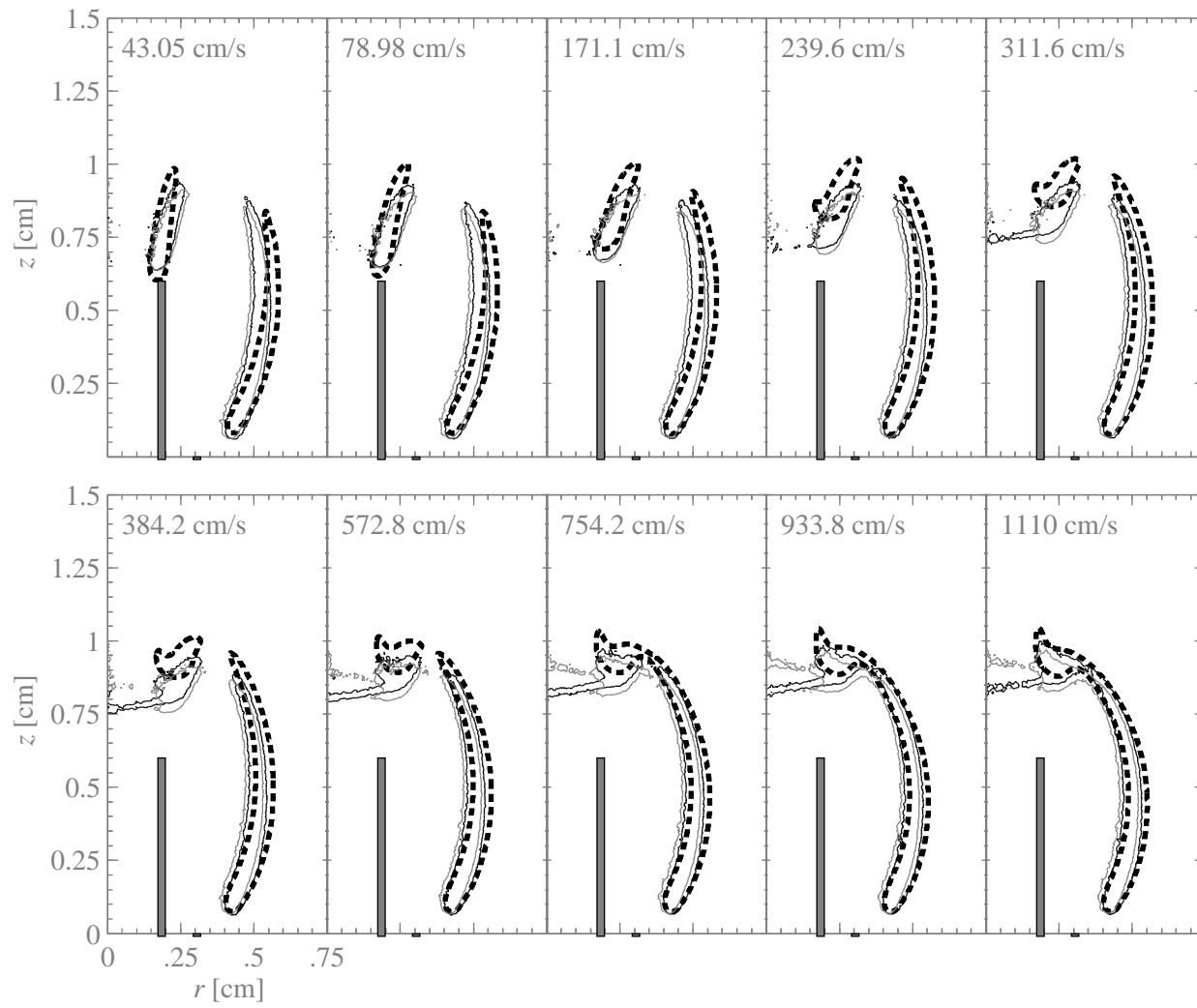


Figure C.3: Air co-flow, $u_{cf}=18.4$ cm/s, air tube raised 6 mm.

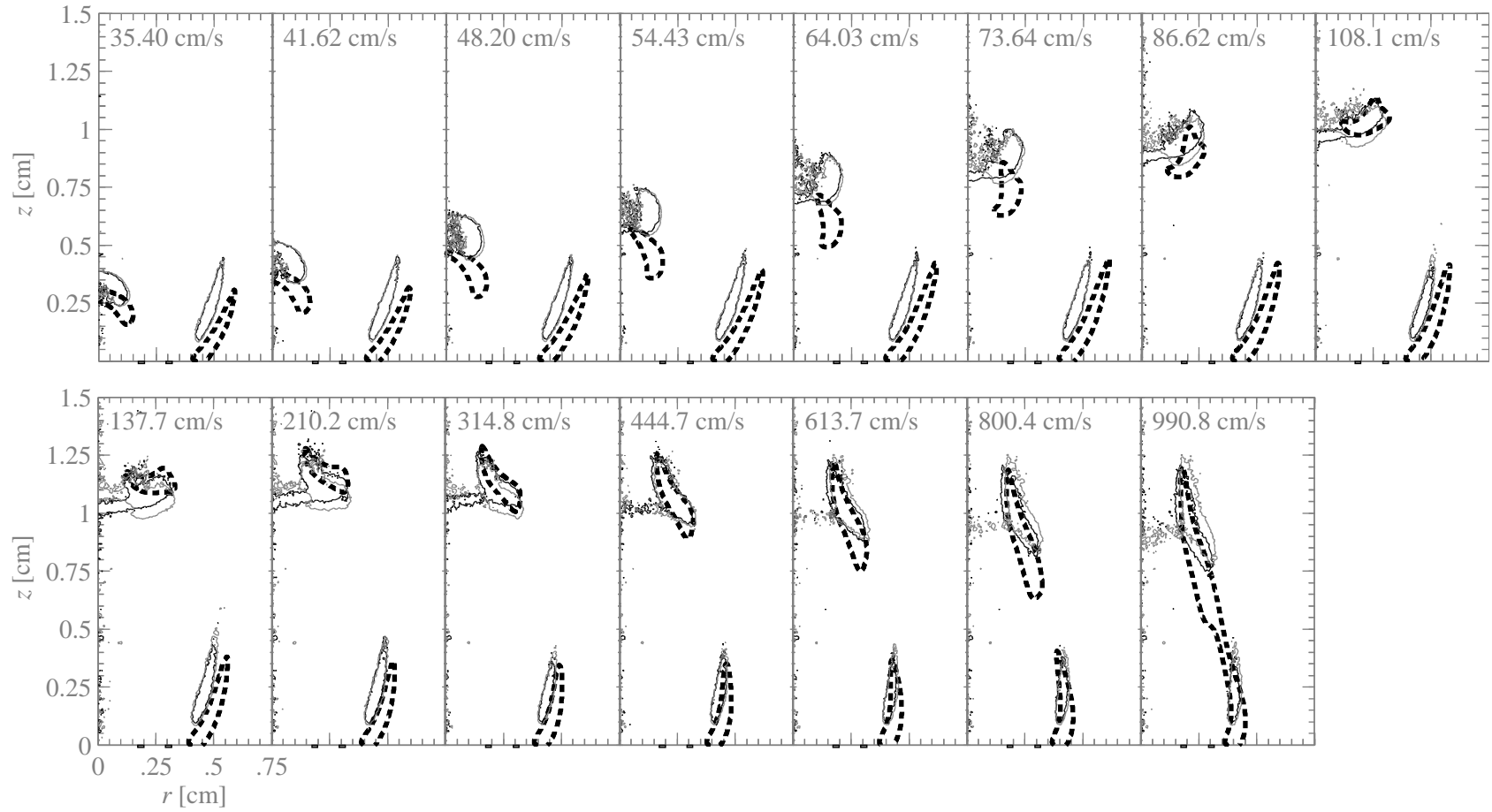


Figure C.4: $\Phi = 0.78$ co-flow, $u_{cf}=18.4$ cm/s, air tube flush.

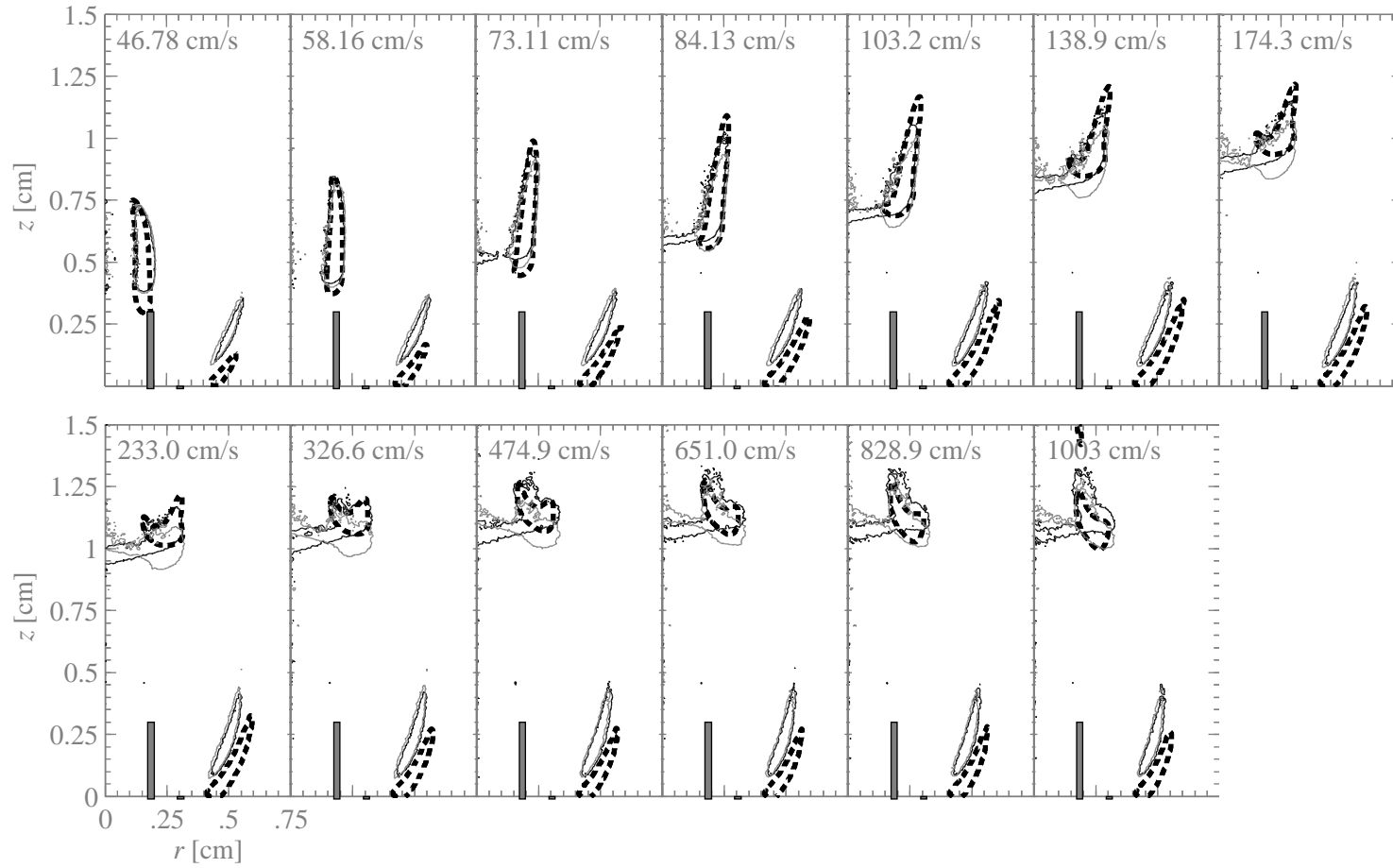


Figure C.5: $\Phi = 0.78$ co-flow, $u_{cf}=18.4$ cm/s, air tube raised 3mm.

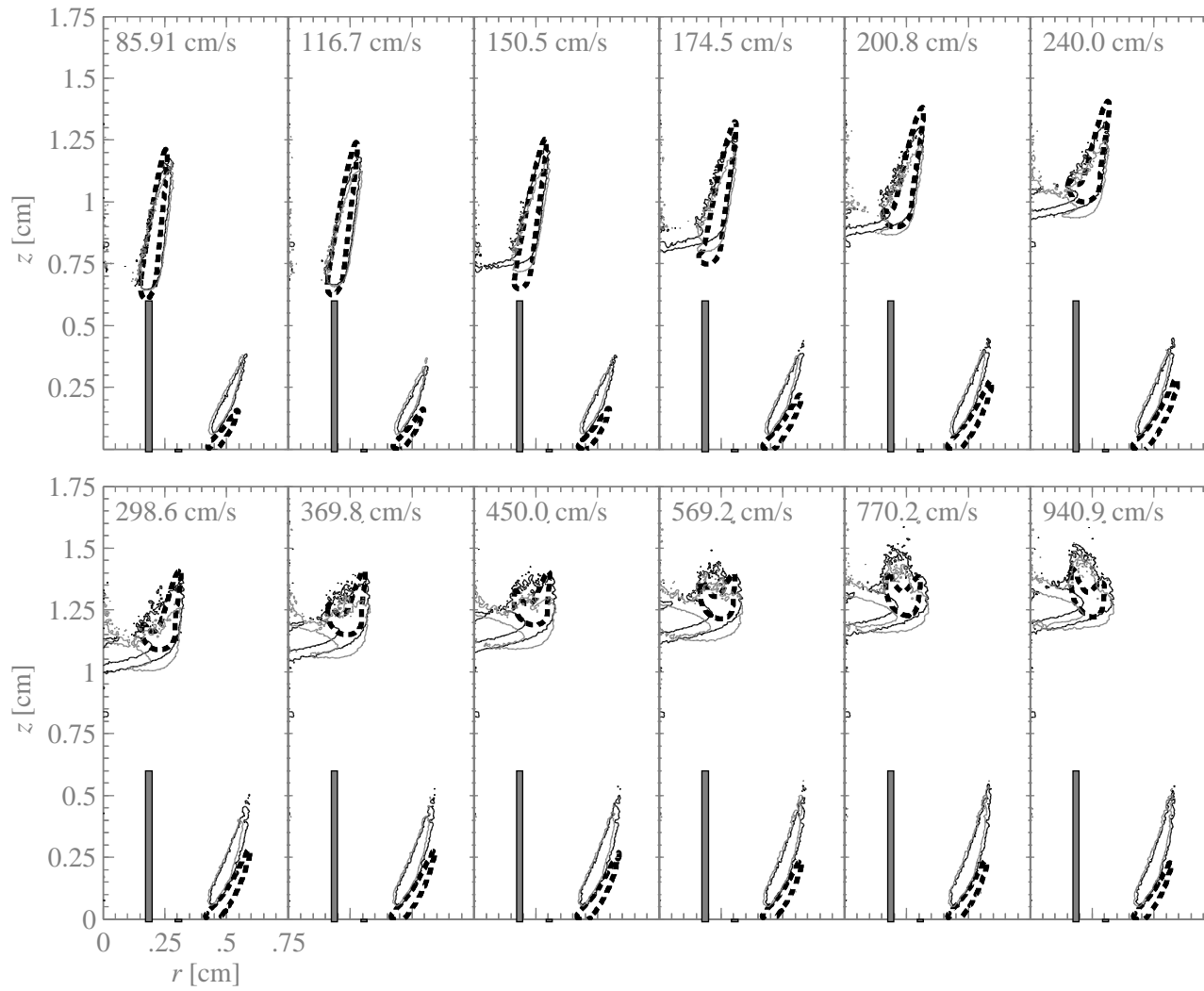


Figure C.6: $\Phi = 0.78$ co-flow, $u_{cf}=18.4$ cm/s, air tube raised 6mm.

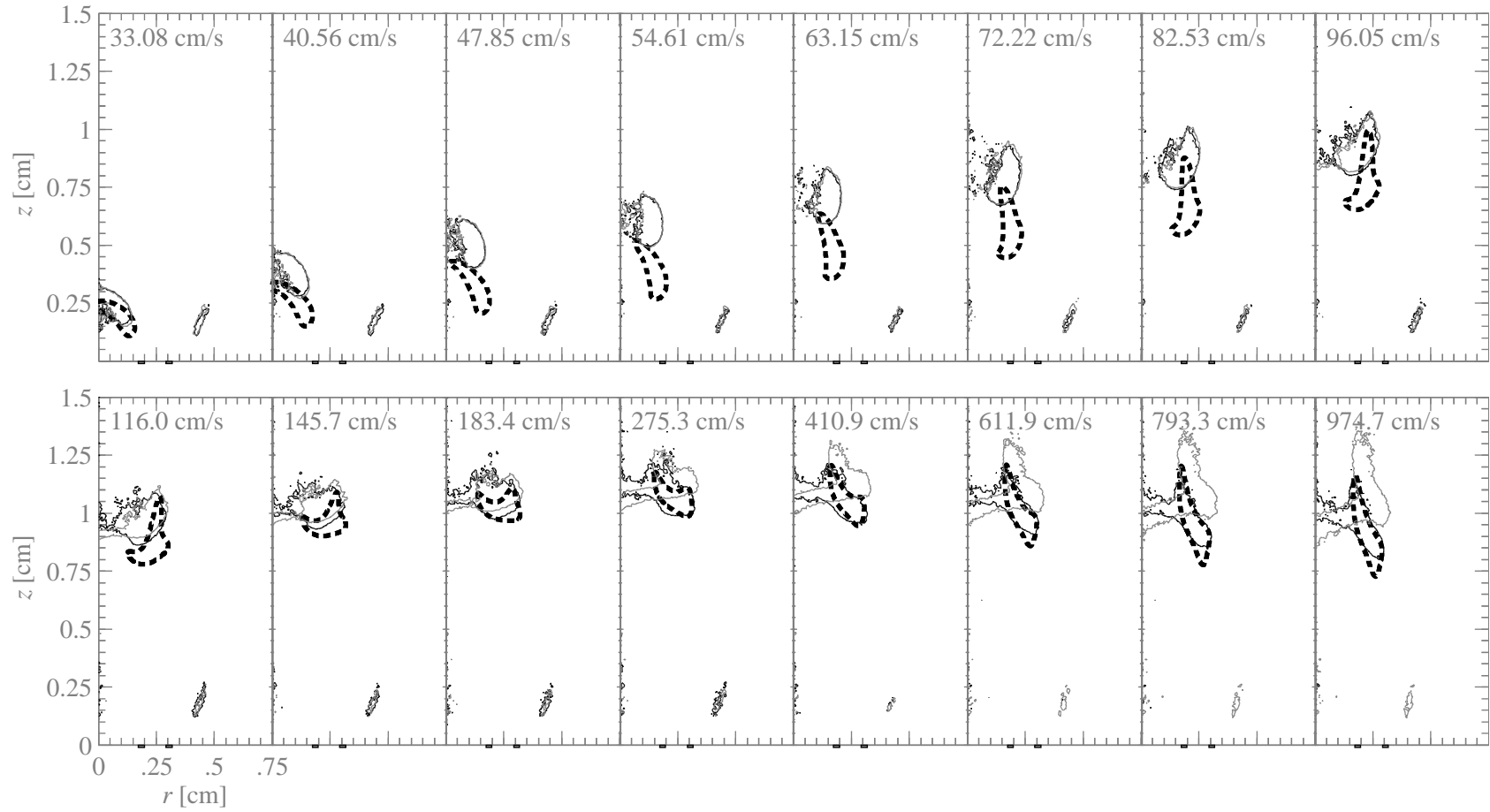


Figure C.7: $\Phi = 1.0$ co-flow, $u_{cf}=18.4$ cm/s, air tube flush.

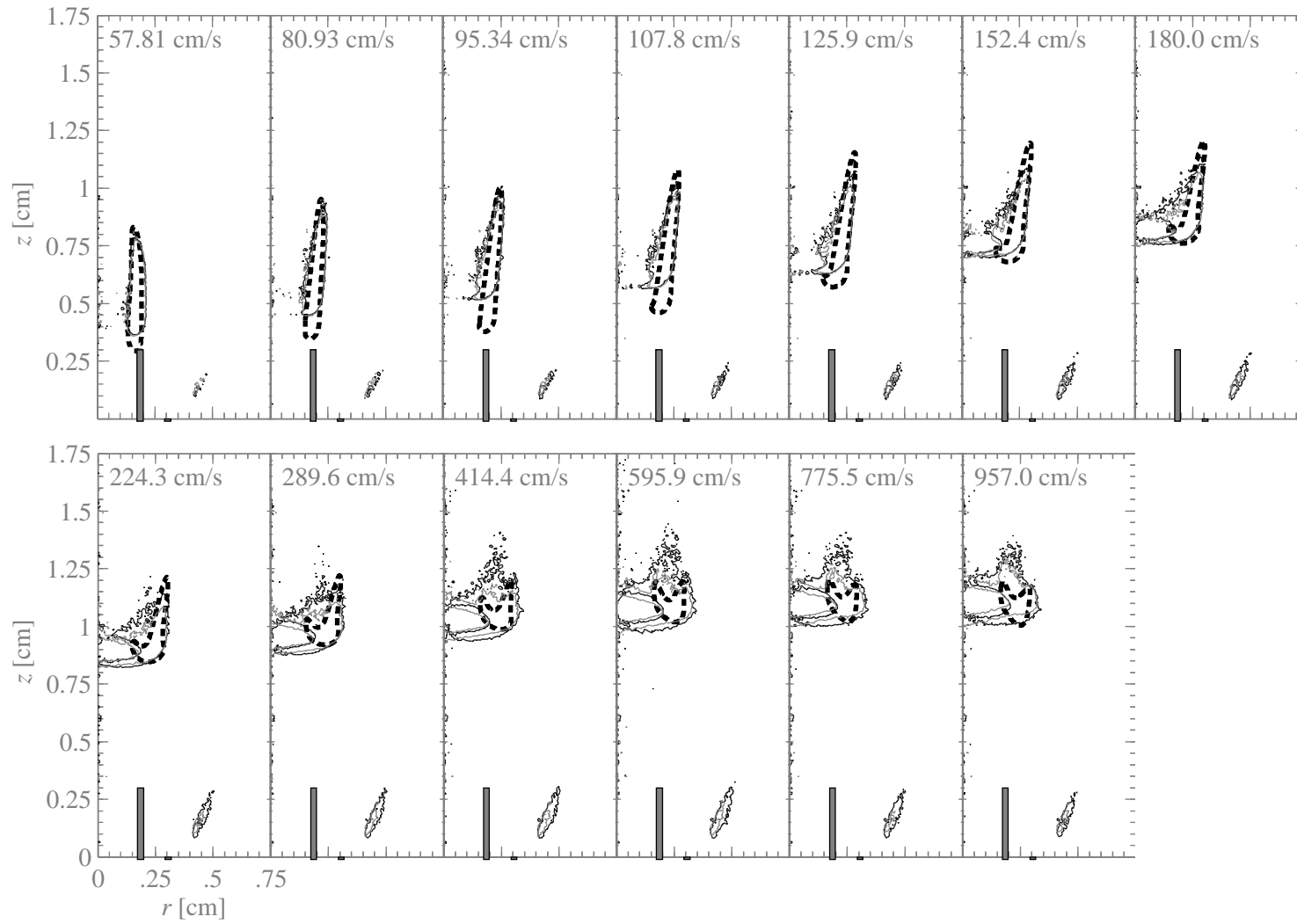


Figure C.8: $\Phi = 1.0$ co-flow, $u_{cf}=18.4$ cm/s, air tube raised 3mm.

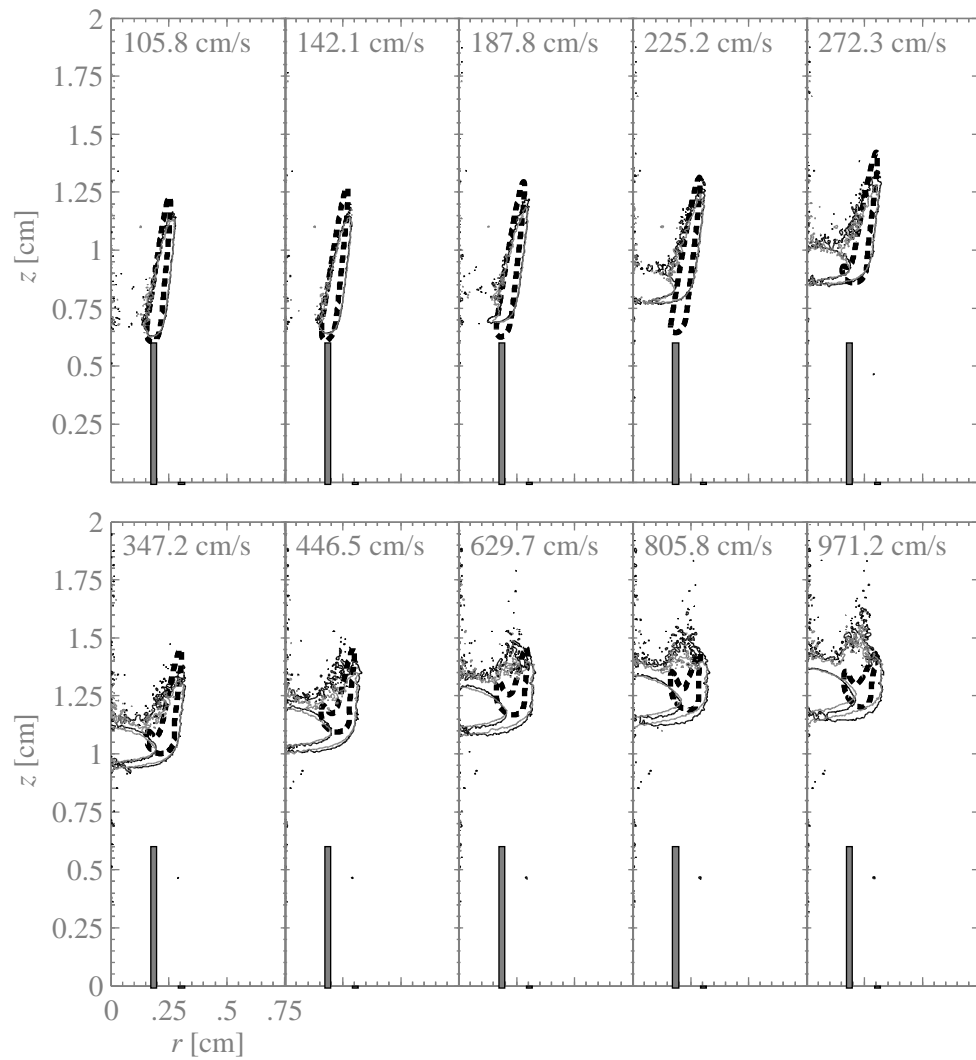


Figure C.9: $\Phi = 1.0$ co-flow, $u_{cf}=18.4$ cm/s, air tube raised 6mm.

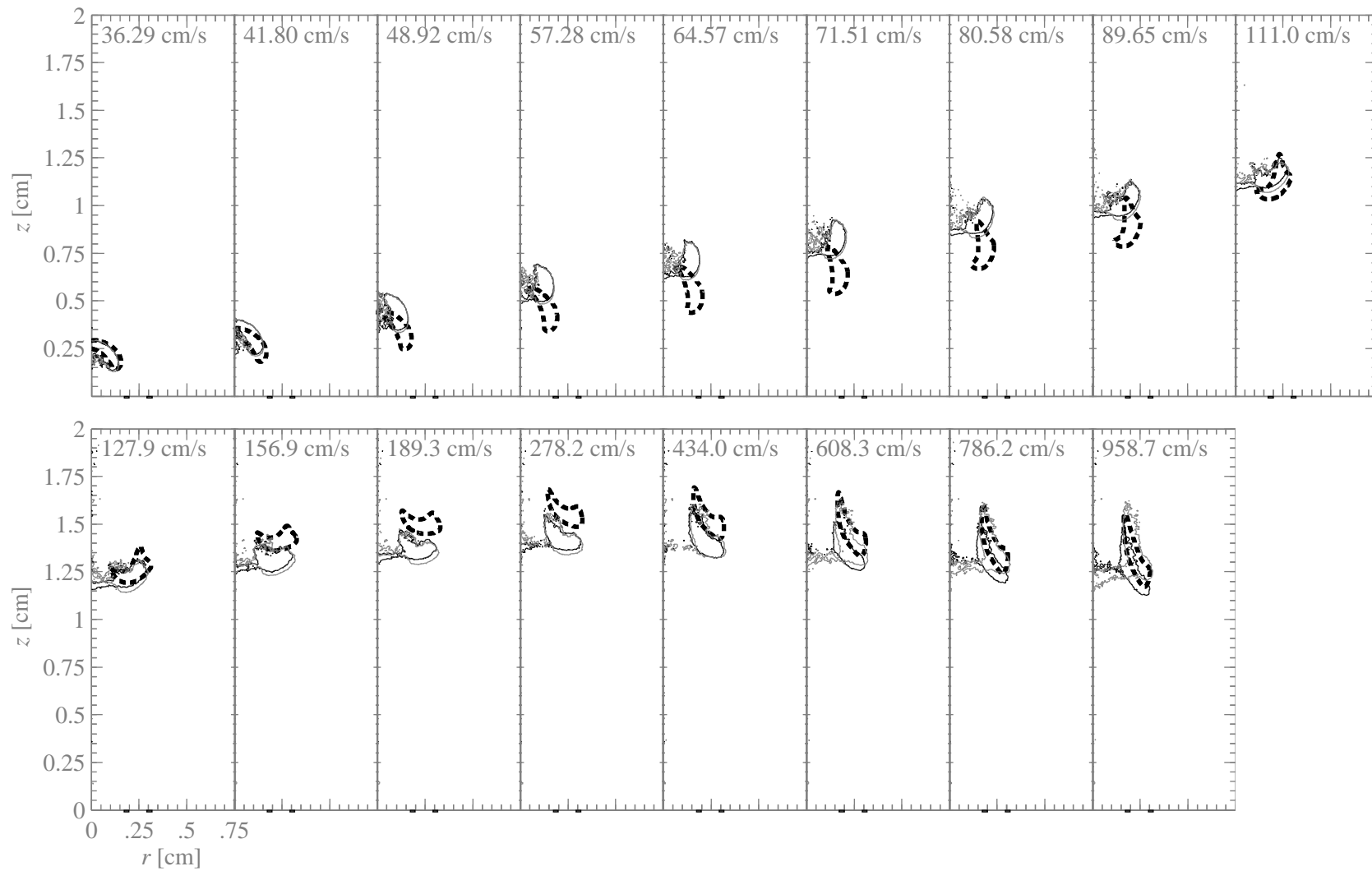


Figure C.10: $\Phi = 1.2$ co-flow, $u_{cf}=18.4$ cm/s, air tube flush.

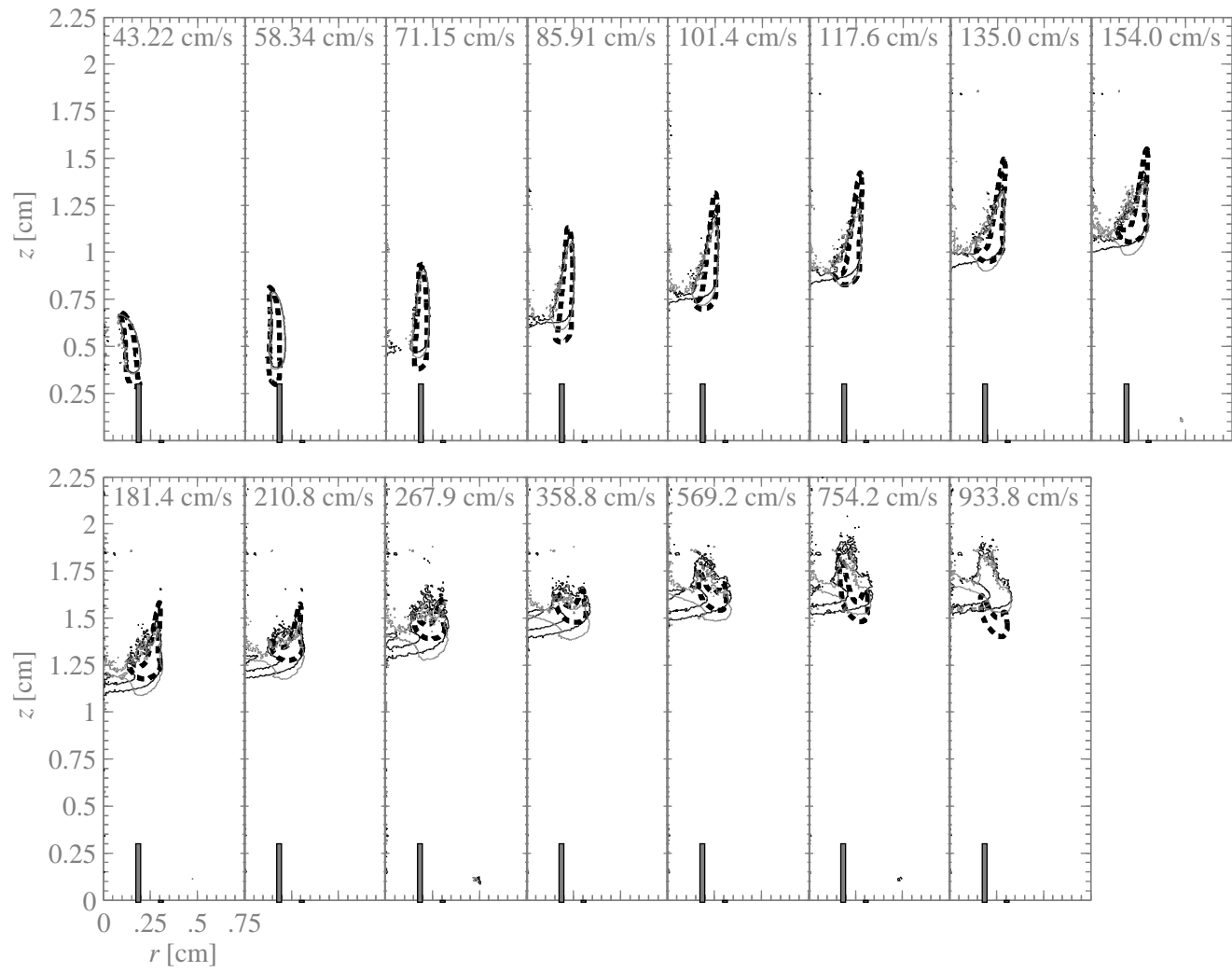


Figure C.11: $\Phi = 1.2$ co-flow, $u_{cf}=18.4$ cm/s, air tube raised 3 mm.

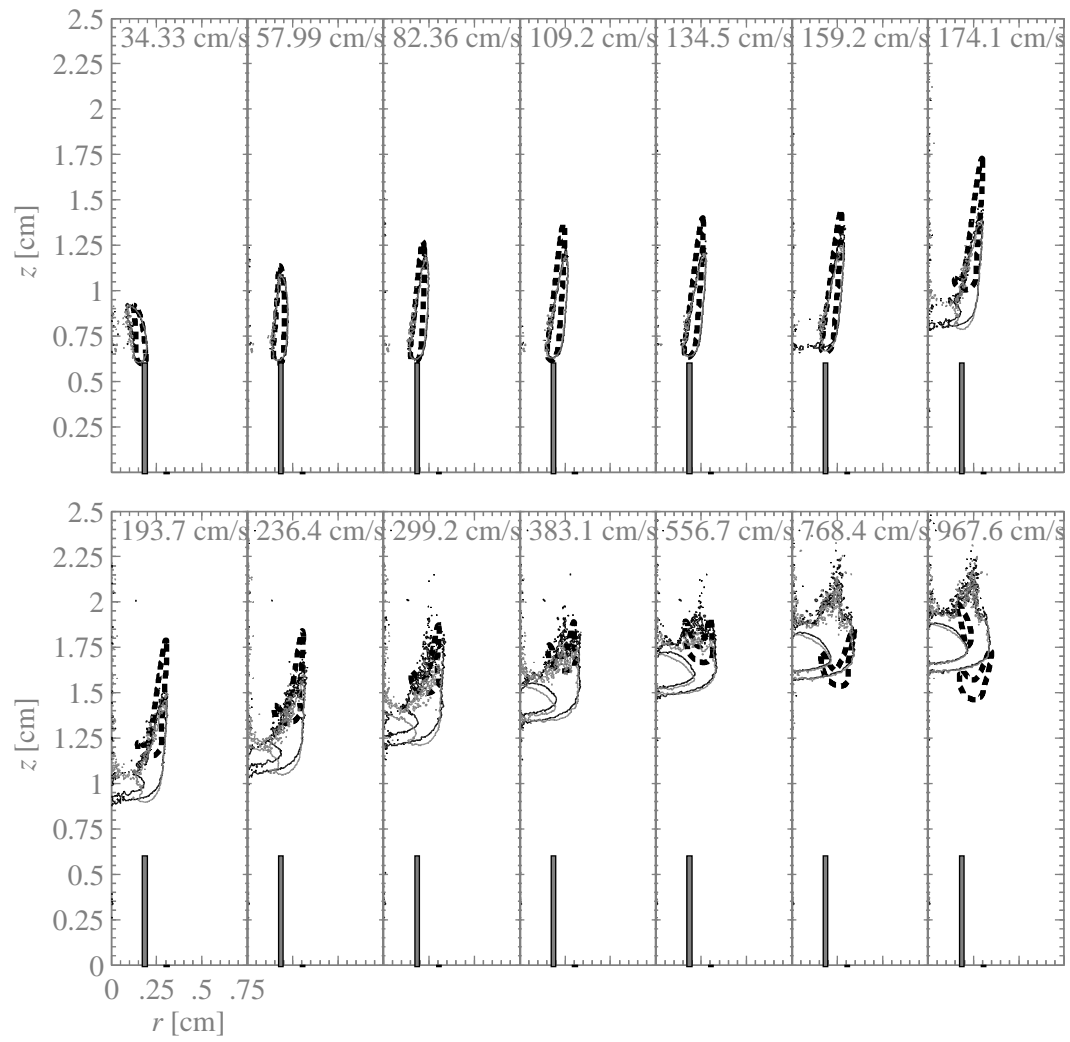


Figure C.12: $\Phi = 1.2$ co-flow, $u_{cf}=18.4$ cm/s, air tube raised 6 mm.

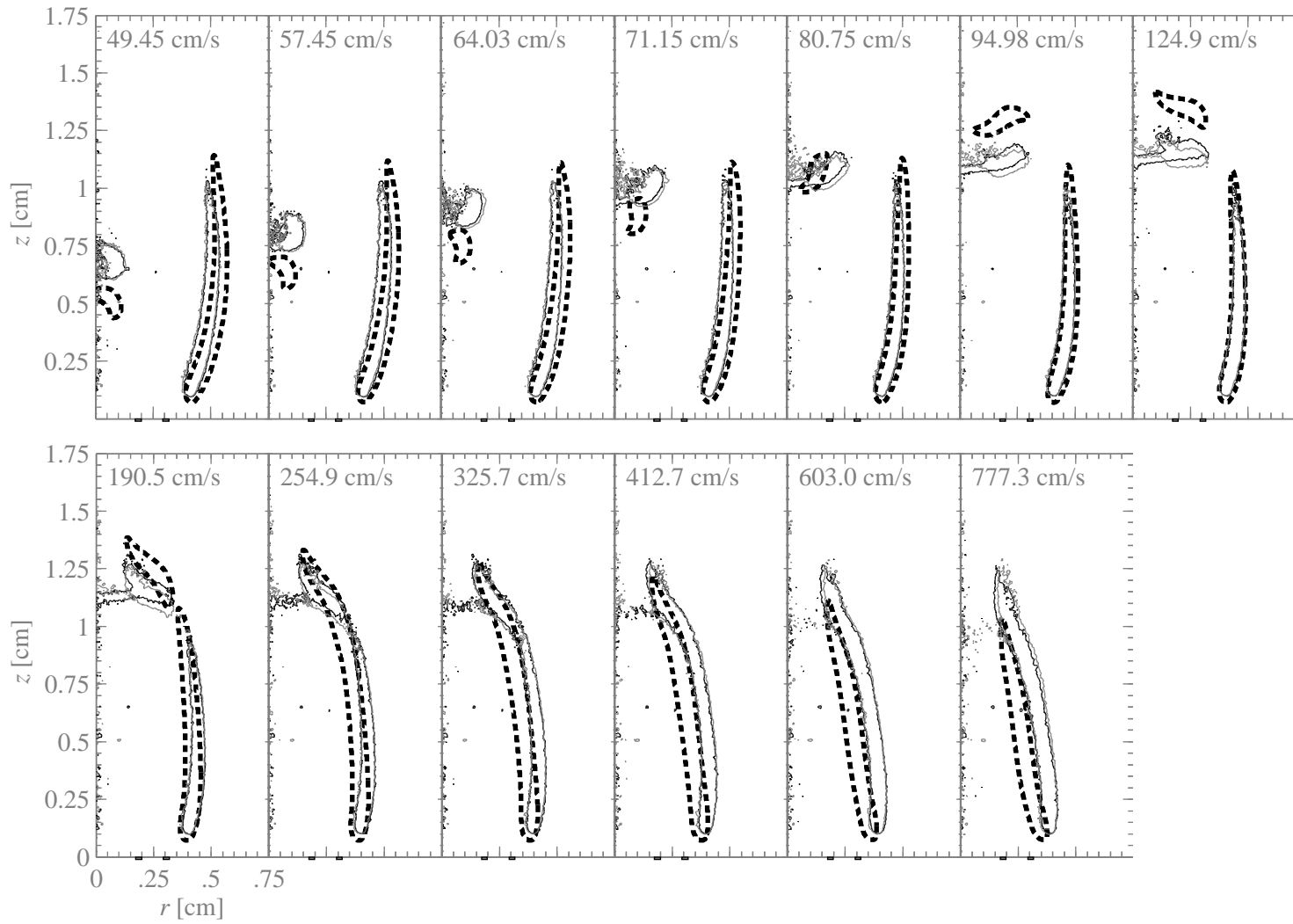


Figure C.13: Air co-flow, $u_{cf} = 23.0$ cm/s, air tube flush.

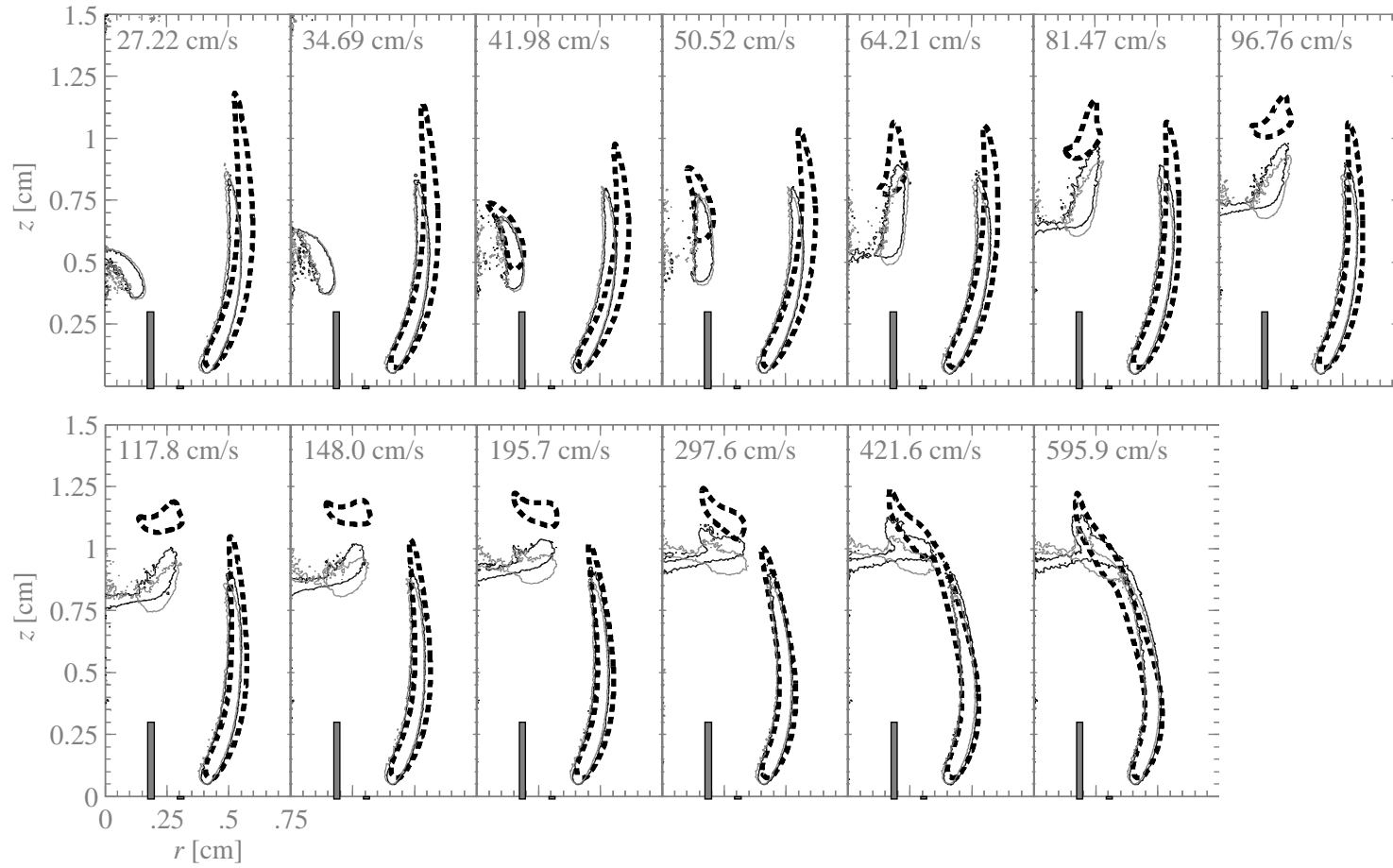


Figure C.14: Air co-flow, $u_{cf}=23.0$ cm/s, air tube raised 3 mm.

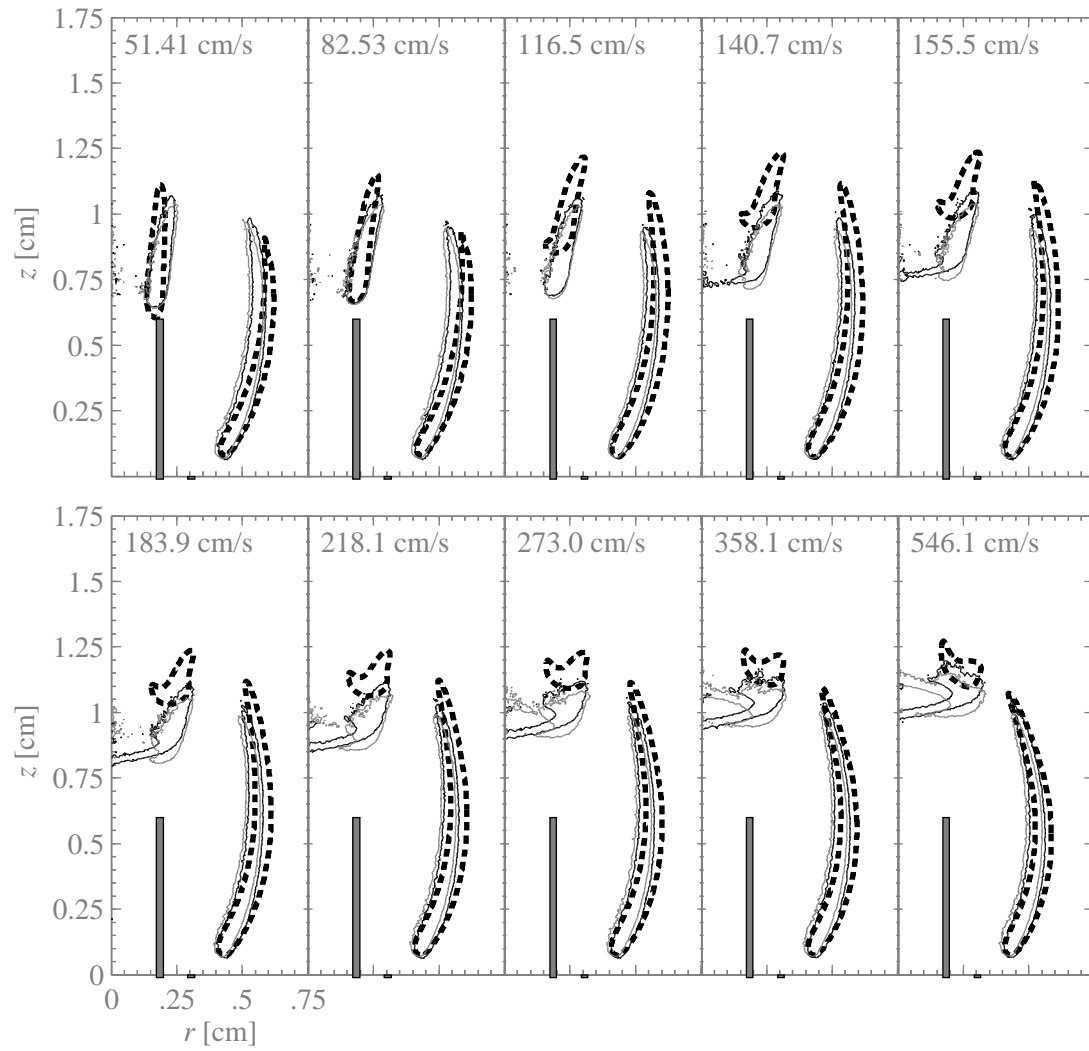


Figure C.15: Air co-flow, $u_{cf}=23.0$ cm/s, air tube raised 6 mm.

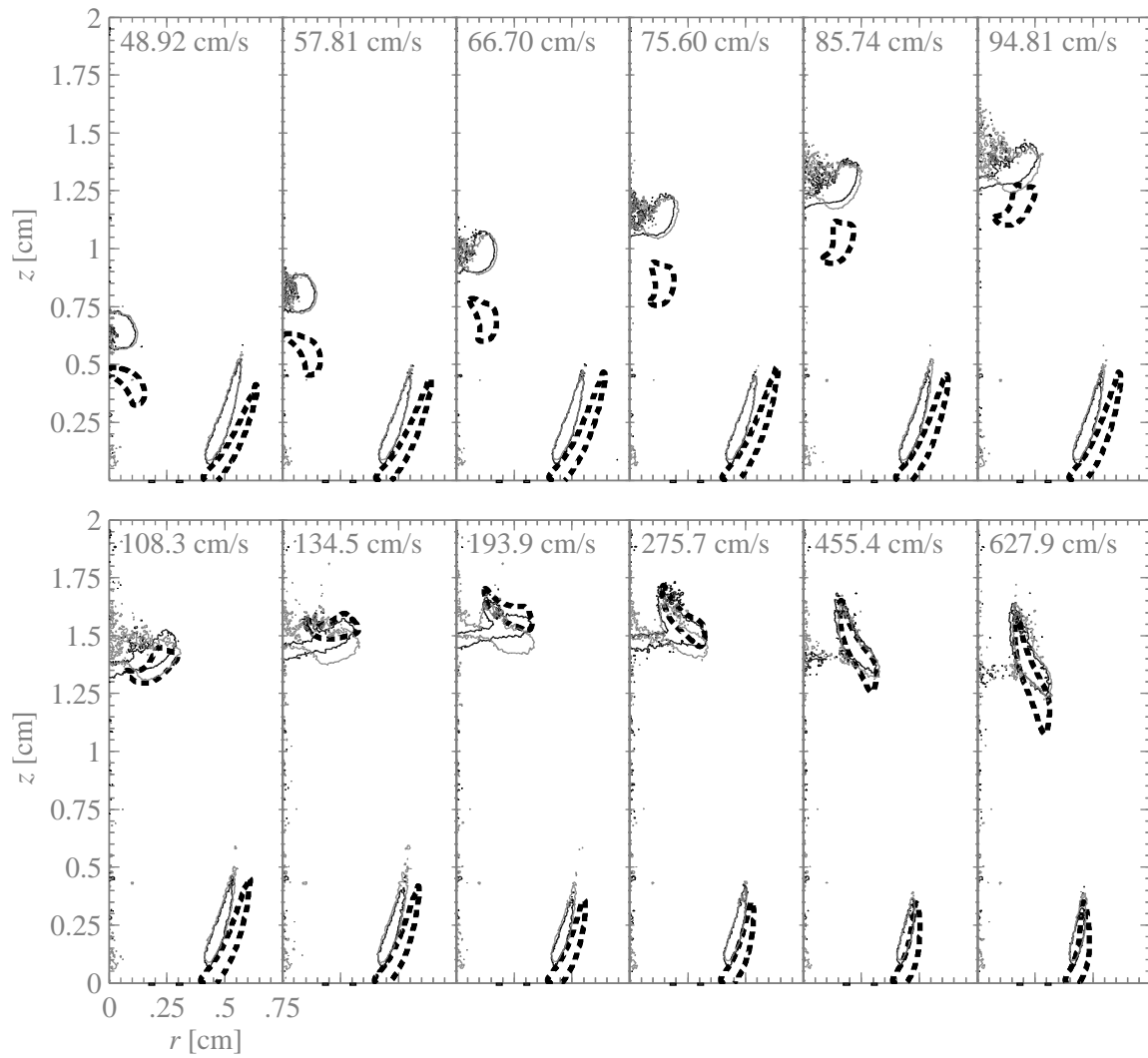


Figure C.16: $\Phi = 0.78$ co-flow, $u_{cf}=23.0$ cm/s, air tube flush.

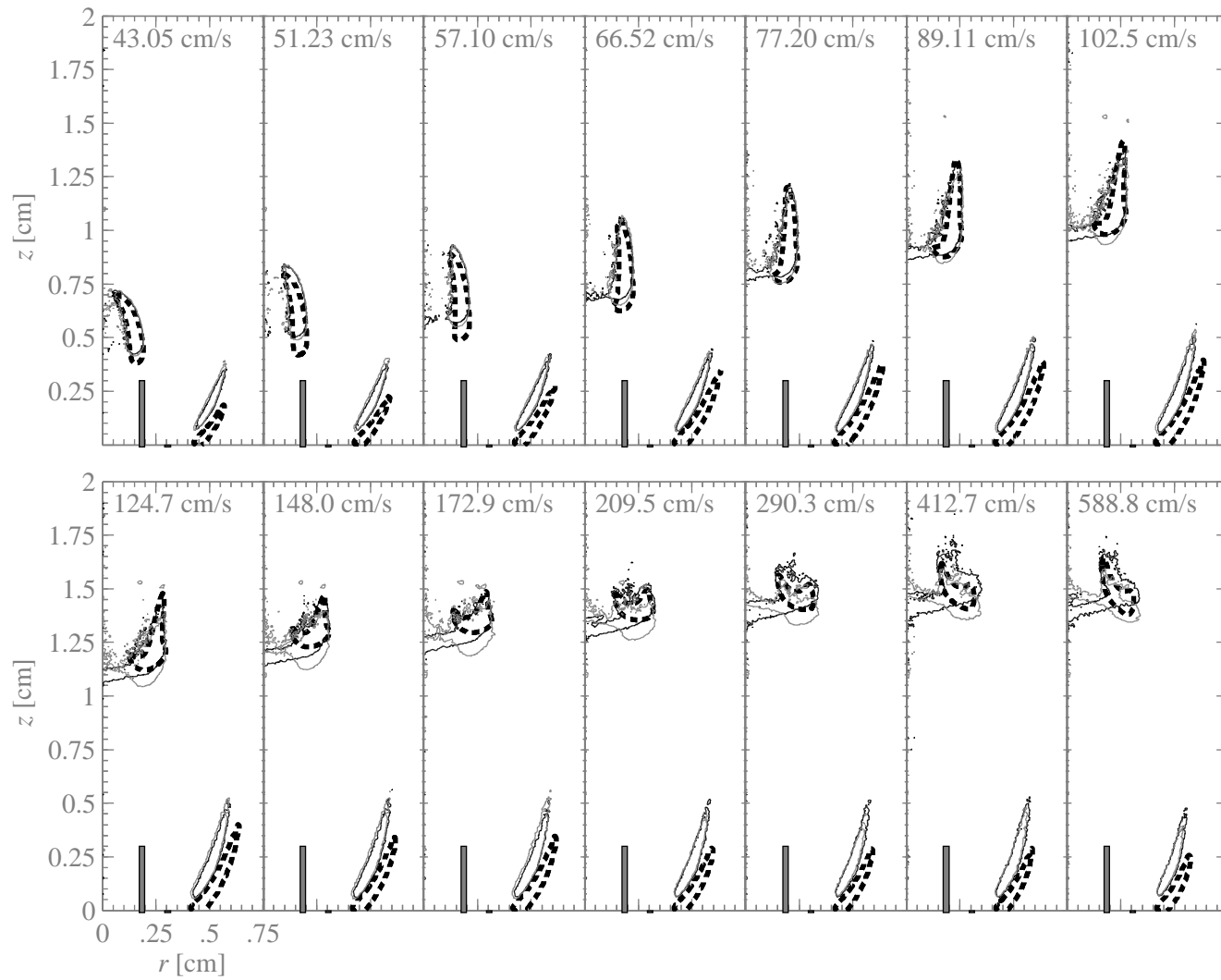


Figure C.17: $\Phi = 0.78$ co-flow, $u_{cf}=23.0$ cm/s, air tube raised 3mm.

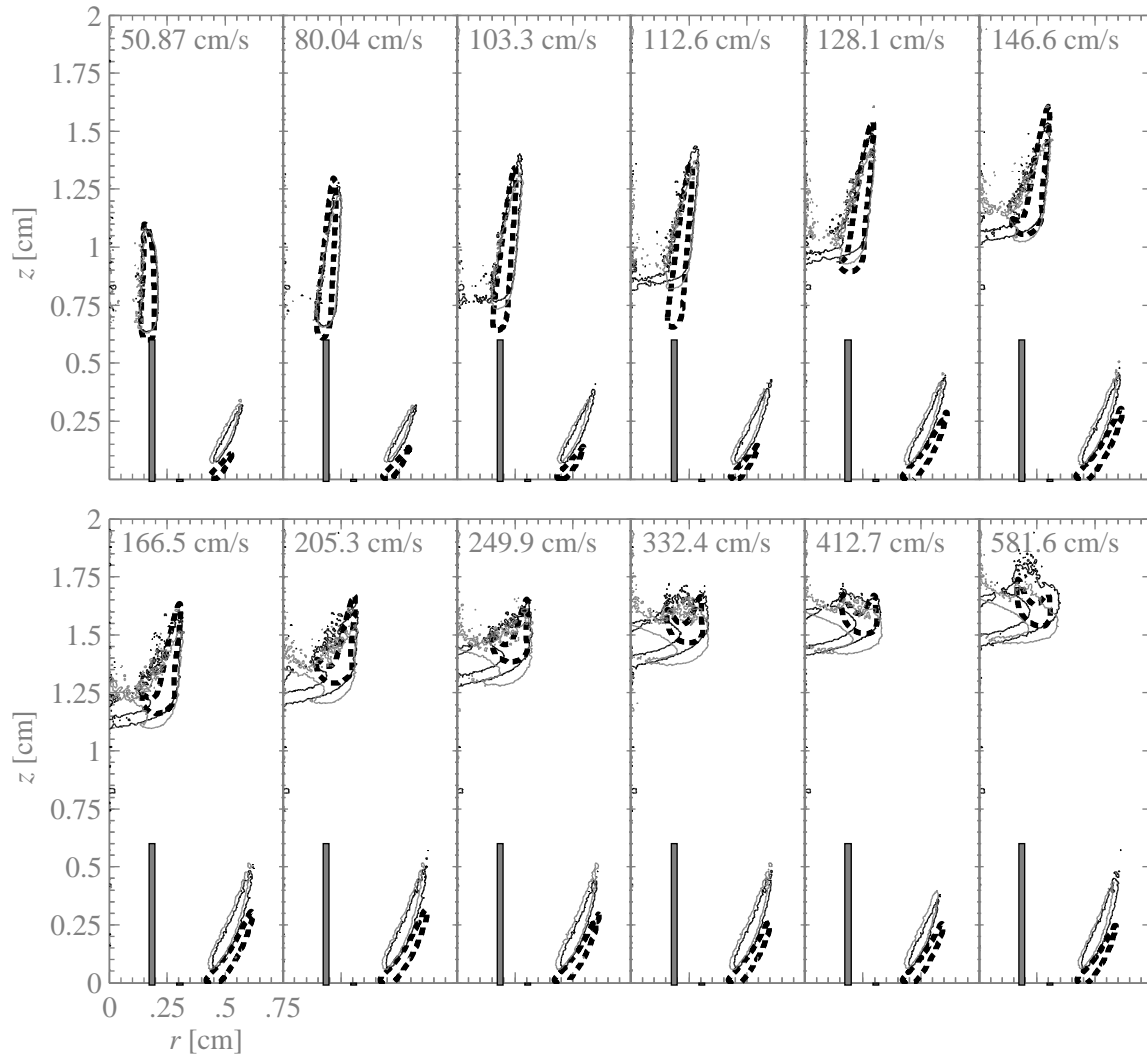


Figure C.18: $\Phi = 0.78$ co-flow, $u_{cf}=23.0$ cm/s, air tube raised 6mm.

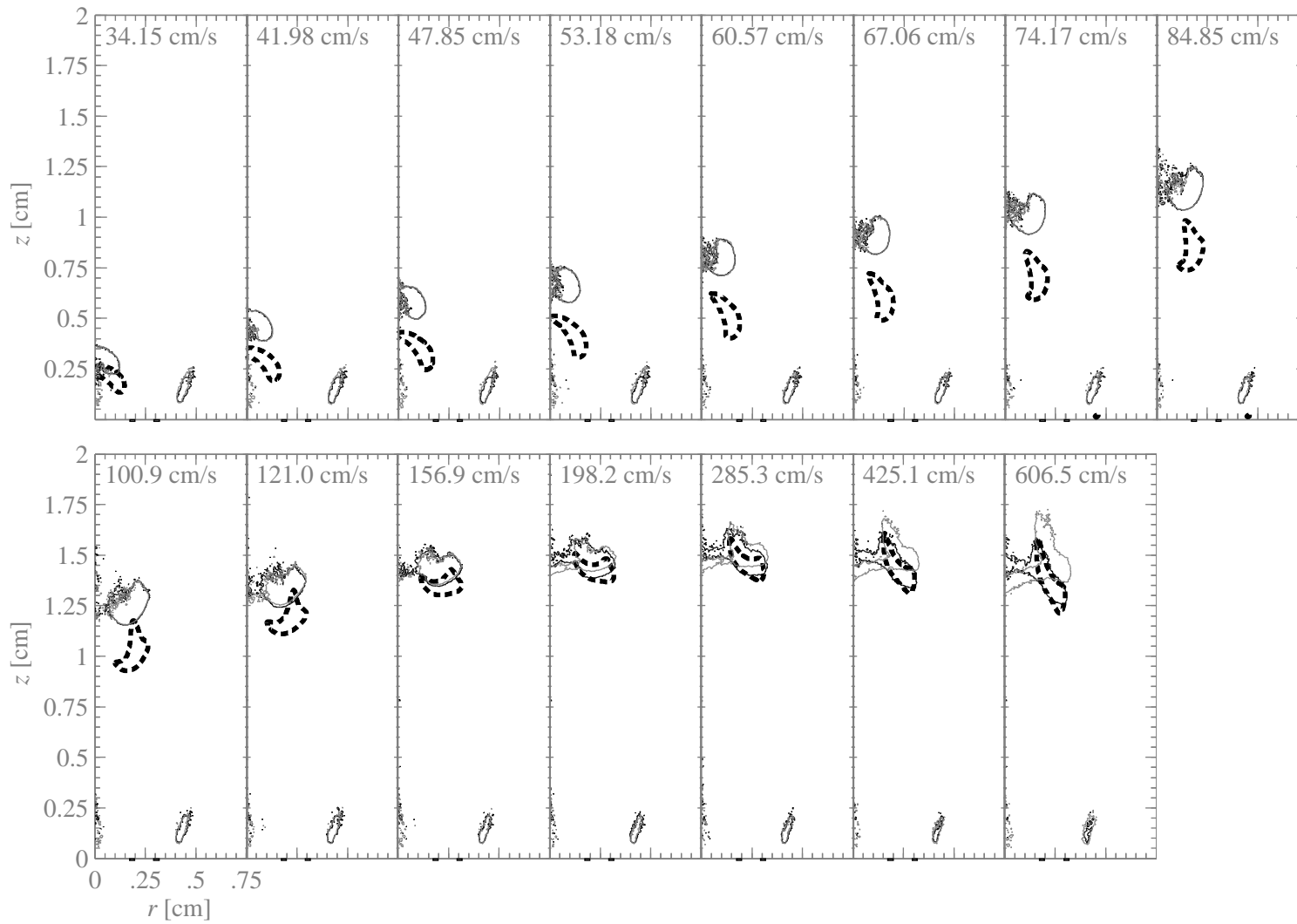


Figure C.19: $\Phi = 1.0$ co-flow, $u_{cf}=23.0$ cm/s, air tube flush.

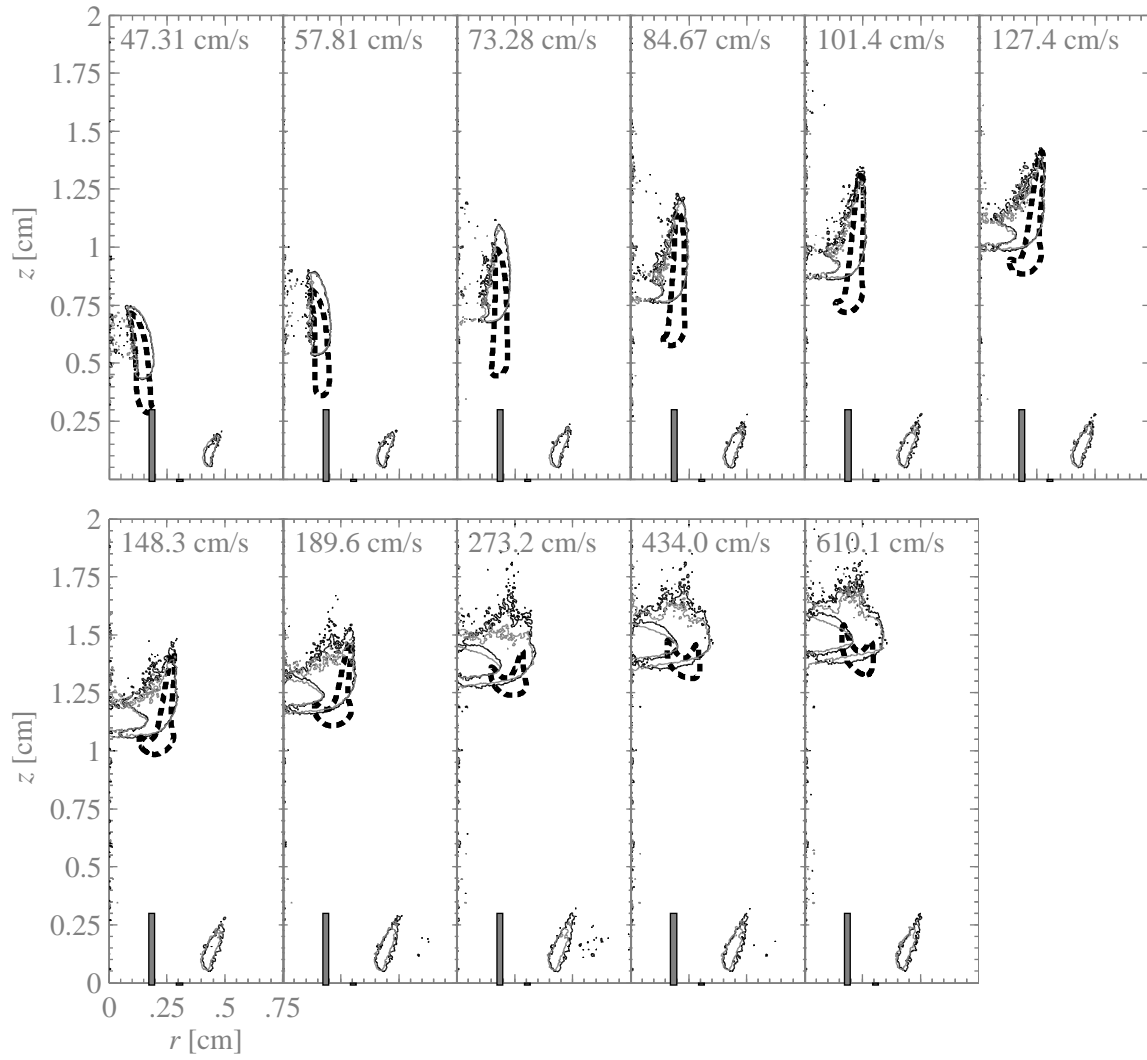


Figure C.20: $\Phi = 1.0$ co-flow, $u_{cf}=23.0$ cm/s, air tube raised 3mm.

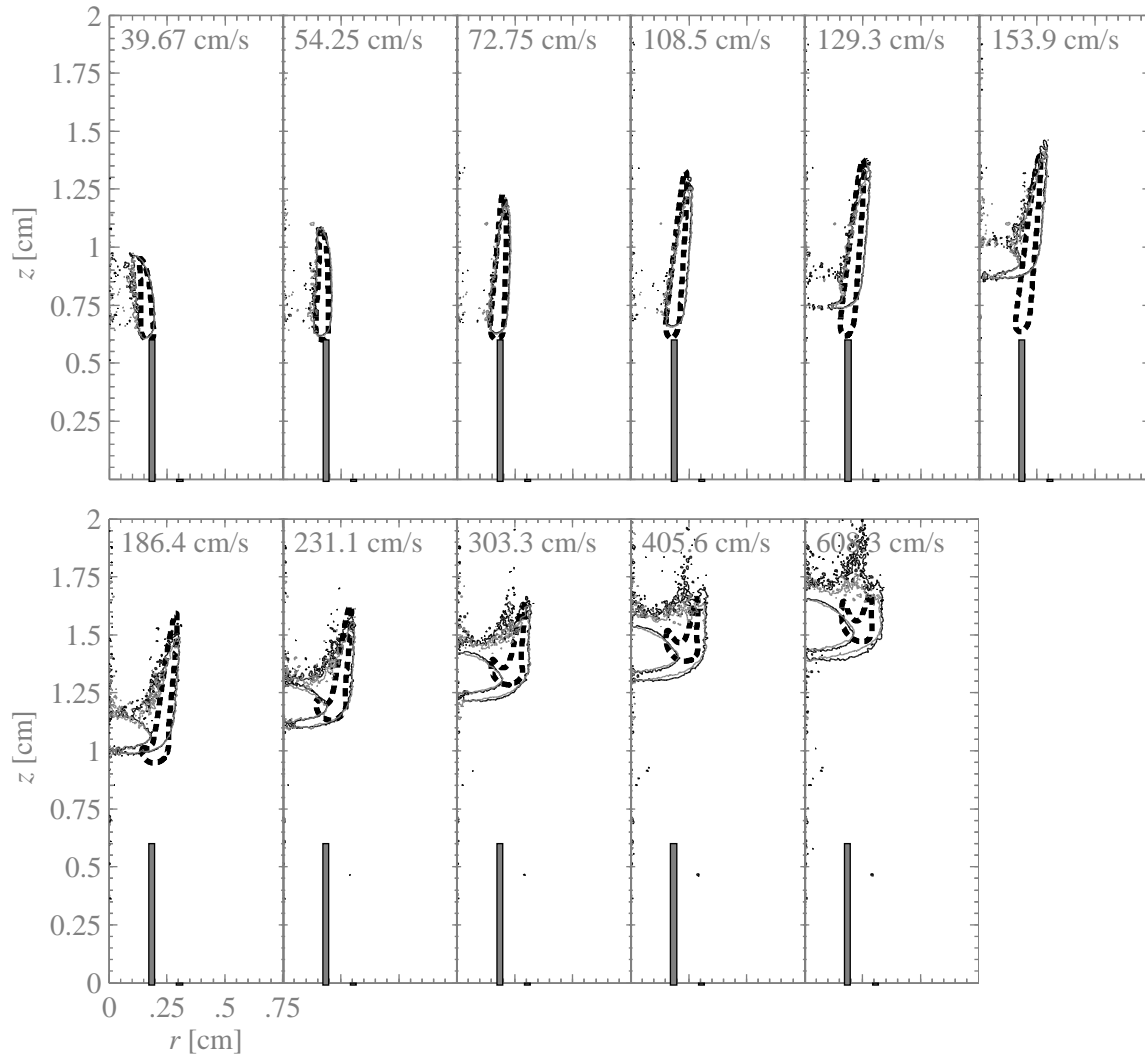


Figure C.21: $\Phi = 1.0$ co-flow, $u_{cf}=23.0$ cm/s, air tube raised 6mm.

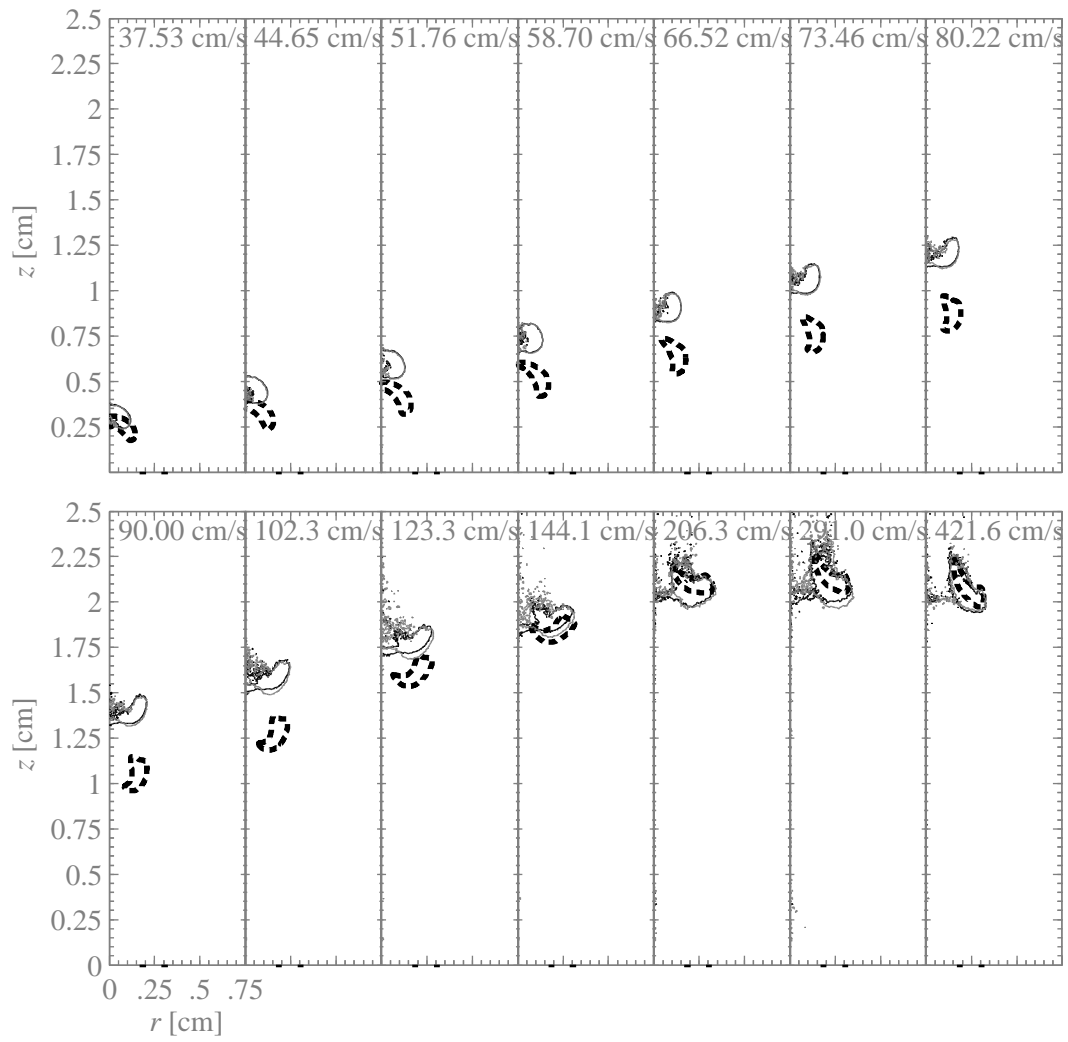


Figure C.22: $\Phi = 1.2$ co-flow, $u_{cf}=23.0$ cm/s, air tube flush.

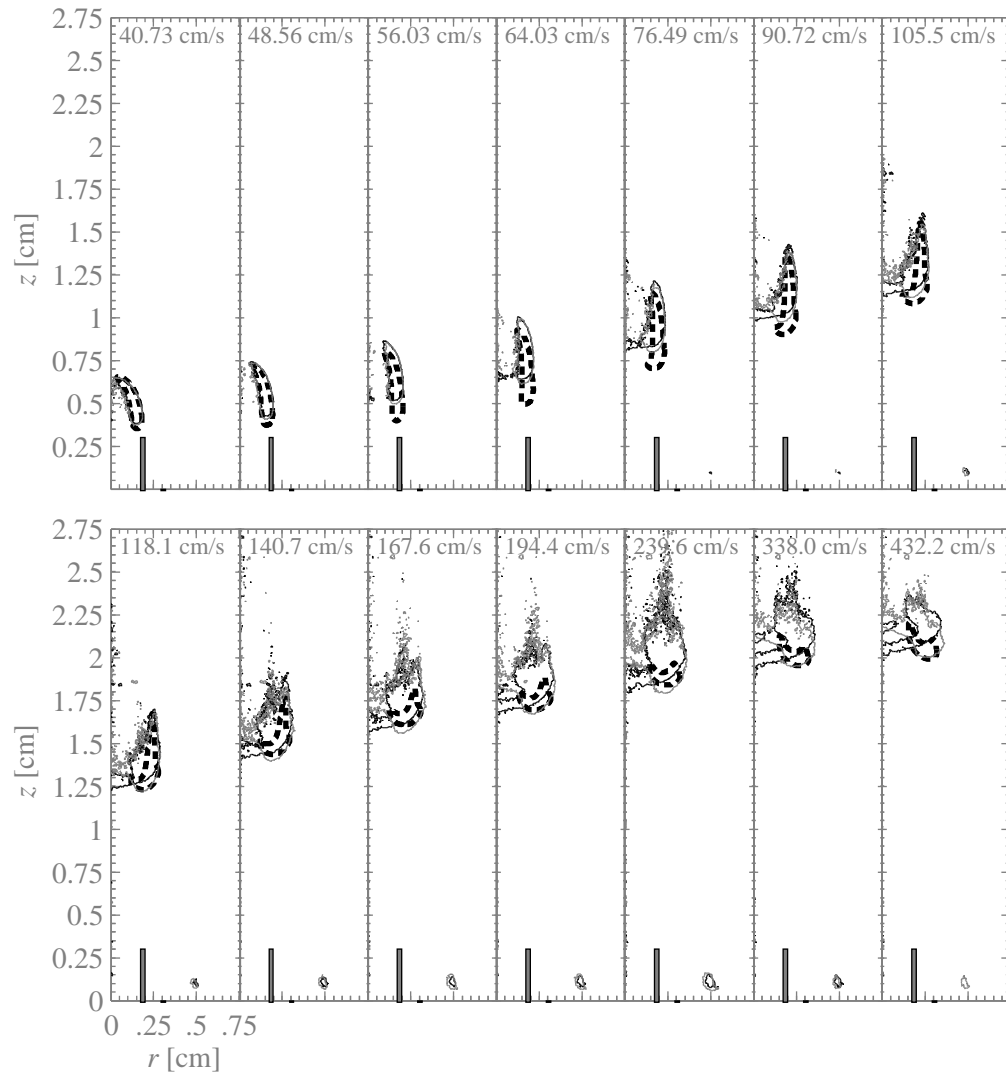


Figure C.23: $\Phi = 1.2$ co-flow, $u_{cf}=23.0$ cm/s, air tube raised 3 mm.

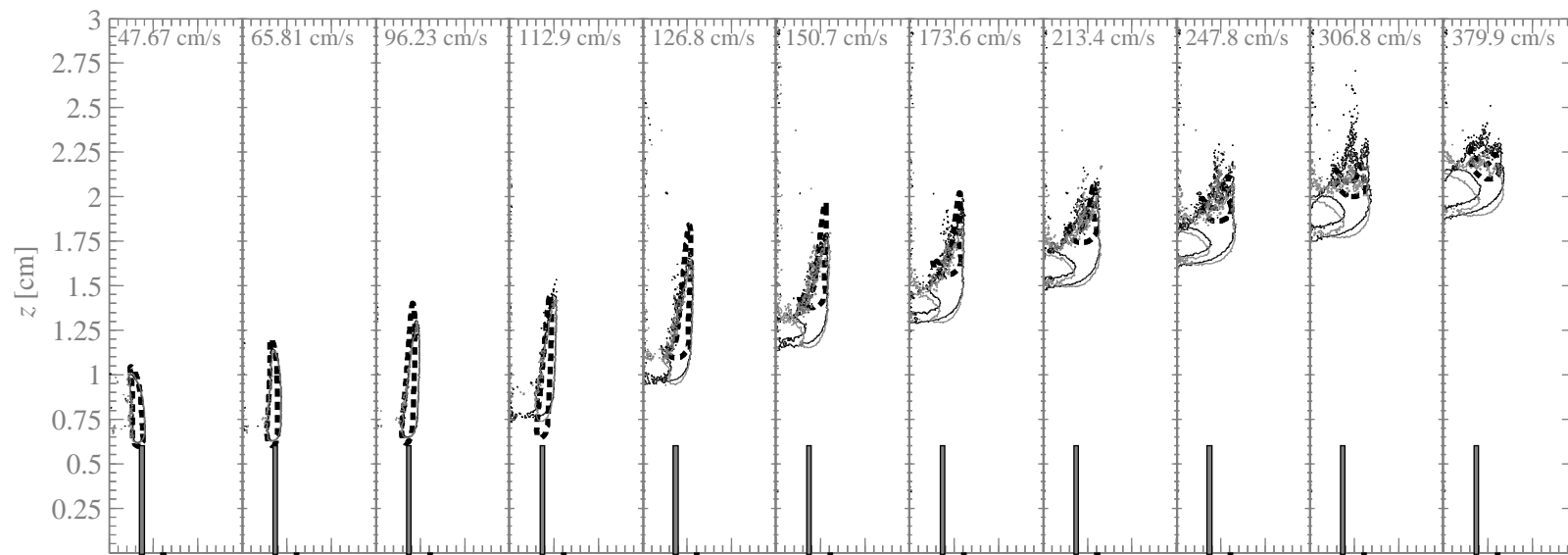


Figure C.24: $\Phi = 1.2$ co-flow, $u_{cf}=23.0$ cm/s, air tube raised 6 mm.

Appendix D

Numerical simulation analysis

D.1 Radial plots of species and temperature

This appendix includes the full selection of radial species and temperature plots for the $\Phi = 1.0$, and $\Phi = 1.2$ co-flows.

Figures D.1–D.3 show the radial distribution of temperature, CH_4 , O_2 , and CO_2 at two different heights, with $\Phi = 1.0$ co-flow and central air tube flush. Characteristics of these flames are similar to those with the $\Phi = 0.78$ co-flow, but the outer diffusion flame is very weak, as there is very little oxygen in the co-flow. For $u_{\text{ca}} = 54.61$ cm/s, central fuel and air near the centreline are consumed through the inner flame, leaving a pocket of fuel and air around $r \sim 0.3$ cm. For $u_{\text{ca}} = 145.7$ cm/s, central air and fuel at $r \sim 0.25$ cm are consumed through the lifted inner flame with a small pocket of unburned fuel near the centreline. For $u_{\text{ca}} = 611.9$ cm/s, central air and fuel at $r \sim 0.25$ cm again consumed through the lifted inner flame with a small pocket of unburned fuel, now away from the centreline at $r \sim 0.15$ cm.

Figures D.4–D.6 show the radial distribution of temperature, CH_4 , O_2 , and CO_2 at two different heights, with $\Phi = 1.0$ co-flow and central air tube raised 6 mm. For $u_{\text{ca}} = 105.8$ cm/s, the inner flame is attached to the lip of the central air tube and most of the central fuel is consumed in the inner flame up to $z = 1.25$ cm. For $u_{\text{ca}} = 272.3$ cm/s, the flame lifts off the central air tube, and shows the characteristic premixed base and attached diffusion flame. The central fuel and air at $r \sim 0.25$ cm are consumed through the premixed flame, with some remaining fuel at $z = 1.25$ cm reacting in the attached diffusion flame. For $u_{\text{ca}} = 446.5$ cm/s, the attached diffusion flame has shortened. Central fuel and air at $r \sim 0.25$ cm are again consumed through the lifted premixed flame, with a small pocket of fuel entrained into the central air jet at $r \sim 0.2$ cm, and a small amount of fuel reacting in the attached diffusion flame.

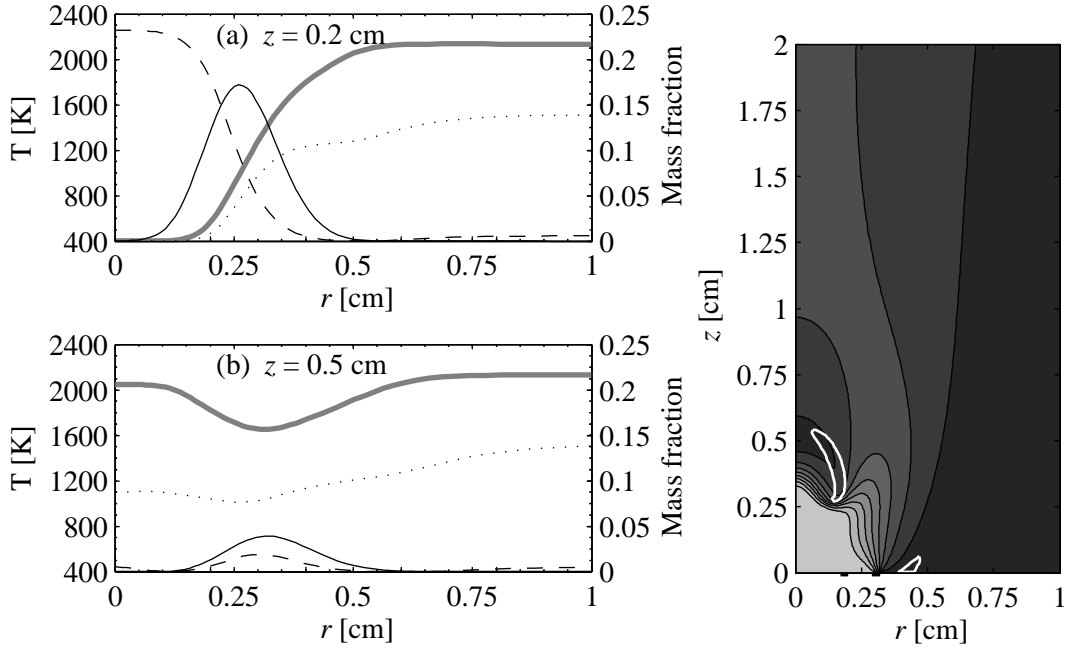


Figure D.1: Radial profiles of species (solid: CH_4 , dashed: O_2 , dotted: CO_2) and temperature (thick grey line) for $\Phi = 1.0$ co-flow, central air tube flush, $u_{cf} = 18.4$ cm/s, and $u_{ca} = 54.61$ cm/s. On the right is a contour of temperature (lightest shade of grey is 400 K, increasing by 200 K each contour line) and 10% of the maximum CH mass fraction in white.

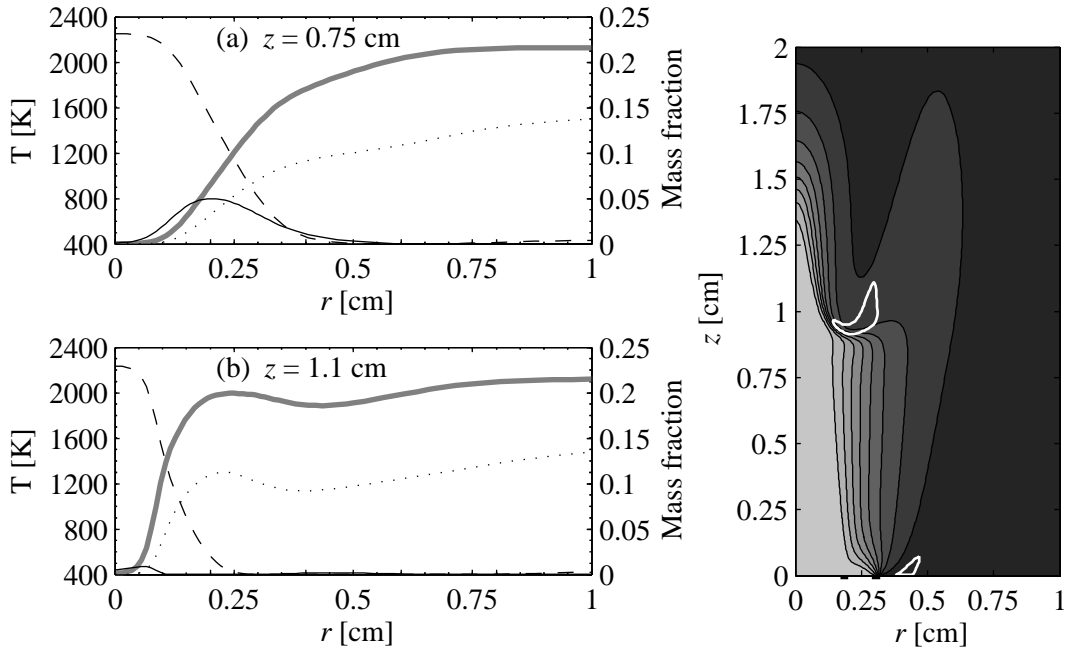


Figure D.2: Radial profiles of species and temperature, and contour plot of temperature and CH for $\Phi = 1.0$ co-flow, central air tube flush, $u_{cf} = 18.4$ cm/s, and $u_{ca} = 145.7$ cm/s (legend as in Fig. D.1).

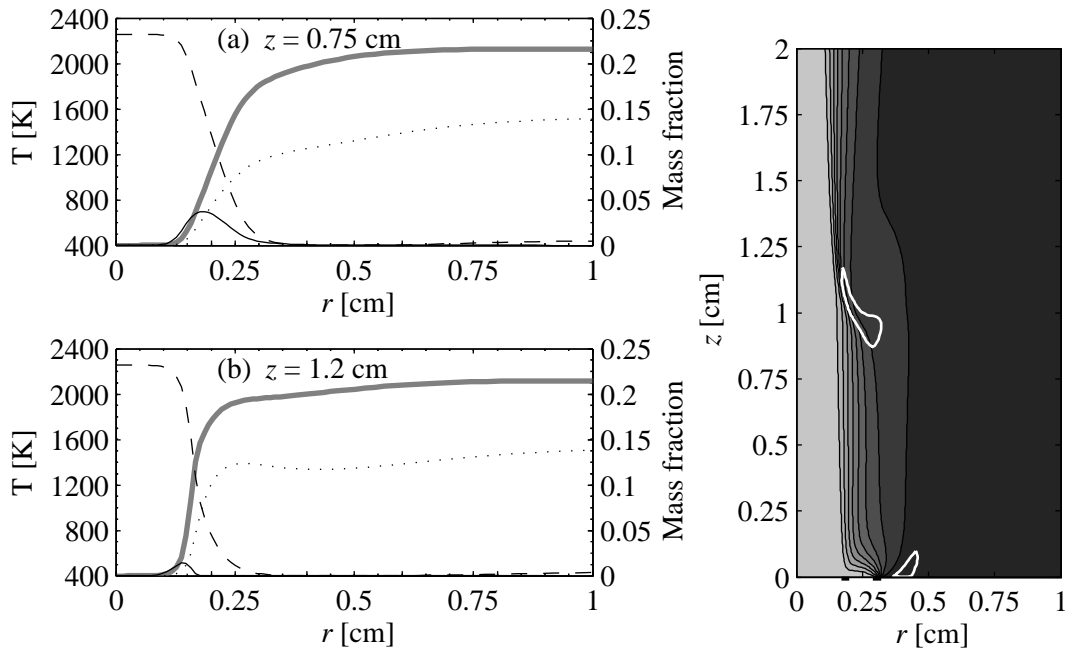


Figure D.3: Radial profiles of species and temperature, and contour plot of temperature and CH for $\Phi = 1.0$ co-flow, central air tube flush, $u_{cf} = 18.4$ cm/s, and $u_{ca} = 611.9$ cm/s (legend as in Fig. D.1).

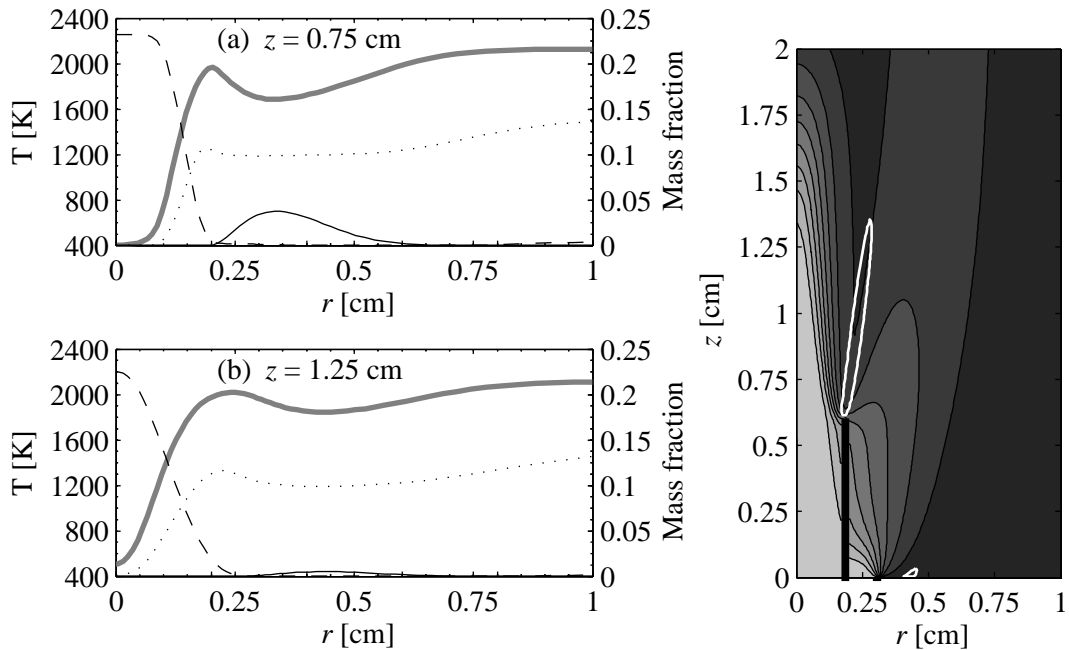


Figure D.4: Radial profiles of species and temperature, and contour plot of temperature and CH for $\Phi = 1.0$ co-flow, central air tube raised 6 mm, $u_{cf} = 18.4$ cm/s, and $u_{ca} = 105.8$ cm/s (legend as in Fig. D.1).

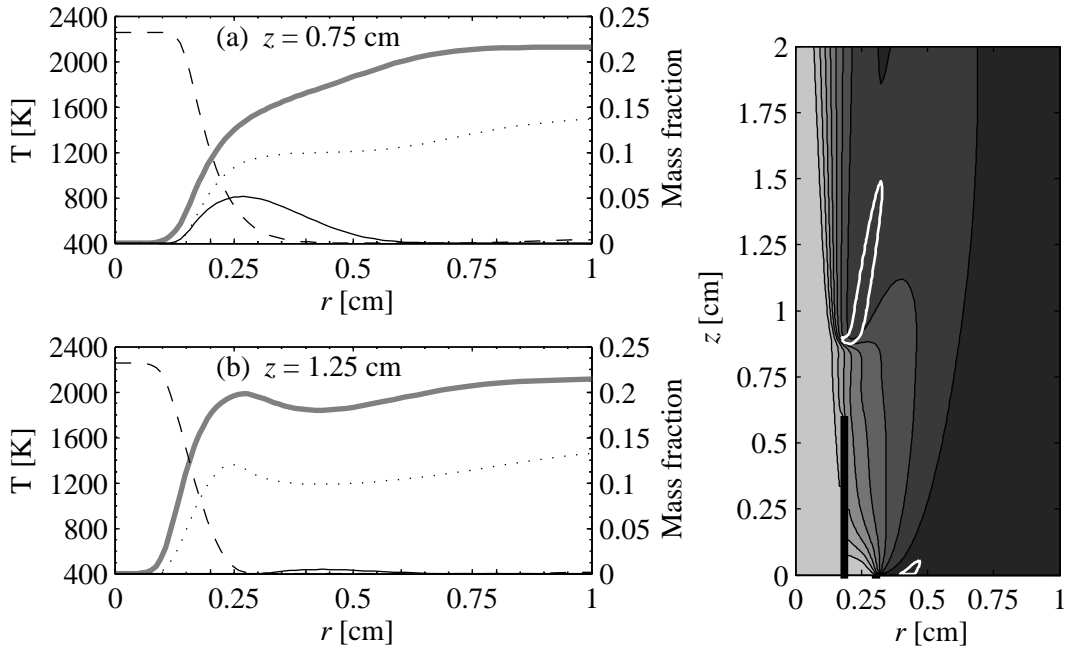


Figure D.5: Radial profiles of species and temperature, and contour plot of temperature and CH for $\Phi = 1.0$ co-flow, central air tube raised 6 mm, $u_{cf} = 18.4$ cm/s, and $u_{ca} = 272.3$ cm/s (legend as in Fig. D.1).

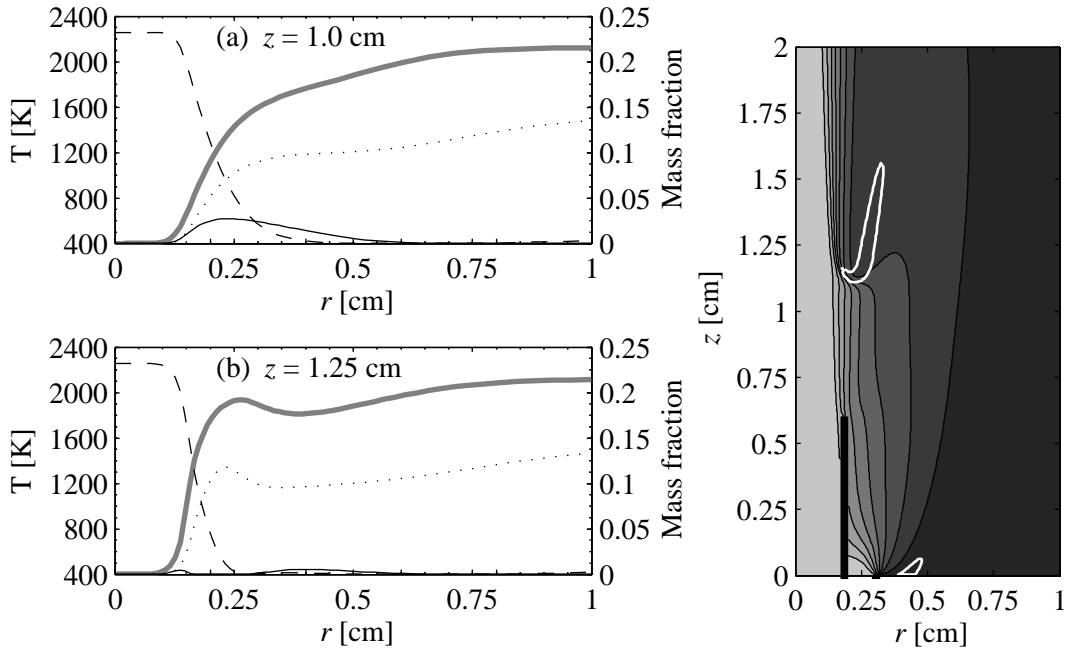


Figure D.6: Radial profiles of species and temperature, and contour plot of temperature and CH for $\Phi = 1.0$ co-flow, central air tube raised 6 mm, $u_{cf} = 18.4$ cm/s, and $u_{ca} = 446.5$ cm/s (legend as in Fig. D.1).

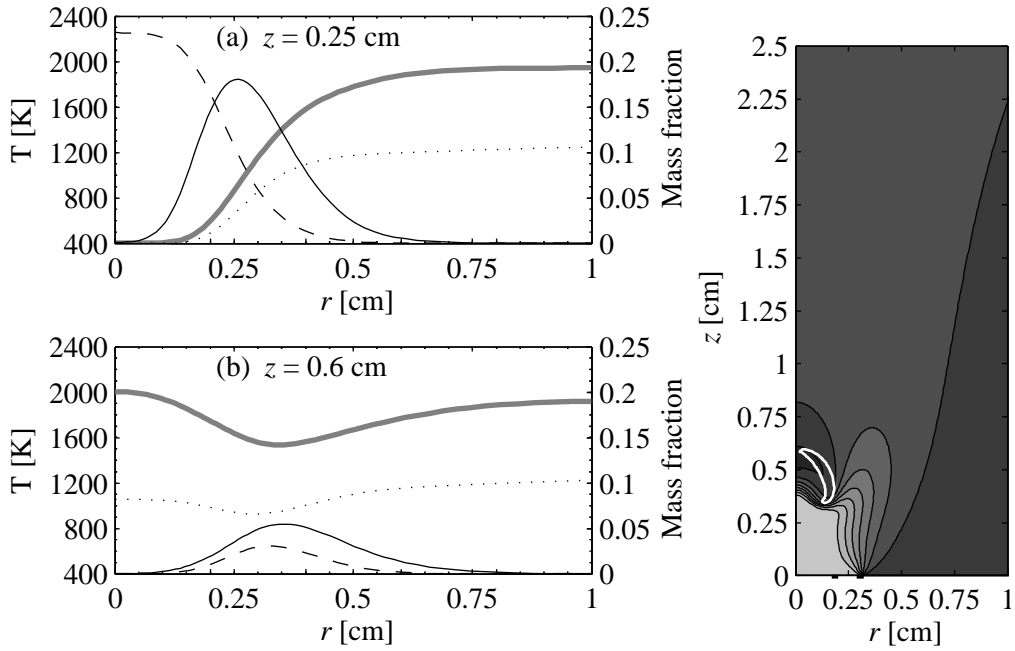


Figure D.7: Radial profiles of species and temperature, and contour plot of temperature and CH for $\Phi = 1.2$ co-flow, central air tube flush, $u_{cf} = 18.4$ cm/s, and $u_{ca} = 57.27$ cm/s (legend as in Fig. D.1).

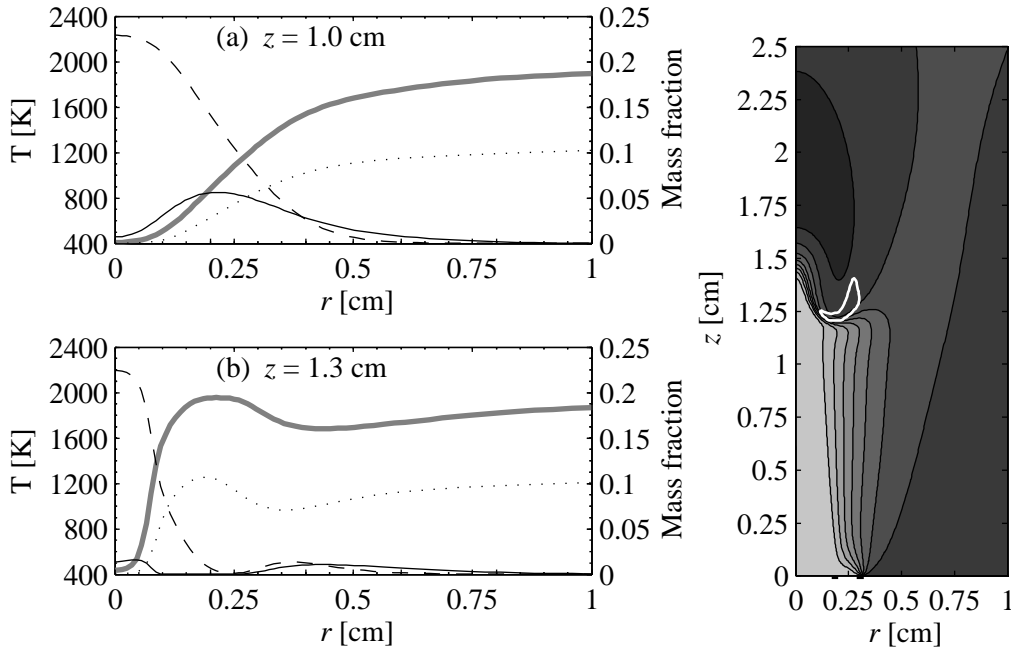


Figure D.8: Radial profiles of species and temperature, and contour plot of temperature and CH for $\Phi = 1.2$ co-flow, central air tube flush, $u_{cf} = 18.4$ cm/s, and $u_{ca} = 127.9$ cm/s (legend as in Fig. D.1).

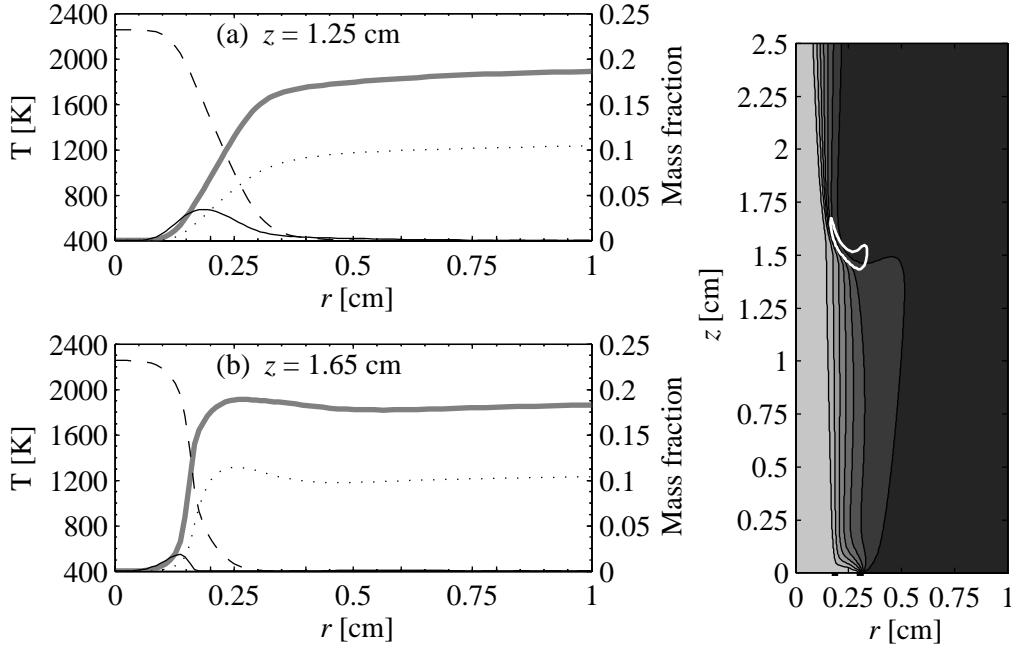


Figure D.9: Radial profiles of species and temperature, and contour plot of temperature and CH for $\Phi = 1.2$ co-flow, central air tube flush, $u_{cf} = 18.4$ cm/s, and $u_{ca} = 434.0$ cm/s (legend as in Fig. D.1).

Figures D.7–D.9 show the radial distribution of temperature, CH_4 , O_2 , and CO_2 at two different heights, with $\Phi = 1.2$ co-flow and central air tube flush. Characteristics of these flames are similar to those with the $\Phi = 0.78$ and $\Phi = 1.0$ co-flow, but the outer diffusion flame is no longer present, as there is no oxygen in the co-flow. For $u_{ca} = 57.27$ cm/s, central fuel and air near the centreline are consumed through the inner flame, leaving a pocket of fuel and air around $r \sim 0.3$ cm. For $u_{ca} = 127.9$ cm/s, central fuel and air at $r \sim 0.2$ cm are consumed in the lifted flame, leaving some unburned fuel entrained into the central air jet near the centreline, and some central fuel and air reacting in a weak diffusion flame with additional central air at $r \sim 0.25$ cm. For $u_{ca} = 434.0$ cm/s, central fuel and air at $r \sim 0.2$ cm are consumed through the lifted flame, leaving some unburned fuel entrained into the central air jet at $r \sim 0.15$ cm.

Figures D.10–D.12 show the radial distribution of temperature, CH_4 , O_2 , and CO_2 at two different heights, with $\Phi = 1.2$ co-flow and central air tube raised 6 mm. For $u_{ca} = 109.2$ cm/s, the inner flame is attached to the central air tube, and at $z = 1.25$ cm there is a broad region of unburned fuel centred at $r \sim 0.5$ cm. For $u_{ca} = 193.7$ cm/s, the flame has lifted off the central air tube, and central fuel and air at $r \sim 0.25$ cm are consumed through the premixed base. There is a small pocket of

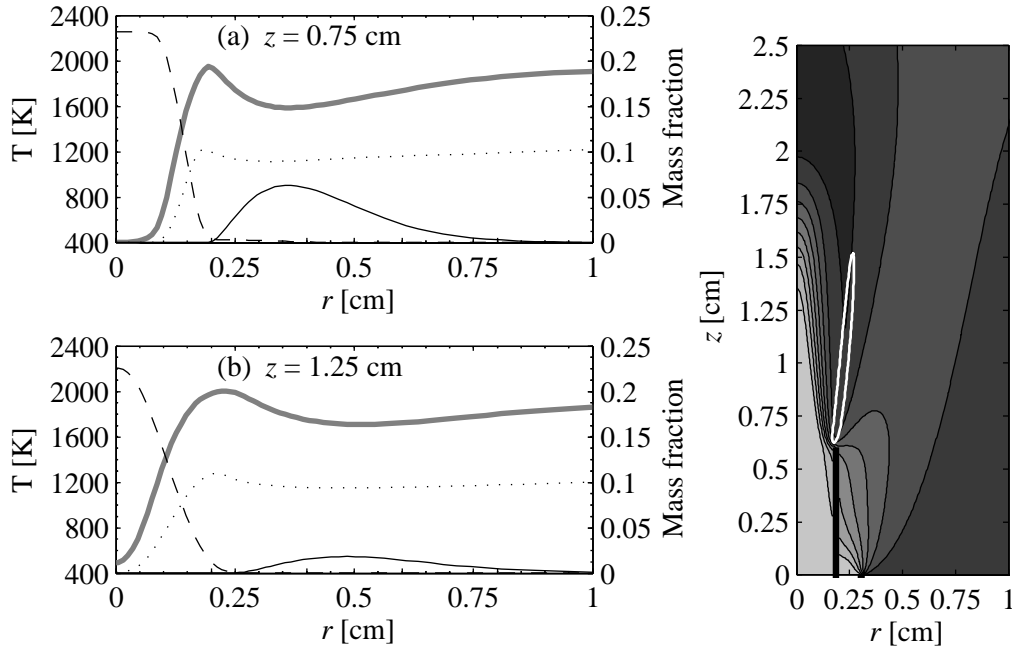


Figure D.10: Radial profiles of species and temperature, and contour plot of temperature and CH for $\Phi = 1.2$ co-flow, central air tube raised 6 mm, $u_{cf} = 18.4$ cm/s, and $u_{ca} = 109.2$ cm/s (legend as in Fig. D.1).

fuel entrained into the central air jet at $r \sim 0.15$ cm, and the remainder of the central fuel is reacting in the attached diffusion flame at $r \sim 0.25$ cm. For $u_{ca} = 383.1$ cm/s, the attached diffusion flame is much shorter, and downstream of the premixed flame is a small pocket of fuel entrained into the central air jet at $r \sim 0.15$ cm.

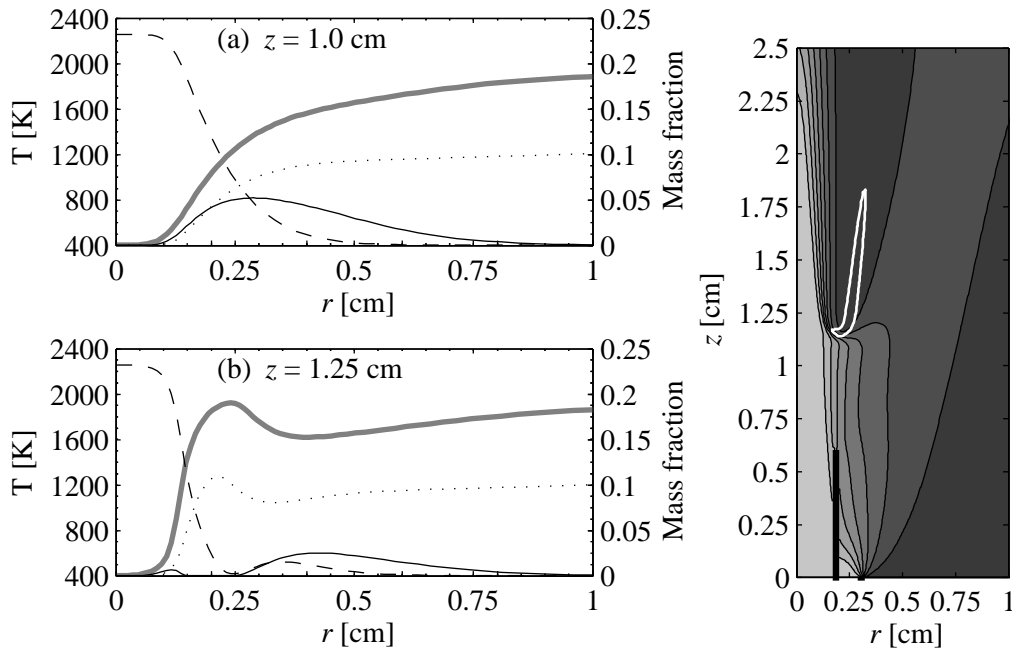


Figure D.11: Radial profiles of species and temperature, and contour plot of temperature and CH for $\Phi = 1.2$ co-flow, central air tube raised 6 mm, $u_{cf} = 18.4$ cm/s, and $u_{ca} = 193.7$ cm/s (legend as in Fig. D.1).

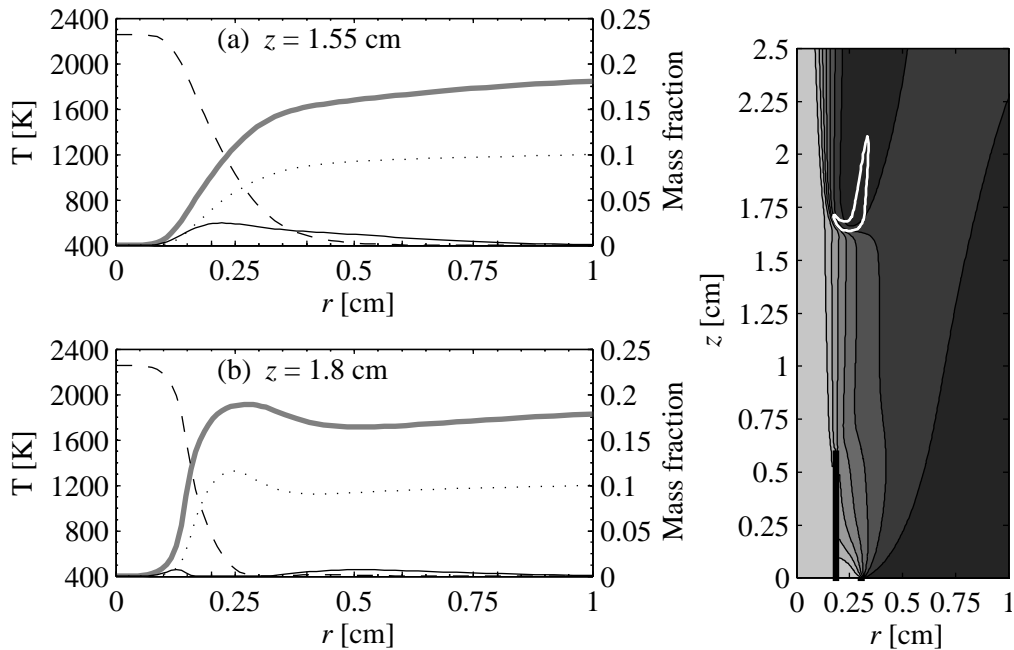


Figure D.12: Radial profiles of species and temperature, and contour plot of temperature and CH for $\Phi = 1.2$ co-flow, central air tube raised 6 mm, $u_{cf} = 18.4$ cm/s, and $u_{ca} = 383.1$ cm/s (legend as in Fig. D.1).

Appendix E

Experiment and simulation matrix

Included in this appendix are tables listing all flames analyzed in this work, and the flow conditions associated with them.

Table E.1: Matrix of experimental conditions for air co-flow and flush central air tube.

exp#	sim#	u_{cf} [cm/s]	u_{ca} [cm/s]	exp#	sim#	u_{cf} [cm/s]	u_{ca} [cm/s]
936		8.523	17.25	973	58	18.43	227.9
937		8.523	20.81	974	59	18.43	321.4
938		8.523	26.15	975	60	18.43	506.9
939		8.523	32.91	976	61	18.43	686.6
940		8.523	42.87	977	62	18.43	864.5
941		8.523	55.32	978	63	18.43	958.7
942		8.523	65.81	979		18.43	1462
943		8.523	82.18	980	220	23.27	49.45
944		8.523	100.9	981	221	23.27	57.45
945		8.523	133.0	982	222	23.27	64.03
946		8.523	191.9	983	223	23.27	71.15
947		8.523	292.6	984	224	23.27	80.75
948		8.523	464.2	985	225	23.27	94.98
949		8.523	649.2	986	226	23.27	124.9
950		8.523	827.1	987	227	23.27	190.5
951		8.523	1009	988	228	23.27	254.9
952		13.82	32.19	989	229	23.27	325.7
953		13.82	39.13	990	230	23.27	412.7
954		13.82	46.96	991	231	23.27	603.0
955		13.82	57.63	992	232	23.27	777.3
956		13.82	70.26	993	233	23.27	962.3
957		13.82	89.83	994		23.27	1466
958		13.82	115.1	995		27.64	62.61
959		13.82	170.9	996		27.64	69.01
960		13.82	264.0	997		27.64	76.31
961		13.82	441.1	998		27.64	83.78
962		13.82	620.8	999		27.64	93.03
963		13.82	802.2	1000		27.64	108.1
964		13.82	983.6	1001		27.64	126.8
965		13.82	1475	1002		27.64	160.3
966	40	18.43	37.71	1003		27.64	214.3
967	51	18.43	45.71	1004		27.64	288.2
968	53	18.43	54.43	1005		27.64	396.7
969	54	18.43	62.79	1006		27.64	581.6
970	55	18.43	74.35	1007		27.64	759.5
971	56	18.43	89.11	1008		27.64	976.5
972	57	18.43	138.7	1009		27.64	1464

Table E.2: Matrix of experimental conditions for air co-flow and central air tube raised 3 mm.

exp#	sim#	u_{cf} [cm/s]	u_{ca} [cm/s]	exp#	sim#	u_{cf} [cm/s]	u_{ca} [cm/s]
1113		13.82	18.32	1148	324	23.04	27.21
1114		13.82	25.61	1149	325	23.04	34.69
1115		13.82	32.73	1150	326	23.04	41.98
1116		13.82	41.62	1151	327	23.04	50.52
1117		13.82	58.16	1152	328	23.04	64.21
1118		13.82	92.85	1153	329	23.04	81.47
1119		13.82	158.0	1154	330	23.04	96.76
1120		13.82	241.6	1155	331	23.04	117.8
1121		13.82	425.1	1156	332	23.04	148.0
1122		13.82	606.5	1157	333	23.04	195.7
1123		13.82	775.5	1158	334	23.04	297.6
1124		13.82	949.8	1159	335	23.04	421.6
1125		13.82	1133	1160	336	23.04	595.9
1126		13.82	1311	1161	337	23.04	777.3
1127		13.82	1466	1162	338	23.04	957.0
1128		13.82	1676	1163		23.04	1464
1129		13.82	1853	1164		23.04	1656
1130	116	18.43	25.44	1165		23.04	1839
1131	117	18.43	32.02	1166		27.64	25.61
1132	118	18.43	39.67	1167		27.64	31.84
1133	119	18.43	50.87	1168		27.64	39.13
1134	120	18.43	71.33	1169		27.64	46.78
1135	121	18.43	92.85	1170		27.64	55.50
1136	122	18.43	127.5	1171		27.64	65.46
1137	123	18.43	188.5	1172		27.64	74.71
1138	124	18.43	271.8	1173		27.64	88.22
1139	125	18.43	441.1	1174		27.64	107.1
1140	126	18.43	610.1	1175		27.64	131.3
1141	127	18.43	775.5	1176		27.64	167.4
1142	128	18.43	953.4	1177		27.64	247.8
1143		18.43	1327	1178		27.64	421.6
1144		18.43	1469	1179		27.64	599.4
1145		18.43	1679	1180		27.64	782.6
1146		18.43	1859	1181		27.64	948.1
				1182		27.64	1466
				1183		27.64	1663
				1184		27.64	1841

Table E.3: Matrix of experimental conditions for air co-flow and central air tube raised 6 mm.

exp#	sim#	u_{cf} [cm/s]	u_{ca} [cm/s]	exp#	sim#	u_{cf} [cm/s]	u_{ca} [cm/s]
1440	208	18.43	15.65	1466	399	23.04	358.1
1441	209	18.43	25.61	1467	400	23.04	546.1
1442	210	18.43	43.05	1468	401	23.04	748.8
1443	211	18.43	78.98	1469	402	23.04	928.5
1444	212	18.43	171.1	1470		23.04	1286
1445	213	18.43	239.6	1471		23.04	1469
1446	214	18.43	311.6	1472		23.04	1647
1447	215	18.43	384.2	1473		23.04	1821
1448	216	18.43	572.7	1474		27.64	26.15
1449	217	18.43	754.2	1475		27.64	36.11
1450	218	18.43	933.8	1476		27.64	46.96
1451	219	18.43	1110	1477		27.64	60.30
1452		18.43	1290	1478		27.64	78.98
1453		18.43	1469	1479		27.64	97.12
1454		18.43	1645	1480		27.64	107.8
1455		18.43	1821	1481		27.64	124.7
1456	389	23.04	27.21	1482		27.64	146.9
1457	390	23.04	37.35	1483		27.64	188.7
1458	391	23.04	51.41	1484		27.64	247.1
1459	392	23.04	82.53	1485		27.64	351.7
1460	393	23.04	116.5	1486		27.64	556.7
1461	394	23.04	140.7	1487		27.64	754.2
1462	395	23.04	155.5	1488		27.64	935.6
1463	396	23.04	183.9	1489		27.64	1467
1464	397	23.04	218.1	1490		27.64	1645
1465	398	23.04	273.0	1491		27.64	1825

Table E.4: Matrix of experimental conditions for $\Phi = 0.78$ co-flow and flush central air tube.

exp#	sim#	u_{cf} [cm/s]	u_{ca} [cm/s]	exp#	sim#	u_{cf} [cm/s]	u_{ca} [cm/s]
1010		8.523	52.47	1047	111	18.43	444.7
1011		8.523	60.48	1048	112	18.43	613.7
1012		8.523	74.71	1049	113	18.43	800.4
1013		8.523	95.70	1050	114	18.43	990.8
1014		8.523	125.4	1051		18.43	1466
1015		8.523	175.9	1052		18.43	1466
1016		8.523	269.7	1053	234	23.04	48.91
1017		8.523	446.5	1054	235	23.04	57.81
1018		8.523	633.2	1055	236	23.04	66.70
1019		8.523	811.1	1056	237	23.04	75.60
1020		8.523	989.0	1057	238	23.04	85.73
1021		8.523	1467	1058	239	23.04	94.81
1022		13.82	32.73	1059	240	23.04	108.3
1023		13.82	43.93	1060	241	23.04	134.5
1024		13.82	53.90	1061	242	23.04	193.9
1025		13.82	62.79	1062	243	23.04	275.7
1026		13.82	71.50	1063	244	23.04	455.4
1027		13.82	86.98	1064	245	23.04	627.9
1028		13.82	115.8	1065	246	23.04	809.3
1029		13.82	174.5	1066	247	23.04	989.0
1030		13.82	266.1	1067		23.04	1460
1031		13.82	437.6	1068		23.04	1466
1032		13.82	615.4	1069		27.64	80.40
1033		13.82	793.3	1070		27.64	86.62
1034		13.82	967.6	1071		27.64	93.38
1035		13.82	1467	1072		27.64	102.3
1036	100	18.43	35.40	1073		27.64	112.8
1037	101	18.43	41.62	1074		27.64	130.6
1038	102	18.43	48.20	1075		27.64	166.1
1039	103	18.43	54.43	1076		27.64	228.7
1040	104	18.43	64.03	1077		27.64	302.9
1041	105	18.43	73.64	1078		27.64	428.7
1042	106	18.43	86.62	1079		27.64	572.7
1043	107	18.43	108.1	1080		27.64	757.7
1044	108	18.43	137.7	1081		27.64	958.7
1045	109	18.43	210.2	1082		27.64	1469
1046	110	18.43	314.8	1083		27.64	1475

Table E.5: Matrix of experimental conditions for $\Phi = 0.78$ co-flow and central air tube raised 3 mm.

exp#	sim#	u_{cf} [cm/s]	u_{ca} [cm/s]	exp#	sim#	u_{cf} [cm/s]	u_{ca} [cm/s]
1185		8.523	11.74	1217	151	18.43	25.97
1186		8.523	18.14	1218	152	18.43	33.80
1187		8.523	25.44	1219	153	18.43	46.78
1188		8.523	34.33	1220	154	18.43	58.16
1189		8.523	51.05	1221	155	18.43	73.11
1190		8.523	151.5	1222	156	18.43	84.13
1191		8.523	276.2	1223	157	18.43	103.2
1192		8.523	451.8	1224	158	18.43	138.9
1193		8.523	633.2	1225	159	18.43	174.3
1194		8.523	816.4	1226	160	18.43	233.0
1195		8.523	989.0	1227	161	18.43	326.6
1196		8.523	1172	1228	162	18.43	474.9
1197		8.523	1345	1229	163	18.43	651.0
1198		8.523	1485	1230	164	18.43	828.9
1199		8.523	1663	1231	165	18.43	1003
1200		8.523	1843	1232		18.43	1475
1201		13.82	22.23	1233		18.43	1661
1202		13.82	30.42	1234		18.43	1845
1203		13.82	42.51				
1204		13.82	60.65				
1205		13.82	97.65				
1206		13.82	122.2				
1207		13.82	160.1				
1208		13.82	256.5				
1209		13.82	366.4				
1210		13.82	469.6				
1211		13.82	645.7				
1212		13.82	823.6				
1213		13.82	1001				
1214		13.82	1471				
1215		13.82	1654				
1216		13.82	1834				

Table E.5 (cont.): Matrix of experimental conditions for $\Phi = 0.78$ co-flow and central air tube raised 3 mm.

exp#	sim#	u_{cf} [cm/s]	u_{ca} [cm/s]	exp#	sim#	u_{cf} [cm/s]	u_{ca} [cm/s]
1235	339	23.04	30.24	1255		27.64	28.10
1236	340	23.04	43.05	1256		27.64	36.64
1237	341	23.04	51.23	1257		27.64	45.89
1238	342	23.04	57.10	1258		27.64	55.50
1239	343	23.04	66.52	1259		27.64	64.92
1240	344	23.04	77.20	1260		27.64	74.53
1241	345	23.04	89.11	1261		27.64	85.02
1242	346	23.04	102.5	1262		27.64	95.16
1243	347	23.04	124.7	1263		27.64	111.0
1244	348	23.04	148.0	1264		27.64	133.0
1245	349	23.04	172.9	1265		27.64	164.0
1246	350	23.04	209.5	1266		27.64	223.4
1247	351	23.04	290.3	1267		27.64	405.5
1248	352	23.04	412.7	1268		27.64	585.2
1249	353	23.04	588.8	1269		27.64	763.1
1250	354	23.04	772.0	1270		27.64	948.1
1251	355	23.04	944.5	1271		27.64	1469
1252		23.04	1485	1272		27.64	1665
1253		23.04	1660	1273		27.64	1836
1254		23.04	1845				

Table E.6: Matrix of experimental conditions for $\Phi = 0.78$ co-flow and central air tube raised 6 mm.

exp#	sim#	u_{cf} [cm/s]	u_{ca} [cm/s]	exp#	sim#	u_{cf} [cm/s]	u_{ca} [cm/s]
1492		13.82	23.12	1527	403	23.04	30.42
1493		13.82	38.78	1528	404	23.04	50.87
1494		13.82	58.88	1529	405	23.04	80.04
1495		13.82	94.81	1530	406	23.04	103.3
1496		13.82	128.8	1531	407	23.04	112.6
1497		13.82	165.1	1532	408	23.04	128.1
1498		13.82	199.2	1533	409	23.04	146.6
1499		13.82	239.2	1534	410	23.04	166.5
1500		13.82	296.7	1535	411	23.04	205.3
1501		13.82	349.7	1536	412	23.04	249.9
1502		13.82	435.8	1537	413	23.04	332.4
1503		13.82	597.7	1538	414	23.04	412.7
1504		13.82	754.2	1539	415	23.04	581.6
1505		13.82	937.4	1540	416	23.04	761.3
1506		13.82	1466	1541	417	23.04	944.5
1507		13.82	1647	1542		23.04	1475
1508		13.82	1827	1543		23.04	1656
1509	248	18.43	21.34	1544		23.04	1836
1510	249	18.43	40.02	1545		27.64	28.46
1511	250	18.43	57.27	1546		27.64	44.29
1512	251	18.43	85.91	1547		27.64	57.81
1513	252	18.43	116.7	1548		27.64	74.71
1514	253	18.43	150.5	1549		27.64	80.04
1515	254	18.43	174.5	1550		27.64	88.76
1516	255	18.43	200.8	1551		27.64	98.01
1517	256	18.43	240.0	1552		27.64	111.3
1518	257	18.43	298.6	1553		27.64	128.8
1519	258	18.43	369.8	1554		27.64	154.4
1520	259	18.43	450.0	1555		27.64	185.2
1521	260	18.43	569.2	1556		27.64	228.4
1522	261	18.43	770.2	1557		27.64	313.6
1523	262	18.43	940.9	1558		27.64	410.9
1524		18.43	1466	1559		27.64	594.1
1525		18.43	1647	1560		27.64	775.5
1526		18.43	1830	1561		27.64	957.0
				1562		27.64	1476
				1563		27.64	1660
				1564		27.64	1837

Table E.7: Matrix of experimental conditions for $\Phi = 1.0$ co-flow and flush central air tube.

exp#	sim#	u_{cf} [cm/s]	u_{ca} [cm/s]	exp#	sim#	u_{cf} [cm/s]	u_{ca} [cm/s]
865		8.639	78.44	845	97	18.43	611.9
866		8.639	120.8	846	98	18.43	793.3
867		8.639	166.3	847	99	18.43	974.7
868		8.639	233.7	848		18.43	1459
869		8.639	405.5	814	290	23.27	34.15
870		8.639	594.1	815	291	23.27	41.98
871		8.639	784.4	816	292	23.27	47.85
872		8.639	969.4	817	293	23.27	53.18
873		8.639	1464	818	294	23.27	60.57
849		13.94	44.65	819	295	23.27	67.06
850		13.94	51.76	820	296	23.27	74.17
851		13.94	58.70	821	297	23.27	84.85
852		13.94	67.59	822	298	23.27	100.9
853		13.94	76.66	823	299	23.27	121.0
854		13.94	93.03	824	300	23.27	156.9
855		13.94	118.8	825	301	23.27	198.2
856		13.94	156.7	826	302	23.27	285.3
857		13.94	206.3	827	303	23.27	425.1
858		13.94	319.6	828	304	23.27	606.5
859		13.94	492.7	829	305	23.27	784.4
860		13.94	668.8	830	306	23.27	955.2
861		13.94	828.9	831		23.27	1457
862		13.94	973.0	1084		27.64	62.43
863		13.94	1464	1085		27.64	72.04
832	84	18.43	33.08	1086		27.64	79.51
833	85	18.43	40.55	1087		27.64	88.76
834	86	18.43	47.85	1088		27.64	99.25
835	87	18.43	54.61	1089		27.64	112.2
836	88	18.43	63.14	1090		27.64	135.2
837	89	18.43	72.22	1091		27.64	163.1
838	90	18.43	82.53	1092		27.64	215.2
839	91	18.43	96.05	1093		27.64	296.0
840	92	18.43	116.0	1094		27.64	437.6
841	93	18.43	145.7	1095		27.64	601.2
842	94	18.43	183.4	1096		27.64	793.3
843	95	18.43	275.3	1097		27.64	958.7
844	96	18.43	410.9	1098		27.64	1467
				1099		27.64	1473

Table E.8: Matrix of experimental conditions for $\Phi = 1.0$ co-flow and central air tube raised 3 mm.

exp#	sim#	u_{cf} [cm/s]	u_{ca} [cm/s]	exp#	sim#	u_{cf} [cm/s]	u_{ca} [cm/s]
1274		13.82	25.26	1309	356	23.04	28.28
1275		13.82	33.97	1310	357	23.04	37.89
1276		13.82	43.05	1311	358	23.04	47.31
1277		13.82	60.83	1312	359	23.04	57.81
1278		13.82	82.36	1313	360	23.04	73.28
1279		13.82	106.9	1314	361	23.04	84.67
1280		13.82	141.6	1315	362	23.04	101.4
1281		13.82	194.6	1316	363	23.04	127.4
1282		13.82	279.4	1317	364	23.04	148.3
1283		13.82	441.1	1318	365	23.04	189.6
1284		13.82	615.4	1319	366	23.04	273.2
1285		13.82	796.9	1320	367	23.04	434.0
1286		13.82	944.5	1321	368	23.04	610.1
1287		13.82	1494	1322	369	23.04	782.6
1288		13.82	1676	1323	370	23.04	958.7
1289		13.82	1855	1324		23.04	1466
1290	172	18.43	26.50	1325		23.04	1654
1291	173	18.43	36.11	1326		23.04	1837
1292	174	18.43	45.54	1327		27.64	34.15
1293	175	18.43	57.81	1328		27.64	45.00
1294	176	18.43	80.93	1329		27.64	53.36
1295	177	18.43	95.34	1330		27.64	63.86
1296	178	18.43	107.8	1331		27.64	72.75
1297	179	18.43	125.9	1332		27.64	82.71
1298	180	18.43	152.4	1333		27.64	94.09
1299	181	18.43	180.0	1334		27.64	115.1
1300	182	18.43	224.3	1335		27.64	138.7
1301	183	18.43	289.6	1336		27.64	182.0
1302	184	18.43	414.4	1337		27.64	217.7
1303	185	18.43	595.9	1338		27.64	328.9
1304	186	18.43	775.5	1339		27.64	439.3
1305	187	18.43	957.0	1340		27.64	604.8
1306		18.43	1491	1341		27.64	789.8
1307		18.43	1668	1342		27.64	949.8
1308		18.43	1843	1343		27.64	1469
				1344		27.64	1645
				1345		27.64	1832

Table E.9: Matrix of experimental conditions for $\Phi = 1.0$ co-flow and central air tube raised 6 mm.

exp#	sim#	u_{cf} [cm/s]	u_{ca} [cm/s]	exp#	sim#	u_{cf} [cm/s]	u_{ca} [cm/s]
1565		13.82	24.19	1596	418	23.04	27.04
1566		13.82	39.31	1597	419	23.04	39.67
1567		13.82	62.26	1598	420	23.04	54.25
1568		13.82	90.00	1599	421	23.04	72.75
1569		13.82	127.9	1600	422	23.04	108.5
1570		13.82	187.1	1601	423	23.04	129.3
1571		13.82	277.5	1602	424	23.04	153.9
1572		13.82	368.2	1603	425	23.04	186.4
1573		13.82	441.1	1604	426	23.04	231.1
1574		13.82	620.8	1605	427	23.04	303.3
1575		13.82	804.0	1606	428	23.04	405.5
1576		13.82	971.2	1607	429	23.04	608.3
1577		13.82	1464	1608	430	23.04	793.3
1578		13.82	1649	1609	431	23.04	969.4
1579		13.82	1830	1610		23.04	1478
1580	263	18.43	26.15	1611		23.04	1656
1581	264	18.43	40.91	1612		23.04	1835
1582	265	18.43	70.44	1613		27.64	23.83
1583	266	18.43	105.8	1614		27.64	36.46
1584	267	18.43	142.1	1615		27.64	47.85
1585	268	18.43	187.8	1616		27.64	74.35
1586	269	18.43	225.2	1617		27.64	92.85
1587	270	18.43	272.3	1618		27.64	108.1
1588	271	18.43	347.2	1619		27.64	124.7
1589	272	18.43	446.5	1620		27.64	143.7
1590	273	18.43	629.7	1621		27.64	171.3
1591	274	18.43	805.8	1622		27.64	218.2
1592	275	18.43	971.2	1623		27.64	288.2
1593		18.43	1469	1624		27.64	383.1
1594		18.43	1649	1625		27.64	579.9
1595		18.43	1832	1626		27.64	784.4
				1627		27.64	969.4
				1628		27.64	1471
				1629		27.64	1652
				1630		27.64	1836

Table E.10: Matrix of experimental conditions for $\Phi = 1.2$ co-flow and flush central air tube.

exp#	sim#	u_{cf} [cm/s]	u_{ca} [cm/s]	exp#	sim#	u_{cf} [cm/s]	u_{ca} [cm/s]
874		8.523	67.41	911	140	18.43	189.3
875		8.523	85.73	912	141	18.43	278.2
876		8.523	102.3	913	142	18.43	434.0
877		8.523	132.5	914	143	18.43	608.3
878		8.523	190.1	915	144	18.43	786.2
879		8.523	275.9	916	145	18.43	958.7
880		8.523	441.1	917		18.43	1457
881		8.523	627.9	918	307	23.27	37.53
882		8.523	820.0	919	308	23.27	44.65
883		8.523	999.6	920	309	23.27	51.76
884		8.523	1498	921	310	23.27	58.7
885		13.82	44.47	922	311	23.27	66.52
886		13.82	53.34	923	312	23.27	73.46
887		13.82	60.65	924	313	23.27	80.22
888		13.82	71.33	925	314	23.27	90.00
889		13.82	80.58	926	315	23.27	102.3
890		13.82	93.03	927	316	23.27	123.3
891		13.82	112.1	928	317	23.27	144.1
892		13.82	138.9	929	318	23.27	206.3
893		13.82	186.9	930	319	23.27	291.0
894		13.82	285.5	931	320	23.27	421.6
895		13.82	467.8	932	321	23.27	595.9
896		13.82	656.4	933	322	23.27	773.7
897		13.82	836.0	934	323	23.27	951.6
898		13.82	953.4	935		23.27	1462
899		13.82	1451	1100		27.64	112.1
900	129	18.43	36.29	1101		27.64	119.9
901	130	18.43	41.80	1102		27.64	134.5
902	131	18.43	48.91	1103		27.64	151.4
903	132	18.43	57.27	1104		27.64	177.0
904	133	18.43	64.57	1105		27.64	246.2
905	134	18.43	71.50	1106		27.64	321.6
906	135	18.43	80.58	1107		27.64	442.9
907	136	18.43	89.65	1108		27.64	613.7
908	137	18.43	111.0	1109		27.64	795.1
909	138	18.43	127.9	1110		27.64	980.1
910	139	18.43	156.9	1111		27.64	1466
				1112		27.64	1467

Table E.11: Matrix of experimental conditions for $\Phi = 1.2$ co-flow and central air tube raised 3 mm.

exp#	sim#	u_{cf} [cm/s]	u_{ca} [cm/s]	exp#	sim#	u_{cf} [cm/s]	u_{ca} [cm/s]
1346		8.523	14.94	1381	188	18.43	24.01
1347		8.523	27.75	1382	189	18.43	43.22
1348		8.523	47.31	1383	190	18.43	58.34
1349		8.523	83.60	1384	191	18.43	71.15
1350		8.523	101.4	1385	192	18.43	85.91
1351		8.523	121.0	1386	193	18.43	101.4
1352		8.523	157.6	1387	194	18.43	117.6
1353		8.523	206.5	1388	195	18.43	135.0
1354		8.523	289.0	1389	196	18.43	154.0
1355		8.523	389.5	1390	197	18.43	181.4
1356		8.523	535.4	1391	198	18.43	210.8
1357		8.523	652.8	1392	199	18.43	267.9
1358		8.523	788.0	1393	200	18.43	358.8
1359		8.523	965.8	1394	201	18.43	569.2
1360		8.523	1466	1395	202	18.43	754.2
1361		8.523	1651	1396	203	18.43	933.8
1362		8.523	1829	1397		18.43	1469
1363		13.82	29.17	1398		18.43	1651
1364		13.82	43.22	1399		18.43	1830
1365		13.82	59.41				
1366		13.82	71.33				
1367		13.82	89.83				
1368		13.82	106.0				
1369		13.82	123.1				
1370		13.82	144.1				
1371		13.82	171.1				
1372		13.82	203.5				
1373		13.82	263.4				
1374		13.82	357.5				
1375		13.82	535.4				
1376		13.82	748.8				
1377		13.82	944.5				
1378		13.82	1471				
1379		13.82	1658				
1380		13.82	1836				

Table E.11 (cont.): Matrix of experimental conditions for $\Phi = 1.2$ co-flow and central air tube raised 3 mm.

exp#	sim#	u_{cf} [cm/s]	u_{ca} [cm/s]	exp#	sim#	u_{cf} [cm/s]	u_{ca} [cm/s]
1400	371	23.04	30.59	1421		27.64	48.56
1401	372	23.04	40.73	1422		27.64	57.81
1402	373	23.04	48.56	1423		27.64	68.30
1403	374	23.04	56.03	1424		27.64	76.66
1404	375	23.04	64.03	1425		27.64	88.94
1405	376	23.04	76.49	1426		27.64	103.0
1406	377	23.04	90.72	1427		27.64	118.1
1407	378	23.04	105.5	1428		27.64	133.0
1408	379	23.04	118.1	1429		27.64	152.4
1409	380	23.04	140.7	1430		27.64	185.7
1410	381	23.04	167.6	1431		27.64	230.9
1411	382	23.04	194.4	1432		27.64	324.3
1412	383	23.04	239.6	1433		27.64	430.5
1413	384	23.04	338.0	1434		27.64	601.2
1414	385	23.04	432.2	1435		27.64	777.3
1415	386	23.04	608.3	1436		27.64	932.1
1415	386	23.04	608.3	1437		27.64	1464
1416	387	23.04	784.4	1438		27.64	1656
1417	388	23.04	958.7	1439		27.64	1830
1418		23.04	1473				
1419		23.04	1651				
1420		23.04	1836				

Table E.12: Matrix of experimental conditions for $\Phi = 1.2$ co-flow and central air tube raised 6 mm.

exp#	sim#	u_{cf} [cm/s]	u_{ca} [cm/s]	exp#	sim#	u_{cf} [cm/s]	u_{ca} [cm/s]
1631		8.523	19.57	1660	276	18.43	34.33
1632		8.523	35.04	1661	277	18.43	57.99
1633		8.523	50.16	1662	278	18.43	82.36
1634		8.523	67.95	1663	279	18.43	109.2
1635		8.523	85.91	1664	280	18.43	134.5
1636		8.523	138.4	1665	281	18.43	159.2
1637		8.523	277.1	1666	282	18.43	174.1
1638		8.523	457.1	1667	283	18.43	193.7
1639		8.523	636.8	1668	284	18.43	236.4
1640		8.523	814.7	1669	285	18.43	299.2
1641		8.523	992.5	1670	286	18.43	383.1
1642		8.523	1466	1671	287	18.43	556.7
1643		8.523	1651	1672	288	18.43	768.4
1644		8.523	1834	1673	289	18.43	967.6
1645		13.82	18.50	1674		18.43	1467
1646		13.82	38.42	1675		18.43	1652
1647		13.82	66.52	1676		18.43	1820
1648		13.82	94.27				
1649		13.82	121.8				
1650		13.82	190.0				
1651		13.82	285.0				
1652		13.82	343.3				
1653		13.82	423.3				
1654		13.82	603.0				
1655		13.82	796.9				
1656		13.82	980.1				
1657		13.82	1469				
1658		13.82	1649				
1659		13.82	1836				

Table E.12 (cont.): Matrix of experimental conditions for $\Phi = 1.2$ co-flow and central air tube raised 6 mm.

exp#	sim#	u_{cf} [cm/s]	u_{ca} [cm/s]	exp#	sim#	u_{cf} [cm/s]	u_{ca} [cm/s]
1677	432	23.04	27.93	1695		27.64	26.15
1678	433	23.04	47.67	1696		27.64	38.60
1679	434	23.04	65.81	1697		27.64	54.78
1680	435	23.04	96.23	1698		27.64	72.57
1681	436	23.04	112.9	1699		27.64	81.82
1682	437	23.04	126.8	1700		27.64	94.98
1683	438	23.04	150.7	1701		27.64	110.6
1684	439	23.04	173.6	1702		27.64	135.2
1685	440	23.04	213.4	1703		27.64	166.8
1686	441	23.04	247.8	1704		27.64	210.6
1687	442	23.04	306.8	1705		27.64	248.0
1688	443	23.04	379.9	1706		27.64	299.2
1689	444	23.04	585.2	1707		27.64	387.8
1690	445	23.04	786.2	1708		27.64	492.7
1691	446	23.04	973.0	1709		27.64	633.2
1692		23.04	1466	1710		27.64	796.9
1693		23.04	1652	1711		27.64	973.0
1694		23.04	1843	1712		27.64	1467
				1713		27.64	1649
				1714		27.64	1830

Bibliography

- AYRANCI, I., VAILLON, R., SELÇUK, N., ANDRÉ, F., AND ESCUDIÉ, D., 2007. Determination of soot temperature, volume fraction and refractive index from flame emission spectrometry. *J. Quant. Spec. & Rad. Transfer*, 104:266–276.
- BERGTHORSON, J. M., 2005. *Experiments and modeling of impinging jets and pre-mixed hydrocarbon stagnation flames*. Ph.D. thesis, California Institute of Technology, Pasadena, CA.
- BURKE, S. P. AND SCHUMANN, T. E. W., 1928. Diffusion flames. *Indust. Eng. Chem.*, 20(10):998.
- CABRA, R., CHEN, J.-Y., DIBBLE, R. W., KARPETIS, A. N., AND BARLOW, R. S., 2005. Lifted methane-air jet flames in a vitiated coflow. *Combust. Flame*, 143:491–506.
- CHUNG, S. H. AND LAW, C. K., 1984. Burke-Schumann flame with streamwise and preferential diffusion. *Comb. Sci. Tech.*, 37:21–46.
- CROSLY, D. R., 1989. Semiquantitative laser-induced fluorescence in flames. *Combust. Flame*, 78:153–167.
- DALLY, B. B., KARPETIS, A. N., AND BARLOW, R., 2002. Structure of turbulent non-premixed jet flames in a diluted hot coflow. *Proc. Comb. Inst.*, 29:1147–1154.
- DASCH, C. J., 1992. One-dimensional tomography: a comparison of Abel, onion-peeling, and filtered backprojection methods. *App. Optics*, 31(8):1146–1152.
- DELABROY, O., HAILE, E., LACAS, F., CANDEL, S., POLLARD, A., SOBIESIAK, A., AND BECKER, H. A., 1998. Passive and active control of NO_x in industrial burners. *Exp. Thermal Fluid Sci.*, 16:64–75.

- DOCQUIER, N., BELHALFAOUI, S., LACAS, F., DARABHIA, N., AND ROLON, C., 2000. Experimental and numerical study of chemiluminescence in methane/air high-pressure flames for active control applications. *Proc. Comb. Inst.*, 28:1765–1774.
- FLECK, B. A., 1998. *Experimental and numerical investigations of the novel low-NO_x CGRI burner*. Ph.D. thesis, Queen’s University, Kingston, ON.
- FLECK, B. A., SOBIESIAK, A., AND BECKER, H. A., 2000. Experimental and numerical investigation of the novel low NO_x CGRI burner. *Comb. Sci. Tech.*, 161: 89–112.
- GOODWIN, D. G., 2003. An open-source, extensible software suite for CVD process simulation. *Proceedings of CVD XVI and EuroCVD Fourteen*. Electrochemical Society.
- GRANDMAISON, E. W., YIMER, I., BECKER, H. A., AND SOBIESIAK, A., 1998. The strong-jet/weak-jet problem and aerodynamic modelling of the CGRI burner. *Combust. Flame*, 114:381–396.
- GUO, H., LIU, F., SMALLWOOD, G. J., AND GÜLDER, Ö., 2002. The flame preheating effect on numerical modelling of soot formation in a two-dimensional laminar ethylene-air diffusion flame. *Comb. Theory Mod.*, 6:173–187.
- IKEDA, Y., KOJIMA, J., NAKALIMA, T., AKAMATSU, F., AND KATSUKI, M., 2000. Measurement of the local flamefront structure of turbulent premixed flames by local chemiluminescence. *Proc. Comb. Inst.*, 28:343–350.
- JONES, R. C., 1958. On the point and line spread functions of photographic images. *J. Optical Society America*, 48(12):934–937.
- KAMAL, M. M., 2008. Innovative study of co-axial normal and inverse diffusion flames. *Proc. IMechE, Part A: J. Power and Energy*, 222:253–270.
- KO, Y.-C., HOU, S.-S., AND LIN, T.-H., 2005. Laminar diffusion flames in a multiport burner. *Comb. Sci. Tech.*, 177:1463–1484.
- KOJIMA, J., IKEDA, Y., AND NAKAJIMA, T., 2005. Basic aspects of OH(A), CH(A), and C₂(d) chemiluminescence in the reaction zone of laminar methane-air premixed flames. *Combust. Flame*, 140:34–45.

- LAW, C. K., 2006. *Combustion physics*. Cambridge University Press.
- LEE, B. J. AND CHUNG, S. H., 1997. Stabilization of lifted tribrachial flames in a laminar nonpremixed jet. *Combust. Flame*, 109:163–172.
- DE LEO, M., SAVELIEV, A., KENNEDY, L. A., AND ZELEPOUGA, S. A., 2007. OH and CH luminescence in opposed flow methane-oxy flames. *Combust. Flame*, 149: 435–477.
- MARLEY, S. AND ROBERTS, W., 2005. Measurements of laminar burning velocity and markstein number using high-speed chemiluminescence imaging. *Combust. Flame*, 141:473–477.
- MCENALLY, C. S., KÖYLÜ, Ü. Ö., PFEFFERLE, L. D., AND ROSNER, D. E., 1997. Soot volume fraction and temperature measurements in laminar nonpremixed flames using thermocouples. *Combust. Flame*, 109:701–720.
- MILLER, J. A. AND BOWMAN, C. T., 1989. Mechanism and modeling of nitrogen chemistry in combustion. *Prog. Energy Comb. Sci.*, 15:287–338.
- NORI, V. N. AND SEITZMAN, J. M., 2009. CH* chemiluminescence modeling for combustion diagnostics. *Proc. Comb. Inst.*, 32:895–903.
- ÖZDEMİR, I. B. AND PETERS, N., 2001. Characteristics of the reaction zone in a combustor operating at mild combustion. *Exp. Fluids*, 30:683–695.
- PARTRIDGE, JR., W. P., REISEL, J. R., AND LAURENDEAU, N. M., 1999. Laser-saturated fluorescence measurements of nitric oxide in an inverse diffusion flame. *Combust. Flame*, 116:282–290.
- PLESSING, T., PETERS, N., AND WÜNNING, J. G., 1998. Laseroptical investigation of highly preheated combustion with strong exhaust gas recirculation. *Proc. Comb. Inst.*, 27:3197–3204.
- RAY, S. F., 1988. *Applied Photographic Optics*. Focal Press.
- RENFRO, M. W., CHATURVEDY, A., AND LAURENDEAU, N. M., 2001. Semi-quantitative measurements of CH concentration in atmospheric-pressure counter-flow diffusion flames using picosecond laser-induced fluorescence. *Comb. Sci. Tech.*, 169:25–43.

- ROPER, F. G., 1977. The prediction of laminar jet diffusion flame sizes: Part I. Theoretical model. *Combust. Flame*, 29:219–226.
- SCHEFER, R. W., 1997. Flame sheet imaging using CH chemiluminescence. *Comb. Sci. Tech.*, 126:255–270.
- SINGLA, G., SCOUFLAIRE, P., ROLON, C., AND CANDEL, S., 2005. Transcritical oxygen/transcritical or supercritical methane combustion. *Proc. Comb. Inst.*, 30:2921–2928.
- SMITH, G. P., GOLDEN, D. M., FRENKLACH, M., MORIARTY, N. W., EITENEER, B., GOLDENBERG, M., BOWMAN, C. T., HANSON, R. K., SONG, S., W. C. GARDINER, J., LISSIANSKI, V. V., AND QIN, Z. GRI-MECH 3.0. http://www.me.berkeley.edu/gri_mech/.
- SNELLING, D. R., THOMSON, K. A., SMALLWOOD, G. J., AND GÜLDER, Ö., 1999. Two-dimensional imaging of soot volume fraction in laminar diffusion flames. *App. Optics*, 38:2478–2485.
- SOBIESIAK, A., RAHBAR, S., AND BECKER, H. A., 1998. Performance characteristics of the novel low-NO_x burner for use with high air preheat. *Combust. Flame*, 115:93–125.
- SOBIESIAK, A. AND WENTZELL, J. C., 2005. Characteristics and structure of inverse flames of natural gas. *Proc. Comb. Inst.*, 30:743–749.
- WALSH, K. T., LONG, M. B., TANOFF, M. A., AND SMOOKE, M. D., 1998. Experimental and computational study of CH, CH*, and OH* in an axisymmetric laminar diffusion flame. *Proc. Comb. Inst.*, 27:615–623.
- WEBER, R., ORSINO, S., LALLEMANT, N., AND VERLAAN, A., 2000. Combustion of natural gas with high-temperature air and large quantities of flue gas. *Proc. Comb. Inst.*, 28:1315–1321.
- WEBER, R., ORSINO, S., VERLAAN, A. L., AND LALLEMANT, N., 2001. Combustion of light and heavy fuel oils in high-temperature air. *J. Inst. Energy*, 74:38–47.
- WEBER, R., VERLAAN, A. L., ORSINO, S., AND LALLEMANT, N., 1999. On emerging furnace design methodology that provides substantial energy savings and drastic reductions in CO₂, CO and NO_x emissions. *J. Inst. Energy*, 72:77–83.

- WEBER, R., SMART, J. P., AND VON DER KAMP, W., 2005. On the (MILD) combustion of gaseous, liquid, and solid fuels in high temperature preheated air. *Proc. Comb. Inst.*, 30:2623–2629.
- WENTZELL, J. C., 1998. *Characteristics and Structure of Inverse Flames of Natural Gas*. Master's thesis, Queen's University, Kingston, ON.
- WU, K.-T. AND ESSENHIGH, R. H., 1984. Mapping and structure of inverse diffusion flames of methane. *Proc. Comb. Inst.*, 20:1925–1932.
- WÜNNING, J. A. AND WÜNNING, J. G., 1997. Flameless oxidation to reduce thermal NO-formation. *Prog. Energy Comb. Sci.*, 23:81–94.
- YANG, W. AND BLASIAK, W., 2005. Numerical simulation of properties of a LPG flame with high-temperature air. *Int. J. Thermal Sci.*, 44:973–985.
- YOO, S. W., LAW, C. K., AND TSE, S. D., 2002. Chemiluminescent OH* and CH* flame structure and aerodynamic scaling of weakly buoyant, nearly spherical diffusion flames. *Proc. Comb. Inst.*, 29:1663–1670.

Vita Auctoris

Michael Bernard Johnson was born (Michael Bernard Niederhoffer) in Vancouver, B.C. on April 22, 1977. He attended Queen's University, where he obtained his Bachelor of Science, Engineering, in Mathematics and Engineering, Applied Mechanics option. He received his Master of Science degree in 2000, and his Engineer degree in 2005, both in Aeronautics, from the California Institute of Technology.